Development of optofluidic fiber-based SERS platform for efficient biosensing applications

Amine Benazza

Ph.D. Thesis

Université de Limoges

University of Limoges

ED 653 - Sciences et Ingénierie (SI)

XLIM CNRS UMR-7252 Fiber photonics and coherent sources
Translational Biophotonics Lab, Institute of Bioengineering and Bioimaging, Agency for Science Technology and Research, A*STAR

A thesis submitted to University of Limoges
in partial fulfillment of the requirements of the degree of

Doctor of Philosophy

High Frequency Electronics, Photonics and Systems

Presented and defensed by

Amine BENAZZA

October 22, 2024

Development of optofluidic fiber-based SERS platform for efficient biosensing applications

Thesis supervisor:

XLIM Research Institute:

Dr. Georges Humbert	Director of Research CNRS - XLIM
Dr. Jean-Louis Auguste	Research Engineer CNRS - XLIM

A*STAR:

Assoc. Prof. Dinish U. S	Principal Scientist in A*STAR

JURY:

Reporters

Prof. Marc Lamy de la chapelle	University Professor - Le Mans University
Prof. Olivier Piot	University Professor - University of Reims

Examiners

Prof. Stefan Andersson-Engels	Head of Biophotonics, Tyndall, University College Cork

Dedication

I dedicate my manuscript to my parents, FZ&H, for your unwavering love and unwavering belief in me!

Amine BENAZZA

Acknowledgements

This work is supported by institutional grants from the National Research Agency under the Investments for the future program with the reference ANR-18-EURE-0017 TACTIC, the ANR-NRF grant NRF2021-NRF-ANR002 FUNSENS, the project “FibOsome” funded by Nouvelle Aquitaine. This work was conducted within the frame of the International Research Project “FiberMed” from CNRS, A*STAR and Univ. Limoges.

The work of this thesis was carried out at the Xlim Research Institute in the University of Limoges in collaboration with the Translational Biophotonics Laboratory (TBL), A*STAR Singapore. Therefore, I would like to express my deepest gratitude to these organizations for the hospitality, trust, funding, and support they provided me throughout this journey.
Secondly, I would like to thank the members of the jury for evaluating my work. I am grateful to Professor Marc LAMY DE LA CHAPELLE, University Professor at Le Mans University, and Professor Olivier PIOT, University Professor at the University of Reims, for agreeing to rigorously review this work. I also extend my thanks to Professor Stefan Andersson-Engels, Head of Biophotonics at Tyndall, University College Cork, for examining it. I appreciate your interest in this thesis work, as well as the questions, remarks, and suggestions that have contributed to improving this manuscript.

I am immensely grateful to my two direct supervisors, Dr. Georges Humbert in France and Dr. Dinish U.S. in Singapore, for their invaluable guidance and unwavering support throughout these three years. This thesis is the product of the remarkable collaboration between XLIM and TBL, particularly thanks to the synergy between Georges and Dinish. I deeply appreciate their willingness to include me in this project and their invaluable advice throughout my Ph.D. journey. I want to express my heartfelt gratitude to Dr. Jean-Louis Auguste for his expertise and assistance during the fiber fabrication, and my deepest thanks also to Prof. Malini Olivo from Singapore.

In France, I extend my thanks to Flavien Beffara, who was a postdoctoral researcher at the start of my thesis. His guidance in fibers, Raman spectroscopy, and SERS was invaluable. My thanks also go to Sébastien Rougier for the time he dedicated to taking the SEM pictures. Lastly, I want to extend my gratitude to the team and everyone who contributed in any way during my time at XLIM. While the list is far from exhaustive, I want to specifically mention Philippe, Raphaël, Baptiste, Romain, Lynn, Mohamed, Ali, Joelle, Ardi and all those whom I may unintentionally overlook.
In Ireland, my deepest thanks to Professor Stefan Andersson-Engels and Dr. Rekha GAUTAM for the hospitality and their help and support to facilitate my stay in Ireland. Thanks also to Siddra and Sanathana for their help during my experiments at Tyndall. Thanks also to my friends at tyndall; Daniyal, Hui, Suraj, Kasia for all the moments we shared during my stay. Finally, my gratitude goes out to the whole Biophotonics group for embracing me so warmly specially Sarah Donovan. I hope our paths cross again in the near future.

To my wonderful parents, I thank you for your support and sacrifices for me. Words cannot fully express my love and gratitude. To my brothers, and my sisters, thank you for your unconditional support and love. Thank you for everything

Rights

Table of Contents

Acknowledgements 3
Rights 4
Table of Figures 8
List of Tables 16
Abbreviations 17
Introduction 22
Chapter I. State of art on SERS-based biosensing probes 27
I.1. Introduction to Raman spectroscopy method 27
I.1.1. Brief history of Raman spectroscopy 27
I.1.2. Principle of Raman scattering 27
I.1.3. Applications and limitations of Raman spectroscopy 29
I.1.3.1. Applications 29
I.1.3.2. Limitations of Raman spectroscopy 30
I.2. Principle of Surface-Enhanced Raman Spectroscopy (SERS) 30
I.2.1. History 30
I.2.2. Principle of Surface-Enhanced Raman Spectroscopy 32
I.2.2.1. Electromagnetic mechanism 32
I.2.2.2. Chemical Enhancement 34
I.2.3. Factors influencing the SERS enhancements 35
I.2.3.1. Effect of metallic nature on SERS enhancement 35
I.2.3.2. Size and shape impact on SERS response 37
I.2.3.3. Distance dependence of SERS enhancement 38
I.2.3.4. Raman cross-section of molecules 40
I.3. SERS-based substrates sensors 40
I.3.1. Principal features of SERS substrates 41
I.3.2. SERS substrates for direct detection 42
I.3.2.1. Colloidal solutions for SERS 43
I.3.2.2. Nanoparticle immobilization on Planar Substrates 44
I.3.2.3. Nanopatterning: structured surfaces 47
I.3.2.4. Applications: Label-free detection. 51
I.3.3. SERS Nanotags for indirect detection 52
I.3.3.1. SERS Nanotags features 52
I.3.3.2. Applications: Labeled detection 53
I.4. SERS-Active Photonic Crystal Fiber probes 55
I.4.1. Introduction 55
I.4.2. Hollow- and solid-core Photonic Crystal Fibers 56
I.4.2.1. Hollow-core Photonic Crystal Fibers 56
I.4.2.2. Solid-core Photonic Crystal Fibers 58
I.4.3. Interests of PCFs for SERS sensing 59
I.4.3.1. State-of-the-art in PCF SERS-sensing 60
I.4.3.2. Method of functionalization of the PCFs for SERS 61
I.4.3.3. The performance of SERS-active PCFs 61
I.4.4. Biosensing applications of SERS-based PCFs 67
I.4.5. Objectives of this thesis 73

I.4.6. Conclusion 73
Chapter II. Tapered-SuC-PCF, a novel approach to create easy-to-use SERS-based fiber sensors 78
II.1. Experimental setup for opto-fluidic fiber based SERS spectroscopy....78
II.1.1. Presentation of the setup developed at XLIM....78
II.1.2. Evaluation of SERS perfermances of SuC-PCF in different configurations....81
II.1.2.1. Comparison of SERS measurements in a cuvette and in SuC-PCF using the injected configuration 82
II.1.2.2. Evaluation of SERS performances of SuC-PCFs using the anchored configuration with an injected solution....84
II.1.3. Comparison of SERS sensitivity and reliability for different core sizes of SuC-PCFs using the anchored configuration....85
II.2. Development of high perfermance and user-friendly SERS fiber probes....88
II.2.1. Improvement of the coupling between the fiber and the excitation laser on XLIM setup..88
II.2.2. Towards tapered-SuC-PCF for associating SERS sensitivity and efficient fiber coupling 90
II.2.3. Development of Tapered-PCFs as sensitive, reliable and user-friendly SERS fiber probes 92
II.2.3.1. Fabrication process of 6 µm core size SuC-PCF....92
II.2.3.2. Fabrication of tapered-SuC-PCF 95
II.2.3.3. Evaluation of the coupling efficiency of the tapered-PCF 98
II.2.3.4. Evaluation of SERS perfermances of the tapered-PCF 99
II.2.3.5. Development of a plug-and-play system for SERS sensing. 101
II.3. Conclusion 102
Chapter III. Investigating Nanoparticle Properties in SERS-active PCFs....106
III.1. Relationship between the excitation wavelength and the LSPR peak position....107
III.2. Investigation of 60 nm BBI Au Nanospheres (Au NP) 108
III.2.1. Absorption characteristics of Au NP....108
III.2.2. Transmission measurements of fibers functionalized with NPs 109
III.2.3. Comparison of SERS signal measured with different concentration of Au NPs & fiber length....112
III.2.4. Investigations of different NPs inside the SuC-PCFs using anchored configuration 114
III.2.4.1. Silica-Core Gold Nanoshell....114
III.2.4.2. Hollow-Core Gold Nanoshell 117
III.2.4.3. Gold Nanostars....118
III.2.5. SERS performances of the different NPs....119
III.2.5.1. Comparison of SERS signal measured from cuvette and fiber (injected configuration) 119
III.2.5.2. Comparison of SERS signal of different NPs functionalized into fibers with the anchored configuration 121
III.2.6. Numerical study of nanoparticles properties 122
III.2.6.1. Simulation....122
III.2.6.2. FDTD simulation of Gold Nanospheres and comparison with the Mie theory 123
III.2.6.3. Limitation of the FDTD method....123
III.2.6.4. Electric field localization near the surface of Au NPs with different diameter 125
III.2.6.5. Electromagnetic properties of different nanoparticles 127
- Silica-Core gold Nanoshell 127
- Hollow-Core gold Nanoshell....129
III.2.6.6. Correlation between absorption factor and Electric field intensity 130

III.2.7. Conclusion 132
Chapter IV. Biosensing applications using SuC-PCFs 136
IV.1. Disease biomarkers detection in liquid saliva by Raman spectroscopy using an opto-fluidic fiber 136
IV.1.1. Study context 136
IV.1.2. Investigation of Raman spectroscopy of liquid saliva with an opto-fluidic fiber 138
IV.1.2.1. Setup developed at Tyndall institute 138
IV.1.2.2. Sample preparation 139
IV.1.2.3. Results 140
IV.2. Optofluidic fiber with sandwich-based SERS method 141
IV.2.1. Context 141
IV.2.2. Protocol of sandwich-based SERS immuno-detection of TNF-alpha into an SuC-PCF 144
IV.2.3. Results 145
IV.2.4. Conclusion 147
General conclusion and Perspectives 152
Bibliogphy 155
Published work and conferences 168

Table of Figures

Figure 1 Illustration of the two scattering phenomena when a monochromatic beam excites a molecule. 28

Figure 2 Energy diagram illustrating Rayleigh, Stokes and Anti-Stokes Scattering. 29

Figure 3 (a) Raman spectrum of a silver electrode immersed in 0.2 M KCI. (b) Raman spectrum of 50 mM aqueous pyridine and 0.1 M KC1. (c) Raman spectrum of pyridine adsorbed on a silver electrode from a bulk solution of 50 m M pyridine and 0.1 M KCI. Reproduced from [18]. 31

Figure 4 (a) Illustration of the cloud of electrons delocalized when an electromagnetic wave interacts with metallic NPs (b) Spatial distribution of $|E|^2$ around the spherical silver NP of 70 nm diameter in vacuum at LSPR wavelength. Reproduced from [21]. 32

Figure 5 The main values of the (a) real and (b) the imaginary part of the permittivity for silver (Ag), copper (Cu), gold (Au) and aluminum (Al), according to the incident wavelength. Reproduced from [36]. 36

Figure 6 Excitation wavelength of conduction electrons of principal metals used in SERS. Reproduced from [39]. 36

Figure 7 (A) LSPR peaks showing λmax shift towards shorter wavelength after chronocoulometry measurements. (B) Atomic force microscopy (AFM) images before electrochemical measurements. LSPR $\lambda max = 654\ nm$. (solide line). (C) AFM image after one chronocoulometry measurement. LSPR $\lambda max = 579\ nm$ (dashed line). (D) AFM image after two chronocoulometry measurements. LSPR $\lambda max = 506\ nm$ (dotted line). Reproduced from [41]. 37

Figure 8 Diversity in plasmonic nanostructures with different sizes and shapes. Reproduced from [44]. 38

Figure 9 (a) SERS spectra of pyridine molecule adsorbed on different value of thicknesses of AL_2O_3 film coated on AgFON. (b) Behavior of normalized SERS intensity of Raman peak 1594 cm^{-1} of pyridine in function of alumina thicknesses. Reproduced from [49]. 39

Figure 10 Variation of the SERS signal of the 2892 cm^{-1} peak of trimethyl aluminum with the distance from the film of AgFON. In the insets, A picture of the Ag film over Nanospheres taken by scanning electron microscopy (SEM) and a simulation of the electric field are presented. Reproduced from [50]. 40

Figure 11 Diagram illustrating the evolving characteristics of SERS structures from the unstructured to the highly structured type. Reproduced from [51]. 41

Figure 12 Illustrations depicting the concepts of reproducibility and repeatability of SERS measurements. 42

Figure 13 Illustration of the chemical reduction process for synthesizing colloidal Ag NPs. Silver ions (Ag+) are transformed into silver atoms (Ag) through a chemical reduction process. These atoms undergo nucleation to create primary Ag NPs, which then continue to merge with each other, ultimately resulting in the formation of the final Ag NPs. Reproduced from [55]. 43

Figure 14 (a) Diagram depicting the process for anchoring Au NPs onto a quartz substrate. (b) Scanning Electron Microscopy (SEM) image revealing the Au NPs successfully immobilized on the quartz substrate. Reproduced from [65]. 45

Figure 15 (a) SEM image displaying the deposition of Au NPs on filter paper. (b) SERS spectra of TNT with concentrations indicated. The inset illustrates the change in SERS intensity of the NO_2 band relative to concentration. Reproduced from [66]..... 45

Figure 16 (a) Transmission electron microscopy (TEM) images depicting the cross-sectional profile of Ag SIMO glass samples subjected to 30 seconds of ion exchange with a) 13.000x, b) 87.000x and c) 380.000x magnification. The inset displays both the size distribution and statistical outcomes related to the subsurface area, denoted as Area 1 (b). Reproduced from [68]. 46

Figure 17 Illustration outlining the procedure for creating substrates with porous anodic alumina filled with silver. Reproduced from [69]. 47

Figure 18 (a) Microscopic view of silicon surfaces featuring an array of microsquares. (b) SEM images captured within these squares showing laser ablation effects at a fluence of 21.0 J/cm^2. Reproduced from [70]. 48

Figure 19 Diagram illustrating template methods for creating SERS-active substrates using nanosphere lithography. Reproduced from [75]. 49

Figure 20 Illustration of the two fabrication procedures employed for the preparation of nanostructured SERS substrates. Reproduced from [81]. 50

Figure 21 Illustration of the various stages of NIL employed by Ou *et al.* for the fabrication of nanopillars. Reproduced from [83]..... 50

Figure 22 The method employed for prostate cancer detection involves the extraction of RNA from urine, followed by the measurement of the SERS signal. Reproduced from [84]..... 51

Figure 23 Illustration of a SERS tag composed of a plasmonic core, Raman reporter. Reproduced from [95]. 52

Figure 24 Illustration of the sensor used for the molecular sentinel (MS) technique. Reproduced from [15]. 54

Figure 25 Design and scheme for a SERS-based immunoassay chip: (A) utilization of a capture substrate to selectively extract and concentrate antigens from a solution; (B) application of surface-functionalized Au NPs (ERLs) to selectively bind to captured antigens, producing robust SERS signals; and (C) implementation of a sandwich immunoassay with SERS readout. Reproduced from [112]. 55

Figure 26 Cross-section of (a) HC-PCF [118]. (b) Kagome PCF [119]. (c) NANF [120]. (d) LC-PCF [121]. 56

Figure 27 (a) Transmission spectra of the 1060 nm fiber obtained using supercontinuum source, and (b) of the 1550 nm fiber obtained using a tungsten lamp. The spectra were recorded both before and after the holes of the HC-PCF were filled with liquid D2O, indicated by the light and dark grey areas, respectively. The vertical lines denote the positions of the newly shifted bandgaps, while the arrows indicate the location of the respective transmission peaks. Reproduced from [123] 57

Figure 28 SEM pictures of the Cross-sections of (a) SC-PCF [128]. (b) SuC-PCF [129]. (c) SiC-PCF [130]. (d) Core-array PCF [131]..... 59

Figure 29 Illustration of the sensor used for the molecular sentinel (MS) technique c'est quoi ce terme, il faut le définir. Je pense qu'il est plus simple de décrire SERS applications for biosesing. 60

Figure 30 Schematic representation includes (a) the injected configuration, in which Au NPs and the analyte are pre-mixed and then pumped into the fiber; (b) the anchored configuration, where ATP is

pumped into the fiber, binding to immobilized Au NPs within the fiber holes; and (c) the backscattering configuration. Reproduced from [144]. 61

Figure 31 SERS spectra for a 10^{-5} M solution of Rhodamine 6G and the corresponding hyperspectral Raman images were recorded at the end of (a) an SC-PCF and (b) an HC-PCF treated with Ag NPs. Reproduced from [145]. 62

Figure 32 SERS intensity of 10^{-6} M R6G varies with the length of the fiber, as depicted for (a) solid-core PCF (b) hollow-core PCF. The Raman excitation wavelength was 632.8 nm, with a laser power of 5 mW and an acquisition time of 60 s. Reproduced from [145]. 63

Figure 33 (a) SERS spectrum of R6G demonstrating changes in the intensity of the Raman peak with the length of HC-PCF. (b) Changes in the EF of the Raman peak at 1357 cm^{-1} with the length of HC-PCF. Reproduced from [146]. 64

Figure 34 Variation of SERS intensity with the concentration of R6G solution. (Inset) Displays SERS spectra for various concentrations of R6G solutions. Reproduced from [130]. 65

Figure 35 SERS spectra of various concentrations of R6G (0.5×10^{-13} and 5×10^{-12} M) were obtained using a SERS-active capillary. Additionally, a normal Raman spectrum (NRS) of 1×10^{-2} M R6G in solution within a glass cuvette (dimensions: 10 mm × 10 mm × 10 mm) was recorded with 10x magnification. Reproduced from [131]. 66

Figure 36 (a) SEM picture of the cross-section of a 3H-PCF (SuC-PCF). (b) Variations in the Raman intensity the ATP peak at 1080 cm^{-1} for 14 measurements from the optimized SuC-PCF SERS-platform. Corresponding Raman spectra are plotted in the inset. Reproduced from [151]. 67

Figure 37 (a) Transmission spectra of the HC-PCF filled with air (red dashed line) and with water (blue continuous line). The excitation line at 532 nm (green dashed line) and the spectral range (green band) considered in our Raman experiments are also shown. (b) Comparison between Raman spectra acquired by direct sampling (blue, black lines) and using the HC-PCF (red lines) of Mb at 1 mM (black lines) and 50 μM (blue, red lines). (c) Raman spectra of Aβ42 acquired by direct sampling (blue lines) and with an HC-PCF (red lines): 40 μg⁄ml. Shaded regions identify amide I (red) and amide III (blue) bands of Aβ. Reproduced from [154]. 68

Figure 38 (a) Concentration-dependent Raman intensities of glucose (1,127 cm^{-1}) measured by the liquid-filled PCF probe. Each datum indicates five measurements for each PCF sample. Each error bar indicates the standard deviation (b) Raman spectra of (a) glucose, (b) fructose and (c) mixture of glucose and fructose. Reproduced from [155]..... 69

Figure 39 (A) Comparison of the antibiotic Raman spectrum obtained by the HC-PCF (red) and the conventional Raman spectrum (black) of 20 μM moxifloxacin with an excitation laser at 532 nm. (B) Raman intensity dependency from the drug concentration (HC-PCF (red), conventional (black)). A very good linearity and thus a robust calibration can be achieved. The inset shows the chemical structure of moxifloxacin. Reproduced from [156]. 69

Figure 40 Raman spectrum of a biogenic multigas composition, consisting of climate relevant gases CO_2 , CH_4 , and N_2O together with N_2 , O_2 (each ~1 vol %, in Raman inactive argon carrier gas), which was acquired with one single measurement within a 40 ms acquisition time. Reproduced from [156]. 70

Figure 41 Raman spectra of 40 μg⁄ml Aβ42 achieved with a bare HC-PCF (blue line) and with the AuBPs-coated HC-PCF (red line). Reproduced from [154]..... 70

Figure 42 (a) Enhancement of Raman signal of HL60 cells in HC-PCF using silver NPs. (b) SERS spectra of different concentrations of live HL60 cells, expressed as cells/ml. Reproduced from [158]. 71

Figure 43 (a) Schematic of HC-PCF as a SERS platform. (b) Schematic of the bending of anti-EGFR antibody-conjugated SERS tags to the target proteins immobilized on the inner wall of the core of HC-PCF. Reproduced from [160]. 72

Figure 44 (A) Raman spectra of cells under different CH concentrations. (B) Intensity curve of the alkyne Raman peak at 2113 cm^{-1}. Reproduced from [162]..... 72

Figure 45 (a) The Raman setup used for Raman and SERS measurements. The inset picture illustrates the cross-section of the fiber and the position of the laser beam on the fiber core, corresponding to the alignment at the maximum Raman signal. (b) The Raman spectrometers used for the SERS measurements. 79

Figure 46 Picture of the fiber cross-section (a) before measurements and (b) during the measurement at the optimal Raman signal 79

Figure 47 comparison of the silica signal after and before setup improvement using 3.5 µm-PCF. 80

Figure 48 (a) Diagram illustrating the functionalization process of SuC-PCF holes with Au NPs and the subsequent binding of ATP molecules. (b) Depiction of APTES interactions with the metallic NPs. 82

Figure 49 (a) Schematic of the cuvette used for SERS measurements. (b) Image of the end of the capillary fiber filled with CV. (c) SERS spectrum of 100 nM of CV into the 3.5 µm-PCF (black curve), the capillary fiber (red curve) and in the cuvette (blue curve) using injected configuration. ... 83

Figure 50 SERS spectrum of CV with different concentrations using injected configuration measured in the 3.5 µm-PCF. 84

Figure 51 SERS spectrum of R6G with different concentration using injected configuration measured with 3.5 µm-PCF. 85

Figure 52 The schematic representing how the ATP molecule binds to the metallic NP. 85

Figure 53 (a) Picture of the entry face of the 3.5µm-PCF. (b) Picture of the input of the 3.5µm-PCF excited by focusing the laser directly into the core using 40x objective lens. (c) SERS spectrum of ATP measured within 3.5 µm-PCF, the two main peaks are located at 1080 cm^{-1} and 1590 cm^{-1}. 86

Figure 54 (a) SERS spectrum of 1 mM of ATP molecule using different fibers. (b) Normalized SERS intensity of 1080 cm^{-1} of 1 mM of ATP measured with 3.5 µm-PCF with different core sizes. SD in average normalized SERS intensity with black lines. (c) ATP SERS spectra measured with different concentrations using 2 µm-PCF. 87

Figure 55 Visualization of laser beam spot diameter measurement 89

Figure 56 (a) Design of SuC-PCFs with varying core sizes used in the simulation. (b) Random distribution of the laser beam center sampled 200 times within a 1 µm radius circle centered on the fiber. (c) Maximum and average coupling coefficients for SuC-PCFs with various core diameters. ... 90

Figure 57 (a) Schematic of the structure used in the simulation to approximate the reel design of the SuC-PCF. 1 represents the silica core. 2 represents the effective layer and 3 represents water. (b) Fundamental mode simulation for a 1 µm rod with an effective layer and water surrounding. The bar represents the color scale..... 91

Figure 58 Variation of percentage of HE11 mode intensity in the effective layer of SuC-PCFs with different core sizes..... 91

Figure 59 Schematic illustrating the design of the tapered- PCF. 92

Figure 60 (a) Schematics of the different steps during the stack and draw process. 93

Figure 61 (a) Schematics of the systems of the pressure using while the drawing of (a) the cane and (b) the fiber. The blue sections on the top view of the stack preform means that the capillaries are closed during the drawing. The notations P- and P+ represent respectively the application of the vacuum and the pressure during the drawing. 94

Figure 62 SEM pictures of SuC-PCFs fabricated with different sizes of the core: (a) 2 µm, (b) 3.5 µm, 6 µm and (d) Zoom-in on the fiber core of 6 µm-PCF. 95

Figure 63 fabricated taper in the waist part in first attempt. The target outer diameter was 200 µm.... 96

Figure 64 (a) Fabricated taper with the preserved inner structure in the waist part. (b) zoom-in on the core region for the fabricated taper. 97

Figure 65 (a) Variation of the outer diameter with Z-position obtained for the first attempt. (b) Variation of the outer diameter with Z-position for the fabricated taper. The red and blue curves represent the variation of the X and Y center of the fiber relative to the screen, respectively. 97

Figure 66 (a) Setup used for light transmission measurements. Pin: laser power measured just after the objective lens. Pout: laser power measured at the fiber output. (b) Coupling loss measurements for (Black) 6 µm-PCF, (Red) Tapered-PCF, (blue) 3.5 µm-PCF and (Magenta) 2 µm-PCF. 98

Figure 67 (a) SERS spectra of ATP molecules using 1 mm cuvette, 2 µm-PCF, 6 µm-PCF, and Tapered-PCF. (b) Close-up image of the spectral intensity at the 1080 cm^{-1} peak. 99

Figure 68 SERS intensity variations of the 1080 cm^{-1} Peak for ATP (Seven Measurements) from (a) a single 2 µm-PCF fiber and (b) a single tapered fiber. Error bars indicate the standard deviation across the seven measurements. Variation in peak SERS intensity at 1080 cm^{-1} using (c) five distinct 2 µm-PCF fibers and (d) Six distinct tapered fibers. 100

Figure 69 (a) Experimental setup for SERS measurements using the Plug and Play system. The inset image shows a photograph of the Plug and Play system with the Tapered-PCF inserted into a Bare Fiber Connector. (b) SERS intensity variations of the 1080 cm^{-1} Peak for 1 mM ATP (Fourteen Measurements) and (c) 100 nM ATP (Thirteen Measurements) with the PCF-Tapered inserted in the system. Error bars represent the SD of all measurements. 101

Figure 70 (a) Diagram of the dimer displaying the gap (g) between two NPs, with the excitation light polarized along the primary axis. (b) Coefficient of extinction versus wavelength for a single Au NP and for the dimer with various gaps. (c) SERS EF for several gaps between the two Au NPs compared to a single Au NP, with the dashed line indicating the average SERS enhancement across the full metallic surface for a dimer with a gap of 2 nm. Reproduced from [35]. 106

Figure 71 (a) Variation of the SERS EF of the 1081 cm^{-1} peak of benzenethiol (dashed line) (679.27 nm) with an excitation wavelength of 632.8 nm (solid line). Reproduced from [170]. (b) Surface-enhanced Raman excitation spectra of the 1081 cm^{-1} of benzenethiol, LSPR = 690 nm, maximum of the profile fit at 662 nm. (c) The excitation spectra of benzenethiol at 1575 cm^{-1}, enhanced by surface plasmon resonance with a wavelength of 810 nm, exhibit a profile fit maximum at 765 nm. Reproduced from [28]. 108

Figure 72 Absorption spectrum of single 60 nm Gold Nanosphere. Reproduced from [172]. 109

Figure 73 Schematic of the optical setup used for measuring the transmission spectrum of 3.5 µm-PCF with anchored NPs..... 109

Figure 74 Transmission spectrum of the supercontinuum source through 10 cm long length of an empty fiber of 3.5 µm-PCF 110

Figure 75 Transmission spectrum of the supercontinuum source through 10 cm long length of an empty 3.5 µm-PCF (bleu curve) and functionalized 3.5 µm-PCF with Au NPs (red curve). 110

Figure 76 Transmission spectrum of the supercontinuum source through 10 cm long length of functionalized 3.5 µm-PCF with different fiber lengths (from 4 to 12 cm) for (a) 0.25x, (b) 0.50x; (c) 0.75x and (d) 1.0x of Au NP concentrations. 112

Figure 77 SERS spectra of 1 mM of ATP with functionalized 3.5 µm-PCF with Au NPs and zoomed around the main Raman peak at 1080 cm^{-1}. 113

Figure 78 (a) TEM image of 150 nm of SC-AuNSH and (b) absorption spectrum of 150 nm of SC-AuNSH. Reproduced From NanoComposix. 115

Figure 79 Transmission spectrum of the supercontinuum source through 10 cm long length of empty fiber and different functionalized 3.5 µm-PCFs with (a) 0.25x, (b) 0.50x; (c) 0.75x and (d) 1.0x of SC-AuNSH concentrations. 115

Figure 80 Transmission spectrum of the supercontinuum source through functionalized 3.5 µm-PCFs with a concentration of (a) 0.01x and (b) 0.05x of SC-AuNSH with different fiber lengths. (c) SERS signal of 1 mM of ATP using functionalized 3.5 µm-PCFs with different concentrations of SC-AuNSH. 117

Figure 81 (a) TEM images of HC-AuNSHs with a total diameter of 60 nm and gold shell of 7 nm. (b) Absorbance spectra of HC-AuNSHs with different diameters. Reproduced from [177] 117

Figure 82 Transmission spectrum of the supercontinuum source through 10 cm long length of functionalized 3.5 µm-PCF with HC-AuNSH (red curve) and through empty fiber (bleu curve). Inset image represents the transverse section of the output side of the fiber. 118

Figure 83 (a) TEM images of Nanostars used in the study. (b) Absorption spectrum of 130 nm Nanostars. Reproduced from [177] (c) Transmission spectrum of the supercontinuum source through 10 cm long length of functionalized 3.5 µm-PCFs with Nanostars. Inset image represents the transverse section of the output side of the fiber. 119

Figure 84 SERS spectrum of 1 mM of ATP measured in a cuvette and into a fiber (injected configuration) with (a) AuNP, (b) 0.1x of SC-AuNSH, (c) HC-AuNSH, (d) Nanostars. 120

Figure 85 For each NP, average SERS intensity at 1080 cm^{-1} measured in a cuvette and in a 3.5 µm-PCF (core diameter of 3 µm) ; error bars represent the standard deviations across ten measurements. 120

Figure 86 Averaged SERS signal of 1 mM of ATP using 3.5 µm-PCFs functionalized with (a) Au NP , (b) SC-AuNSH, (c) HC-AuNSH and (d) Nanostars. 121

Figure 87 SERS intensity at 1080 cm^{-1} of 1 mM ATP with 3.5 µm-PCF functionalized with different NPs using anchored configuration. The error bars represent the standard deviation across ten measurements 122

Figure 88 Absorption spectrum for Au NPs with different diameter obtained with FDTD method and Mie theory. 123

Figure 89 Electric field distribution at XY plan for Au NP at 785 nm using (a) a mesh of 1 nm (Mesh 1) and (b) a mesh of 2 nm (Mesh 2). (c) Absorption spectrum and (d) Scattering spectrum for Au NP using Mesh 1 and 2. The inset pictures shows the pixelating effect obtained with mesh 1 and mesh 2. 124

Figure 90 (a) electric field distribution at x=0 for Au NP. (b) Variation of the electric field intensity in the surface of the Au NP using mesh 1 and 2..... 125

Figure 91 (a) Zoom-in of the electric field distribution near to the NP. The arrow indicates the axis and its origin line in which the intensity of electric field is calculated. (b) Variation of the electric field intensity at 785 nm with distance from the surface of the NP for different diameters. (c) Variation of the electric field intensity at 5 and 10 nm from the surface of the NP for different diameters at 785 nm. (d) The absorption coefficient variation at 785 nm for each Au NP using Mie theory 126

Figure 92 Absorption spectrum of SC-AuNSH given by (a) the FDTD numerical simulation and (b) Mie theory. Scattering spectrum of SC-AuNSH given by (a) the FDTD numerical simulation and (b) Mie theory. 127

Figure 93 Electric field distribution on the XY plan for SC-AuNSH at (a) the LSPR wavelength and (b) at 785 nm. (c) Electric field distribution at x=0 for SC-AuNSH on the wavelength range (400 nm – 1000 nm). 128

Figure 94 Variation of $|E|^2$ with distance from NP surface for SC-AuNSH at 785 nm. 128

Figure 95 Absorption spectrum of HC-AuNSH given by (a) the FDTD numerical simulation and (b) Mie theory. Scattering spectrum of HC-AuNSH given by (a) the FDTD numerical simulation and (b) Mie theory. 129

Figure 96 Electric field distribution at XY plan for HC-AuNSH at (a) LSPR wavelength and (b) 785 nm. (c) Electric field distribution at x=0 for HC-AuNSH. 130

Figure 97 Variation of $|E|^2$ with distance from NP for SC-AuNSH, at 785 nm. 130

Figure 98 Variation of the ratio $|E|^2/Q_{abs}$ at 5 nm from NP and at 785 nm for different gold nanospheres. 131

Figure 99 (a) Illustration of the customized upright Raman microscope in combination with optical microscopy. (b) Picture of the built setup. Setup developed by the biophotonics team at Tyndall [189]. 137

Figure 100 (a) Pre-processed Raman spectra from saliva specimen in liquid and dry form. Right-optical microscope view of (b) Red blood cells (c) Smeared cheek cell on aluminum foil. Study realized by Tyndall [189]. 138

Figure 101 Setup developed during my stay in Tyndall instate for Raman measurements using SuC-PCFs. 139

Figure 102 (a) Raman spectra of benign saliva, measured with a SuC-PCF of a core diameter of 3.5 µm (black curve), 3 µm (red curve), 2 µm (blue curve), Tapered-SuC-PCF (grey curve) and on an aluminum foil (dried form (yellow curve) and liquid form (orange curve). (b) Subfigures showing theses Raman spectra around the Raman peak at 1003 cm^{-1} (with a baseline correction)..... 140

Figure 103 Diagram showing the steps for developing a sandwich-type SERS immunoassay: immunoprobe and substrate preparation and the immunosensor functioning. Reproduced from [192]. 142

Figure 104 Top: Diagram of a SERS Nanotag, with small blue circles indicating the Raman reporters. bottom: illustration of multiplex detection within an HC-PCF using three Nanotags. Reproduced from [161]. 143

Figure 105 Representation of the sandwich-based SERS immunoassay using fibers based on the use of antibodies and Raman markers..... 144

Figure 106 SERS spectra obtained from the fiber after adding (a) NP+AB and NP+AB+TNF-alpha, (b) NP+AB+TNF-alpha+AB* and (c) NP+AB+AB* as a control sample. All prominent peaks of ATP are observed. The inset in each figure represents a photo (acquired with a camera) of the focused laser on the input facet of a 3.5 µm-SuC-PCF. In (a) an offset has been added to each curve to facilitate the comparison. 146

Figure 107 SERS spectra measured from the fiber after each different configurations using 3.5 µm-PCF. An offset has been added to each curve to facilitate the comparison..... 146

Figure 108 Diagram illustrating the formation of EVs [204]. 147

List of Tables

Table 1 Parameters of SuC-PCFs fabricated measured with a SEM 95

Table 2 Measured average SERS intensity of ATP at 1080 cm^{-1} in the anchored configuration with 3.5 µm-PCF using different NP's concentrations and different fiber lengths 114

Table 3 Comparison of the ratio $|E|^2/Q_{abs}$ at 785 nm between the 60 nm Au NP, SC-AuNSH and HC-AuNSH. 131

Table 4 Measured average Raman intensity of saliva at 1003 cm^{-1}, along with the calculated average reproducibility and repeatability, for different fiber core sizes. 140

Abbreviations

AAO	Anodic alumina oxide
AFM	Atomic force microscopy
AGFON	Ag film nanosphers
APTES	3-Aminopropyltriethoxysilane
ATP	4-aminothiophenol
AUBPS	Bromide-capped gold nanobipyramids
CEA	carcino-embroyonic antigen
CH	Cumene hydroperoxide
CE	Chemical Enhancement
DMSO	Dimethyl sulfoxide
DNA	Deoxyribonucleic acid
dsDNA	Double standard deoxyribonucleic acid
EBL	Electron beam lithography
EF	Enhancement factor
EGFR	Epidermal growth factor receptors
EM	Electromagnetic mechanism
HC-PCF	Hollow-core PCF
HEPG2	Hepatitis G2
ITO	Indium tin oxide
LAA	Linoleamide alkyne
LC-PCF	Liquid-core PCF
LOD	Limit of detection
LSPR	Localized Surface Plasmon Resonance
LSV	Linear sweep voltammetry
MFON	Metal film over nanospheres
MMF	Multimode fiber
MPTMS	(3-Mercaptopropyl) trimethoxysilane
NANF	Nested Anti-Resonant Nodeless Fiber
NIL	Nanoimprint lithography
NIR	Near infrared
NP	Nanoparticle
NSL	Nanosphere Lithography
PCF	Photonic crystal fiber
PEG	Polyethylene glycol
PNBA	P-nitrobenzoic acid
R6G	Rhodamine 6G
RDI	Relative diagnostic index
RHB	Rhodamine B
RI	Refractive index
RNA	Ribonucleic Acid
RSD	Relative standard deviation
SC-PCF	Solid-core PCF
SD	Standard deviation
SEM	Scanning Electron Microscopy
SERS	Surface-enhanced Raman spectroscopy
Si-PCF	Side-channel PCF

SMF	Single-mode fiber
SuC-PCF	Suspended-core PCF
TAED	Template-assisted electrochemical deposition
TEM	Transmission electron microscopy
TIR	Total internal reflection
TNT	Trinitrotoluene

Introduction

Introduction

Until these days, countless patients continue to die from cancer, neurodegenerative diseases, and other conditions. There is a tremendous need to develop efficient and powerful biosensing methods in order to facilitate early detection of several diseases. The development of these methods will lead to start the treatment as soon as possible, determine a personalized treatment for patients and to be able to do continuous patient monitoring. Until now, the gold standard method used in many diagnoses is the traditional tissue biopsy. Nevertheless, it is an invasive method and represent a risk on the patients also it can not be repeatedly performed, also it could not represent a tool for the tumor evolution. An alternative technique used recently for diseases diagnostic is liquid biopsy. It consist in detecting diseases biomarkers in body fluids such as blood, urine, saliva etc. These biomarkers could be Deoxyribonucleic acid (DNA), extracellular vesicles or proteins. This method is very less invasive compared to the previous one and it is able to evaluate the evolution of the disease and the efficiency of the treatment. Liquid biopsy techniques include methods such as polymerase chain reaction (PCR), enzyme-linked immunosorbent assay (ELISA), Western Blot, and immunofluorescence. These techniques suffer from the long time processing, the necessity of many steps of sample preparation and not compatible to be rapidly and easier to use by clinicians.

Surface-enhanced Raman spectroscopy (SERS) could represent a good alternative for these methods since it uses Raman spectroscopy as a powerful tool for biochemical sensing. It allows characterizing the chemical nature and structure of many analytes. This method's advantage is its capability for multiplex detection, which is valuable for analyzing complex fluids. The principle of this method is based on the scattering of incident light at an energy shifted by the vibrational energy of the molecule. The major limit of this method is the extremely low cross-section compared to other optical spectroscopic methods such as infrared absorption, laser-induced fluorescence and ultraviolet-visible absorption which limits its utility. This is why using nonmetallic surface increases significantly the Raman signal of the analyte, the technique based on Raman spectroscopy combined with using nanostructures called SERS. Studies have shown that noble metal nanoparticles (NPs), such as those made from gold, can locally boost both the excitation light and the Raman signal, achieving enhancement factor (EF) between 10^6 and 10^{11}. SERS combines the intrinsic advantages of Raman such as recognition capabilities owing to the vibrational fingerprints of molecules, non-destructive analysis, minimum sample preparation and possibility of carrying out measurements in biological fluids. SERS is typically conducted using nano-functionalized planar substrates embedded with plasmonic structures. The excitation light and analyte interactions, along with the collection of the SERS signal, are confined to a small area, often just a few micrometers in diameter, centered on the laser's focal point. Additionally, the sensitivity, reproducibility, and consistency of SERS measurements are highly affected by irregularities in the plasmonic nanostructures, which can impact the reliability of quantitative analyses. Photonic crystal fibers (PCFs), featuring microfluidic channels adjacent to their cores, have become prominent for SERS spectroscopy of very small fluid volumes. These PCFs extend the length over which SERS interactions occur, greatly amplifying the Raman signal. Unlike planar substrates that offer only two-dimensional interactions, PCFs provide three-dimensional interaction along the entire fiber length where the liquid is introduced, enhancing sensitivity. Additionally, the nano-functionalization of these fibers with plasmonic NP and the optimization of core size (whether hollow or solid) to align with the Raman spectrometer's optics have significantly improved measurement reliability. Moreover, because light interacts with NPs over a larger area, small irregularities in NP deposition have less impact on measurement reliability compared to planar substrates. However, these fibers should be optimized in order to improve the SERS performance.

Translational Biophotonics Laboratory (TBL), Agency for Science, Technology and Research (A∗STAR) from Singapore and XLIM institute of research from France are doing a collaboration in bio-

imaging and optical sensing based on PCFs. TBL is specialized in biosensing and they developed photoacoustic imaging devices [1] and innovative Raman spectroscopy techniques [2]. The Fiber Photonics team at XLIM specializes in the fabrication and characterization of optical fibers. They developed specialized optical fibers for various applications such as biosensing. Multiple works are previously done which demonstrate the performance of these fibers in SERS sensing, For example, they were able to detect 2.5 fmol of sialic acid on the surface of a single cell, whereas previous techniques required 10^5 cells [3].

In this PhD, My focus is on Suspended-Core PCF (SuC-PCF), which already demonstrated its potential in SERS sensing. With this structure a very excellent reliability was achieved (99% in reproducibility and more than 95% in repeatability) which is a very important parameter that lead to avoid wrong diagnosis. In addition, with this structure, detection of cancer biomarker was realized with the identification of the cancer stage as will be detailed later. Using these fibers in biosensing generally involves a substantial investment of time and specialized knowledge to ensure precise alignment and effective measurements. As a result, there is a strong necessity to find alternative approaches that minimize the dependence on microscope-based alignment.

In this manuscript, chapter I will present the principle of SERS and a review about the SERS substrate and the improvements done using PCFs compared to the planar substrates. In addition to some biosensing applications using the SERS sensors. Chapter II demonstrates the work done about the development of Tapered-SuC-PCF that improve the reliability and practicality for SERS sensing. With this configuration, an easy-to-use SERS sensor compatible with a system of plug-and-play type system is developed, which facilitate the use of the sensor and overcome the limitations imposed by using microscopic systems. Chapter III represents the investigation of new shapes of NPs and their impact on SERS performance. For this, an experiment study is realized in order to compare their sensitivity in addition to a numerical study that could reproduce the plasmonic characteristic and explain their performances. The chapter IV is dedicated to present a proof-of-concept of a detection of biological fluids and diseases biomarker, This indicates that our fiber sensors can be utilized for liquid biopsy to detect severe diseases.

Chapter I. State of art on SERS-based biosensing probes

Chapter I. State of art on SERS-based biosensing probes

This chapter discusses the Raman spectroscopy method, covering its history and applications. The general background of Raman spectroscopy is explained to facilitate a better understanding of the experimental work presented in the subsequent chapters. The importance of this method and its applications, which have made it a powerful detection technique, are highlighted. Additionally, the inherent weaknesses of Raman spectroscopy, which have limited its widespread utilization, are presented. Subsequently, Surface Enhanced Raman Spectroscopy (SERS) is then presented, with the different requirements that underscore the remarkable sensitivity and potential applications of SERS in diverse scientific domains. Afterward, the state-of-the-art development and application of SERS-active substrate sensors are discussed. The fabrication and functionalization of these sensors with metallic nanoparticles (NPs), along with their advantages and limitations, are demonstrated. Finally, the state-of-the-art of Photonic Crystal Fibers (PCFs) used for SERS biosensing is provided.

I.1. Introduction to Raman spectroscopy method

I.1.1. Brief history of Raman spectroscopy

Many researches were conducted in the 19th century and 20th century to understand light scattering principle. Rayleigh scattering was named after Lord Rayleigh discovery. In 1871, he published "on the light from the sky, its polarization and colour" [4], in which he explained the phenomenon of light scattering by molecules and particles suspended in the atmosphere. Then, in 1923, Adolf Smekal was behind the prediction of the possibility that the light could be scattered in shorter and longer wavelengths [5].

In 1928, Chandrasekhara Venkata Raman and his student K. S. Krishnan conducted a set of experiments to study the dispersion of light by various liquid, solid and gaseous substances. They used a spectrometer to analyze the scattered light. The Raman effect was highlighted then by these two physicists in the famous publication "A new Type of Secondary Radiation" in which the theory of Adolf Smekal was confirmed [6]. The beam of sunlight was concentrated by using several optical lenses then filtered by a blue-violet filter in order to select small range of wavelengths. This filtered beam was focused on purified liquid. The observer's eye detected a longer wavelength after putting a yellow-green filter between the scattering liquid and the observer. This means that the scattered light has a different wavelength than the incident one. If only Rayleigh scattering happened, the scattered light would possess the same wavelength as the excitation one and it would be stopped by the filter. Thus, the Raman effect was first reported by C.V. Raman and K.S. Krishnan. Grigory Landsberg and Leonid Mandelstam also demonstrated the Raman effect when they worked on the crystalline quartz in 1928, so that they confirmed the discover of Raman scattering.

I.1.2. Principle of Raman scattering

When a monochromatic beam ($\lambda 1$) is directed at a molecule, the light scatters in different directions. Most of this scattered light maintains the same energy and wavelength ($\lambda 1$), known as Rayleigh scattering or elastic scattering, since there is no change in photon energy. A small portion of light (approximately one photon per 10^6) is scattered with a shift of wavelength λ_2 (Raman scattering), the energy photons in this case have different energy than the excitation ones. Figure 1 illustrate the two scattering phenomenon that occur when a monochromatic light interacts with a molecule.

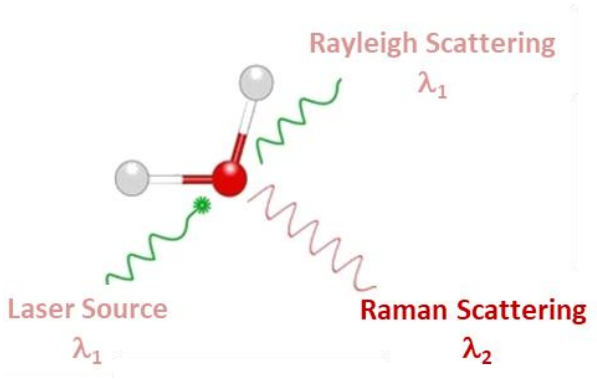

Figure 1 Illustration of the two scattering phenomena when a monochromatic beam excites a molecule.

The fundamental principle of Raman scattering is based on the interaction of the incident light with the molecules. When the molecules are submitted to an electromagnetic wave, the distortion of the electrons cloud is happened, which result in the creation of an electric dipole. The ability of a molecule to develop a dipole moment in response to this external disturbance is quantified by its polarizability. The polarization created could be defined like:

$$\vec{P} = [\alpha]\vec{E} \quad (1)$$

[α] is defined as the polarizability tensor of the molecule. E is the monochromatic electromagnetic wave.

The origin of the different wavelength of the scattered light comes from the fact that the radiation of the created dipole oscillates with a different frequency (ν_2) than the incident one (ν_1). Thus, we can express the energy of the incident photon and the Raman photon by Planck-Einstein relation:

$$E_1 = h.\nu_1 = h.\frac{c}{\lambda_1} \neq h.\frac{c}{\lambda_2} \quad (2)$$

With: E_1, E_2 are respectively the energy of the incident photon and the Raman photon (J). $h = 6.62.10^{-34}$: Planck constant (J.s), ν_1 : incident electromagnetic filed frequency (Hz), $c = 299{,}792{,}458$ (m.s^{-1}), λ_1 and λ_2 are respectively the wavelength of the incident electromagnetic field and the scattered electromagnetic field (Raman) (m).

Considering the energy of the incident photon, we can distinguish between the absorption effect and scattering effect. If the incident photon has the same energy than the energy of the vibrational level of the molecule, it will absorb the photon, which is the principle of infrared spectroscopy [7]. If the energy of the incident photon is higher than the energy of the vibrational level of the molecule, three types of emission are possible. The first known emission is the Rayleigh scattering; it is when the emitted photon has the same wavelength of the incident one. The second one is stokes Raman scattering, in this case the emitted photon has a smaller energy than the incident photon, which means a longer wavelength. The third one is anti-stokes Raman scattering, in this type of emission, the emitted photon has a bigger energy than the incident photon, which means a smaller wavelength. It is worth to note that the intensity of the stokes scattering is bigger than the intensity of the anti-stokes scattering by approximately 1000 times, this is why the Raman scattering is generally studied in the stokes region. Figure 2 summarize the three type of emission when a molecule is submitted to a monochromatic wave.

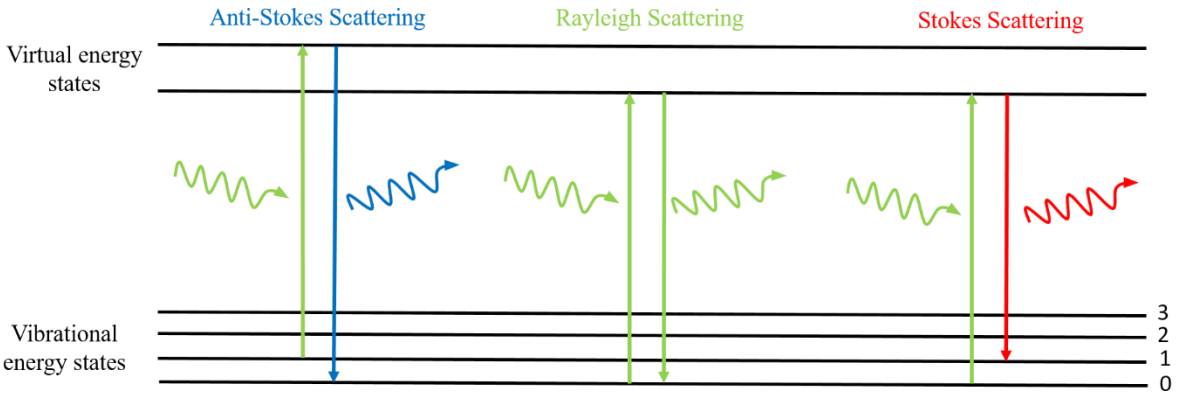

Figure 2 Energy diagram illustrating Rayleigh, Stokes and Anti-Stokes Scattering.

Each molecule possesses a three-dimensional structure, which differentiate it from another molecule. When the molecule is excited by an incident electromagnetic wave, several structural variations can occur like bending, stretching, twisting or rotation. Each type of these structural variations leads to a Raman peak, which give a Raman spectrum of the molecule. Since every molecule has a unique Raman spectrum, it led to the development of a novel detection technique known as Raman spectroscopy. It is worth to note that the positions of the Raman peaks do not change with changing the excitation wavelength, because they are directly related to the vibrational energy modes of the molecules. Thus, a conventional scale called Raman shift (cm^{-1}) is chosen for the Raman spectra whatever the excitation light and leads to quantify the wavelength shift and facilitate the comparison between the Raman spectra taken from different excitation wavelengths.

$$Ramanshift = \frac{1}{\lambda_{excitation}} - \frac{1}{\lambda_{scattered}} \quad (3)$$

I.1.3. Applications and limitations of Raman spectroscopy

I.1.3.1. Applications

As mention above, Raman spectroscopy is a non-destructive method of chemical analysis of solids, liquids and gases. Therefore, Raman spectroscopy is applied in several domains such as science, medicine, energy and environment etc… For example, in the medical domain, the Raman spectroscopy can be particularly used as a diagnostic tool between healthy and diseased cells based on their chemical and structural properties [8]. In the field of environmental science, issues like water contamination and air pollution necessitate innovative analytical tools such as Raman spectroscopy, which offers high chemical selectivity and enables rapid identification of microparticles [9]. Raman spectroscopy is also crucial in the energy sector. It is used to develop and analyze materials for reliable, efficient, and powerful energy sources by studying their structural and electronic properties or conducting failure analysis. Additionally, Raman spectroscopy is employed in quality control processes and stability studies, highlighting its wide-ranging applications in this field [10]. In addition, since the Raman effect is sensitive to the slight chemical composition variations, it could be used to identify the illicit drugs [11] and analysis of in situ inks on paper surfaces to identify the false documents.

Therefore, we can notice that the Raman spectroscopy is widely used in many fields. It requires only minute quantities of sample; also, the Raman peaks are very narrow compared to Fluorescence peaks [12], which allow to achieve multiplex detection [13]. It is worth to note that the intensity of the Raman peaks can be correlated to the concentration of the detected molecule in the sample. Nevertheless, the Raman spectroscopy present several limitations.

I.1.3.2. Limitations of Raman spectroscopy

In spite of its efficiency, the Raman spectroscopy has several limitations because of the weak of Raman scattering cross-section of numerous molecules. The Raman scattering cross-section quantifies the efficiency with which a molecule can absorb a photon and emit a Raman photon. That means, as mentioned above, that not all the scattered photons follow the Raman scattering. It has been demonstrated that the cross section of the Raman scattering is from 10^6 to 10^{12} times smaller than the spectroscopy of fluorescence or infrared [14]. Increasing the sensitivity, i.e. the increase of the Raman photons number, would be the ideal solution in order to benefit of its high and excellent selectivity.

One solution is to increase the incident light power, which lead in increasing the intensity of the Raman peaks. However, high-power lasers can heat the sample, which can denature the sample and cause changes in its properties, especially in biosensing applications. Another approach consists in increasing the concentration of the targeted molecules for intensifying the Raman signals and making the measurements more sensitive.

An alternative strategy to overcome the drawbacks of the Raman spectroscopy is to increase the integration time (the duration of measurements) in order to increase the number of Raman photons collected from the sample. The development of commercial Raman spectrometers are significantly since 1953s. They offer relatively long integration time to obtain high-quality Raman spectra, but this solution prevent from doing real-time sensing and could be restrictive for end use applications.

I.2. Principle of Surface-Enhanced Raman Spectroscopy (SERS)

Many researches have been conducted in order to improve the sensitivity of Raman measurements even with very low concentration of analytes and with low laser power. SERS is a powerful technique to increase the sensitivity of Raman measurements while preserving the ability to realize multiple detection [15]. Simply, this technique consists in amplifying the Raman peaks of the molecules when they are absorbed onto noble metal surfaces or on colloidal NPs.

I.2.1. History

About fifty years ago, M. Fleischmann *et al.*, measured Raman spectra of pyridine absorbed on a silver electrode [16]. This result highlighted a significant amplification of Raman signals in the presence of nanostructured metal surfaces, paving the way for a new ultrasensitive chemical analysis technique. In 1977, M. Grant Albrecht and J. Alan Creighton revealed that the Raman spectra of the absorbed pyridine showed an EF of ~ 10^5 [17], which confirm the considerable increasing of the cross-section of Raman scattering by the noble metal surface effects. In the same year, Jeanmaire and Van Duyne are confirmed this enhancement using a silver electrode (Figure 3) [18]. In addition, they highlighted the significant improvements in spectro-electrochemistry techniques allowing better understanding of molecular interactions at the electrode-solution interface.

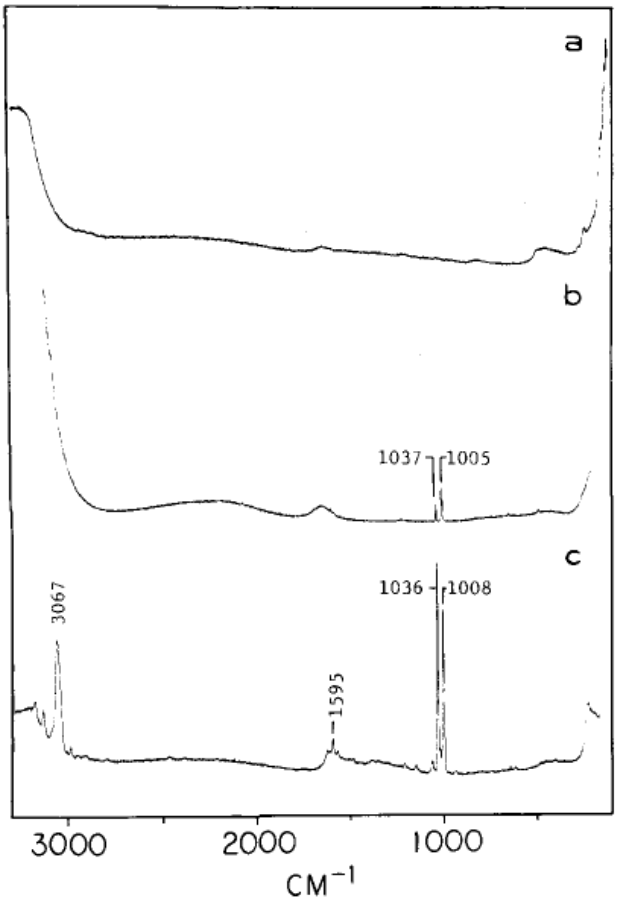

Figure 3 (a) Raman spectrum of a silver electrode immersed in 0.2 M KCI. (b) Raman spectrum of 50 mM aqueous pyridine and 0.1 M KC1. (c) Raman spectrum of pyridine adsorbed on a silver electrode from a bulk solution of 50 m M pyridine and 0.1 M KCI. Reproduced from [18].

Subsequently, many works established the relationship between the roughness of the noble metal surfaces and the enhancement of the Raman signals [19, 20]. Although the phenomenon of SERS has been extensively explored and comprehensively studied over a significant period, it remains the focal point of numerous discussions and debates. Generally, SERS is based on two mechanisms. The electromagnetic mechanism and chemical mechanism.

I.2.2. Principle of Surface-Enhanced Raman Spectroscopy

I.2.2.1. Electromagnetic mechanism

The electromagnetic mechanism (EM) of SERS effect can be understood from the nature of the interaction between the incident electromagnetic wave and the metal surface. Each metal is composed of atoms that contain electrons cloud and nucleus. The conduction electrons that can move randomly characterize the metal surface, while the nucleus is considered motionless because of its big mass compared to electrons. When the cloud of electrons are submitted to an electromagnetic wave, they orient themselves according to the Lorentz force resulting in a delocalization as shown in Figure 4. This delocalization result in creating a shift in the barycenter position of the electrical charges (Figure 4(a)). In this case, the positive charge and negative charge attract each other until the electrons are back again in their original place. This process will repeat again while the excitation is still on, leading to the creation of a collective oscillation of conduction electrons band. This phenomenon is known as Localized Surface Plasmon Resonance (LSPR), and the quantification of the electrons plasma is named "plasmon" [21].

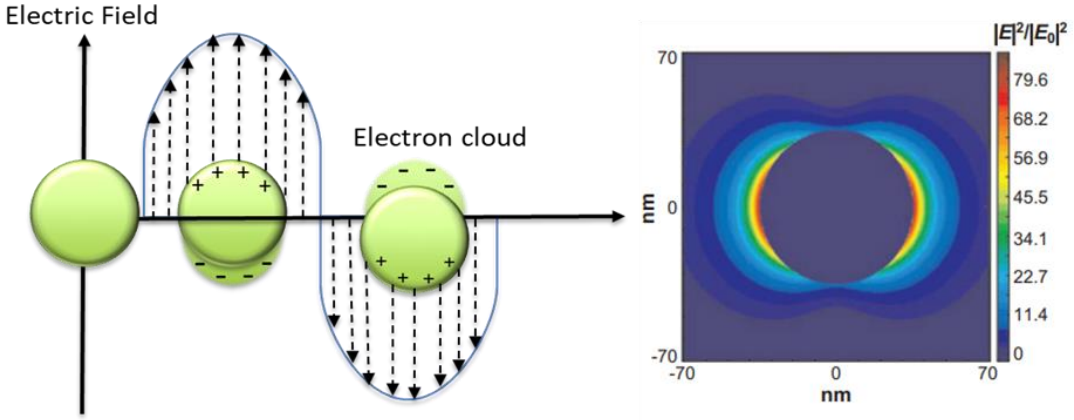

Figure 4 (a) Illustration of the cloud of electrons delocalized when an electromagnetic wave interacts with metallic NPs (b) Spatial distribution of $|E|^2$ around the spherical silver NP of 70 nm diameter in vacuum at LSPR wavelength. Reproduced from [21].

The created oscillations result in a high localization of the electromagnetic field close of the metal surface (Figure 4(b)). Thus, the molecules located near the surface of NPs, will be under the influence of the enhanced field localization. The frequency of the oscillation is determined by several parameters such as the materiel, the size, the shape of the NP and the wavelength of the electromagnetic wave. This frequency could be express as:

$$f_p = \frac{\omega_p}{2\pi} = \sqrt{\frac{ne^2}{\pi m_e}} \tag{4}$$

With ω_p is the plasma pulsation, n the electrons number, e is the elementary charge of the electron and m_e is the electron mass [22]. In the following, in order to express the electromagnetic field outside the NPs, we consider the Drude model for a spherical particle of a radius (a) irradiated by a light polarized in z-direction characterized by a wavelength of λ in a quasi-static regime, such as $(\frac{a}{\lambda} < 0.1)$. Therefore, in these conditions, the Laplace equation could replace the Maxwell's equation while the electric field is uniform around the NPs [23]. By an analytic resolution of this equation, we can express the

electromagnetic field inside and outside the NPs, thus, the resulting electric field outside the nanosphere, E_{out}, is expressed as:

$$\vec{E}_{out} = E_0\vec{k} - \alpha E_0[\frac{\vec{k}}{r^3} - \frac{3z}{r^5}(z\vec{k} + x\vec{\imath} + y\vec{\jmath})] \quad (5)$$

With E_0 is the incident electric field, r is the radial distance, x, y and z are the cartesian coordinates, $\vec{\imath}$, $\vec{\jmath}$ and $\vec{k}$ are the unit vectors of the Cartesian coordinates system and α is the polarizability of the metal mentioned above. The expression of the polarizability in the metal sphere can be expressed as:

$$\alpha = ga^3 = \frac{\varepsilon_m - \varepsilon_{out}}{\varepsilon_m + 2\varepsilon_{out}} a^3 \quad (6)$$

With ε_m is the metal permittivity and ε_{out} is the permittivity of the outer medium. According to the free-electron Drude model, the permittivity of the metal can be expressed as:

$$\varepsilon_m = 1 - \frac{{\omega_p}^2}{{\omega_p}^2 - i\gamma\omega} \quad (7)$$

With γ is the plasmon width.

From the equation 6, we can evaluate the polarizability that represent the ability of the metal to form an electric dipole. Thus, the condition with which the plasmon resonance is happening continuously is:

$$\varepsilon_m = -2\,\varepsilon_{out} \quad (8)$$

Under this condition, the g parameter tends to infinity, which means that the polarizability tends also to infinity. We can notice from the equation 5 that the field enhancement depends to the radial distance. It decays with the increasing of r^{-3}, which means that the SERS sensing depends to the distance between the NP and the molecule as this will be explained later.

So far, Mie theory remains the only exact solution to the equations of Maxwell that is well adapted to spherical particles. The Mie theory offers a solution that describes the extinction spectrum of a given NP. Extinction refers to the total loss of light intensity due to both absorption and scattering as the light interacts with the NPs [24]:

$$E(\lambda) = \frac{24\pi^2 N a^3 {2\varepsilon_{out}}^{3/2}}{\lambda \ln(10)} [\frac{\varepsilon_{i\,m}(\lambda)}{(\varepsilon_{r\,m}(\lambda) + \chi\varepsilon_{out})^2 + \varepsilon_{i\,m}(\lambda)^2}] \quad (9)$$

Where $\varepsilon_{r\,m}(\lambda), \varepsilon_{i\,m}(\lambda)$ are the real part and imaginary part of the permittivity of the metal, respectively.

This equation is generalized from the sphere solution by changing the factor 2 appears in equation 6 by χ that represents the shape factor, so that it takes different values according to the shape of NPs [25]. The reason of doing this is that the Mie theory cannot be employed for other structures than spheroids.

In Raman spectroscopy, the intensity of the scattered electromagnetic field is linear with the intensity of the incident electromagnetic filed ${E_0}^2$ [26]. Therefore, the Raman intensity is related to the absolute square of the electric filed outside the NPs (E_{out}), by manipulating the equations 5-6, it can be expressed as :

$$|E_{out}|^2 = {E_0}^2[\,|1-g|^2 + 3\cos^2\theta(2Re(g) + |g|^2\,] \quad (10)$$

Where θ is the angle between the vector of incident field and the vector to the molecule position on the surface.

It appears from this equation that the maximum enhancement occurs when $\theta = 0°$ and $\theta = 180°$, while the minimum is when $\theta = 90°$. knowing that g has to tend towards infinity for the resonance existence,

so that $g \gg 1$ and $g \gg 2Re(g)$. Thus, we can express both the maximum and the minimum of the enhancement as the following:

$$|E_{out}|^2{}_{max} = 4{E_0}^2\,|g|^2 \qquad \text{and} \qquad |E_{out}|^2{}_{min} = {E_0}^2|g|^2 \tag{11}$$

We can notice that the average enhancement is $|E_{out}|^2{}_{min} = 2\,{E_0}^2|g|^2$ while the ratio of the maximum and the minimum enhancement is being 4. This treatment concerns the enhancement of the incident electromagnetic field in the surface of NPs. In SERS, when the molecules are located near the metal surface, a portion of the incident light could be shifted into stokes photons by the vibrational frequency of the molecules, which may participate in the total enhancement of the result electromagnetic field. The analytical treatments of this aspect is more complex than the enhancement of the incident light [27]. Nevertheless, it can be understood by doing the first-order approximation. Therefore, the theoretical electromagnetic EF could be expressed as:

$$EF = \frac{|E_{out}|^2|E\prime_{out}|^2}{|E_0|^4} = 4\,|g|^2|g'|^2 \tag{12}$$

Where g' is defined by the permittivity of the metal (ε'_m) and of the outer medium permittivity(ε'_{out}).

This is commonly named E^4 enhancement in the literature or the fourth power of field enhancement at the NP surface. The EF can reach 10^8 in some metal nanostructures [28]. Experimentally, this EF can be measured by:

$$EF = \frac{I_{SERS}/N_{surf}}{I_{NRS}/N_{vol}} \tag{13}$$

Where I_{SERS} is the SERS intensity, N_{surf} is the molecules number on the metallic substrate, I_{NRS} is the normal Raman intensity and N_{vol} is the molecules number in the excitation volume.

Although it represents the majority of the enhancement in SERS, the EM does not alone explain the importance of the amplification of Raman signal observed. Other theories have been proposed based on electronic exchanges between NPs and analytes.

I.2.2.2. Chemical Enhancement

The Chemical Enhancement (CE) is the enhancement due to the chemical nature of the interaction between the molecules and the SERS substrates in which are adsorbed. Despite the CE is extensively studied such as the EM, but it stills less understood. Thus, it seems that the CE is limited to occur only on the molecules that are directly adsorbed on the metallic surface [29]. This is called short-range interaction [30]. The CE is based on the resonant and the non-resonant charge transfer because of different interaction forces between the NPs and the analytes [31].

The interactions between the NPs and analytes can occur via Van Der Walls type force (physisorption) or by the formation of ionic or complex bonds (chemisorption). The modification in the electronic structure of the molecule due to the creation of the molecular bonds, can induce modifications in the distribution of the electronic charges of the analyte, therefore in the shape of the electronic cloud, which can affect the Raman shift values, and the intensity of Raman peaks [32].

A resonant charge transfer occurs when an electron is transferred to the adsorbed molecule. It is responsible for the enhancement (excitation) of certain modes, such as C–C in C_2H_4 molecule for example. This component of CE is responsible of an enhancement up to 10^3 fold. On the other hand,

non-resonant charge transfer happens when an electron is briefly transferred to the adsorbed molecule but returns to the metal within less than one femtosecond. Because the electron does not remain on the molecule long enough to achieve resonance, this process does not selectively enhance specific modes. Instead, it generally enhances a wide range of vibrational modes by about 30 to 40 times [31].

In opposite to the electromagnetic enhancement, the CE enhancement remains difficult to individualize and to characterize because it occurs simultaneously with the EM enhancement (that is considered more intense). Many works have been conducted in order to propose complete theories on the different enhancement mechanisms in SERS. The correct understanding of all these mechanisms allowed the development of ultrasensitive technique of the detection down to a limit of detection (LOD) of a single molecule in a sample [33] with an EF up to 10^{12} (under well-controlled conditions), with molecules of large Raman cross section such as dyes [34].

After having briefly described the physical principle and enhancement origins observed in SERS, the main parameters influencing the SERS performances are presented in the following section.

I.2.3. Factors influencing the SERS enhancements

As shown above, the electromagnetic enhancement depends on serval parameters such as the distance between the analyte and the metal surface, the excitation wavelength, the shape and the size of NPs used. The optimization of all these parameters is a crucial step in order to benefit from the total enhancement of SERS. Furthermore, the application of SERS realized until now showed that other parameters related to the experiments should to be taken into account, such as the contact duration between the molecules and the metal surface, the acquisition time of the optical spectrometer and the power of the laser used… Mastering these conditions is to date one of the challenges in the development of SERS application. In 2008, E. Le Ru and P. Etchegoi articulated a precise overview of the principal characteristics of the SERS technique by elaborating on its abbreviation. They identified the essential parameters for its application [35]:

Surface: SERS spectroscopy is a surface spectroscopy, so the molecule to be studied must be as close as possible to the NPs. This essential parameter in SERS involves interactions between the NPs and the analyte essential for the enhancement.

Enhanced: The observed amplification is mainly due to the amplification of the electric field on the surface of the NPs, secondary, to the interaction between the electric field and the metallic NPs. The excitation wavelengths vary based on the metal's properties, as well as the size and shape of NPs. Consequently, selecting the appropriate SERS substrate and laser wavelength are two particularly crucial parameters.

Raman Spectroscopy: SERS is only the enhancement of the Raman scattering signal. Consequently, the better the initial Raman response, the better the enhancement will be. This response is proportional to the cross section.

This synthetic description of the SERS effect allow distinguishing the key points to control and optimize the synthesis and choice of NPs as well as their interaction with the analyte. In the following, we will describe each parameter and its influence on SERS response.

I.2.3.1. Effect of metallic nature on SERS enhancement

The metallic nature is represented via the permittivity of the metal used. We remarked in the equation 6 that the resonance condition is realized when $\varepsilon_m = -2\varepsilon_{out}$. In this scenario, an assumption is made regarding the imaginary component of the metal permittivity, which is considered very low compared to the real part. Thus, the condition of the resonance relies on the reel and the imaginary part of metal

dielectric constant. Many works had been conducted in order to define for a given wavelength the metal properties for the best enhancement in SERS according to the values of their permittivity [36]. Noble metals mainly have values of $\varepsilon_m < 0$ and are therefore good candidates for their use in SERS as shown in figure 5.

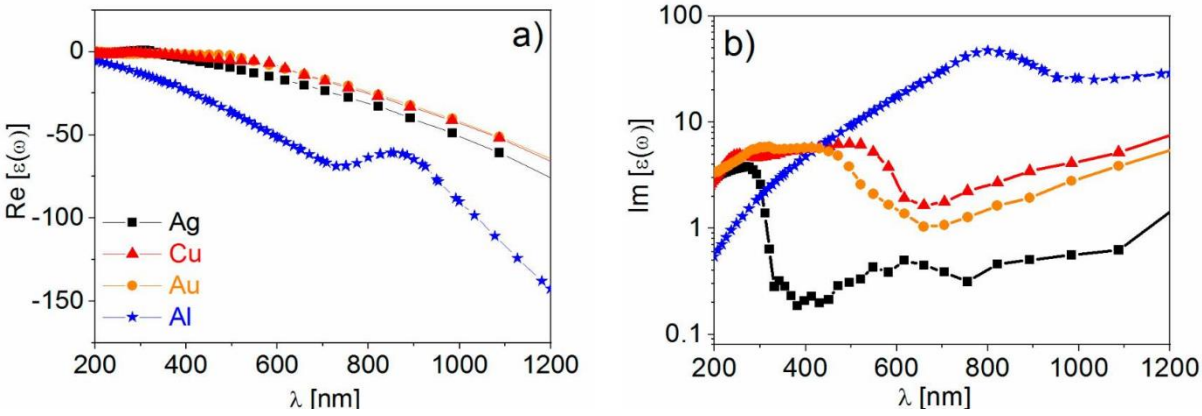

Figure 5 The main values of the (a) real and (b) the imaginary part of the permittivity for silver (Ag), copper (Cu), gold (Au) and aluminum (Al), according to the incident wavelength. Reproduced from [36].

It is worth to note that the imaginary part of the metal permittivity accounts for the losses generated during the polarization process [37]. From the figure 5, we can see that the silver possess less losses, that means that is has the largest SERS enhancement in this region. However, in the near infrared, Au, Ag and Cu are expected to have a similar SERS performance. This explained by the fact that the interband transitions onset is around 600 nm for Au and Cu, and 300 nm for silver [38]. Thus, the wavelength used of the laser can be adapted according to the metal used. Typically, lasers used in Raman spectroscopy have wavelengths between 500 and 1000 nm (from visible to near infrared). The metals that respond to these criteria are Au, Ag and Cu (Figure 6), which explain their frequent use in SERS applications. In SERS applications, it is necessary to take into account the stability of such metals. For instance, silver and copper oxidize easily while gold is very chemically stable. Other criteria must also be taken account for their use, such as their biocompatibility.

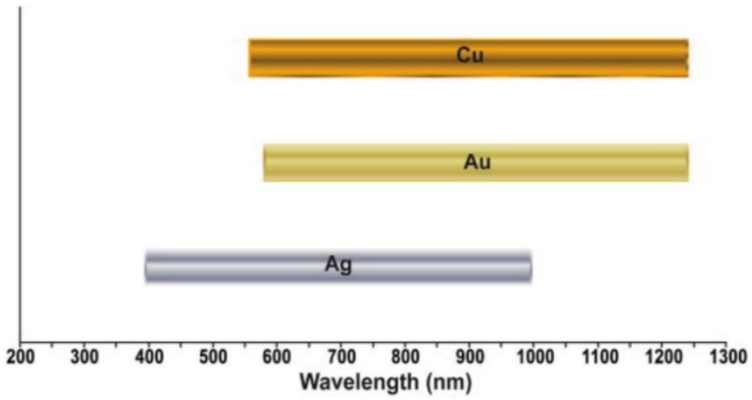

Figure 6 Excitation wavelength of conduction electrons of principal metals used in SERS. Reproduced from [39].

I.2.3.2. Size and shape impact on SERS response

As mentioned above, the enhancement of the electric field on noble metal surfaces is attributed to the LSPR effect. Various methods have been employed to study how the LSPR peak behaves in relation to variations in size and shape parameters. For example, arrays produced using Nanosphere Lithography (NSL) feature masks with varying nanosphere diameters and different silver film thicknesses [40]. Furthermore, Xiayu Zhang *et al*. utilized an electrochemical process to oxidize NPs, thereby modifying their surface structure in a controlled manner [41]. Subsequently, the extinction spectra were measured for each structure to evaluate the impact of these variations on the LSPR response (Figure 7). The measurements were conducted using multiple chronocoulometric runs on NSL-fabricated silver triangles prepared on an indium tin oxide substrate, illustrating the correlation between LSPR peaks and changes in NP morphology.

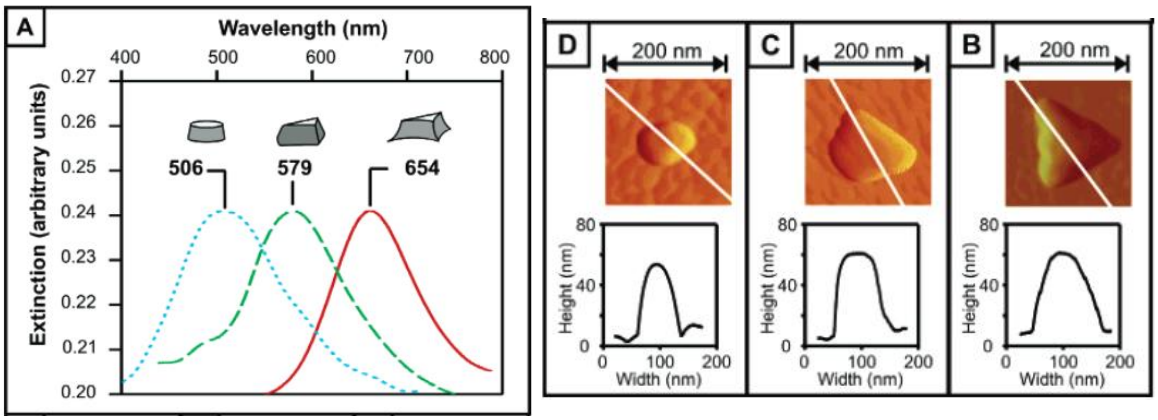

Figure 7 (A) LSPR peaks showing λ_{max} shift towards shorter wavelength after chronocoulometry measurements. (B) Atomic force microscopy (AFM) images before electrochemical measurements. LSPR $\lambda_{max} = 654\ nm$. (solide line). (C) AFM image after one chronocoulometry measurement. LSPR $\lambda_{max} = 579\ nm$ (dashed line). (D) AFM image after two chronocoulometry measurements. LSPR $\lambda_{max} = 506\ nm$ (dotted line). Reproduced from [41].

In the SERS application, it is important to calculate the electromagnetic enhancement near of the NP surface. It has been shown that for isotropic NP, such as spherical, the electrons are distributed uniformly. However, for more complex, anisotropic structures, electrons are preferentially concentrated in areas with large radius of curvature such as the points of a triangle or the ends of an ellipse or a rod, in the nanogaps between NPs or nanogaps between an NP and a metallic surface, this is called by hot spots [42]. To optimize the enhancement it is possible to adapt the wavelength of the laser to the nature of the metal and the geometry of the NPs. For spherical structure, there is a single resonance mode; while for elongated NPs like nanorods, there are two modes with a transverse mode and a longitudinal mode [43]. NPs with complex shapes such as Nanostars, Nanourchins present more hotspots. However, the protocols for synthesizing NPs with anisotropic geometries such as Nanostars, Nanourchins or Nanoflowers remain more and more complex and not very efficient. In our case, we will use the NPs in colloidal suspension as explained later. Several examples representing the diversity of NPs shapes found in the literature are illustrated on Figure 8.

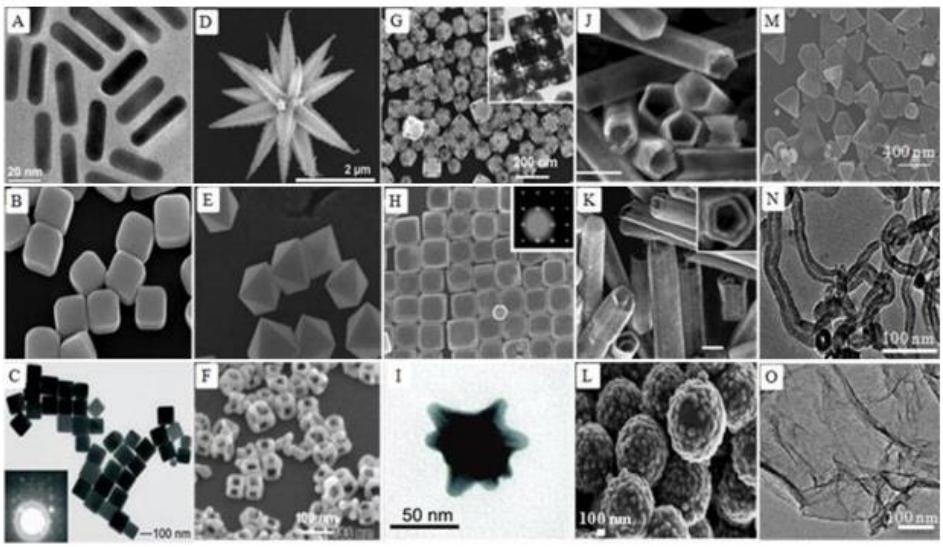

Figure 8 Diversity in plasmonic nanostructures with different sizes and shapes. Reproduced from [44].

The shape and the size of NPs are not the only parameters that play an important role in the SERS enhancement. In practical point of view, the advantages of these parameters are useful when the analyte is located near to the NPs. Thus, the distance from the metal surface plays a crucial role for SERS biosensing.

I.2.3.3. Distance dependence of SERS enhancement

In SERS biosensing applications, in some cases, the targeted molecules are not adsorbed on the surface of NPs. They are immobilized near to the surface via the capture layer such as antibodies [45]. This results in important distance between the surface of the metal and the molecules. However, several works showed that the direct connection of the molecules with the metal surfaces is not required to benefit from the SERS enhancement, and the variations of SERS intensity can be monitored for different distances between the targeted molecules and the metallic surface [46].

In order to quantify the dependence of the SERS intensity with the distance to the metal surface, the equation 5 showed that the enhancement of the electromagnetic field decays with r^{-3}. Taking into account the E^4 enhancement, it becomes r^{-12}. It is worth to note that number of the excited molecules near to the surface evolves according to r^2 [47]. Due to all these considerations, it has been shown that the SERS intensity expressed as:

$$I_{SERS} = \left(\frac{a+r}{a}\right)^{-10} \quad (14)$$

Here, a stands for the radius of curvature of the metal surface's roughness feature or the radius of a nanosphere, and r is the distance between the analyte and the metal surface. According to Equation 14, it is evident that the SERS intensity decreases as the distance from the metal surface increases. In 1981, C. A. Murray and D.L. Allara experimentally studied the Raman intensity enhancement as a function of their spacing from a rough metal surface [48]. They measured the Raman intensity of p-nitrobenzoic acid (PNBA) after putting poly(methylmethacrykate) as a spacer between PNBA and a rough silver film. They demonstrated that the Raman intensity fall-off by a factor of 10 for each 35-50 Å. In addition, in 2006, Dieringer *et al*. measured SERS signal of pyridine spaced from Ag film nanosphers (AgFON) by different thicknesses of AL_2O_3 films [49] (Figure 9).

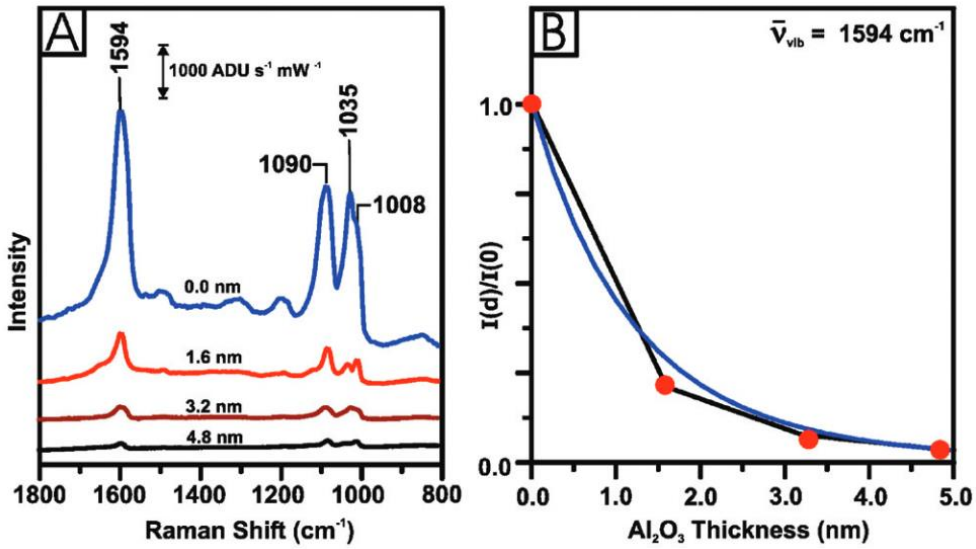

Figure 9 (a) SERS spectra of pyridine molecule adsorbed on different value of thicknesses of AL_2O_3 film coated on AgFON. (b) Behavior of normalized SERS intensity of Raman peak 1594 cm^{-1} of pyridine in function of alumina thicknesses. Reproduced from [49].

The SERS spectra shown in Figure 9(a) shows the variation of SERS peaks with the changing in the thicknesses of AL_2O_3 film. Figure 9(b) shows that the SERS intensity decreases by ten times after adding 2.8 nm of AL_2O_3 film. In addition, Masango *et al.* showed in some cases that the equation 14 does not describe the variation of the Raman intensity with the distance from the NPs [50]. In their experiments, they deposited different thicknesses of Al_2O_3 by atomic layer deposition as a spacer between the sensed molecule trimethyl aluminum and the Ag film over silica nanospheres (Ag-FON). The monitored Raman peak of the molecule is 2892 cm^{-1}, it is measured for different distances from the metal surface. Figure 10 displays the outcomes of the experiments. The experimental data revealed a distinct division into two sections. The first section was fitted with a small curvature radius (2 nm), while the second section was accommodated by an equation featuring a larger radius of curvature (8.5 nm). Thus, they proposed the following equation:

$$I_{SERS} = C_1\left(\frac{a_1 + r}{a_1}\right)^{-10} + C_2\left(\frac{a_2 + r}{a_2}\right)^{-10} \quad (15)$$

Where a_1 and a_2 the radii of curvature of AgFON features corresponding respectively to the long-range and short-rang effect. C_1 and C_2 are the constants for the contribution for each term.

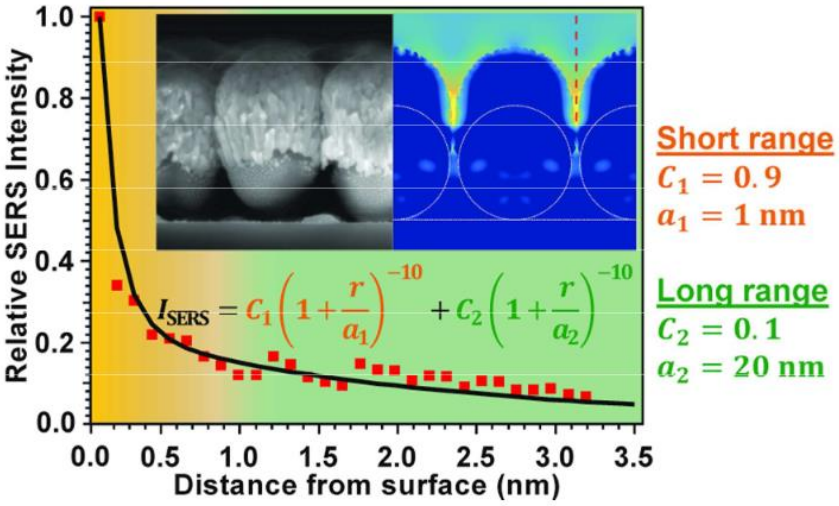

Figure 10 Variation of the SERS signal of the 2892 cm^{-1} peak of trimethyl aluminum with the distance from the film of AgFON. In the insets, A picture of the Ag film over Nanospheres taken by scanning electron microscopy (SEM) and a simulation of the electric field are presented. Reproduced from [50].

I.2.3.4. Raman cross-section of molecules

The Raman intensity of a certain Raman mode (k) (a specific vibrational or rotational state of a molecule that can interact with incident light to produce Raman scattering) is proportional to the Raman cross-section of the molecule, which can be expressed as [26]:

$$\sigma_k \propto \tilde{\nu}_0(\tilde{\nu}_0 - \tilde{\nu}_k)^3 \quad (16)$$

With $\tilde{\nu}_0$ is the wavenumber of the excitation laser, $\tilde{\nu}_k$ is the Raman shift of the mode k and $(\tilde{\nu}_0 - \tilde{\nu}_k)$ is the stokes-Raman wavenumber. This equation demonstrates that for the same molecule, more Raman photons are scattered when it excited with visible light compared to near infrared (NIR) light. For instance, the cross- section at some wavelengths of excitation normalized to the cross-section at 514 nm lead to:

$$\frac{\sigma(\lambda_{ex} = 633\ nm)}{\sigma(\lambda_{ex} = 514\ nm)} = 0.44 \text{ and } \frac{\sigma(\lambda_{ex} = 785\ nm)}{\sigma(\lambda_{ex} = 514\ nm)} = 0.18 \text{ and } \frac{\sigma(\lambda_{ex} = 1064\ nm)}{\sigma(\lambda_{ex} = 514\ nm)} = 0.054 \quad (17)$$

We noticed from the equation (17) that from the visible to NIR the intensity fall by approximately a factor of 20 (It is well known that the Raman intensity is proportional to λ^{-4}, so that the Raman intensity will fall with the increasing of the laser wavelength). There is additional enhancement of the cross-section by two or three orders of magnitude in the case where the excitation wavelength is resonant with the electronic transition. This resonance phenomenon occurs when the energy of the incident light matches the energy difference between electronic energy levels of the molecule. This is more inclined to occur in the UV-visible region than NIR where many organic molecules exhibit an absorption band. However, the use of a short excitation wavelength, coupled with the resonant effect, raises the risk of sample damage due to the higher photon energy involved in resonant excitation. Also may introduce fluorescence interference and background noise, which can obscure the Raman signal of interest

I.3. SERS-based substrates sensors

Typically, SERS spectroscopy is conducted on nano-functionalized planar substrates that contain plasmonic structures. By using a microscope to focus the laser beam, interactions between the excitation light and the analyte, as well as the collection of the SERS signal, occur over a very small area, usually only a few micrometers in diameter, which corresponds to the laser's focal point. In this section, we will

introduce the principal features of SERS substrates required for SERS applications, the manner how these substrates are functionalized with NPs or nanostructures, and finally, some applications of SERS substrates and their advantages and limitations are presented.

I.3.1. Principal features of SERS substrates

Brown et al. shown that SERS substrates that exhibit the highest enhancement are the less reproducible and vice versa [51]. They argue that as the reproducibility and uniformity increase across the substrate order, the maximum enhancement tends to decrease. This trend is illustrated in Figure 11.

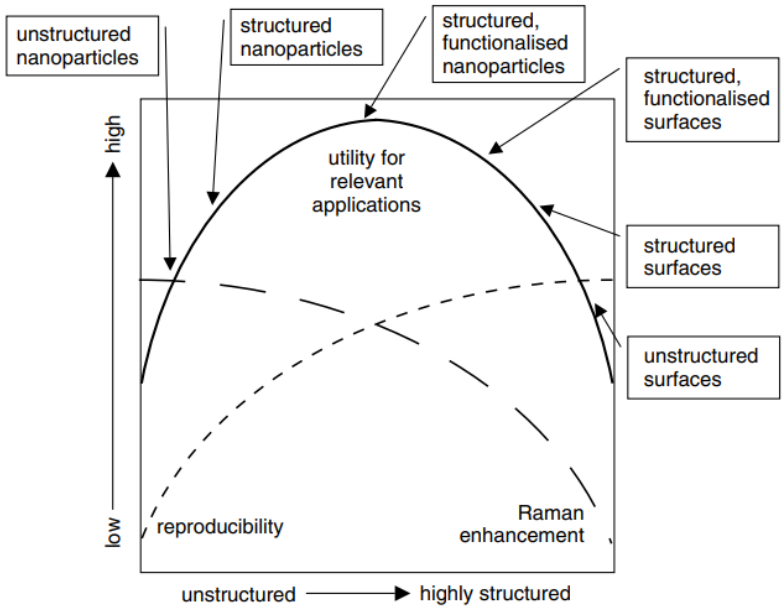

Figure 11 Diagram illustrating the evolving characteristics of SERS structures from the unstructured to the highly structured type. Reproduced from [51].

The sensitivity and reliability represent the principal keys to take into account in the fabrication process of a SERS substrate. Balancing these two parameters is essential for creating a sensor that holds clinical significance. If a sensor possesses a high sensitivity but lacks in reliability, it may lead to false positives. Conversely, a highly reliable sensor might struggle to detect trace amounts of the analyte. Furthermore, a reliable clinical sensor must exhibits the necessary sensitivity to identify low analyte concentrations within small sample volumes. Additionally, selectivity and specificity hold great significance in biosensing, particularly when dealing with analytes present in small quantities within complex matrices like blood, which may introduce parasitic Raman signals. Consequently, sensors capable of specifically targeting the analyte provide a substantial advantage. Various criteria are commonly employed to assess the sensitivity and reliability of SERS measurements. Regarding the sensitivity, the primary criterion for comparing the sensitivity of different substrates prepared under the same conditions is based on the measured Raman intensity. For instance, certain molecules serve as common Raman reporters and exhibit strong Raman signature peaks. By monitoring the intensity of one of these peaks, sensitivity can be directly correlated with the Raman intensity of that specific peak. The most sensitive sensor will yield the highest intensity. Another criterion involves determining LOD, which corresponds to the lowest concentration of analyte that the sensor can detect. In this context, the most sensitive sensor is capable of detecting the lowest concentration.

Reliability signifies the sensor's capability to provide consistent and uniform SERS signals. The reliability is often defined by two parameters: reproducibility and repeatability (Figure 12). In an ideal scenario, when measuring the Raman signal emitted by an analyte at different times, a SERS sensor should consistently display an identical spectrum. This means that all the characteristic peaks of the analyte should be consistently present, and each peak should maintain the same intensity. Reproducibility refers to a sensor's ability to produce consistent signals across multiple measurements. SERS sensors that exhibit a relative standard deviation (RSD) of less than 5% are regarded as highly reproducible [52]. Repeatability represents the capacity of several sensor samples prepared under the same conditions to give uniform signals. This aspect is of immense significance because it signifies the capacity to produce sensors that exhibit consistent responses in identical conditions. While repeatability is crucial for the commercialization of SERS sensors and their practical use in clinical settings, it is sometimes overlooked in research papers. Nevertheless, Michael J. Natan *et al.* suggested that a batch of SERS sensors with variations below 20% could be deemed acceptable [60].

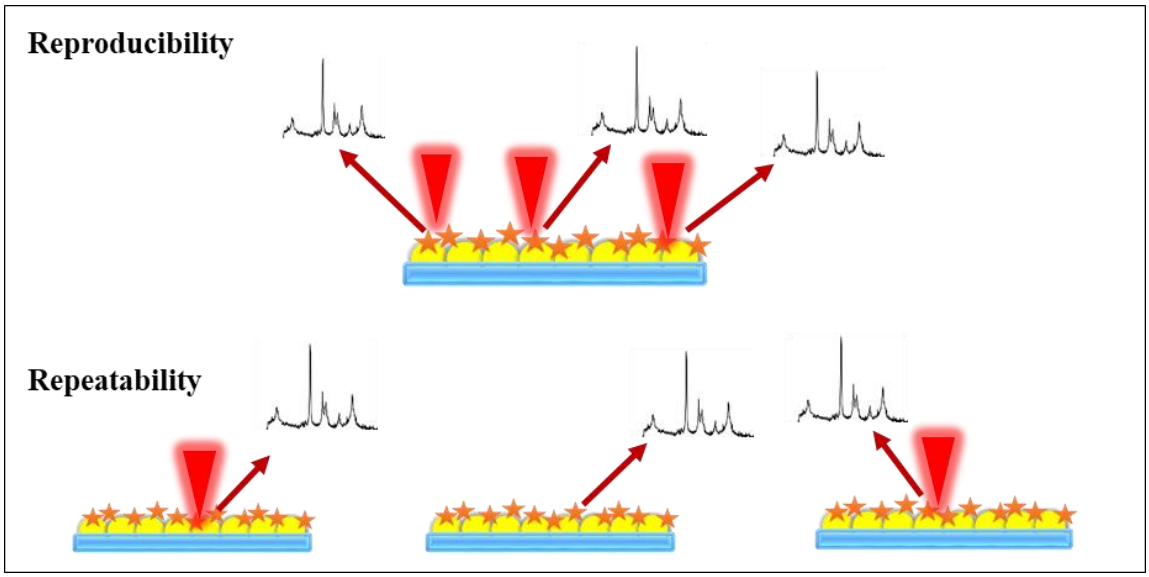

Figure 12 Illustrations depicting the concepts of reproducibility and repeatability of SERS measurements.

Stability is another vital parameter that demands attention during the fabrication of the SERS substrate to ensure its long-term performance. Furthermore, the solvents to which the substrate is exposed during operational conditions should not degrade the SERS substrates. Additionally, the ease of fabrication and the cost of production are critical factors for the widespread adoption of the SERS technique.

I.3.2. SERS substrates for direct detection

Direct detection in SERS, or called label-free detection, is a detection scheme used to identify compounds through their own Raman spectrum and are suitable for targeted analyte that possess a strong Raman cross-section, such as conjugated organic molecules (i.e., explosive [53], contaminants like many pesticides and food dyes [54]). However, it might be difficult to apply in the biological field because the biomolecules possess small Raman cross-sections. The primary substrates employed for direct detection involve NPs in colloidal solutions, which are typically prepared through chemical

reduction. Other types include the immobilization of NPs onto planar substrates and nano-patterning, a technique that entails creating ordered arrays of NPs on the surface.

I.3.2.1. Colloidal solutions for SERS

Colloidal solution, also known as colloidal suspension, is a two-phase mixture (a dispersed phase and a dispersing phase) of particles suspended in a fluid. The figure 13 represents the main steps of the preparation of such solutions [55]. As mentioned above, the colloidal solutions are prepared by the chemical reduction method. The process starts by the chemical reduction that consist in converting silver ions (Ag^+) to silver atoms (Ag^0) by the addition of electrons. This reduction reaction can be represented as follow:

$$Ag^+ + e^- \rightarrow Ag^0$$

In this reaction, a sliver ion (Ag^+) gains an electron (e^-), which reduces its oxidation state from +1 to 0. As a result, the silver ion is converted into a neutral silver atom, Ag^0. This reduction process is a common step in the synthesis of silver NPs and is often achieved by using a reducing agent, such as a chemical compound that can donate electrons to reduce the silver ions to silver atoms. These atoms are combined into small groups called nuclei through the nucleation process initiated by adding sodium borohydride or sodium citrate. The subsequent stages involve enlarging the nuclei to create the final NP. The choice of the reducing agent is important regarding the size of the final NP. Strong reducing agent such as sodium borohydride gives relatively small NPs whereas weaker reducing agent like sodium citrate gives larger NPs [56]. Besides reducing agents, the chemical synthesis of NPs necessitates capping agents, which function as electrostatic stabilizers to prevent NP agglomeration. [57]. Chemical synthesis offers the benefit of producing diverse NP shapes, including nanorods, nanospheres, nanotriangles, and nanostars. These specific shapes are achieved through the introduction of surfactants in the synthesis process. Regarding the SERS applications, the colloidal solutions contain the nanospheres principally made of silver or gold. Silver and gold exhibit LSPR peaks at around 400 nm and 520 nm, respectively [31]. The size of the NPs used is generally below 100 nm range, as explained above, the size, the shape and the metal play a role in the LSPR maximum wavelength [58]. Gold NPs are considered more chemically stable, whereas silver is a more effective plasmonic material [59].

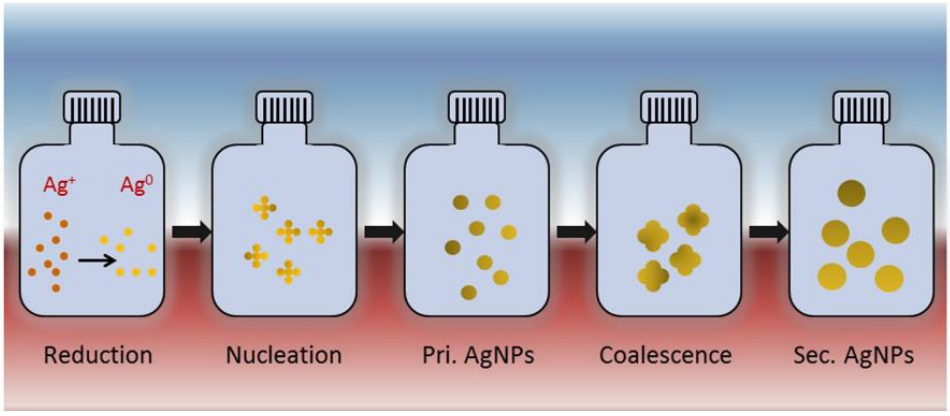

Figure 13 Illustration of the chemical reduction process for synthesizing colloidal Ag NPs. Silver ions (Ag+) are transformed into silver atoms (Ag) through a chemical reduction process. These atoms undergo nucleation to create primary Ag NPs, which then continue to merge with each other, ultimately resulting in the formation of the final Ag NPs. Reproduced from [55].

The commonly employed approach for SERS measurements entails mixing NPs with the target analyte. In this setup, the analyte molecules are uniformly dispersed throughout the solution alongside the NPs. Consequently, when the laser is directed at this mixture, it interacts with both the analyte molecules and the NPs, resulting in an amplified SERS signal. To prevent potential NP agglomeration that may occur in the mixture, the SHINERS technique (Shell Isolated NP Enhanced Raman Spectroscopy) is employed [59]. This method involves encapsulating the metallic NPs with an electronically and chemically inert shell, such as SiO2 or Al2O3. While this approach enhances NP stability compared to standard NPs, it also leads to a reduced enhancement since direct contact between NPs and analyte molecules is restricted in this configuration. Within the mixture of NPs and analyte molecules, there is free movement within the sensing volume. As a result, SERS measurements often lack the level of reliability required, which is a crucial criterion in the context of SERS sensing.

I.3.2.2. Nanoparticle immobilization on Planar Substrates

In the concept of using NPs for SERS sensing of small molecules, dyes, or biological molecules, different methods of metal deposition were employed. The utilization of the optical properties of metals, specifically the excitation of their localized surface plasmons, leads to the emergence of a highly intense local field on the metal surface, enabling the amplification of the detected signal from the target molecule. Depositing NPs onto planar substrates has the potential to enhance the reliability of the substrate. However, achieving such reliability necessitates an exceptional level of precision in NPs deposition. This implies that the NPs are arranged in an extremely orderly manner on the substrate. Another advantage of arranging NPs on planar substrates is possibility to place them in close proximity to each other to create gaps with enhanced field localization. However, all the benefits derived from immobilizing NPs may be constrained by the quality of their placements on the planar substrates.

One initial approach employed for the immobilization of NPs on a flat substrate is through chemical anchoring. A wide range of planar substrates such as silica substrate, quartz, plasma-treated Teflon and platinum could be prepared with this method [61]. To do this, the substrate has to be functionalized by salinization, which is chemical process used to modify the surface properties of materials. It involves the attachment of organosilane molecules such as 3-Aminopropyltriethoxysilane (APTES) and (3-Mercaptopropyl) trimethoxysilane (MPTMS) to the material surface. Silica substrates have hydroxyl groups (R--OH) on their surface. When a silane compound comes into contact with these hydroxyl groups, it displaces the alkoxy groups (R—O—R') of the silane, facilitating the formation of a covalent bond between the silane and the silica [62], as illustrated in the figure 14. Subsequently, the treated substrates may be immersed in a colloidal solution containing NPs, facilitating the chemical binding of the NPs to the silane additional functional group. For APTES, the amine group ($-NH_2$) is able to bind with the NPs, whereas for the MPTMS the liaison will be with the thiol group (–SH) [63]. The SERS signal measured from the functionalized substrates do not interfere with the silane signal due to its very low intensity. This technique enabled the immobilization of a diverse range of NPs, varying in size, shape, and material on substrates with relatively large surfaces (cm^2), which could improve the sensitivity and reliability of SERS measurements [64].

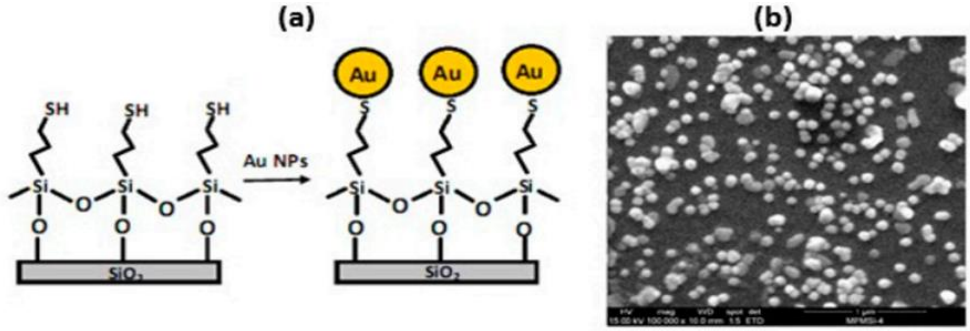

Figure 14 (a) Diagram depicting the process for anchoring Au NPs onto a quartz substrate. (b) Scanning Electron Microscopy (SEM) image revealing the Au NPs successfully immobilized on the quartz substrate. Reproduced from [65].

SERS substrates could be prepared also on paper [66] and alumina filter [67]. To create these substrates, the nanoscale gold colloids are first dispersed in a solution of isopropyl alcohol and then applied onto the filter paper using a thermal inkjet printer [66]. AuNPs clusters on the cellulose fibers of the paper are shown in the Scanning Electron Microscopy (SEM) images in Figure 155(a). The hotspots formed in these papers result in large SERS enhancement. In order to evaluate this type of SERS substrate, a hot spots were created on the substrate by depositing 5 µL portions of trinitrotoluene (TNT) in ethanol. Upon application, the sample quickly spread across the substrate, forming a circular area with a diameter of approximately 1 cm. The SERS spectra of TNT are displayed in Figure 15(b), revealing a prominent peak at 1330 cm^{-1}, which corresponds to the symmetric NO_2 stretching vibration. The inset graph illustrates the variation in SERS intensity of the 1330 cm^{-1} band as it relates to TNT concentration.

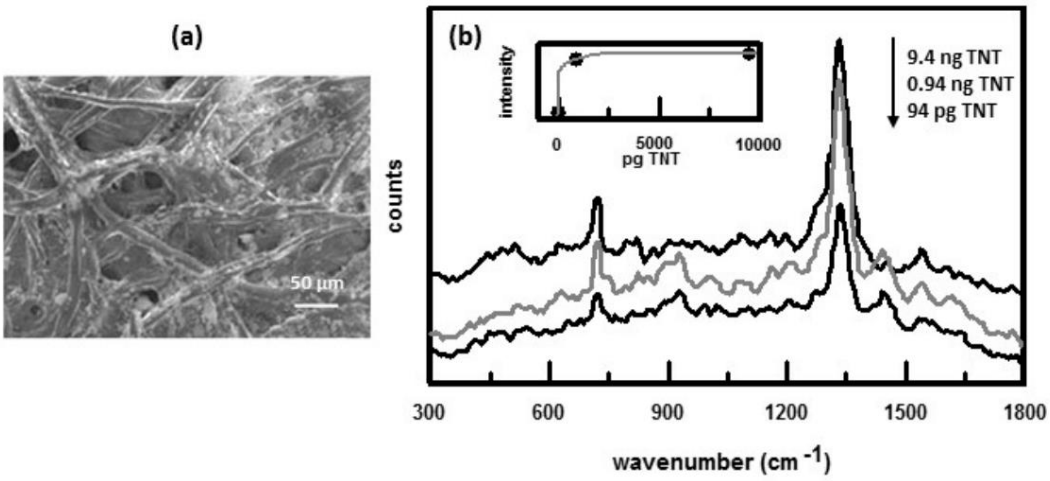

Figure 15 (a) SEM image displaying the deposition of Au NPs on filter paper. (b) SERS spectra of TNT with concentrations indicated. The inset illustrates the change in SERS intensity of the NO_2 band relative to concentration. Reproduced from [66].

The approach used to create SERS substrates involves vacuum deposition of silver metal onto alumina filters [67]. It is known that the alumina filters are comprised of alumina oxide, which have a capillary pore structure and exhibit a Raman signal that does not show any significant peaks. In addition, one method to decrease the background and get high signal-to-noise Raman spectrum is to do a plasma treatment of the substrate prior the SERS measurements. *Muniz-Miranda M. et al.* prepared solid, stable

and nanostructured SERS-active substrates by filtering Ag and Au NPs through alumina membrane filters [67]. AFM was used to examine the surface morphology of the metal films. Both films were spotted with a drop of adenine aqueous solution with a concentration of 10^{-4} M. The Ag film exhibited the highest SERS enhancement with 514.5 nm laser excitation, whereas the Au film showed the greatest SERS enhancement with 785 nm laser excitation. These findings align with the predictions of the electromagnetic theory concerning SERS enhancement.

Another way to prepare SERS substrates is by imbedding Ag or Au NPs in soda lime glass [68]. This is could be done by synthesizing Ag NPs in soda lime silicate glass by a combination of thermal and chemical methodology. Silver ions were incorporated into the glass by immersing it in a molten salt bath mixture consisting of $AgNO_3$ and $NaNO_3$ in a 1:2 ratio. In this scenario, ions replace sodium in both the surface and subsurface regions of the glass. Silver ions take the place of sodium ions on both the surface and subsurface layers of the glass. The slides impregnated with silver ions undergo multiple heat treatment cycles to convert the ions into silver metal and encourage particle growth.

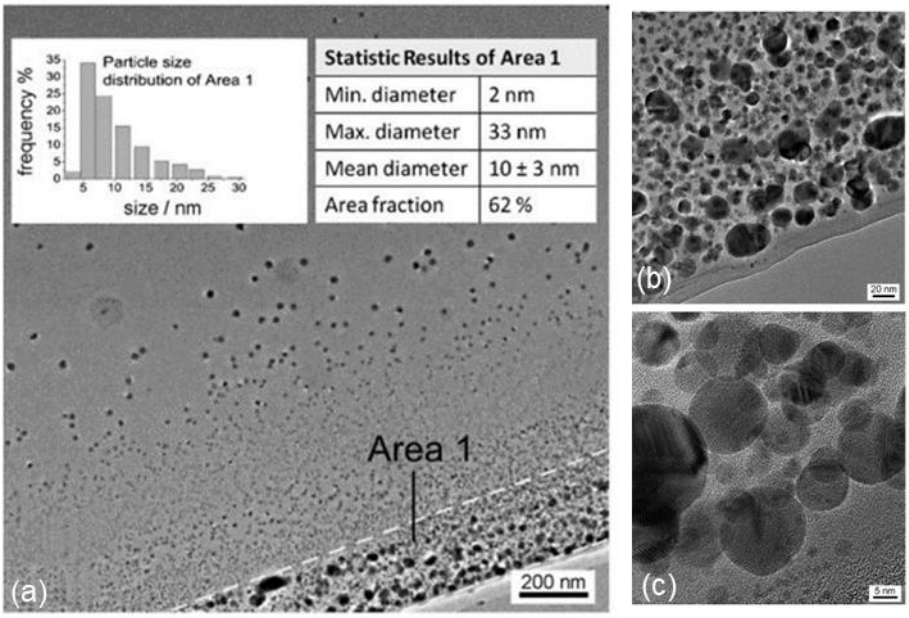

Figure 16 (a) Transmission electron microscopy (TEM) images depicting the cross-sectional profile of Ag SIMO glass samples subjected to 30 seconds of ion exchange with a) 13.000x, b) 87.000x and c) 380.000x magnification. The inset displays both the size distribution and statistical outcomes related to the subsurface area, denoted as Area 1 (b). Reproduced from [68].

TEM images shown in figure 16 illustrates that the NPs are concentrated in the subsurface of 200 nm thick area. The particles exhibit a spherical shape and demonstrate notable crystallinity, as evidenced by the clear observation of individual atomic planes (Figure 16(c)). The subsurface silver particles embedded within the surface layer of soda-lime silicate glass benefit from both mechanical and chemical protection. These stable glass composites can be securely transported and stored over extended periods before being employed in analytical techniques. To acquire a SERS spectrum, it is necessary to expose the subsurface Ag NPs. The required exposure can be attained using either chemical etching with an aqueous HF solution or by utilizing mechanical methods. Embedding NPs rather than immobilizing them onto SERS substrates has the advantage of reducing uncontrolled aggregation, leading to enhanced sensitivity and reliability. With these substrates, the EF was estimated at 10^7. This technique could be used with different types of materials such as polymers.

I.3.2.3. Nanopatterning: structured surfaces

Nanopatterning is a process refers to the creation of patterns or structures at the nanoscale, typically in the range of 1 to 100 nanometers, in order to create active-SERS substrates. Several techniques were used to create these patterns. The first method is template-assisted electrochemical deposition (TAED), which enables the controlled deposition of metals with specific geometries. For instance, Huai-Hsien Wang *et al.* created silver-filled porous anodic alumina oxide (AAO) substrates by doing several operations as shown in Figure 17 [69].

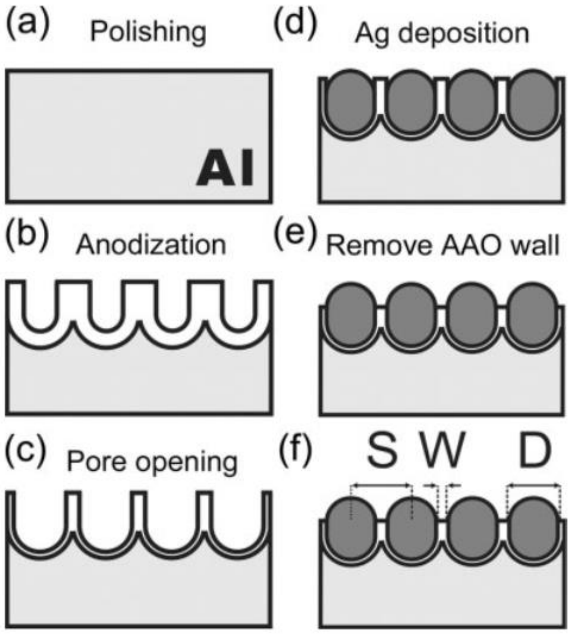

Figure 17 Illustration outlining the procedure for creating substrates with porous anodic alumina filled with silver. Reproduced from [69].

AAO Nanochannel substrates are produced through the anodization of a finely polished aluminum foil. Then, a 5 % phosphoric acid is used to etch the substrate to widen the pore diameters. By controlling the time of the etching, the wall thickness between the Nanochannels arrays is about 5 ± 2 nm. This etching process enables precise adjustment of the gap between the NPs in an array. The walls serve to separate the Ag deposited into the Nanochannels during the subsequent electrodeposition process, as depicted in Figure 17(d). After this step, in order to expose the Ag NPs, the alumina is partially etched. The final geometry obtained is shown in Figure 17(f) where the Ag NPs are partially embedded in an AAO substrate and the letters S, D and W are the interparticle spacing, particle diameter and interparticle gap, respectively. In order to evaluate the SERS enhancement with this type of SERS substrate, a solution (10^{-6}) of Rhodamine 6G (R6G) was adsorbed in the subsurface. High-intensity Raman peaks are noted as the fluorescence background is brought to a quenched and stable state. The EF for the Ag/AAO substrate was determined to be at least 10^5 times greater than that of SERS substrates created by depositing approximately 30 nm of silver onto a silicon surface. This enhancement can be related to the fact that in this type of substrate, there is high density of both Ag NP (~ 1×10^{11} cm^{-2}) and 'hot junctions' (~ 3×10^{11} cm^{-2}) that are formed by the gaps between the neighboring NPs, as discussed above.

Another technique used to create the patterns is the laser ablation. It consists of ablating sections of a substrate using a laser to obtain the desired shape. Subsequently, thin metal layers could be deposited in the surface of the substrate. For example, *Jing Yang et al.* applied a nanosecond laser with 100 µm pitch along both vertical and horizontal directions on Si substrates to create micorsquare arrays as illustrated in Figure 18(a) [70]. Figure 18(b) shows that during the laser ablation process, Si NPs are formed with various shapes and sizes in the center of the microsquares. Then, a film of 40 nm Ag is deposited over the entire structure, which lead to form Ag coated silica NPs. This configuration lead to abundant nanogaps, ranging within a few nanometers, and can serve as hotspots during SERS detection. The SERS spectra of 4-methylbenzenthiol molecule was measured to evaluate the EF. It has been shown that the EF is superior to 10^6 and standard deviation (SD) of 6 % across eight measurements. In certain cases, the Nanostructuration and the deposition of NPs could be done simultaneously. As an illustration, Lin *et al*. employed a femtosecond laser source on positioned silicon wafers immersed in an aqueous solution of silver nitrate [71]. The laser application initiated the photoreduction of silver, leading to the formation of NPs on the wafer surface. This substrate enabled the attainment of an EF of up to 10^9. However, While the laser ablation method provides sensitive and dependable SERS substrates, the fabrication process for large substrates is time-consuming.

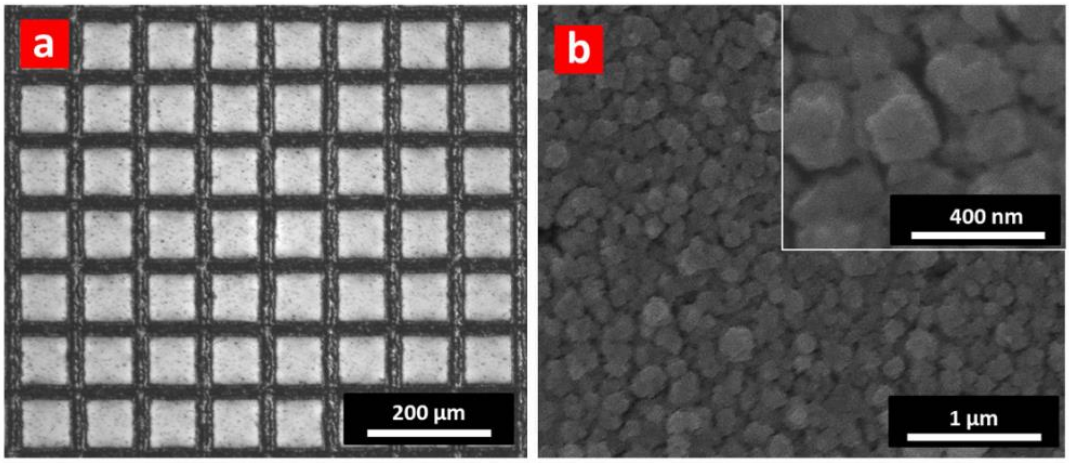

Figure 18 (a) Microscopic view of silicon surfaces featuring an array of microsquares. (b) SEM images captured within these squares showing laser ablation effects at a fluence of 21.0 J/cm^2. Reproduced from [70].

NSL is another technique that allows for creating well-ordered 2D periodic arrays of NPs for SERS [72-74]. *De-Yin Wu et al*. delineated the three categories of ordered substrates that can be created using NSL techniques, as illustrated in Figure 19 [75]. The initial stage of the procedure is to drop coat a suspension of monodisperse polystyrene or SiO2 nanospheres, with the specified diameter, onto a clean conductive substrate like indium tin oxide (ITO) or an evaporated metal substrate on glass. The nanospheres spontaneously arrange themselves, creating a highly organized mask for the deposition of metal. Following this, a metal layer of the intended thickness can be deposited onto the formed mask using either physical vapor deposition or electrochemical deposition. The three varieties of structured substrates depicted in Figure 19 are (1) the Ag or Au metal film over nanospheres (MFON); (2) the nanospheres could be removed by sonicating in a solvent and an array of nanotriangles remains; (3) After electrochemical deposition, the subsequent step involves removing the spheres, resulting in a thin nanostructured film containing a regular hexagonal array of uniformly sized voids. Obviously, the size of nanoshperes and the thickness of the deposited metal has a direct impact on the dimension of the final NPs array. So that the LSPR response could be matched to the excitation laser used in order to obtain

the strongest SERS enhancement [76]. A LOD of 1 ppb was achieved using these Ag NPs/AuFON substrates.

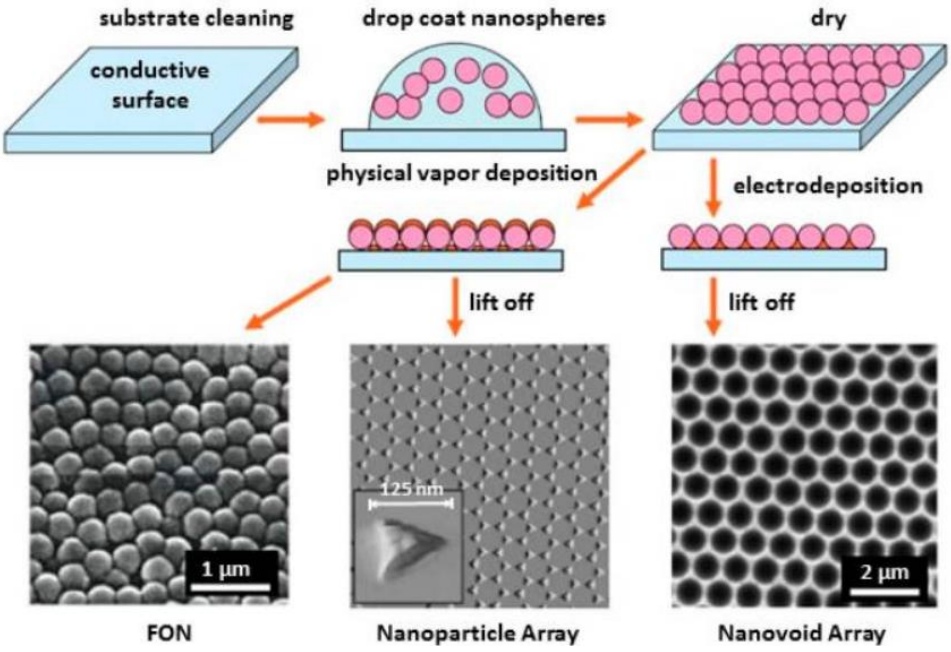

Figure 19 Diagram illustrating template methods for creating SERS-active substrates using nanosphere lithography. Reproduced from [75].

Electron beam lithography (EBL) is also another method used to create nonpatterns on the substrates surfaces [77-80]. The process of the fabrication starts with the deposition of a polymer on the substrate, this polymer called resist, is sensitive to electrons beam. By scanning the focused electron beam, the solubility of the resist is changed, allowing for the creation of a pattern within the resist. Subsequently, the substrate is immersed in a solution to eliminate the soluble resist. Figure 20 illustrates two approaches for creating an active SERS substrate. One method involves the evaporation of gold into the template, followed by a lift-off process. This method allows the creation of metallic NPs with well-defined geometries. The alternative method utilizes plasma etching. The advantage of EBL method over other techniques is that it can draw patterns with sub-10 nm resolution, which lead to fabricate SERS substrates with desired shapes, sizes and arrangement of nanostructures allowing to better SERS enhancement. In addition, those SERS sensors generally exhibit good reproducibility of SERS measurement.

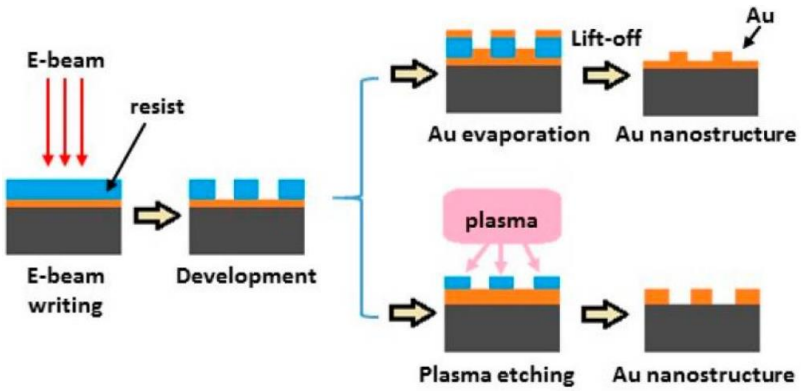

Figure 20 Illustration of the two fabrication procedures employed for the preparation of nanostructured SERS substrates. Reproduced from [81].

Another technique that allow for micro and Nanofabrication is soft lithography. This method compared to others, is much cheaper and accessible. It consists in using an already Nanopatterned substrate as a mold of stamp to create the desired substrate [82]. *Ou et al.* used EBL and dry silicon etching to fabricate a silicon array of Nanopillars, which are used as a mold to create the daughter mold using tU-curable nanoimprint lithography (NIL) [83]. Subsequently, the tips were coated with a gold layer with an 80 nm of thickness and a diameter of 140 nm, while the tall of the Nanopillars was about 520 nm. After immersing these arrays on a solvent and draying it. The capillary forces yielded to the Nanopillars collapse on each other. Figure 21 illustrates the different steps used to fabricate such SERS substrates. In certain cases, depending on the specific array employed, it has been reported that digon, trigon, tetragon, pentagon and hexagon structures are fabricated [83]. In addition, using the pentagon structure, they were able to achieve an EF of ~ 10^{11}.

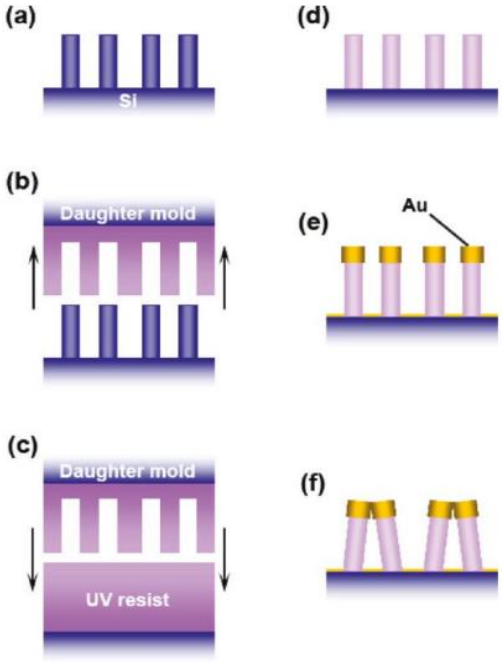

Figure 21 Illustration of the various stages of NIL employed by Ou *et al.* for the fabrication of nanopillars. Reproduced from [83].

I.3.2.4. Applications: Label-free detection.

As mentioned above, the SERS biosensing can be realized depending on the Raman-cross section of the target analyte. In the case of direct detection, or label-free detection, the target molecules contain a strong Raman cross-section.

For instance, *Wang et al.* prepared extracted Ribonucleic Acid (RNA) from urine of patients in order to detect prostate cancer [84]. The figure 22 presents the steps followed to prepare this type of sample. After the extraction, the target RNA are amplified into double standard deoxyribonucleic acid (dsDNA) sequences named amplicons. After the purification, these amplicons are then incubated with positively charged Ag NPs. With this configuration, SERS spectra were measured of the target amplicons. The detection of prostate cancer exhibited high specificity (93.0%), sensitivity (95.3%), and accuracy (94.2%). Alternatively, colloidal Ag NPs have been successfully used to detect and differentiate the blood plasma of people with gastric cancer from the healthy people [85]. This is realized by mixing the Ag NPs with the plasma then using a polarized laser. SERS measurements were obtained with a sensitivity of 100% and a specificity of 97%.

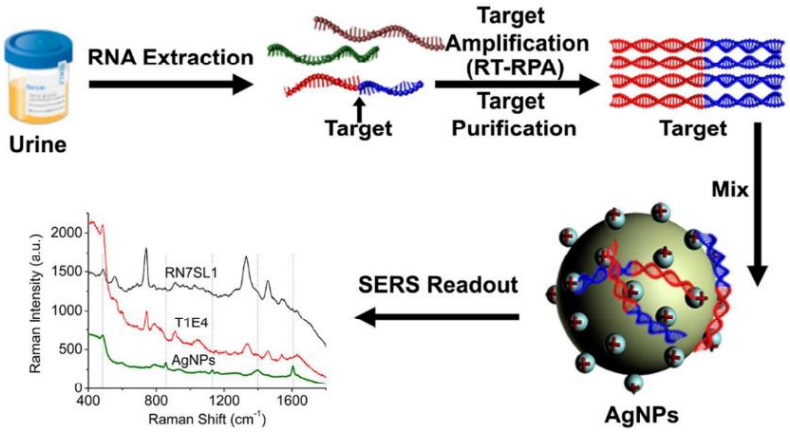

Figure 22 Method employed for prostate cancer detection involves the extraction of RNA from urine, followed by the measurement of the SERS signal. Reproduced from [84].

In addition, SERS can be realized to analyze the cellular functions and components in the cells. For that, the NPs had to be incorporated into the biological samples. As mentioned above, the colloidal Au NPs are the most suitable for this case thanks to their biocompatibility, chemical inactivity and their high Raman EF within the excitation range corresponding to the biological window [86-90]. Furthermore, adjusting the size, shape, and surface functionalization of Au NPs allows for the specification of which cellular barrier they will traverse and their precise localization within cells [91]. For instance, Kneipp, K *et al.* were able to map the distribution of phenylalanine and DNA over 30×30 mm^2 cell monolayer in intestinal epithelial cells using 60 nm gold NPs [89]. Moreover, Walter *et al.* identified nine strains of Escherichia Coli through the using of Ag NPs in a microfluidic chip [90].

SERS was additionally employed for the characterization of proteins through various methods [91]. At the individual molecule level, SERS spectra were captured from myoglobin attached to immobilized structures of 100-nm size [92]. Alternatively Han *et al.* integrated SERS with Western Blot to identify multiple proteins [93]. A mixture containing myoglobin and bovine serum albumin (BSA) was subjected to electrophoresis separation and then immobilized onto a nitrocellulose membrane through electroblotting. The molecules were then stained using a solution Ag NPs, enabling the acquisition of

SERS spectra for each molecule. Through the synergistic application of both techniques, the researchers successfully detected as little as 4 ng of myoglobin.

Colloidal solutions can be employed to detect bacteria and viruses. *Efrima et al.* were the first to report the utilization of Ag nanocolloids on bacterial cells; they explored "Escherichia coli" bacteria using Ag NPs inside the bacteria and on the outer walls [94]. Doing this, a strong SERS signal was recorded thanks to the hotspots formed by the Ag NPs. This resulted also in Raman signal of proteins, amino acids and functional groups present in the proximity of the colloidal NPs.

I.3.3. SERS Nanotags for indirect detection

I.3.3.1. SERS Nanotags features

Until now, we presented the SERS method used in case of direct detection, which means that the analyte molecules possess a strong Raman cross-section. SERS Nanotags or SERS labels are used in order to detect biomarkers molecules that possess weak cross-section. This can be realized by attaching the target molecule to these Nanotags through a specific procedure. The Nanotags will emit a very strong Raman signal, which reveals the presence of the target molecule. In the case of the absence of the Raman signal of the Nanotags, one can confirm the absence of the target molecule in the analyte.

Generally, Nanotags are composed of four components: the metallic nanostructure (usually a metallic NP), the Raman reporter, the protection shell functionalized with the targeting molecules [96]. The figure 23 illustrates the design of a SERS tag.

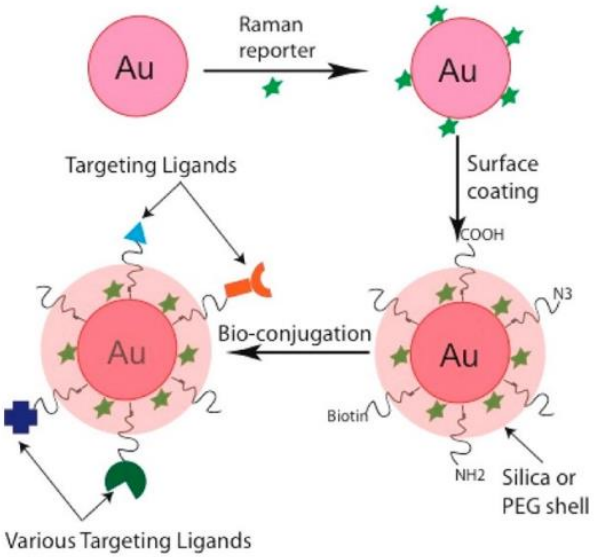

Figure 23 Illustration of a SERS tag composed of a plasmonic core, Raman reporter. Reproduced from [95].

The first requirement for the metallic nanostructure chosen to fabricate the Nanotags is that it has to be biocompatible as well as the other components as they will be used in biosensing. This is to ensure the patient safety and preserving the integrity of the analyte sample with the necessary precautions. Generally, the gold metal is used as the core of the Nanotag because of its long-term stability and high biocompatibility. Hence, studies of fundamental structures or applications involving living organisms typically employ Au NPs [97]. In broad terms, although its poor biocompatibility, the silver serves as a significantly more effective material for enhancing Raman signals, leading to SERS signals that are 10

to 100 times greater than those produced by comparable gold nanostructures. Therefore, many studied had been conducted in order to optimize the size of the gold nanostructures in order to benefit from biocompatible and sensitive SERS tags [98]. In addition, several shapes are tested to fabricate SERS tags, such as Au Nanoshell [99], Au Nanorods [100] and sliver-gold bimetallic NPs [101-104]. Conducting these studies is crucial to align the plasmon resonance with the excitation wavelength and the Raman signal, leading to increased enhancement and improved sensitivity.

Regarding the Raman reporter chosen in the SERS nanotag composition, it should to have a large cross-section with sufficiently strong Raman peaks and good photochemical stability. Generally, the Raman reporters used in SERS Nanotags are principally malachite green, Rhodamines and crystal violet [105]. Nevertheless, using these dyes, if the excitation wavelength aligns with or is close to their optical absorption band, this will increase the risk of overheating and damaging the reporter molecules. To circumvent this issue, alternative options can be suggested. For instance, employing small organic molecules like benzenthiol, which exhibit favorable cross-sections, allows for binding to the metallic surface of NPs. The protective layer used in SERS Nanotags serves principally to prevent the aggregation of the NPs, which result in keeping the Raman reports attached to the NP the surface. The nature of this layer is often the polyethylene glycol (PEG) or silica [106]. Both of them can be functionalized with ligands like peptides, aptamers or antibodies, which allow targeting specific target molecules [104]. In addition, the thickness of this layer is important in order to decrease the SERS enhancement decay with the distance. Furthermore, the shell serves to hinder the adsorption of undesired molecules onto the surface of the nanotags.

I.3.3.2. Applications: Labeled detection

In this section, we will describe some biomedical application using SERS Nanotags as substrates for indirect detection of DNA sequences, cellular functions and proteins. For instance, Vo Dinh's group developed a method that can detect DNA sequences [15] indirectly. The name of the method used is molecular sentinel. The method operates on the principle of a DNA hairpin that is functionalized with a Raman dye at one end and a molecule featuring a thiol group at the other end. The thiol function will allow the DNA hairpin to bind with the gold film deposited on the close-packed nanosphers as illustrated in Figure 24. In its initial state, the DNA hairpin (molecular sentinel) adopts a conformation where it forms a stem, closing in on itself. This configuration ensures the proximity of the Raman dye to the gold film and allows having a strong Raman signal. It is important to highlight that the DNA hairpin serves as the complementary sequence to the target DNA. Consequently, in the presence of the target DNA sequence, the two DNA strands hybridize, leading to the unfolding of the hairpin loop. In this altered configuration, the Raman dye relocates from the gold film, causing a significant decrease in the SERS signal. This reduction indicates the presence of the target DNA. Moreover, certain studies have introduced a novel parameter known as the relative diagnostic index (RDI). This parameter is employed to denote the transition from an active to an inactive state in the SERS signal. It is utilized to assess the alteration in the SERS signal when the molecular sentinel binds to its target [107].

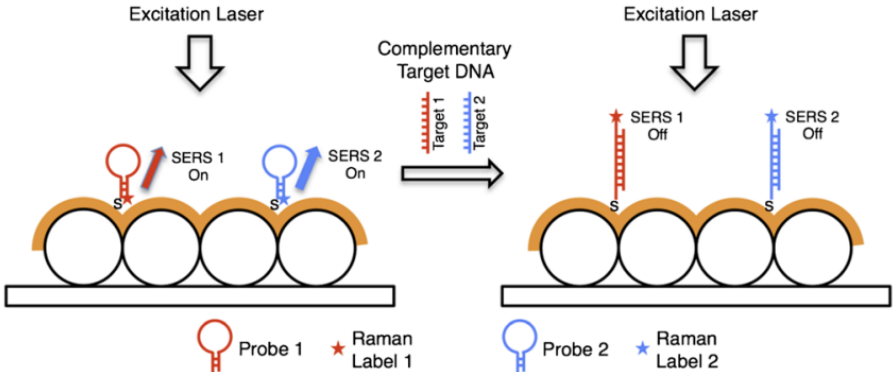

Figure 24 Illustration of the sensor used for the molecular sentinel (MS) technique. Reproduced from [15].

In addition, SERS nanotags are used also to detect the changes in the cell microenvironment, such as intracellular pH. This an important factor in order to understand the cell physiological functions. Maintaining the right pH level is crucial for various cellular processes, as enzymes and other biomolecules function optimally within specific pH ranges. *Kong, K. V et al* developed a SERS-based sensors that consists of using a Raman active molecule that are covalently attached to either gold or silver NPs, which then cause changes in the SERS signal as a function of the pH of the surrounding media [108]. Changes in redox potential also play a crucial role in comprehending cellular functions, such as signaling pathways, apoptosis as well as cell cycle [109]. The measurement of the oxidative or reductive state within a living cell, as encapsulated by this element, contributes to understanding changes occurring during diseases such as cancer. EL Said *et al.* created a chip based on single-cell analysis to quantitatively measure both the intracellular and extracellular redox potential of neural cells (PC12) [110]. The approach involved integrating SERS with linear sweep voltammetry (LSV) to observe biochemical alterations within the cells. To achieve this, a solitary PC12 cell is fixed onto an adapted ITO substrate, featuring a hexagonal arrangement of gold nanodots positioned within a micrometer-sized space between two gold microelectrodes. They examined the impact of applied redox potentials on a dopamine solution using SERS and LSV to assess cellular biochemical compositions. They identified variations in responses between cell lysates and living cells. Moreover, they successfully examined the electrochemical activity of both bulk and individual PC12 cells, establishing this as a proficient substrate for the analysis of cellular processes. Additional studies have been carried out to observe changes in redox potential and biochemical responses in Hepatitis G2 (HepG2) cells when exposed to three distinct anticancer drugs [111]. The detection and quantification of specific protein markers are crucial for diagnostics and understanding the progression of diseases like cancer [112]. The use of SERS nanotags is indispensable to detect protein markers.

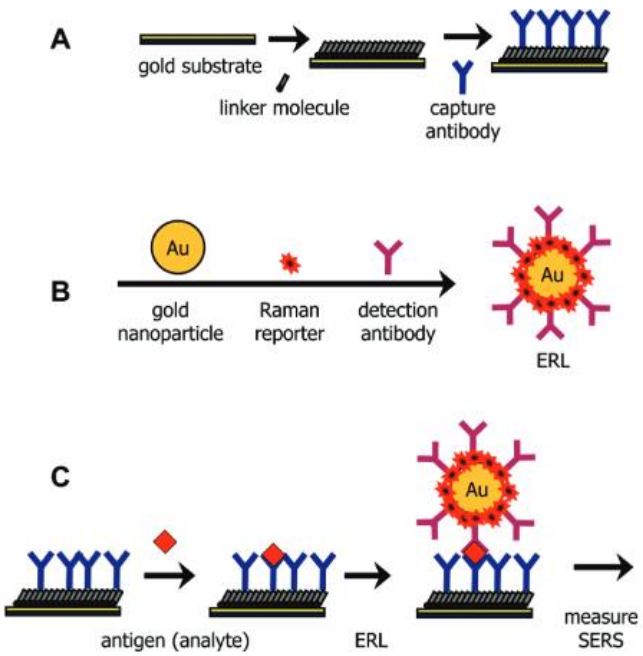

Figure 25 Design and scheme for a SERS-based immunoassay chip: (A) utilization of a capture substrate to selectively extract and concentrate antigens from a solution; (B) application of surface-functionalized Au NPs (ERLs) to selectively bind to captured antigens, producing robust SERS signals; and (C) implementation of a sandwich immunoassay with SERS readout. Reproduced from [112].

For example, Wang et al. designed a simple sandwich-type SERS immunoassay for the identification of the pancreatic cancer biomarker, MUC4 [113]. They engineered a nanochip composed of MUC4 antibody-functionalized Au NPs, capable of extracting and concentrating antigens from solutions. Subsequently, SERS tags containing a Raman reporter were introduced (figure 25), resulting in the generation of robust SERS signals. In this study, the introduction of a sleek mica layer onto the nanochip was observed to enhance the detection sensitivity of MUC4 [114]. Lung cancer marker called carcino-embroyonic antigen (CEA) was also detected in the blood of patients using sandwich-like immunoassays [115]. In a different study, an immunosensor was employed for the detection of PSA, a widely recognized biomarker for prostate cancer. The sensor utilized a liquid-chitosan nanocomposite incorporating multiwalled carbon nanotubes as the biomarker [116]. Other studies had showed the role of using SERS tags in detecting protein markers [117].

I.4. SERS-Active Photonic Crystal Fiber probes

I.4.1. Introduction

Since the advent of optical fibers, their widespread utilization has been evident for various purposes, including communication and sensing. The structure of the fiber may vary depending on its intended use. Typically, an optical fiber consists of a solid or hollow core that guides the light and a cladding that surrounds the core. In this manuscript, our emphasis will be on a category of fibers known as Photonic Crystal Fibers (PCFs). These fibers are also called microstructured optical fibers. They are composed of air-holes in their cross section, i.e. running along the fiber length, that give rise to numerous properties for guiding light and for enhancing light-matter interactions. In the next section, the two main categories of PCFs will be introduced, along with their optical properties and their practical applications.

I.4.2. Hollow- and solid-core Photonic Crystal Fibers

I.4.2.1. Hollow-core Photonic Crystal Fibers

Hollow-core PCFs (HC-PCFs) are composed of a large air hole acting as a hollow-core that is surrounded by an arrangement of air-holes, i.e. the photonic crystal cladding. Some examples of HC-PCFs are presented in figure 26. As will be explain in the following, there are two main types of HC-PCFs : Photonic bandgap (PBG) fibers and anti-resonant fibers.

For the first type, the guiding mechanism relies on the refractive index (RI) of the analyte injected in the core. In this fiber, when the filled analyte has a RI lower than the index of silica, the light will be guided by the photonic band gap effect (PBG). This guiding mechanism operates by inhibiting specific wavelength ranges from being guided within the silica cladding. Consequently, when light at wavelength in the PBG range is introduced into the hollow-core, it is unable to exit into the cladding and remains confined within the core of the HC-PCF. The opto-geometric parameters of the crystal cladding such as the pitch (distance between two adjacent air holes), RI in the holes and RI of the material play an important role in the creation of PBG. One of the advantages of these fibers for Raman and SERS applications is the ability to fill the hollow core with liquid analytes, allowing light to propagate directly through the liquid. This eliminates unwanted Raman signals from the fiber material.

.

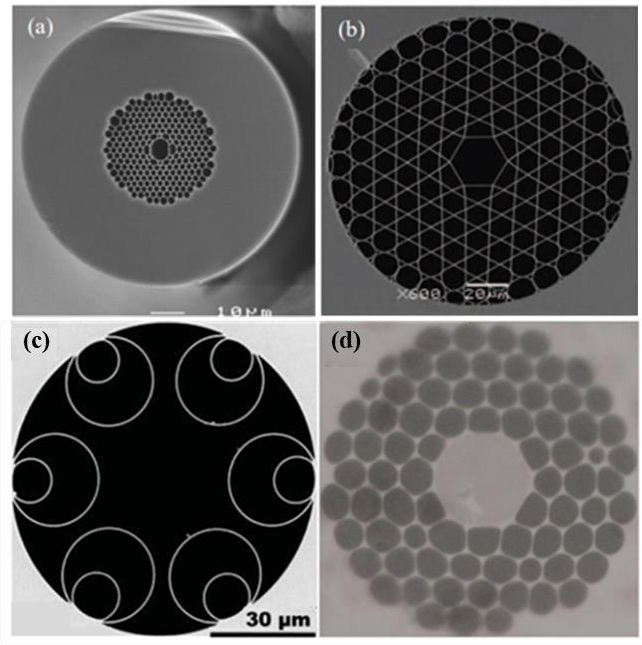

Figure 26 Cross-section of (a) HC-PCF [118]. (b) Kagome PCF [119]. (c) NANF [120]. (d) LC-PCF [121].

The HC-PCF design illustrated in Figure 26(a) is one of the fiber that operates with PBG principle, it facilitates direct interaction with a relatively large core diameter and extended interaction length, while avoiding parasitic signals from the fiber material. However, its effectiveness may be limited by the fiber's attenuation coefficient and the analyte's absorption coefficient. Additionally, the transmission windows are relatively narrow (a few hundred nanometers), and introducing the analyte into the HC-PCF alters the refractive indices of the core and cladding holes, leading to a shift in the transmission bandwidth. [122]. The figure 27 represents the experiments done by *Antonopoulos et al*. showed this propriety by measuring the transmission spectra of a HC-PCF before and after filling it with liquid D_2O [123]. This study demonstrated the necessity of anticipating the shift in the transmission window to accurately guide the excitation laser and Raman signal when the fiber is filled.

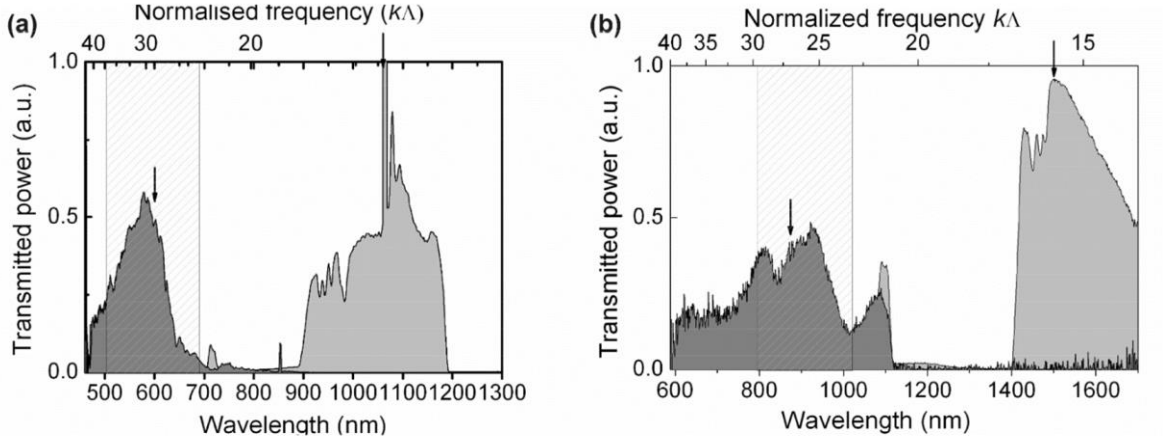

Figure 27 (a) Transmission spectra of the 1060 nm fiber obtained using supercontinuum source, and (b) of the 1550 nm fiber obtained using a tungsten lamp. The spectra were recorded both before and after the holes of the HC-PCF were filled with liquid D2O, indicated by the light and dark grey areas, respectively. The vertical lines denote the positions of the newly shifted bandgaps, while the arrows indicate the location of the respective transmission peaks. Reproduced from [123]

Another structure, referred to as "kagomé," is characterized by a cladding lattice made up of unit cells arranged in the shape of a star-of-David as showed in Figure 26(b). With this fiber, the cladding structure acts like a Fabry-Perot resonator [124]. For resonant wavelengths, the light may extend beyond the fiber core, whereas for anti-resonant wavelengths, the light is partially reflected within the hollow core, ensuring it stays confined inside [125]. This mechanism provides a wide transmission window, mitigating the impact of RI changes when the fibers are filled with the analyte. Nevertheless, Kagome HC-PCF demonstrates high attenuation loss, measuring at 0.5 dB/m [126]. Additionally, the fiber is constrained by the attenuation of both the excitation and Raman signals, which imposes limitations on the effective length of the fiber in SERS sensing applications. Figure 26(c) illustrates an innovative variant of anti-resonant HC-PCF that has attracted attention for its efficient guidance with minimal loss. This fiber, known as Nested Anti-Resonant Nodeless Fiber (NANF), demonstrates an impressive record-low loss of 0.65 dB/km at approximately 1550 nm when filled with air [120]. Therefore, this fiber structure could serve as a viable substitute for HC-PCF, given its broader transmission bandwidth and reduced attenuation loss. Another structure that allow the light to be guided by total internal reflection (TIR) is the liquid-core PCF (LC-PCF). TIR mechanism states that when light encounters the interface between two medias with different refractive indices at a sufficiently large angle, it undergoes TIR and remains confined in the medium with the higher RI, this mechanism is based on Snell-Descartes' law. Figure 26(d) represents the LC-PCF filled with ethanol [121]. The guiding mechanism relies on TIR

with this fiber because the core is surrounded by air-filled holes. Consequently, the variation in RI between the liquid core and the air in the cladding allows for light guidance through TIR. Compared to HC-PCF, LC-PCF exhibits a significantly broader transmission bandwidth. The drawback of this fiber lies in the guidance of light in a highly multimode regime, attributed to the substantial core size.

I.4.2.2. Solid-core Photonic Crystal Fibers

Solid-core PCF (SC-PCF) are composed of a silica core surrounded by a cladding of air-channels that enables light propagation into the core by TIR mechanism. These fibers are manufactured using the stack-and-draw process (as presented in Section II.2.3.1), which offers great flexibility in designing PCFs. As a result, numerous different PCFs have been developed. Figure 28(a) shows the SC-PCF, characterized by a solid core and a cladding with a 2D-periodic arrangement of holes. When the fiber contains the analyte, the interaction between light and the analyte takes place through the evanescent field which is a small portion of light that travels in the air cladding. The size of this light portion is directly correlated with the core size; as the core size increases, the evanescent field diminishes in size. By adjusting various optical and geometric properties, such as the size of the core and the ratio of the hole diameter to the pitch (d/Λ), the regular SC-PCF can show distinctive characteristics like continuous single-mode propagation [127]. To enhance the amount of light interacting with the analyte, it essential to reduce the core diameter. However, this reduction in core diameter results in decreased hole diameters, limiting the incorporation of liquid into the fiber and posing challenges for the sensing application of this fiber.

To address this issue and make it easier to add liquid into the fiber, the fiber shown in figure 28(b) offers a solution. This fiber is known as Suspended-Core PCF (SuC-PCF). It is composed of a small core surrounded by three air holes. Unlike the previous fiber (SC-PCF), there is no regular pattern in the cladding. In the SuC-PCF, TIR guides the light because the RI of the injected liquid is lower than that of the core. Regarding the mode in which light propagates, it relies on the normalized frequency (V), as determined by the following equation:

$$\mathrm{V} = \frac{2\pi}{\lambda} a\, NA = \frac{2\pi}{\lambda} a \sqrt{n_{core}^2 - n_{cladding}^2} \tag{18}$$

Where n_{core} and $n_{cladding}$ are the RI of the fiber core and the cladding respectively, a is the core diameter and NA is the numerical aperture.

If the V is lower than 2.405, the fiber is considered single mode. When the core is relatively large or depending on the liquid injected into the fiber, the light can be guided in a multimode regime [132].

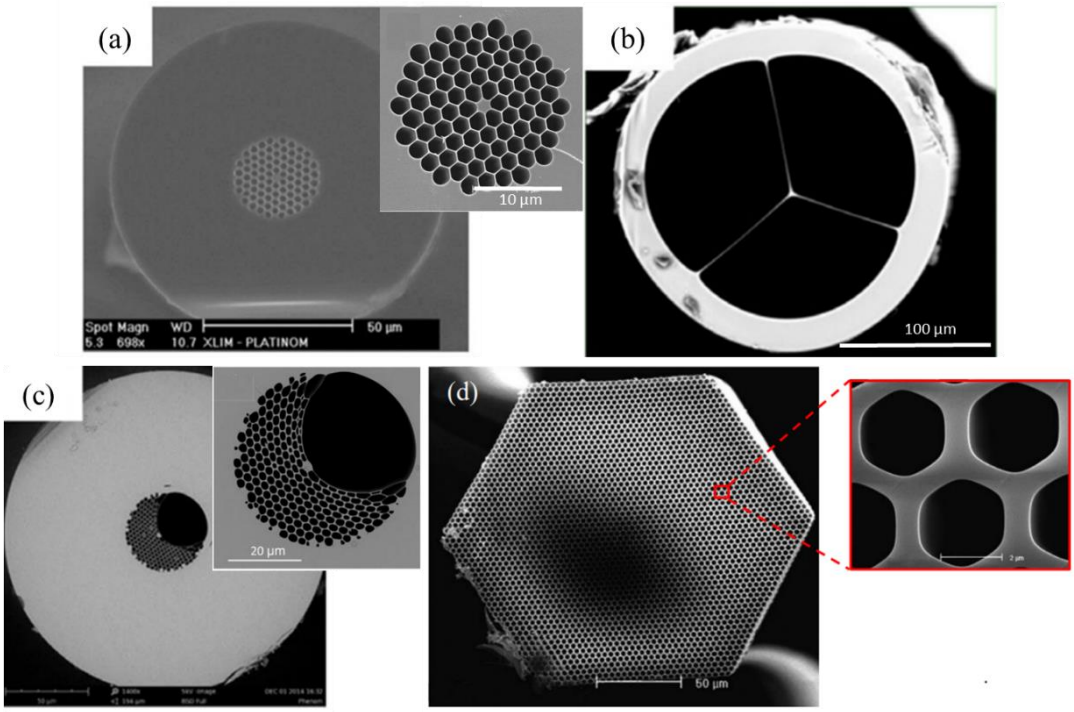

Figure 28 SEM pictures of the Cross-sections of (a) SC-PCF [128]. (b) SuC-PCF [129]. (c) SiC-PCF [130]. (d) Core-array PCF [131].

Another viable option for easily introducing liquid into the fiber involves removing a section of the cladding from a regular SC-PCF, as depicted in Figure 28(c). This type of fiber is known as Side-Channel PCF (SiC-PCF), and it can be viewed as a combination of the standard SC-PCF and SuC-PCF. The inclusion of the side channel enables swift introduction of liquids into the fiber. Moreover, precise control over the parameters allows for accurate management of guiding properties, making it a favorable choice for sensing applications. As an illustration, this fiber was employed as an in-line opto-fluidic lab-in-fiber device [133].

The final fiber structure introduced in this section is known as Core-Array PCF shown in figure 28(d). This configuration features an array of small cores surrounded by silica struts. The abundance of these cores results in a significant portion of the evanescent field that interact with the injected liquid. However, this light is guided in a highly multimode regime, potentially limiting the reliability of the measurements. Moreover, challenges in incorporating liquid, coupled with notable propagation loss (~1 dB/cm) [131] and coupling losses (~ 28 dB) [134], constrain its applicability in sensing applications.

I.4.3. Interests of PCFs for SERS sensing

Unlike all-solid fibers, the PCFs offer the opportunity of the incorporation of liquids or gases into the fiber, thereby enhancing the interaction between the excitation light and the analyte. PCFs have be applied in various biosensing applications, including measuring RI variation in an analyzed sample [135], absorbance measurements in the UV-visible-NIR range [136], detecting surface plasmon resonance signals [137], and recording Raman scattering and luminescence signals while the light interacts with the injected analyte. In these fibers, the core serves as a collection platform since it can collect the signal interacting with the infiltrated analyte along the fiber length. Various comprehensive reviews focus on optical fiber sensors in general, including those based on PCFs [138]. For instance, Fan and White [139] conducted a comparative study on various optofluidic microsystems, which

included PCFs, for chemical and biological analysis. Cubillas *et al.* provide a review dedicated to describing various PCF-based bio and chemical sensors that rely on the measurement of transmission, absorption, and luminescence signals from gaseous and liquid samples [136].

For SERS application, these PCFs could be functionalized by attaching NPs along the entire length of the fiber. The light can interact with NPs/analyte and then the signal is collected (figure 29). In this configuration, the light propagation is influenced by the particular design of the fiber. By improving the fiber design, one can enhance the interaction surface as well as increasing the number of collected Raman photons [140]. This is the reason why PCFs enhance sensitivity compared to direct detection.

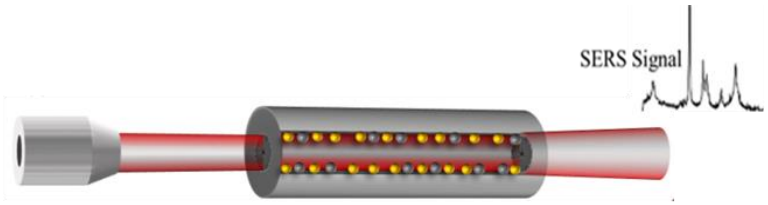

Figure 29 Illustration of the sensor used for the molecular sentinel (MS) technique c'est quoi ce terme, il faut le définir. Je pense qu'il est plus simple de décrire SERS applications for biosesing.

Numerous studies have reported an improvement of two to three orders of magnitude is achievable. For instance, Yang et al. revealed that the Raman signal from nitrogen presented a 700-fold increase in intensity when using PCF for the detection of gaseous nitrogen compared to bulk detection [141]. This substantial improvement in sensitivity positions PCFs as a viable alternative to existing gas sensing devices, which are typically characterized by their bulkiness and high costs. Numerous additional investigations have been undertaken with the objective of integrating PCFs into microfluidic devices such as the study conducted by Unterkolfer *et al.* who have designed a micro-fluidic circuitry that included a HC-PCF [142]. In addition, L. Xiao *et al.* have developed all-in-fiber microcells made by PCFs [143]. A system was built using a HC-PCF, which was filled with an analyte solution and sealed at both ends by splicing SMFs. This integrated HC-PCF device enabled the authors to detect the Raman signals of toluene and ethanol with laser power six orders of magnitude lower than what had been reported previously.

For various compelling reasons, PCFs are recognized as an appealing tool for both preclinical and clinical biosensing applications. The subsequent section of this chapter will delve into the process of functionalizing these fibers with NPs. Then we will explore diverse PCF designs suitable for SERS applications. Subsequently, we will examine noteworthy studies highlighting PCF-based SERS sensors. Finally, we will evaluate the advantages of the two main types of PCFs (HC and SC PCFs) and compare their performance to planar substrates. Additionally, we will discuss the development limitations of fiber-based SERS sensors, especially concerning designing sensors suitable for clinical applications.

I.4.3.1. State-of-the-art in PCF SERS-sensing

This section reviews studies aimed at understanding the various interactions involved in SERS sensing with PCFs. Prior to this, we will discuss the method used for functionalizing PCFs with NPs.

I.4.3.2. Method of functionalization of the PCFs for SERS

As previously stated, PCFs offer the benefit of incorporating liquids or gas analytes within their air-holes. This is could be complemented by the presence of NPs that play a crucial role in SERS. Two main configurations are employed for the functionalization of PCFs with NPs:

- **Injected Configuration :**

In this configuration, the analyte and NPs are mixed. Afterward, the resulting solution is injected inside the PCF for measurements, as illustrated in Figure 30(a). This method has the advantage of requiring fewer preparation steps and shorter sample preparation time, making it suitable for rapid detection. Additionally, the interaction between light and the analyte is not limited to the fiber core surface, especially in HC-PCF designs. However, this configuration allows the analyte to move freely inside the fiber, leading to poor reliability of SERS measurements, similar to what happens in the cuvette case

- **Anchored Configuration :**

The second approach is called the anchored configuration. In this method, the NPs are fixed or attached to the inner walls of the PCFs before injecting the analyte solution. This allows the molecules of the analyte to physically or chemically bind to the NPs. This process involves salinization, as explained in section I.3.2.2. The solutions are sequentially injected into the fiber using a syringe pump. Following this, the fiber is dried, and subsequently, the analyte can be introduced into the fiber. Depending on the nature of the analyte molecules, they may either adhere to the NPs attached to the fiber, allowing for the drying of the fiber, or they may persist in solution within the fiber. Finally, similar to the preceding method, the fiber can be positioned in the setup for SERS measurements. Figure 30(b) shows a simple drawing of the analyte injected into the fiber using the anchored configuration

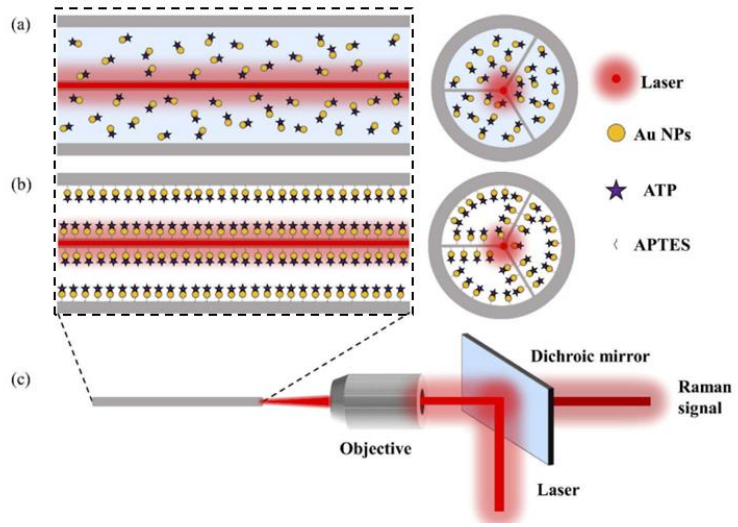

Figure 30 Schematic representation includes (a) the injected configuration, in which Au NPs and the analyte are pre-mixed and then pumped into the fiber; (b) the anchored configuration, where ATP is pumped into the fiber, binding to immobilized Au NPs within the fiber holes; and (c) the backscattering configuration. Reproduced from [144].

I.4.3.3. The performance of SERS-active PCFs

- Light guiding characteristic

Following the characterization of each type of PCF, this section will explore the guiding mechanism of each class when the fiber is modified with NPs. Han *et al.* have conducted a study that demonstrate the guiding principles of each class [145]. Initially, they achieved the development of SERS-active PCF

while retaining the fiber light-guiding characteristics. This was accomplished by managing the uniform integration of Ag NPs inside the air channels throughout the entire length of the fiber, with a controlled surface coverage density. Following the immobilization of AgNPs, 20-cm-long PCFs were loaded with a 10^{-5} M solution of R6G. Subsequently, Raman measurements were carried out in forward propagation, utilizing an excitation source with a wavelength of 632.8 nm.

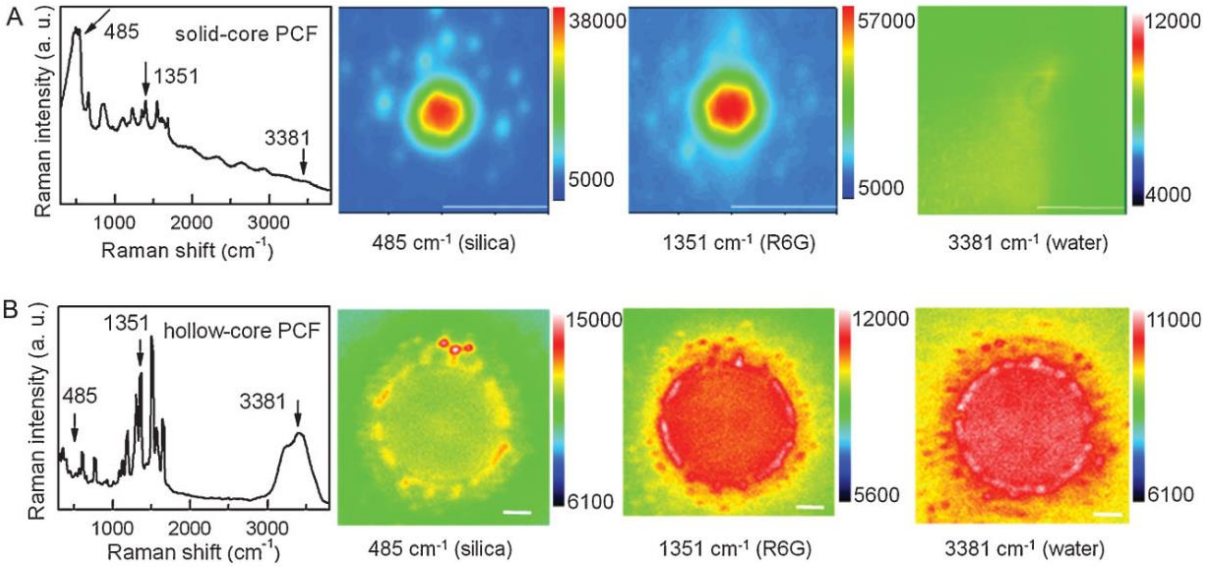

Figure 31 SERS spectra for a 10^{-5} M solution of Rhodamine 6G and the corresponding hyperspectral Raman images were recorded at the end of (a) an SC-PCF and (b) an HC-PCF treated with Ag NPs. Reproduced from [145].

The recorded SERS spectra are presented on the left side of figure 31 for both SC- and HC-PCFs. Notably, in the 400-1200 cm^{-1} range of the SC-PCF spectrum, a prominent silica signature is observed, with the highest peak at 485 cm^{-1}. This signal is absent in the HC-PCF spectrum. Conversely, the HC-PCF exhibits a distinct water signature peak near 3381 cm^{-1}, which is not detected in the SC-PCF spectrum. These results can be attributed to the difference in light guidance in the SC-PCF, light is guided by the silica core, while in the HC-PCF, the light travels through the analyte, leading to a strong water signal. Hyperspectral imaging was used to analyze the distribution of the scattered signal at three specific Raman lines within the two fibers. These Raman lines correspond to the characteristic peaks of silica, R6G, and water (485, 1351 and 3381 cm^{-1}). For the SC-PCF, the Raman signals from silica and R6G are focused within the solid core, while no Raman signal from water is observed (Figure 31(A)). In the case of HC-PCF, Figure 31(B) indicates a weak signal from silica observed in a dashed ring shape. This indicates that only the silica surrounding the liquid core guides a small portion of the light. The Raman distribution of R6G and water is concentrated within the liquid core, demonstrating its effectiveness as a waveguide. Additionally, the SERS signal of R6G effectively couples and propagates forward along the liquid core. The Raman image of the water line seems to have a larger diameter compared to that of R6G, attributed to the dispersion characteristics of light propagation.

- Length effect of PCFs on SERS intensity

As previously discussed, the primary benefit of employing SERS-based PCFs over SERS substrates is their ability to increase the interaction surface (length), consequently enhancing the SERS signal. The presence of NPs on the inner surface of the fiber contributes to absorption and scattering losses. In the same time, each NP will enhance the EM field through the LSPR effect. This necessitates finding a compromise between the density of NPs and the length of the fiber to optimize SERS performance. Han *et al.* investigated this aspect by fixing various concentrations of Ag NPs within several SC-PCFs and HC-PCFs [145]. Subsequently, they infiltrated the fibers with R6G liquid and proceeded to measure the SERS signal based on both the fiber length and the NP coverage density. The variation of the SERS signal was studied through monitoring the 1351 cm^{-1} peak intensity of R6G. The results are presented in Figure 32.

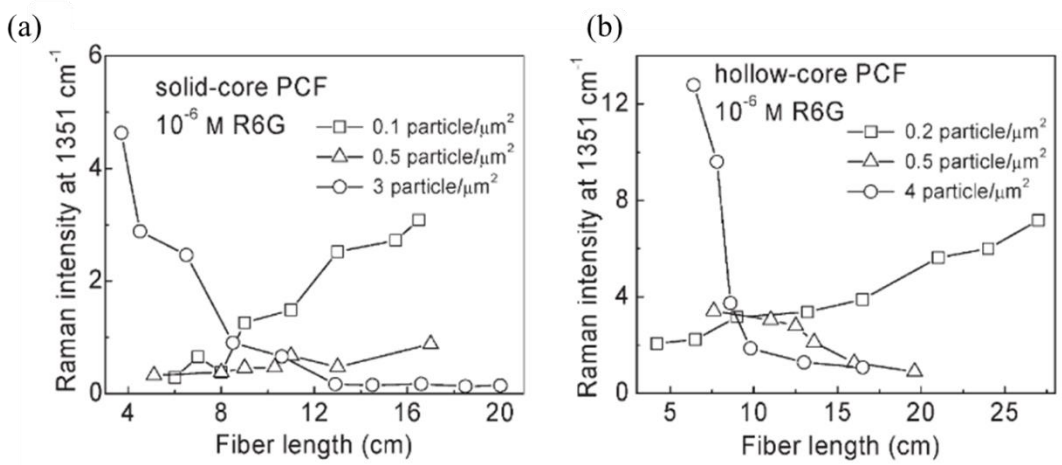

Figure 32 SERS intensity of 10^{-6} M R6G varies with the length of the fiber, as depicted for (a) solid-core PCF (b) hollow-core PCF. The Raman excitation wavelength was 632.8 nm, with a laser power of 5 mW and an acquisition time of 60 s. Reproduced from [145].

This figure illustrates that, in the case of SC-PCF, the SERS intensity increases with the fiber length when the Ag NP coverage is at the lower end (below 0.5 particle/μm²). However, at a coverage density of 3 particles/μm², significant losses are observed in SERS intensity with increasing fiber length. Regarding the HC-PCF, it is observed that the SERS intensity only increases with fiber length when the coverage density is 0.2 particles/μm². In the case of the other two HC-PCFs, the SERS intensity decreases as the fiber length increases. It is noteworthy that, at a high coverage density, the SERS intensity reaches its maximum in a short fiber length. Additionally, an increase in the coverage density of NPs results in a decrease in SERS intensity. These findings underscore the necessity of striking a balance between the density of NPs and the length of the fiber. Zhang *et al*. also investigated this aspect. They examined the influence of fiber length on SERS intensity using an in-house SiC-PCF [130]. The 1310 cm^{-1} peak was monitored following the injection of a mixture of Au NPs and R6G into the fiber. In this experiment, a backscattered configuration was employed, where the fiber was excited, and the SERS signal was collected from the same fiber end. The results indicated that extending the fiber length from 7 cm to 14 cm led to an increase in SERS intensity. Additionally, they simulated how SERS intensity varies with fiber length and found that, in a backscattering configuration, the intensity increases with length up to a certain point, after which further increases have little effect.

Another investigation was conducted by Tiwari et al. [146]. They infused HC-PCFs with a combination of R6G and Ag NPs. The findings revealed that extending the length from 4.7 to 6.5 cm resulted in a proportional increase in the SERS intensity of the R6G signal (Figure 33). Additionally, they conducted a comparison of the EF between the HC-PCF filled solely with R6G and another fiber filled with both NPs and R6G. The results indicated that the EF was 20 times higher for the HC-PCF filled with NPs and R6G.

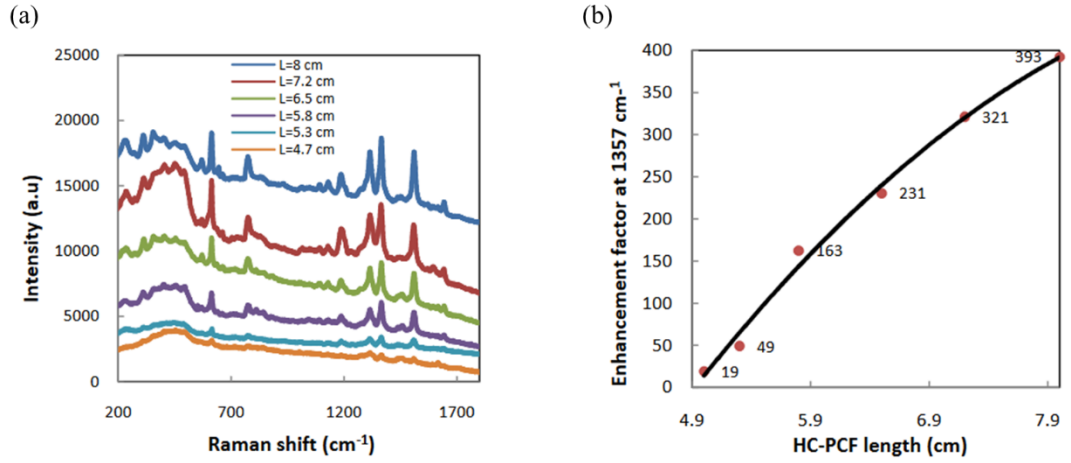

Figure 33 (a) SERS spectrum of R6G demonstrating changes in the intensity of the Raman peak with the length of HC-PCF. (b) Changes in the EF of the Raman peak at 1357 cm^{-1} with the length of HC-PCF. Reproduced from [146].

- Limitation of Hollow-core PCFs and sensitivity improvement

As highlighted earlier, the limited transmission window remains a significant challenge for HC-PCFs. This leads to substantial signal loss, particularly when dealing with large Raman shifts located outside of the transmission window. This constraint restricts the applicability of these fibers in SERS sensing. To effectively use HC-PCFs under these circumstances, it becomes essential to carefully choose the excitation laser based on the solution to be injected into the fiber, given that the transmission window depends on RI of the injected liquid. To anticipate the bandwidth shift based on the RI of silica and the injected liquid, Tiwari et al. employed [146] as a function:

$$\lambda' = \lambda_0 \sqrt{\frac{1-(\frac{n_{liq}}{n_{sil}})^2}{1-(\frac{n_{air}}{n_{sil}})^2}} \quad (19)$$

Here, λ' denotes the shifted wavelength, and λ_0 is the wavelength at which the band gap originally occurred. The variables n_{liq},n_{sil}, and n_{liq} represent the refractive indices of the solvent, silica, and air, respectively. Equation 19 can be utilized to prevent the loss of sensitivity by predicting the bandwidth shift. Gong et al. measured the signal of 2-naphthalenethiol (2-NT) mixed with 60 nm Au NPs using both a SiC-PCF and a HC-PCF under the same conditions [3]. The signal obtained from the HC-PCF was six times weaker than that measured with the SiC-PCF. This result can be attributed to the potential decrease in sensitivity of the HC-PCF due to the PBG shift, while the SiC-PCF, guided by TIR, was not subject to this shift. The higher sensitivity offered by SC-PCF in comparison to HC-PCF has driven scientists to continually enhance these fibers to further elevate sensitivity. Oo et al. suggested that augmenting the evanescent field's proportion could enhance the sensitivity of SERS-based PCF probes [147]. This enhancement is achieved by reducing the core size of the fiber. They conducted a sensitivity

comparison involving SuC-PCF with six rings of air channels and a core size of 2.6 µm, along with two SuC-PCFs featuring three air channels and core diameters of 3.1 µm and 1.1 µm, respectively. Ag NPs were anchored in each fiber, and the fibers were filled with R6G solution. Their findings revealed that the SuC-PCF featuring the smallest core size delivered the highest sensitivity, detecting concentrations as low as 10^{-10} M, whereas the other two could detect concentrations as low as 10^{-6} M. This shows that decreasing the core size of the SC-PCF could improve its sensitivity.

Zhang et al. used other geometry previously presented in figure 28(c) (SiC-PCF) with a 2.8 µm of core diameter [130] in order to evaluate the LOD of the R6G. To achieve this, they introduced a combination of Au NPs and R6G into the fiber. This led to the detection of an unprecedented R6G concentration of 50×10^{-15} M, as shown in figure 34.

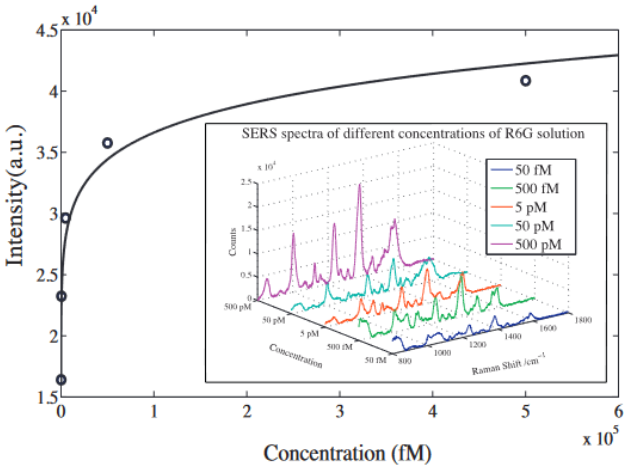

Figure 34 Variation of SERS intensity with the concentration of R6G solution. (Inset) Displays SERS spectra for various concentrations of R6G solutions. Reproduced from [130].

In addition, it has been also demonstrated the detection of sialic acid on the surface of a single cell with a record concentration as low as 2.5 fM [3]. The efficiency of this preliminary platform associated with novel bio-sensing method was also demonstrated for monitoring lipid peroxidation derived protein modifications in cells [162]. *Zhang et al.* conducted an additional investigation utilizing the offset launch method [148], which involves exciting the cladding of the fiber rather than the core of an SC-PCF presented in Figure 28(a). The outcomes revealed a robust signal of Rhodamine B (RhB) compared to direct excitation of the core. Guo *et al.* fabricated the Core-array PCF presented in Figure 28(d), and used it to investigate the detection of R6G at very low concentrations. Within this configuration, light is directed within the triangular junctions created by three holes along the capillary through TIR [131], and it is quasi-guided by the hole through multireflection [149]. Achieving ultrasensitive SERS detection of low concentrations of R6G molecules adsorbed on individual gold NP, a detection limit superior to 100 femtomolar (fM) as shown in figure 35, a sampling duration of under 5 minutes, and a data acquisition time of 2 seconds were accomplished.

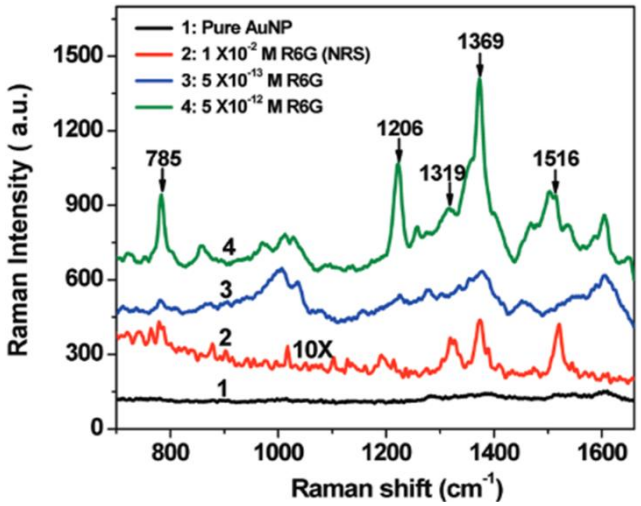

Figure 35 SERS spectra of various concentrations of R6G (0.5×10^{-13} and 5×10^{-12} M) were obtained using a SERS-active capillary. Additionally, a normal Raman spectrum (NRS) of 1×10^{-2} M R6G in solution within a glass cuvette (dimensions: 10 mm × 10 mm × 10 mm) was recorded with 10x magnification. Reproduced from [131].

In term of practicability, beforehand mixing of biochemical analyte with Au NPs solution outside the fiber probe is incompatible for real-life applications. In this prospect, XLIM and Translational Biophotonics Laboratory (TBL) have compared between the two main protocols used to prepare the fibers with the NPs presented above. It was demonstrated that the anchoring protocol results in SERS probes with greater sensitivity compared to those made using the injected configuration [150]. Furthermore, the anchored configuration achieved significantly better reproducibility and repeatability compared to the injected configuration. What it comes to the reliability record, in conventional planar substrates, where light-analyte interactions and SERS signal collection occur within the focused beam size as explained above, it leads to poor SERS measurement reliability due to the nanoscale irregularities. However, fiber-probe has large potential for improving SERS measurement reliability as light injection and SERS signal collection depend on the coupling between Raman spectrometer and the fiber-core, while light-analyte interactions occur along the entire fiber length yielding increased sensitivity and averaging of irregularities. By optimizing the core size of a SuC-PCF (figure 36(a)). It has been demonstrated that with this SERS-platform, a RSD of only 1.5% in reproducibility (figure 36(b)) and 4.6% in repeatability, which makes it more reliable than any existing SERS sensor platforms [151]. This SERS fiber-platform was successfully used for differentiating the different stages of ovarian cancer in clinical cyst fluids by quantifying the concentration of a haptoglobin biomarker [151].

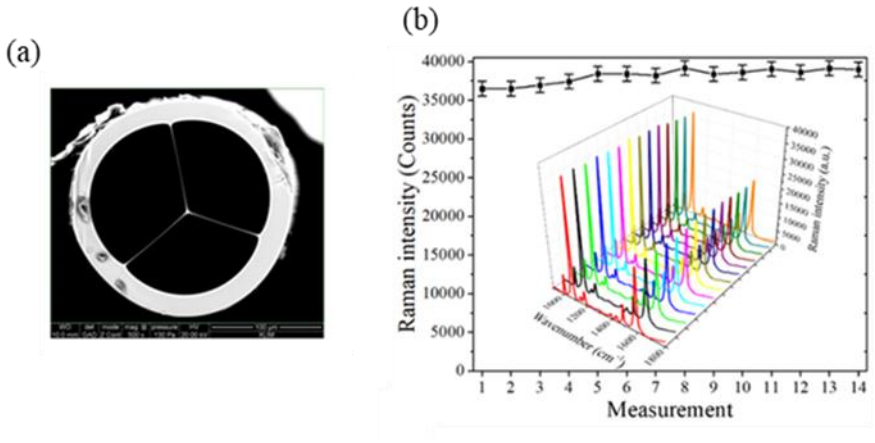

Figure 36 (a) SEM picture of the cross-section of a 3H-PCF (SuC-PCF). (b) Variations in the Raman intensity the ATP peak at 1080 cm^{-1} for 14 measurements from the optimized SuC-PCF SERS-platform. Corresponding Raman spectra are plotted in the inset. Reproduced from [151].

For planar substrates, a notable investigation by Liu *et al.* aimed to assess the sensitivity of six commercially available substrates [152]. The six substrates were prepared using different techniques and employed diverse NP materials. The authors examined the SERS response of these substrates by employing three widely used Raman tags and utilized microscope objectives with magnifications of 10x, 50x, and 100x to focus the lasers. The 10x objective yielded more consistent signals, as the excitation light could effectively interact with a greater number of NPs, according to their findings. The sensor with the highest level of reproducibility demonstrated an average RSD below 10% and a maximum RSD of 14% across 49 measurements, while the less reproducible sensor displayed RSD lower than 20% under specific conditions, but it also manifested multiple instances of RSD surpassing 40% which queit far from the performances offered by the PCFs. In addition, the most efficient planar substrates are limited by detection in the order of the nano-Mole (nM) with low reproducibility and repeatability which limit their use in analysis laboratories [153].

I.4.4. Biosensing applications of SERS-based PCFs

Within this section, we will explore various techniques employed in biosensing applications utilizing tools like PCFs. The studies can be categorized based on the detection technique employed, namely label-free Raman detection, label-free SERS detection, and Labeled-SERS detection.

- **Label-Free Raman detection**

Biosensing can be realized by using the PFCs via direct Raman spectroscopy. In this technique, there is no need for external labels or enhancers. The inherent structure of PCFs allows precise control and manipulation of light, enabling enhanced interaction with analytes along the fiber length. This allows in simplifying the sensing process. The direct detection can be achieved with biomolecules that possess relatively high Raman cross-section in order to get sufficient sensitivity. For example, J. Pinkie *et al.* detected the Myoglobin (MB) which is a protein found in muscle tissues that functions as an oxygen-storage molecule, facilitating the storage and release of oxygen for muscular activity and Amyloid β(1-42) peptide (Aβ42), which a major Alzheimer's disease biomarker using HC-PCF [154]. For them, high chemical specificity, noninvasiveness, reproducibility, and rapidness make present Raman-based methods a promising option for the detection of AD. In their study, MB and Aβ42 were purchased from Sigma-Aldrich and used as received. An excitation laser at 532 nm was used and focused into the fiber core using a 50× microscope objective (NA 0.55, Olympus) with the incident power on the sample

measured at 5 mW, they collected the Raman signal in a backscattered configuration using the same objective. The acquisition times for MB and Aβ42 were 10 and 15s. In this study, the authors filled 5 cm long HC-PCF with MB and Aβ42, then they carried out Raman measurements with HC-PCF and with a conventional direct sampling method (cuvette). Preliminarily, they verified that once the HC-PCF is filled with water, due to a change in the RI, its transmission spectrum is shifted from NIR (centered at 1060 nm) to the visible range with maximum transmission in the region from 500 to 900 nm (figure 37(a)). They were able to detect MB with a concentration of 50 µM (figure 37(b)) where prominent vibrational peaks of MB are observed which are observed also by direct sampling of a highly concentrated (1 mM) protein solution. It is worth noting that with the cuvette, most of the peaks were undistinguishable or noisy in the spectrum. Moreover, they conducted Raman detection of Aβ42 with a concentration of 40 µg/ml. The Raman peaks appeared strongly enhanced compared to those obtained by conventional Raman, which were noisy without any distinct Raman peaks detected (figure 37(c)).

.

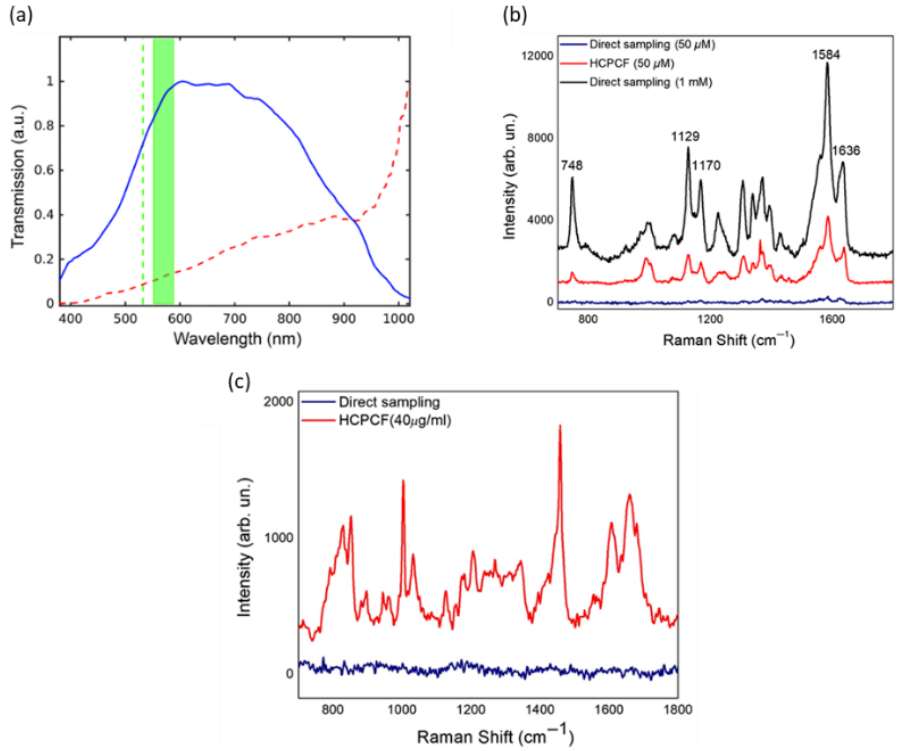

Figure 37 (a) Transmission spectra of the HC-PCF filled with air (red dashed line) and with water (blue continuous line). The excitation line at 532 nm (green dashed line) and the spectral range (green band) considered in our Raman experiments are also shown. (b) Comparison between Raman spectra acquired by direct sampling (blue, black lines) and using the HC-PCF (red lines) of Mb at 1 mM (black lines) and 50 µM (blue, red lines). (c) Raman spectra of Aβ42 acquired by direct sampling (blue lines) and with an HC-PCF (red lines): 40 µg⁄ml. Shaded regions identify amide I (red) and amide III (blue) bands of Aβ. Reproduced from [154].

Yang et al. additionally examined the application of commercial HC-PCFs for detecting glucose solutions at concentrations commonly encountered in clinical environments [155]. This is an interesting study since it allows to monitor the centration of glucose in their blood, which does not have a large Raman cross-section. A concentration range of 0-25 mM with lower laser power and shorter acquisition time was detected as shown in figure 38(a). Furthermore, they successfully distinguished glucose from fructose in a multiplex configuration, leveraging the high molecular specificity provided by Raman spectroscopy. (figure 38(b))

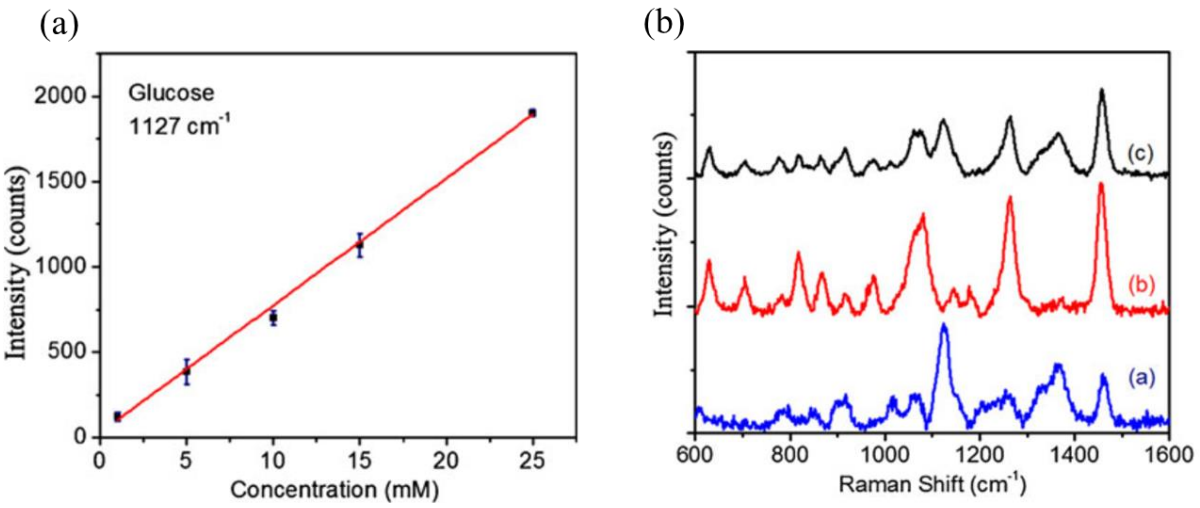

Figure 38 (a) Concentration-dependent Raman intensities of glucose (1,127 cm^{-1}) measured by the liquid-filled PCF probe. Each datum indicates five measurements for each PCF sample. Each error bar indicates the standard deviation (b) Raman spectra of (a) glucose, (b) fructose and (c) mixture of glucose and fructose. Reproduced from [155].

In other study, Di Yan *et al.* conducted a study that allowed them to detect an antibiotic moxifloxacin with low-concentration down to 1.7 µM in only a 4 nL sample volume [156]. In their study, in order to overcome the narrow band gap in nonselectively filled HC-PCFs, they change the RI by filling the fiber core by the interest liquid that possess a RI higher than the effective RI of the cladding structure. In doing so, the light is guided by TIR, i.e. by the analyte solution which allow a very broad spectral range with various excitation wavelengths. The figure 39(a) shows the Raman spectrum of the moxifloxacin with a concentration of 20 µM with an excitation laser at 532 nm. It exhibits one order of magnitude higher signal intensity in comparison to the conventional Raman spectra of the same sample. Additionally, the authors developed a calibration curve depicting the Raman intensity against increasing concentrations of moxifloxacin, achieving a LOD of 1.7 µM (figure 39(b)).

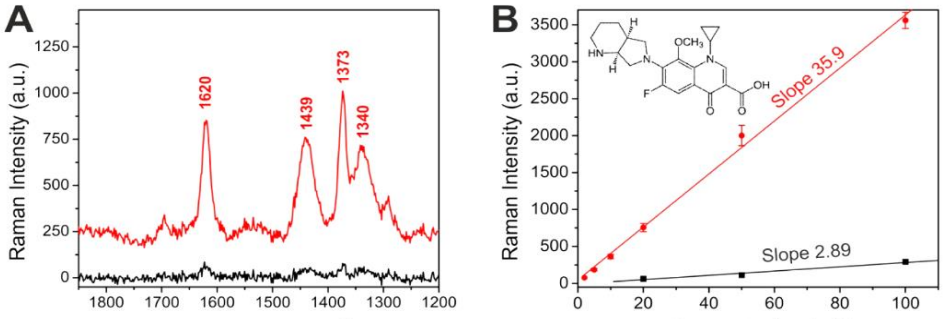

Figure 39 (A) Comparison of the antibiotic Raman spectrum obtained by the HC-PCF (red) and the conventional Raman spectrum (black) of 20 µM moxifloxacin with an excitation laser at 532 nm. (B) Raman intensity dependency from the drug concentration (HC-PCF (red), conventional (black)). A very good linearity and thus a robust calibration can be achieved. The inset shows the chemical structure of moxifloxacin. Reproduced from [156].

The PCFs sensors can be used also for gas detection. For instance, S. Hanf *et al.* had detected multiple gazes (CH_4, CO_2, N_2O, N_2 and O_2) with just one single measurement as shown in figure 40 using HC-PCF [157]. A highly improved analytical sensitivity was achieved, down to a sub-parts per million LOD with a high dynamic range of 6 orders of magnitude and within a second measurement time. They were able to detect disease markers in breath gas analysis by measuring an exhaled human breath.

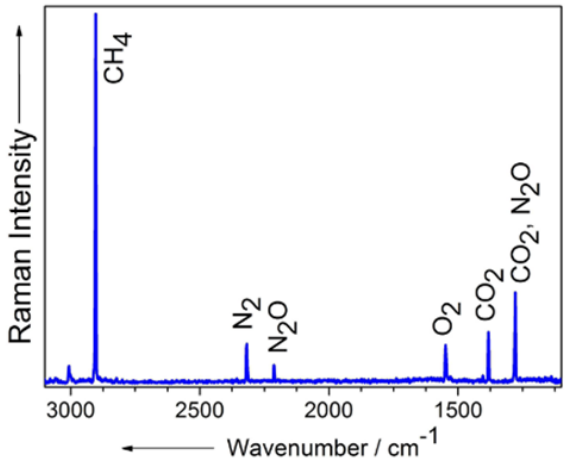

Figure 40 Raman spectrum of a biogenic multigas composition, consisting of climate relevant gases CO_2 , CH_4 , and N_2O together with N_2 , O_2 (each ~1 vol %, in Raman inactive argon carrier gas), which was acquired with one single measurement within a 40 ms acquisition time. Reproduced from [156].

In addition, in other study, it was reported that 30 cm long HC-PCF was used to remotely detect toluene, acetone and 111-trichlorethane independently inside a sealed chamber [10]. The EF with HC-PCF was ~ 700 compared to conventional detection method.

- **Label-Free SERS detection**

Now, we present the interesting achievements with PCF-based biosensing where the Raman intensity is enhanced using metallic NPs. Let us take the previous reported example of the detection of Aβ42 [154]. The authors used the colloidal solution of cetrimonium bromide-capped gold nanobipyramids (AuBPs, 1 mg/ml in water) with a diameter of 35 nm and a length of 105 nm.

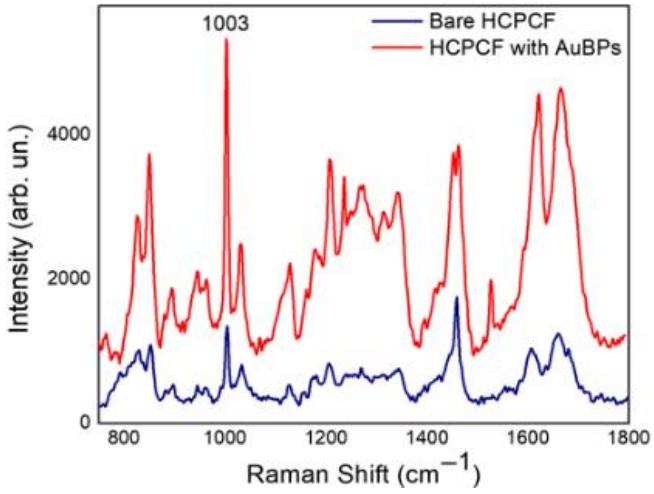

Figure 41 Raman spectra of 40 μg⁄ml Aβ42 achieved with a bare HC-PCF (blue line) and with the AuBPs-coated HC-PCF (red line). Reproduced from [154].

The authors had functionalized the fiber core with Au BPs by electrostatic-mediated surface immobilization between positively charged NPs and the negative surface charge of the inner silica core of the fiber. Figure 41 shows the comparison of Raman spectra obtained by SERS-active HC-PCF and a non-functionalized standard HC-PCF. They obtained approximately ten times signal enhancement using the NPs. All the prominent characteristic peaks of Aβ42 were identified in the SERS spectrum.

Khetani et al detected leukemia cells using Raman spectroscopy with a 785-nm laser diode coupled to a HC-PCF [158]. This interesting study allow doing an early diagnostic and monitoring of the disease, which could improve the survival rate of the patients. Figure 42(a) shows the Raman spectra of leukemia cells done in cuvette and with the HC-PCF containing spherical Ag NPs with a diameter of ~ 60 nm. The authors reported an enhanced EF of 2700 times compared to the cuvette system.

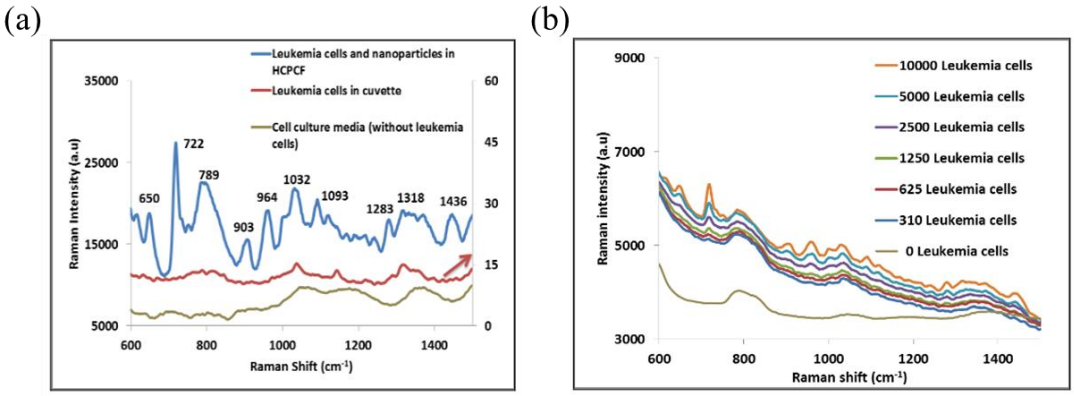

Figure 42 (a) Enhancement of Raman signal of HL60 cells in HC-PCF using silver NPs. (b) SERS spectra of different concentrations of live HL60 cells, expressed as cells/ml. Reproduced from [158].

They also established a linear calibration curve for rising cell concentrations in the solution and were able to detect a limit of approximately 310 leukemia cells per milliliter, as shown in figure 42(b). They also were able to differentiate the stage of leukemia cells. A comparable study was conducted using a 6 cm long HC-PCF to detect adenosine, a biomolecule involved in regulating extracellular physiological activity [159]. This study compared the Raman spectra in a cuvette of pure adenosine, Ag NPs mixed with adenosine in a cuvette, and the same mixture within HC-PCF. The NPs increased drastically the signal compared to the pure adenosine in a cuvette. Then, the Raman signal of the mixture filled in HC-PCF was 2700 times higher than the mixture filled in a cuvette.

- **Labeled SERS detection**

As explained above, for the biomolecules that not possess strong Raman cross-sectionDetection is carried out using SERS nanotags. A ligand that is specific to a biomarker, like antibodies, is utilized to bring the bio-analyte into contact with NP and a Raman reporter. The HC-PCF have been combined with SERS for *in vivo* sensing/imaging, showing desired flexibility.

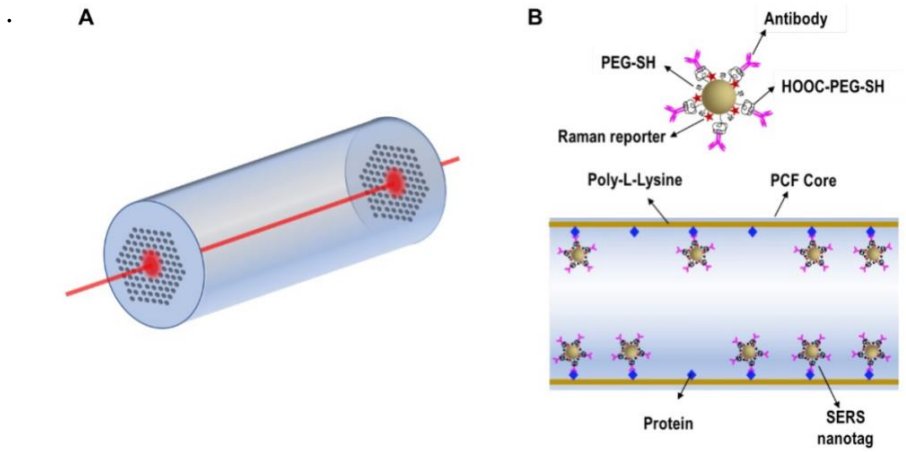

Figure 43 (a) Schematic of HC-PCF as a SERS platform. (b) Schematic of the bending of anti-EGFR antibody-conjugated SERS tags to the target proteins immobilized on the inner wall of the core of HC-PCF. Reproduced from [160].

The incorporation of liquid analytes and SERS tags into air holes facilitates an extended laser light-analyte interaction length, as shown in figure 43A. Dinish *et al.* developed a highly sensitive protein sensing methodology by combining SERS with HC-PCF, using epidermal growth factor receptors (EGFRs) as a model of analyte [160]. EGFR is a protein often utilized as a biomarker in clinical environments since it is upregulated in various cancers. In this study, the HC-PCFs were firslty modified with poly-L-Lysine, then EGFR was imobilized on the wall. After dipping into the suspension of anti-EGFR antibody-conjugated SERS tags, the tags specifically bound with the target proteins (figure 43B). This sensing method enables detection of ~100 pg protein in a sample volume of ~10 nL. The same research group have been conducted multiplex detection of alphatocellular carcinoma markers, AFP and alpha-1-antitrypsin (A1AT), which are two biomarkers for liver cancer [161]. This time the Raman reporters used are respectively Cy5-labeled SERS tags and MGITC-labeled SERS tags in conbination with HC-PCF in a sample volume of only 20 nL. Additionally, they successfully detected both Cy5 and MGITC signals at the same time, identifying AFP and A1AT in the cell supernatant. In other study, SC-PCFs were used for labelerd-SERS biosensing. For example, *T. Gong et al Mylonas C.* detected lipid peroxidation [162], For example, T. Gong *et al.* detected lipid peroxidation [162], an oxidative degradation process affecting polysaturated lipids. Although this typically occurs in small quantities within the body, its increased frequency can be a marker of cancer or neurodegenerative disorders.

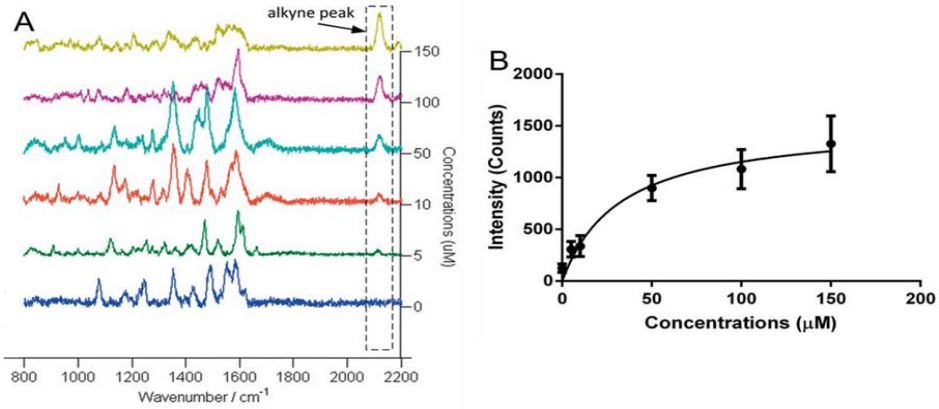

Figure 44 (A) Raman spectra of cells under different CH concentrations. (B) Intensity curve of the alkyne Raman peak at 2113 cm^{-1}. Reproduced from [162].

In this study, cumene hydroperoxide (CH) at different concentrations (from 5 to 150 µM) was used to induce lipid peroxidation. HepG2 liver cancer cells were treated with linoleamide alkyne (LAA). Upon lipid peroxidation, LAA is oxidized and modify the proteins in cells with alkyne group. To accomplish this, they introduced a mixture of 60 nm Au NPs and the previously described solutions into a SiC-PCF. They then measured the Raman spectrum of cells treated with different concentrations of Cumene hydroperoxide (CH), as illustrated in figure 44(A). They used 2113 cm^{-1} in order to monitor the intensity if the alkyne peak with increasing concentrations of CH as illustrated in figure 44(B). Noting that with LLA alone, any alkyne signal was prsented. Once the CH was added and increased in term of concentration, the peak intensity of lipid peroxidattion was increased.

I.4.5. Objectives of this thesis

Typically, employing these fibers for biosensing requires considerable time and expertise to achieve accurate alignment and effective measurements. Therefore, there is a pressing need to explore alternative methods that reduce the reliance on microscope-based alignment. The main goal of this project is to continue the developments initiated during F. Beffara's thesis, aiming towards the development of a SERS fiber-probe sensor that could eventually be utilized daily. The development of a sensitive and reliable sensor depends on several factors such as a high fraction of evanescent field in the sensing areas, low transmission losses at the excitation light and scattered Raman signal, a large area of light-analyte interactions, a large surface for collecting Raman signal scattered in all directions, a high coupling efficiency of the excitation light into the fiber core and an ease to use.

In order to meet all or most of these requirements, several parameters of the fiber have to be taken into account such as the core size of the fiber and the used NPs.

In this context, my work aims to:

- Create a platform that is easy to use and ensures highly reliable SERS measurements without relying on the operator. This platform would remove the necessity for microscopic analysis.
- Enhancement of the sensitivity by investigating NPs other than nanospheres within SuC-PCFs. Currently, only nanospheres have been used in these fibers by our team, and there is no clear guidance on the optimal shape and size of NPs anchored inside fibers for the most sensitive and reliable probes. This research aims to explore and identify the most effective NP shapes for SERS applications using SuC-PCFs.
- Improve the SERS setup at XLIM and test its performance through various experiments, such as measuring LOD for different analytes. Previously, all experiments were conducted at TBL, but this project focuses on advancing these studies at XLIM
- Test the performance of the developed SERS fiber probes in biosensing experiments using biochemical elements. The aim is to evaluate their effectiveness for biomarker detection in fluids, focusing on potential applications in disease diagnostics.

I.4.6. Conclusion

In this chapter dedicated to the SERS-based PCFs, we presented the advantages of using PCFs in comparison to the planar substrates that were widely used for SERS applications and which suffer from the small interaction surface that represent few micrometers wide and also the poorer reliability induced from the small irregularities in the SERS substrate and variation in optical coupling between the SERS substrate and the Raman spectrometer. The cross-sectional design gives the advantages for these fibers because of the easy of the liquid incorporation or gases. This enhances the interaction surface between

the excitation light and the injected liquid, improving sensitivity and enabling the detection of trace amounts of analyte.

We also presented the two main classes of SERS-based PCFs, the hollow- and solid-core PCFs. We have seen that the SC-PCF could guide the light based on TIR if the RI of the liquid is higher than the index of silica. In this chapter, we examined the guiding mechanisms of HC-PCFs and SC-PCFs. HC-PCFs rely on the photonic bandgap (PBG) effect, which restricts their transmission windows and causes shifts when the RI changes after filling the fiber. In contrast, SC-PCFs guide light through TIR principle, where the evanescent field interacts with the analyte, potentially offering better sensitivity than HC-PCFs due to these differing guiding mechanisms. Both types of PCFs are flexible, versatile, and suitable for integration into microfluidic devices for clinical applications. However, this study specifically focuses on SC-PCFs to develop an easy-to-use SERS platform that enhances sensitivity by exploring various NP shapes. Our objectives also include improving the SERS setup at XLIM and evaluating the performance of SC-PCF-based SERS fiber probes in biosensing applications for disease diagnostics.

Chapter II. Tapered-SuC-PCF, a novel approach to create easy-to-use SERS-based fiber sensors

Chapter II. Tapered-SuC-PCF, a novel approach to create easy-to-use SERS-based fiber sensors

This chapter focuses on two primary objectives. The first objective is the development of a SERS spectroscopy setup at XLIM with which SuC-PCFs are used for SERS measurements. This involves optimizing the setup and performing various SERS measurements to evaluate its performance to get high sensitivity and reliability. The second objective is to advance the development of a user-friendly SERS fiber probe. A significant challenge in this development is overcoming the dependence on microscope-based alignment, which is cumbersome and impractical for clinical settings. The aim is to create a clinically relevant biosensor that simplifies the measurement process, enabling rapid and accurate diagnostics without the need for complex alignment procedures. For that, a numerical and experimental investigation were done to determine the impact of fiber parameters on the sensitivity and reliability of SERS measurements. From these findings, a SuC-PCF with particular parameters will be fabricated and characterized to ensure ease of use and compatibility with a plug-and-play system

II.1. Experimental setup for opto-fluidic fiber based SERS spectroscopy

II.1.1. Presentation of the setup developed at XLIM

A few months before the start of my thesis, the Raman setup depicted in figure 45(a) was constructed at XLIM. "A wavelength-stabilized laser diode (Thorlabs LP7856SAV50) with a maximum output of 50 mW at 785 nm is utilized. This diode is coupled to a single-mode fiber (SMF). As illustrated in the figure, the laser beam emerging from the fiber is directed through a collimation lens and a band-pass filter for cleaning, and then it is reflected by a dichroic mirror (Di02-R785-25x36) that has a central wavelength of 785 nm and a reflection band > 98 % at 785 nm and high transmission (typically > 90 %) at longer wavelengths. A system of microscopic objectives turret (OT1 - Objective Lens Turret, 4 RMS-Threaded Objective Ports) with which we can select either 10x, 20x or 40x objective lens is also used. The setup is used in backscattered configuration. The backscattered Raman signal is collected through the same objective lens, then directed through a dichroic mirror and a long-pass filter. It is collected by a multimode fiber (MMF) connected to the Raman spectrometer. The Raman spectrometer used at the beginning of my thesis was a QE PRO – Ocean Insight (in the left figure 45(b)), composed of a grating with a density of 1200 lines per millimeter. The signal readout was enhanced by a CCD detector cooled to -60°C, improving the overall signal readout quality. The setup includes a green LED source for the visualization of the input fiber cross-section. The purpose is to ensure an accurate alignment of the laser beam into the fiber core. This method utilizes green LED to locate the fiber core, which may not be fully illuminated by the 785 nm light. By using a green LED, we can precisely position the fiber core and accurately align the laser beam into it. Furthermore, it facilitates the detection of any capillary effects (the movement of liquid along the surface of the material due to intermolecular forces between the liquid and the surface) that may occur, where liquid on the input surface could potentially disrupt the light coupling process during the measurements. This setup enables to continuously control the alignment of the laser beam with the fiber core, preventing any shifting or displacement that could affect measurement stability.

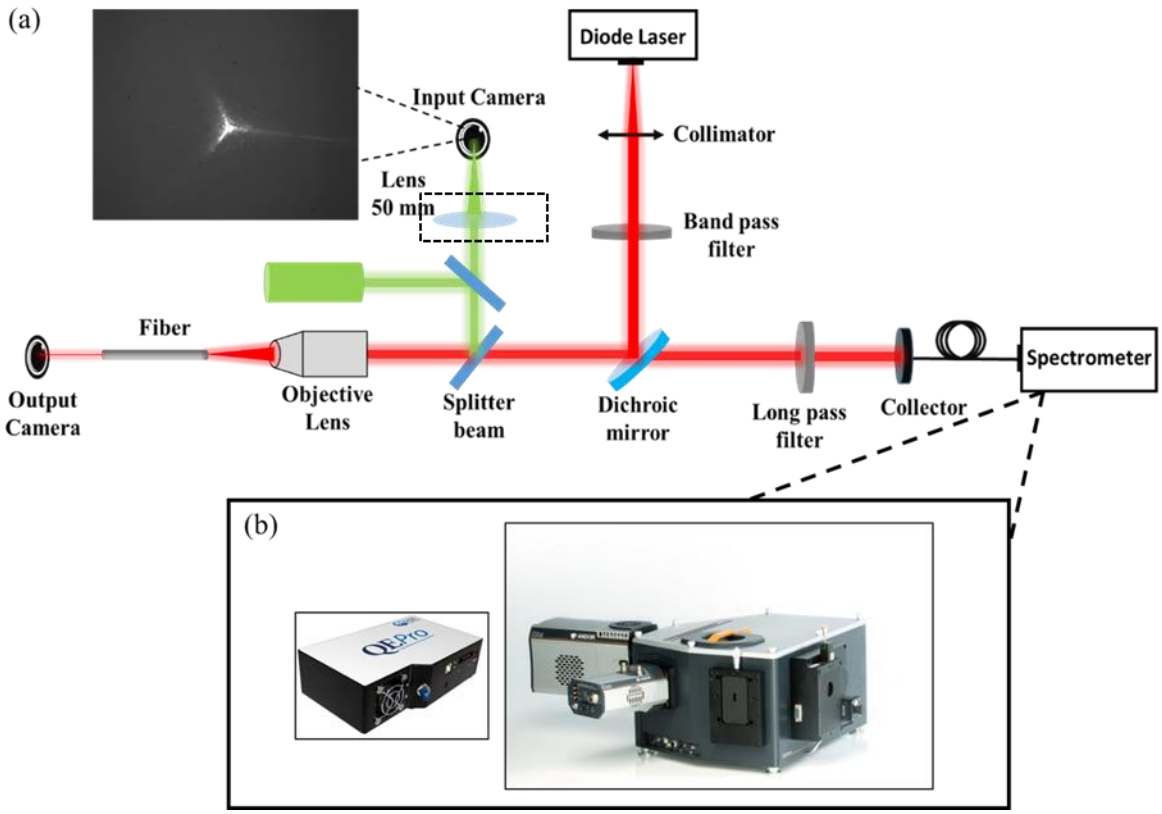

Figure 45 (a) The Raman setup used for Raman and SERS measurements. The inset picture illustrates the cross-section of the fiber and the position of the laser beam on the fiber core, corresponding to the alignment at the maximum Raman signal. (b) The Raman spectrometers used for the SERS measurements.

In the beginning, initial efforts were focused on thoroughly understanding and mastering the experimental setup. This involved familiarizing with the equipment, and doing some first Raman measurements with the conventional system (cuvette) and the fibers. By gaining a solid grasp of the setup, it was possible to identify some issues that could affect the measurements sensitivity and reliability. The first issue observed was a discrepancy between the peak Raman signal, indicating the highest intensity of the target sample, and the actual position of the laser beam on the fiber, as depicted in figure 46.

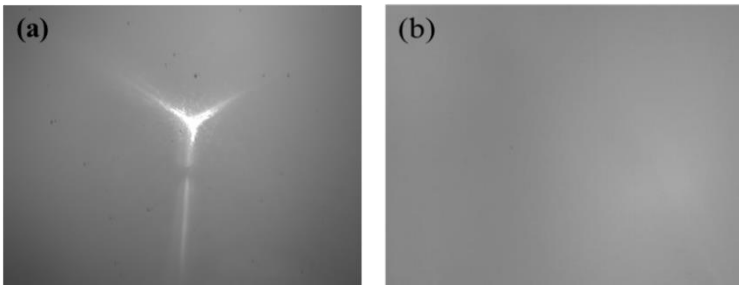

Figure 46 Picture of the fiber cross-section (a) before measurements and (b) during the measurement at the optimal Raman signal

In our experimental setup, signal optimization is achieved by adjusting the fiber's position relative to the focused beam and monitoring the reflected beam on the fiber facet using a CCD camera. Figure 46(a) displays the image of the fiber input with the laser beam directed into the fiber core, while figure 46(b) shows the fiber image captured by the camera at the optimal intensity of the Raman peak. This discrepancy raises concerns regarding the accuracy and consistency of the measurements, particularly in verifying the quality of light guidance during the experimental procedure. Moreover, the microscope objective turret utilized in this configuration exhibits instability causing the camera to capture multiple optimal points, despite the convenience of this system in exchanging objective lenses with varying magnifications, it occupies significant space that could potentially impede measurement sensitivity. Consequently, this setup was replaced with a straightforward objective lens holder for improved performance.

To address the issue of the shift in position between the optimal signal and the fiber image captured by the camera, the optimization of the Raman signal of silica core using a 3.5 µm-PCF was conducted. This optimization involved utilizing a camera positioned at the output side of the fiber to visualize the distribution of the signal guided within the fiber core. Simultaneously, the intensity of the laser diode was gradually decreased until the signal was observed with the less diode intensity possible to ensure the better coupling of the light with the fiber. Once this optimal signal was attained, no changes were made on the fiber input. Subsequently, an LED source was injected from the opposite side of the fiber to determine the optimal camera position corresponding to the fiber image with the laser beam focused on the core of the fiber. It was necessary to add a lens of 50 mm in focal position in front of the camera (the dashed rectangle in the figure 45(a). Doing this, the shift in position was fixed out and the picture in figure 45(a) is obtained for the optimal signal. Additionally, an ANDOR spectrometer (in the right of figure 45(b)) was purchased and associated at the setup to enhance the measurement sensitivity, leveraging its superior specifications, such as a high-performance grating with a density of 1800 lines per millimeter, and a CCD detector cooled to -75°C. It is worth to note that the Ocean Optics spectrometer, being more economical, was initially utilized as part of our aim to develop a compact Raman system with simplified components. Moreover, the inclusion of both spectrometers allows for a direct comparison of sensitivity performance between the ANDOR and Ocean Optics systems. In the figure 45(a), the inset image displays the fiber input cross-section captured by the camera, corresponding to the laser beam alignment with the highest Raman signal of the silica core. Figure 47 illustrates the signal enhancement achieved with the new setup compared to the previous configuration, resulting in an improvement in Raman signal.

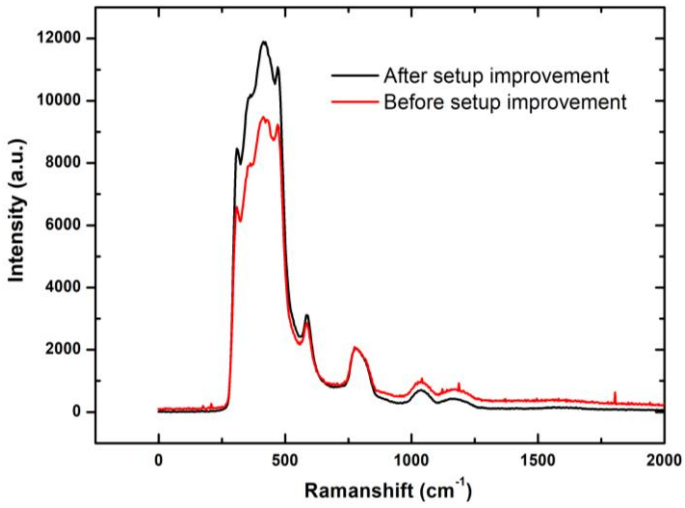

Figure 47 comparison of the silica signal after and before setup improvement using 3.5 µm-PCF.

These modifications are expected to improve the sensitivity of the setup developed at XLIM dedicated to SERS measurements within SuC-PCFs. This setup was used for realizing the following SERS experiments presented in this manuscript.

II.1.2. Evaluation of SERS perfermances of SuC-PCF in different configurations

In SERS sensing, two primary configurations are commonly utilized to facilitate the excitation of the analyte and NPs within fibers, as discussed in Chapter I. The first is the injected configuration, involving the premixing of the analyte and NPs before their injection into the fibers. At XLIM, 60 nm gold nanospheres from BBI solutions (2.6×10^{10} particles/mL) were initially employed without prior investigation into their SERS efficiency compared to other NP shapes. This investigation is detailed in Chapter III. The benefit of using these NPs is that their fabrication is more easily controlled, making them significantly more reliable than other shapes, such as nanorods and Nanostars. In addition, as mentioned in the first chapter, the biocompatibility of gold material is another advantage that make it good choice for biosensing application. The second configuration is the anchored configuration. It involves chemically anchoring of the NPs to the inner walls of the fibers. In order to chemically anchor these NPs inside the 3.5 µm-PCFs, a precise protocol is used for this purpose. The figure 48(a) shows a schematic illustrating the different steps used in this protocol. The silane agent APTES (Sigma-Aldrich) facilitates the chemical bonding of Au NPs to the silica surface of the fiber (as illustrated in figure 48(b)). This is because that silane group serves as an anchor onto the silica while the amine group binds to the NPs.

To be able to inject the different solutions inside the fibers, they were glued inside a needle, and then, they were connected to a syringe containing the solution that has to be injected. The liquids were then introduced into the fiber holes with the aid of a syringe pump. Fistful, the fiber were cleaned with acetone for 3 minutes, and dried by repeatedly pushing air inside the holes to remove the liquid. The dry step is repeated after each time the solution is injected in the fiber. After drying, a solution of APTES in acetone injected then inside the fiber. The duration of the injection was 5 minutes and then we left the solution inside the fiber for 2 minutes in order to ensure the functionalization of the silica walls. Then, the fiber was rinsed again with a solution of acetone for 3 minutes, and the fiber is left for 2 minutes before drying it from acetone to remove the excess of the APTES unbound from the fiber. The following step consists in pumping the colloidal solution of Au NPs for 10 minutes and left it for 5 minutes to ensure the bending of NPs to the APTES molecules. Finally, the fiber is rinsed with deionized water for 3 minutes to remove he unbound NPs and it was dried one last time. Once this protocol is done, the 3.5 µm-PCF are functionalized and ready to be used for the measurements. Based on the desired target molecule for detection, the molecules of the analyte injected can be either anchored to the immobilized NPs or not.

For certain molecules such as Crystal Violet (CV), Dimethyl sulfoxide (DMSO) and R6G, they are not able to bind to the metallic NPs. In this case, the analyte is not dried after the injection, and the molecules interact with the excitation light near the NPs. In other case, there are some molecules able to bind to metallic surfaces such as 4-aminothiophenol (ATP). This molecule is a well-established Raman reporter known for its ability to bind to immobilized Au NPs via its thiol group, as will be demonstrated later.

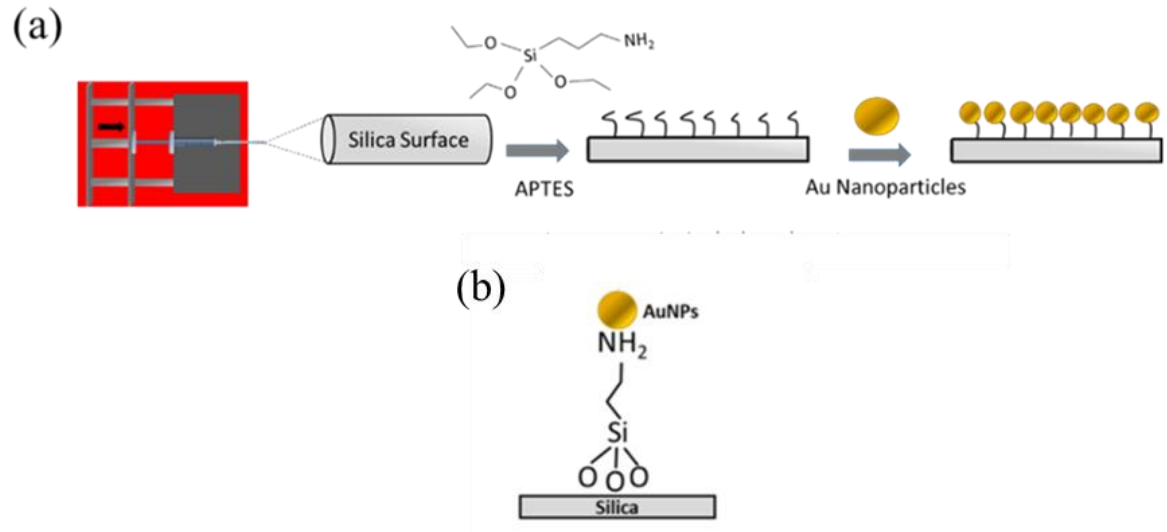

Figure 48 (a) Diagram illustrating the functionalization process of SuC-PCF holes with Au NPs and the subsequent binding of ATP molecules. (b) Depiction of APTES interactions with the metallic NPs.

With the recent construction and improvement of the SERS setup, it is essential to conduct experiments to assess its performance and capabilities in SERS measurements. The injected configuration is utilized to compare the sensitivity of fibers to the cuvette using CV as a Raman probe, followed by a LOD measurement of the same molecule. Additionally, an experiment is conducted using the anchored configuration to determine the LOD of R6G before concluding with a comparative study of sensitivity and reliability of SERS measurements among different fibers.

II.1.2.1. Comparison of SERS measurements in a cuvette and in SuC-PCF using the injected configuration

In this section, a comparative study of SERS sensitivity was conducted by measuring the SERS spectrum of CV in a cuvette, in a capillary fiber and in a 3.5 µm-PCF. A capillary fiber is composed of a hollow core and a silica cladding. In this configuration, the light is not guided. This fiber could be view as a more compact cuvette, without glass wall. CV serves as a model analyte due to its well-established Raman scattering properties and structural characteristics, making it an ideal candidate for studying SERS enhancement mechanisms. Additionally, CV is commonly used as a probe molecule for evaluating the sensitivity and performance of SERS substrates. In instance, Dai et al. had used the CV to evaluate the performance of Ag-modified Cu substrates [163].

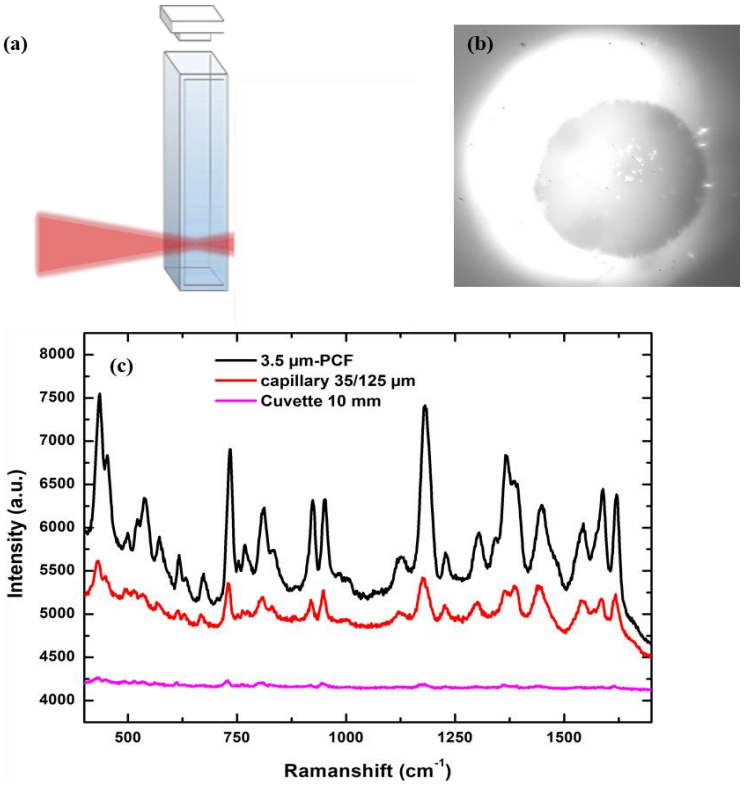

Figure 49 (a) Schematic of the cuvette used for SERS measurements. (b) Image of the end of the capillary fiber filled with CV. (c) SERS spectrum of 100 nM of CV into the 3.5 µm-PCF (black curve), the capillary fiber (red curve) and in the cuvette (blue curve) using injected configuration.

The objective of this study is to determine if the longer interaction length between the light and the analyte inside the 3.5 µm-PCF improves the SERS signal compared to the cuvette and the capillary fiber. To perform this comparison, a mixture comprising 90% Au NPs and 10% of a 1 µM CV solution was prepared. Subsequently, this mixture was introduced into a cuvette with a path length of 10 mm (figure 49(a)), into the hollow-channel of the capillary fiber with a core diameter of 35 µm and an outer diameter of 125 µm (figure 49(b)) and into the 3.5 µm-PCF. A laser power of 10 mW and an integration time of 10 s were used for each measurements. The obtained intensity is averaged over ten measurements for each case. It is essential to note that the objective lens of 10x was used for measurements with the cuvette because it provides a greater depth of field allowing the laser spot to hit the solution inside the cuvette rather than the cuvette walls (glass). For the measurements that involved fibers, 40x objective lens was used. The results, shown in figure 49(c), reveal significant differences in the SERS signal intensity. Notably, the signal measured with the fiber surpasses that obtained with the capillary fiber by 4.5 times and outperforms the cuvette by 42 times. These results underscore the advantages of the extended interaction length between light and analyte afforded by the fiber compared to the limited surface area interaction achievable with the cuvette. The significant enhancement of the capillary fiber compared to the cuvette is likely due to the increased interaction length between the light and the analyte within the capillary fiber. Additionally, the 3.5 µm-PCF abilities to guide light through its core facilitates efficient excitation of LSPR, resulting in enhanced electromagnetic field confinement and intensified Raman scattering signals. In contrast, although the capillary fiber features a hollow core, it do not offer the same degree of control over light propagation and very weak light confinement.

In order to evaluate more the performance of the setup, an experiment of determination of the LOD of CV is realized. For this investigation, a mixture was prepared by combining 900 µL of Au NPs with 100

µL of CV solution at varying concentrations to obtain concentrations of 100, 10 and 1 nM of CV. These mixtures were then injected into different 3.5 µm-PCFs and left to incubate for 5 minutes. For the experiment, a laser power of 10 mW was employed and a 10 s of integration time were used for each measurement. The resulting intensity was averaged over ten measurements.

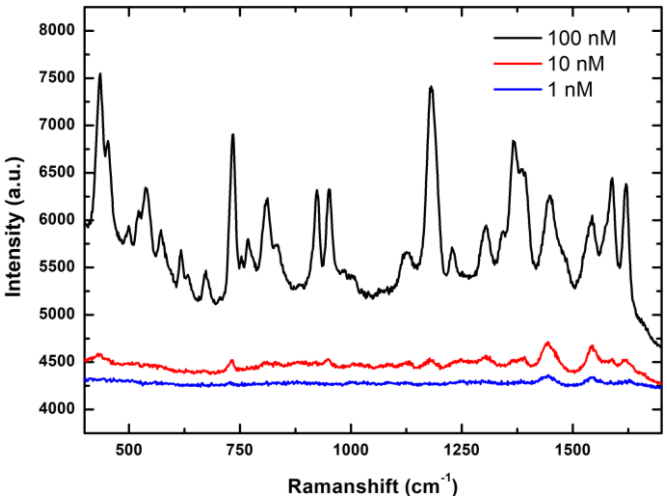

Figure 50 SERS spectrum of CV with different concentrations using injected configuration measured in the 3.5 µm-PCF.

The outcomes of this study are shown in figure 50, indicating that the use of 3.5 µm-PCF enables the detection of a concentration of 1 nM of CV (measured at the peak of 1535 cm^{-1}, which represents C–C stretching). Moreover, such experiment serves as valuable tool to evaluate the performance of the fibers, especially in biosensing applications where the analyte (with targeted molecules) can simply be mixed with the NPs. This streamlined approach can significantly enhance applicability of fiber-based sensing techniques in biosensing applications.

II.1.2.2. Evaluation of SERS performances of SuC-PCFs using the anchored configuration with an injected solution

In this section, the evaluation of SERS measurements within a functionalized 3.5 µm-PCF using anchored configuration was realized. For that, the analyte of R6G is used which is also a commonly used dye molecule in Raman spectroscopy and SERS applications as described in section I.3.3.1. The R6G solution is prepared to get different concentrations (100, 10 and 1 µM). These solutions were then injected in different functionalized fibers for 5 minutes and left to incubate for 5 minutes. The significance of this investigation lies in demonstrating the ability of the SuC-PCFs to detect low concentrations of target molecules, even when they cannot be directly anchored onto the NPs attached along the fiber core. The results are presented in figure 51. They highlight the capability of 3.5 µm-PCF to detect R6G at a concentration as low as 1 µM.

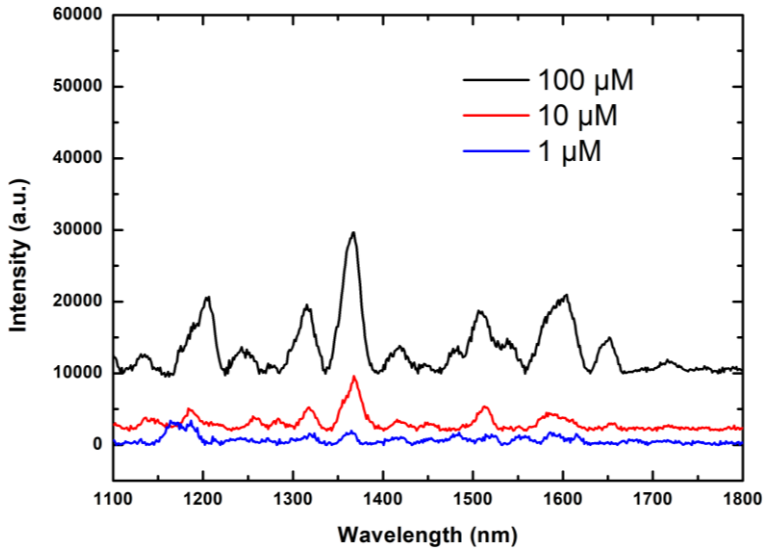

Figure 51 SERS spectrum of R6G with different concentration using injected configuration measured with 3.5 µm-PCF.

One factor can explain why the LOD lower than 1 µM is not achieved is that the dilution effect caused by mixing the R6G with the distilled water to achieve different concentrations. This dilution alters the distribution of the NPs along the fiber core, potentially leading to a decrease in the density of NPs available for interaction with R6G molecules. Consequently, this diluted distribution of NPs may limit the sensitivity of the detection platform, resulting in an inability to detect R6G at concentrations lower than 1 µM. Despite this limitation, the achieved LOD of 1 µM underscores the potential of SuC-PCFs for sensitive detection.

II.1.3. Comparison of SERS sensitivity and reliability for different core sizes of SuC-PCFs using the anchored configuration

Anchoring molecules onto NPs, such as Au NPs, along the core of the fiber enables sensitive detection and quantification of target biomolecules through SERS. ATP molecules have specific chemical functionalities that make them highly effective at binding to Au NP as presented in figure 52. The Thiol Group (-SH) groups present in ATP can form strong coordination bonds with the surface of gold NPs, due to their negative charge and ability to interact with the positively charged gold surface. Once the ATP molecules are bound to the NPs, the liquid inside the fiber can be removed.

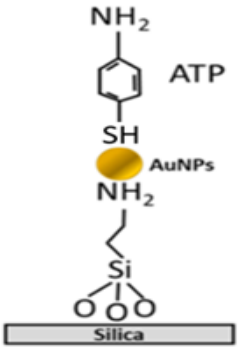

Figure 52 The schematic representing how the ATP molecule binds to the metallic NP.

It is essential to study the role of the core size on the final SERS signal detected by the spectrometer using the anchored configuration. The reason why this study is used with this configuration, is that the NP are anchored over the entire length of the fiber, so that the signal variation could be mainly affected by the core size of the fiber and the coupling condition between the fiber and the Raman spectrometer. As mentioned above, this study was already realized by F. Beffara with different SuC-PCFs composed of a core size of 0.9, 1.4 and 3.5 µm [144]. This time, the 3.5 µm-PCF will be compared to 2 and 3 µm-PCFs with the novel SERS setup. These specific dimensions have not been thoroughly explored in prior research, yet they hold significant potential for enhancing the sensitivity for SERS measurements. The comparison is made by monitoring the intensity of the Raman peak of ATP at 1080 cm^{-1} that corresponds to the stretching modes νCS, 7a (figure 53(c)). Once the fibers are functionalized with Au NPs, a solution of ATP at a concentration of 1 mM was injected over a 5 minutes period and left for an additional 5 minutes to ensure the anchoring of ATP molecules to the Au NPs. Subsequently, the solution was removed from the fiber by applying air pressure. Measurements were conducted using Ocean Optics spectrometer, with an integration time of 10s for each measurement and a laser power of 10 mW (785 nm). An average signal was obtained from 10 measurements, with a selected fiber length of 10 cm. In opposite to the manner used in Beffara's study, where the focus point of the laser was moved into different locations of the core fiber between each measurement, this time, Between each measurement, we removed the fiber and reinserted it into the optical system After localizing the fiber using the CCD camera (figure 53(a)), the laser injection was optimized to correspond to the maximum signal of 1080 cm^{-1} Raman peak (figure 53(b)). This study is more realistic to real-life biosensing applications where the fiber could be put into the optical system and taken off several times to ensure the reproducibility of the measurements.

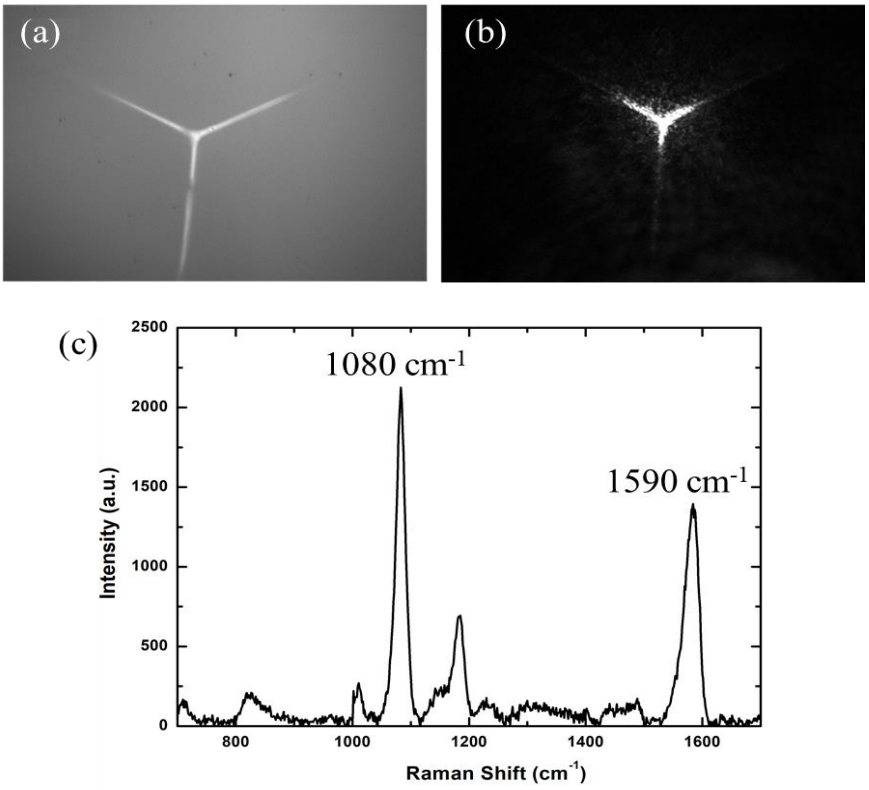

Figure 53 (a) Picture of the entry face of the 3.5µm-PCF. (b) Picture of the input of the 3.5µm-PCF excited by focusing the laser directly into the core using 40x objective lens. (c) SERS spectrum of ATP measured within 3.5 µm-PCF, the two main peaks are located at 1080 cm^{-1} and 1590 cm^{-1}.

SERS spectrum of ATP obtained with different fibers is illustrated in figure 54(a) and the figure 54(b) represents the maximum and the average normalized SERS intensity between the fibers with different core sizes. In addition, SD in average normalized SERS intensity is denoted with black lines. We noted that the maximum of SERS intensity is obtained with the 2 µm-PCF. The average SERS intensities for the 2 µm-PCF and 3 µm-PCF are similar, with normalized values of 0.73 and 0.77, respectively, while the 3.5 µm-PCF is lower at 0.51. These values were normalized using the maximum measured intensity of 1080 cm^{-1} obtained with 2 µm-PCF (32357 Counts). This might be because the evanescent field interacts more with Au NPs with the fibers that have smaller cores compared to those with larger cores. It is worth to notice that the SD of averaged normalized SERS intensity decreases with large core size. These results are confirmed by the numerical study on coupling efficiency of light with the fiber in the following (section II.2.1).

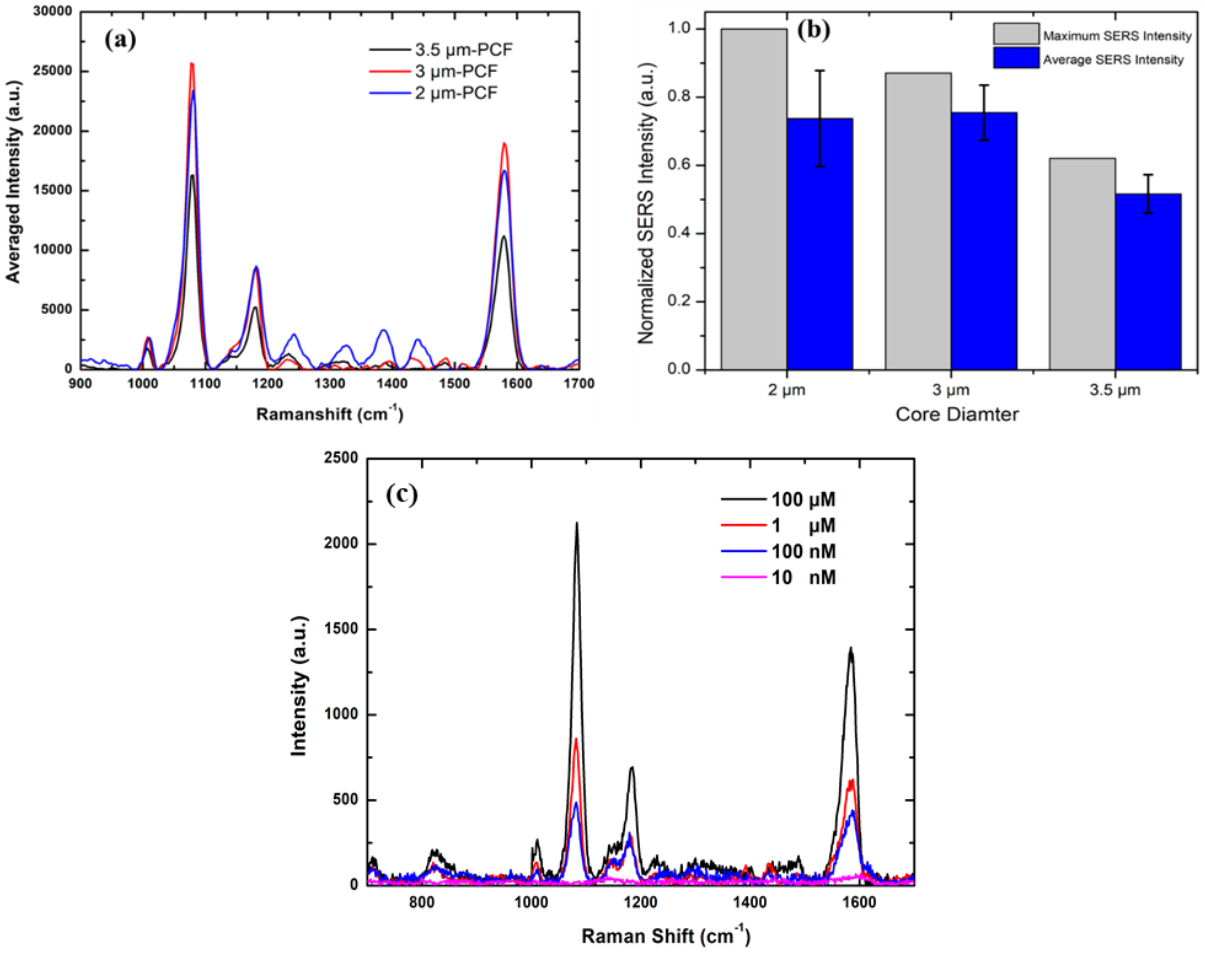

Figure 54 (a) SERS spectrum of 1 mM of ATP molecule using different fibers. (b) Normalized SERS intensity of 1080 cm^{-1} of 1 mM of ATP measured with 3.5 µm-PCF with different core sizes. SD in average normalized SERS intensity with black lines. (c) ATP SERS spectra measured with different concentrations using 2 µm-PCF.

The reproducibility of the SERS measurements varied with the core size of the fibers, as indicated by RSD values: the 2 µm-PCF exhibited a higher RSD of 12%, compared to the 6.2% and 4.5% for the 3

µm-PCF and 3.5 µm-PCF, respectively. This suggests that the measurements are more reproducible with relatively larger core sizes. Our measurement method involved removing and repositioning the fiber between each measurement, making it challenging to consistently reproduce the same injection conditions, especially for smaller core sizes like the 2 µm-PCF. That means for relatively large core sizes, the SERS measurement is more reproducible than the fibers having small core sizes. As 2 µm-PCF provided the highest SERS intensity, despite a higher RSD, it is then chosen for the determination of LOD of the ATP. This study is interesting due to widespread use of ATP as a probe molecule for detecting biomarkers associated with various diseases [129]. For each fiber, a functionalization with NPs is realized, and 100 µM, 1 µM, 100 nM and 10 nM concentrations of ATP were pumped inside the fiber holes. After drying the fibers, SERS intensity was measured and averaged over ten measurements for each fiber. An integration time of 10s and a laser power of 10mW were used for the experiments. The figure 54(c) shows the different SERS spectra of ATP molecule measured with 2 µm-PCF. A LOD of 100 nM of ATP is measured.

In conclusion, the previous experiments confirmed that the fiber possessing the smallest core size is not necessary the best choice for SERS biosensing since it suffers from a higher RSD in reproducibility. For this study, a fiber of 2 µm-PCF gave the maximal intensity and an averaged intensity close to the one obtained with 3 µm. While the 3.5 µm-PCF gives the better reproducibility among the fibers. Thus, it is necessary to find a compromise between the sensitivity and the coupling reliability To develop a fiber with a relatively strong evanescent field for interaction with NPs and a core size in the excitation side (the fiber end where the laser is injected) that exhibits with best coupling efficiency. For that, a numerical investigation will be realized in order to identify which core size exhibits the best coupling efficiency.

II.2. Development of high perfermance and user-friendly SERS fiber probes

II.2.1. Improvement of the coupling between the fiber and the excitation laser on XLIM setup

In PCF-based SERS applications, while much attention is given to the fiber properties, the efficiency of laser coupling into the fiber core is a crucial factor that affects the performance of the system. Efficient coupling ensures the effective injection of the laser into the fiber and the subsequent propagation and collection of the Raman signal, both of which are essential for accurate SERS measurements. These factors underline the importance of evaluating coupling efficiency alongside fiber characteristics. To achieve this, we assessed the coupling efficiency between the fiber core and the excitation light using the finite element method. This process involved calculating the overlap integral of the electromagnetic field profiles of the fundamental mode of the SuC-PCF and the Gaussian distribution of the excitation laser beam [164,165]. The topologies of the SuC-PCFs simulated here are available in figure 56(a). In order to include the laser parameters into the simulation, and to accurately measure the laser spot diameter, an image of the laser spot, at the fiber position, was captured using the CDD camera. The image was then processed using MATLAB to determine the spot dimension. The provided code snippet was utilized to draw a circle around the laser spot on the image, resulting in a visual representation of its size and location. This approach facilitated the precise measurement of the laser spot diameter. The resulting image, shown in figure 55, depicts the circle outlining the boundary of the laser spot, allowing for clear visualization and measurement of its diameter.

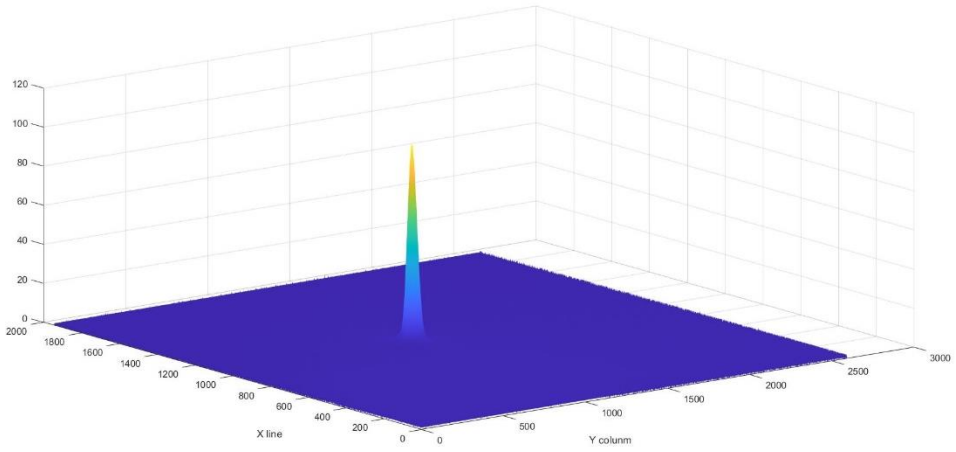

Figure 55 Visualization of laser beam spot diameter measurement

The analysis revealed that the diameter of the laser spot was approximately 2 µm at the emission wavelength of 785 nm. To calculate the coupling efficiency between the fiber and the laser beam, we have simulated with finite element method (Comsol multiphysics software) the properties of the fundamental mode (HE_{11}) propagated within the fiber (under investigation). We then created a 2D matrix for each component of the electromagnetic field distribution for both this mode and the incident beam, which was linearly polarized.

The normalized coupling coefficient (C) was obtained by examining the continuity of the transverse field components across the fiber's cross-section, comparing the incident beam to a fiber mode, as described by the following equation [165]:

$$C = \frac{1}{4} \times \frac{\int (\vec{E}^*_{in}(x,y) \times \vec{H}(x,y) + \vec{E}(x,y) \times \vec{H}^*_{in}(x,y)) dxdy}{\sqrt{\frac{1}{2}\int Re(\vec{E}_{in}(x,y) \times \vec{H}^*_{in}(x,y)) dxdy} \times \sqrt{\frac{1}{2}\int Re(\vec{E}(x,y) \times \vec{H}^*(x,y)) dxdy}} \quad (20)$$

The components $H_{x/y}$ a represent the electric and magnetic fields in the x and y directions of the fundamental mode guided inside the fiber. Similarly, $E_{x/y\ in}$ and $H_{x/y\ in}$ denote the electric and magnetic field components of the laser Gaussian beam in the x and y directions.

To simulate possible misalignment in the measurements, the center of the incident beam was randomly positioned at 200 points within a 1 µm radius disk (figure 56(b)), representing potential laser coupling positioning errors on the fiber core.

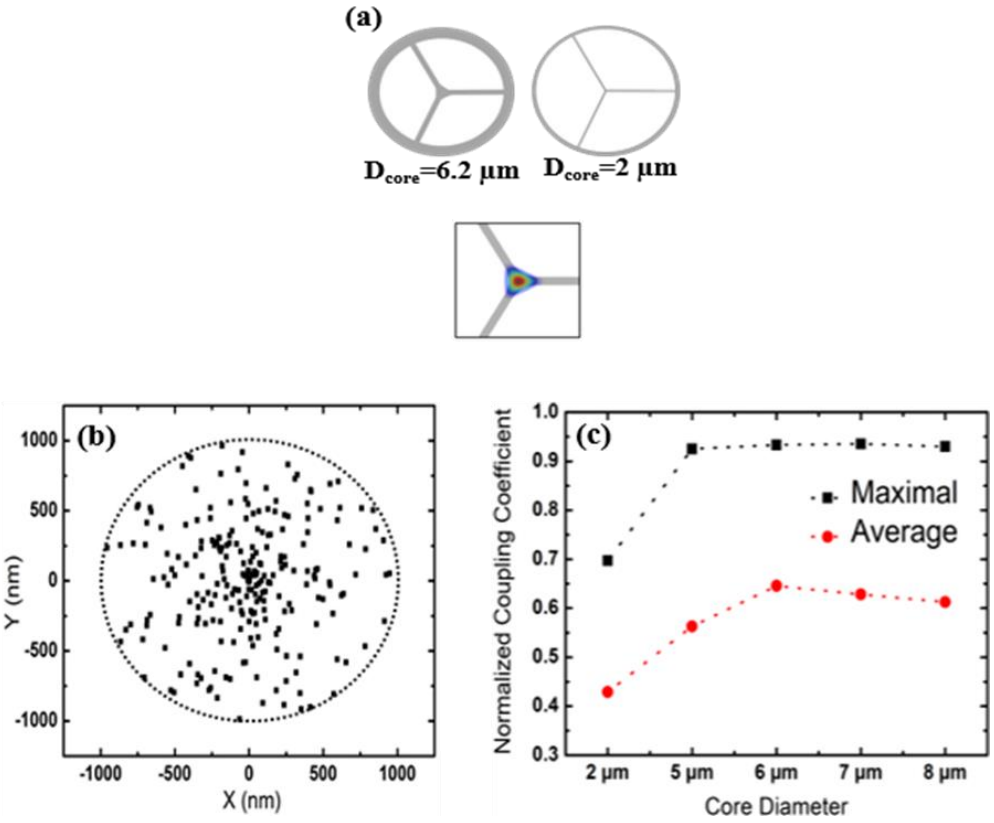

Figure 56 (a) Design of SuC-PCFs with varying core sizes used in the simulation. (b) Random distribution of the laser beam center sampled 200 times within a 1 µm radius circle centered on the fiber. (c) Maximum and average coupling coefficients for SuC-PCFs with various core diameters.

It is important to note that, in practical scenarios, despite careful alignment, the laser beam rarely perfectly centers in the core, leading to increased coupling losses. The goal of this simulation is to evaluate the coupling efficiency in function of the diameter of the fiber core. For this, we simulated five SuC-PCFs with different diameters: 2 µm, 5 µm, 6 µm, 7 µm and 8 µm. Figure 56(c) illustrates the normalized coupling coefficient between the incident Gaussian beam and the fiber's fundamental mode for various core diameters. As anticipated, the greatest coupling efficiency is achieved when the laser beam is centered within the core. The 6 µm-PCF shows the highest average normalized coupling coefficient (0.64) and a peak normalized coupling coefficient (0.93), comparable to other SuC-PCFs, except for the 2 µm diameter. Moreover, the 2 µm-PCF exhibits a lower maximal coupling coefficient (~0.70) and much lower average coupling coefficient (0.43). In order to select the core diameter that will improve the reliability of measurements. One should select the best average and maximal coupling coefficient. In this case, the fiber with 6 µm of core diameters possesses these requirements compared to other diameter values. This particular value was chosen, and subsequently, 6 µm-PCF was fabricated.

II.2.2. Towards tapered-SuC-PCF for associating SERS sensitivity and efficient fiber coupling

After simulating the coupling efficiency. It is time to determine the impact of the core size on the SERS intensity. For that, the most basic model of simulation is used, which is a silica rod surrounded by an effective layer suspended in water as presented in figure 57(a), and figure 57(b) provides a depiction of the simulated fundamental mode.

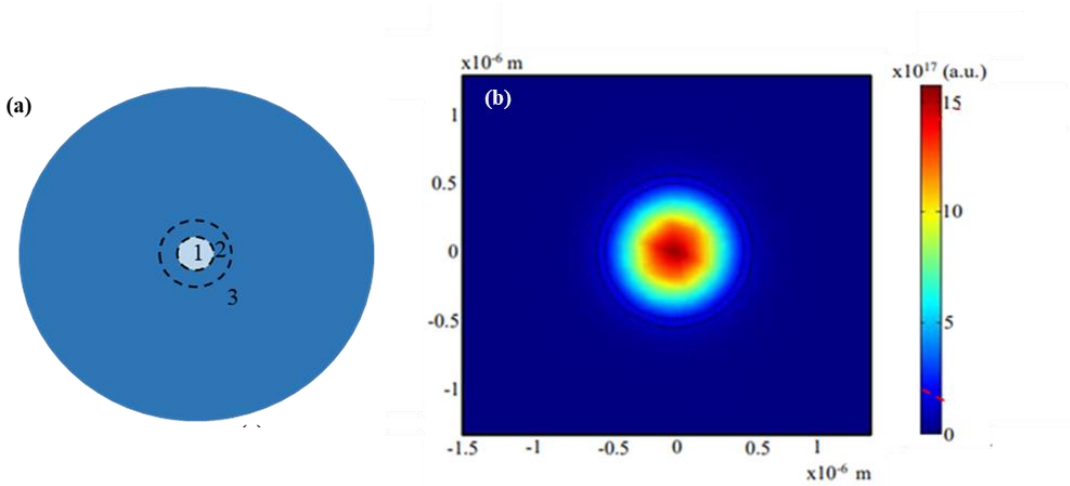

Figure 57 (a) Schematic of the structure used in the simulation to approximate the reel design of the SuC-PCF. 1 represents the silica core. 2 represents the effective layer and 3 represents water. (b) Fundamental mode simulation for a 1 µm rod with an effective layer and water surrounding. The bar represents the color scale.

The zone between the two dashed circles represents the effective layer that could represents the Au NPs anchored into the core in the real case. The design proposed represents the ideal case where the light is confined to the core and does not penetrate the silica struts that support the fiber core. Additionally, it closely resembles the behavior of light within the core of SuC-PCF. In this work, we simulated different rods with several diameters, then we calculated the percentage of light leaking the effective layer. The result is shown in figure 58.

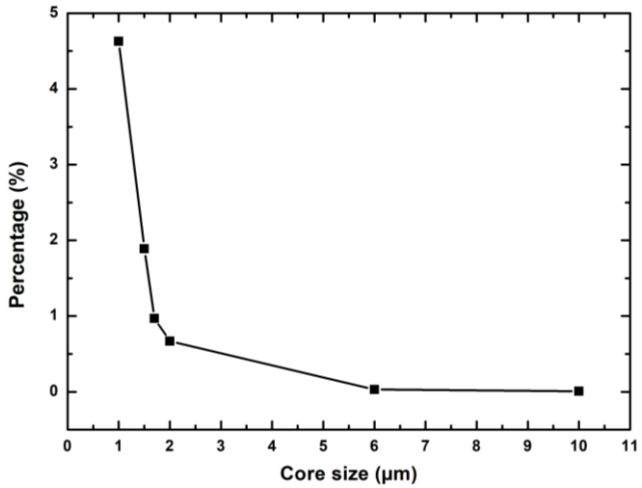

Figure 58 Variation of percentage of HE11 mode intensity in the effective layer of SuC-PCFs with different core sizes.

As expected, smaller core size leads to a larger fraction of evanescent field in the effective layer from about 0.01%% to 5 % for a rod diameter of 10 µm to 1 µm, respectively. It is worth to note that fraction of power in the effective layer increases exponentially for core diameter below 1.7 µm. These results demonstrate the necessity of having a small core size of the fiber in order to get high SERS signal and better sensitivity, which confirm the results presented in section II.1.3 that showed the higher sensitivity

for 2 µm-PCF. Nevertheless, it is crucial to note that this simulation does not take into account the interactions with Au NPs, which represent a significant source of light absorption. These findings suggest that the ideal configuration involves a core size of approximately 6 µm for efficient coupling and a core size below of 2 µm for effective SERS interactions. This can be realized by developing a tapered-SuC-PCF (denoted as tapered-PCF in the following), that have a large core size in the excitation side to ensure the coupling efficiency and the core is decreased with the length until getting the smallest core size that gives excellent sensitivity, a schematic of this tapered fiber is shown in figure 59. These type of systems have been used for several applications such as supercontinuum generation, light coupling or sensing [166,167].

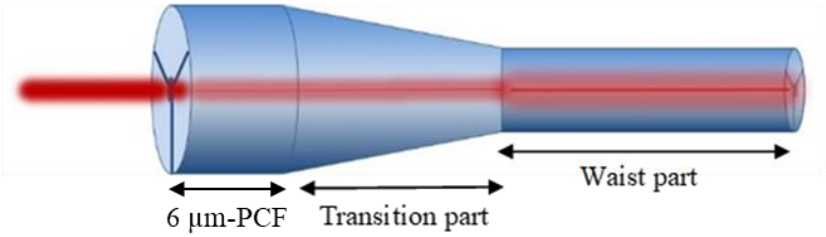

Figure 59 Schematic illustrating the design of the tapered- PCF.

The tapered fiber consists of three parts: the original fiber large core size (6 µm), the transition section (slope part) where the diameter gradually decreases, and the waist section. The desired length was also fixed at 10 cm in order to create a practice biosensor and easy to handle for the application ends. In the following, the fabrication of this taper will be shown, in addition to its characterization and its performances in SERS measurements.

II.2.3. Development of Tapered-PCFs as sensitive, reliable and user-friendly SERS fiber probes

In this section, we present the fabrication method of the 6 µm-PCF. Then, we discuss the fabrication of the tapered-PCF and compare its coupling efficiency with other different fibers. Additionally, we compare the tapered-PCF sensitivity and reliability in SERS measurements with those of the 2 µm-PCF.

II.2.3.1. Fabrication process of 6 µm core size SuC-PCF

At XLIM, the SuC-PCFs were fabricated through the stack-and-draw process [168]. This technique is widely used to fabricate PCFs and microstructured fibers. Figure 60 illustrates a schematic representing the different steps during the stack-and-draw method:

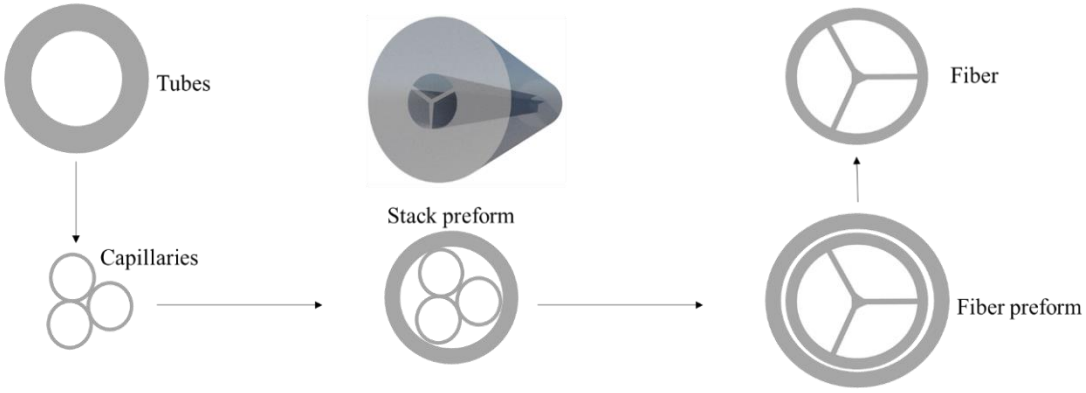

Figure 60 (a) Schematics of the different steps during the stack and draw process.

Step1: The first step consist in drawing capillaries from commercialized tubes. We utilized tubes that were relatively slender, featuring an inner diameter of 19 mm and an outer diameter of 21 mm. We made this choice to limit the amount of silica at the intersection of the three capillaries in the subsequent process steps, which allows us to achieve the desired core.

Step2: After the capillaries were drawn, three of them were arranged within a jacket tube to create a stack preform, which was then further drawn to produce the "cane".

Step3: To fabricate the fiber, the cane is inserted into a tube (called jacket) for increasing the thickness of the cladding up to an external diameter of few hundred micrometers (to facilitate the handling and the cleaving of the fiber). During the fabrication, the pressure is applied inside the holes, to expand them and to reduce the core diameter.

The tube (19 / 21 mm) was drawn to capillaries with an external diameter of 2.9 mm. Once the stack is done, the extremity of the three capillaries are closed at the end, and the stack is inserted into a jacket tube of 7/10 mm. During the fabrication of the canes, vacuum is applied between the jacket tube and the capillaries to facilitate the contact between them and to close the interstice for forming the core (Figure 61(a)). The capillaries are closed at the end to create an overpressure (during the drawing) for helping to get the desired structure (by inflating the capillaries). The cane was put inside a 2/6 mm jacket tube in order to fabricate the final fiber. At this step, we were able to control the core size and the holes size of the fiber by controlling several parameters such as the preform descent speed, drawing speed, the pressure applied inside the holes, the vacuum applied between the fiber preform and the jacket tube and the last parameter of furnace temperature (figure 61(b)).

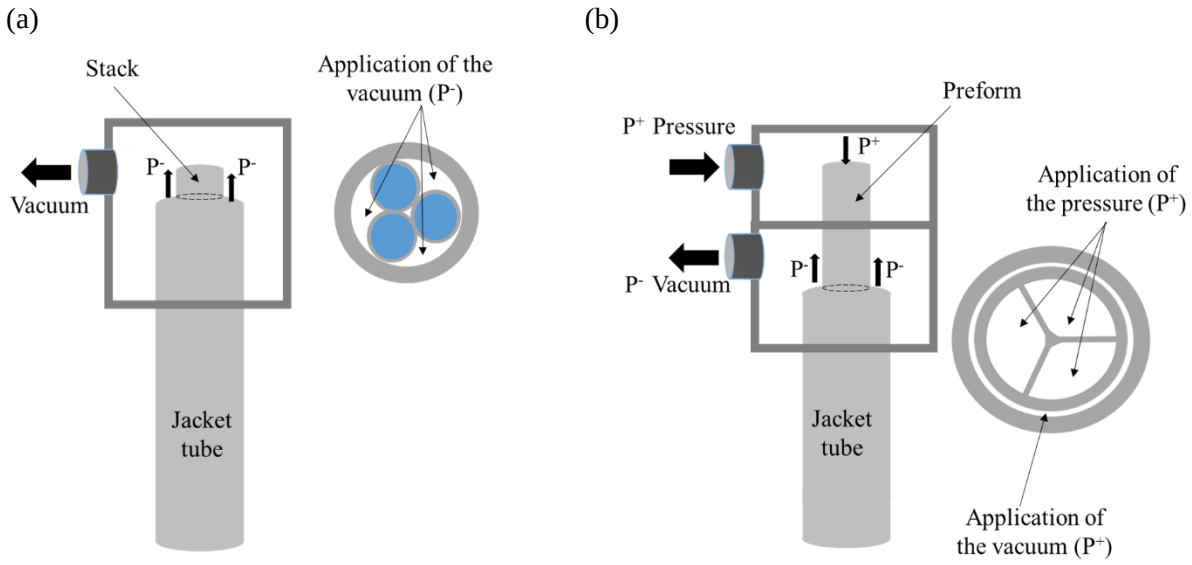

Figure 61 (a) Schematics of the systems of the pressure using while the drawing of (a) the cane and (b) the fiber. The blue sections on the top view of the stack preform means that the capillaries are closed during the drawing. The notations P- and P+ represent respectively the application of the vacuum and the pressure during the drawing.

The outer diameter of the fiber is determined theoretically by the following equation:

$$d_i^2 . V_d = d_f^2 . V_c \quad (21)$$

With d_i is the diameter of the jacket tube (i.e. 6 mm), V_d the speed at which the preform is moved into the furnace (descent speed), d_f is the final diameter and V_c the speed of the capstan that pull the fiber.

We could furthermore control the diameter of the fiber core by applying pressurized neutral gas into the air holes of the cane. The pressure expands the diameter of the fiber leading to higher capstan speed (V_c) to maintain the fiber diameter constant, and consequently reducing the core diameter. For the fabrication of the 6 µm-PCF, we started from a fiber preform that has a core diameter $D_{core} = 54\ \mu m$, $D_{holes} = 537\ \mu m$. We set a temperature of the furnace at 2075°C. We applied a pressure inside the holes of 7 kPa and a vacuum between the jacket tube and the fiber preform of -5kPa. The speeds values were fixed at $V_d = 17\ mm/min$ and $V_c = 1\ m/min$. The SEM pictures of the fiber cross section is shown in figure 62 (a-b) with a core diameter of 2 and 3.5 µm, respectively. These two SuC-PCFs were fabricated before the beginning of my thesis. The parameters of theses fibers are resumed in the table 1. We have successfully fabricated 6 µm-PCF which features a design similar to other fibers (figure 62(c)), the zoom-in SEM picture of the core is shown in figure 62(d). The key parameters of the fiber include an outer diameter of 800 µm and hole diameter of 178 µm. The large air channels are advantageous as they facilitate the liquid incorporation into the fiber.

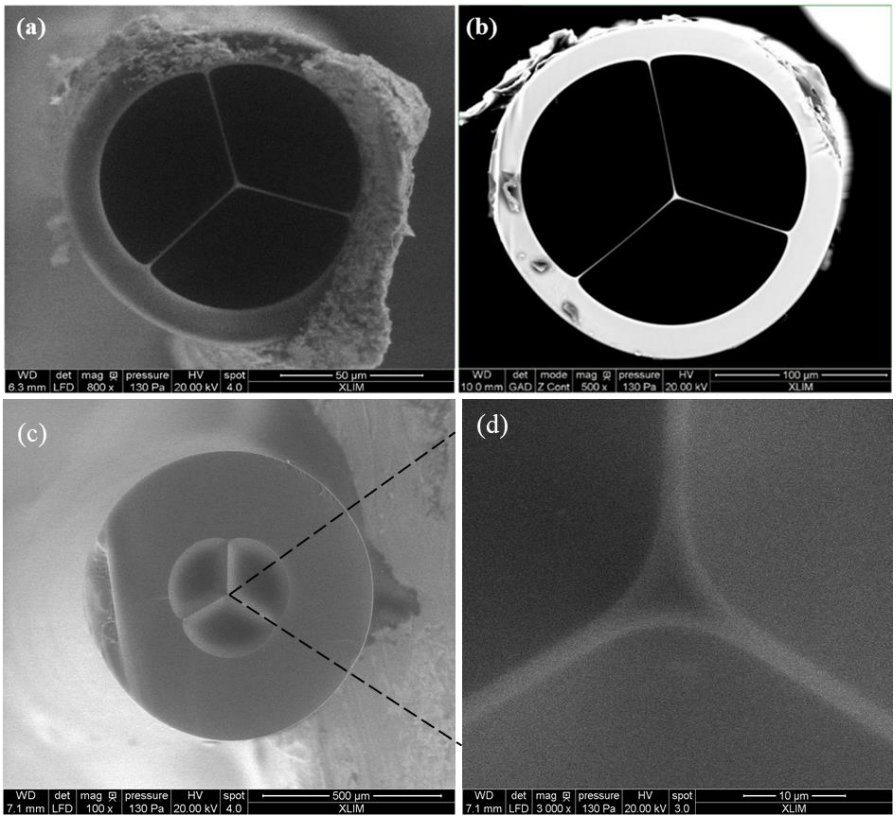

Figure 62 SEM pictures of SuC-PCFs fabricated with different sizes of the core: (a) 2 µm, (b) 3.5 µm, 6 µm and (d) Zoom-in on the fiber core of 6 µm-PCF.

Table 1 Parameters of SuC-PCFs fabricated measured with a SEM

Fiber	Hole diameter (µm)	Core size (µm)	Cladding thickness (µm)	Outer diameter (µm)
Fig. 41(a)	45	2	13	118
Fig. 41(b)	84	3.5	20	204
Fig. 41(c)	178	6	234	815

It is worth noting that the essential parameters that are required are the holes size responsible of the facilitation of the incorporation of the liquid inside the fiber and the core size that has in impact on the evanescent field portion interacting with the analyte.

II.2.3.2. Fabrication of tapered-SuC-PCF

To create tapers from the 6 µm-PCF, a Fujikura LZM 100 fusion splicer is employed. This system provides precise control over positional calibration along both the X and Y axes and features motors that move the fiber and apply a CO2 laser, avoiding the use of filaments or electrodes and thus preventing any deposits on the fiber surface. The tapers are produced by locally heating and stretching the fiber while it transitions in front of the laser beam, with a differential speed between the pulling motor and the feeding motor (the pulling motor moves faster). At the same time, the CO2 laser is focused on a designated area of the fiber. The system comes with on-board tapering program that leads the

configuration of the length of the slope part (L_s), the length of the waist part (L_w), the desired extern diameter in the waist part (D_w) and the different values of the speeds. This program allows precise controlling also the power of the CO_2 applied in the slope and the waist parts. In order to conserve the inner structure of the fiber, we had to find the right combination of all the parameters. The system was used before for standard fibers (D=125 µm) with a defined procedure, but for our case, the fiber has a certain topology that necessitated a specific procedure. Regarding the multiple parameters that are connected, we decided to fix the different geometrical parameters (L_s, L_w) and finding the laser power and the feeding speed. The control software was used to adjust the pulling motor speed to achieve the desired taper profile.

The length of the slope part was fixed at $L_s = 2\ cm$. Since the system is moving and stretching the fiber by the motors, the slope part of the taper is the transition region between the original fiber and the waist part. A simple distortion in this part might causes misalignment with the central axis and then significant transmission losses. The waist part was fixed at $L_w = 5\ cm$, since the goal of the tapering is to benefit from the high evanescent filed portion, it is necessary that this part possesses a long length. Once we fixed the lengths, we would have to tune the parameters one after the other. If the inner structure was distorted, we could decrease either the laser power or the feeding speed. Once we get the inner structure preserved, we decrease further the waist diameter D_w.

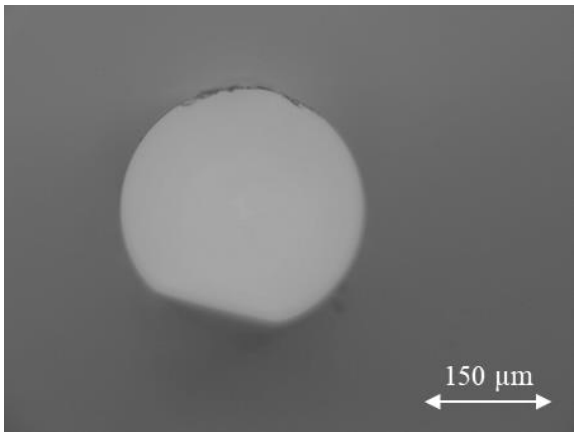

Figure 63 fabricated taper in the waist part in first attempt. The target outer diameter was 200 µm.

We would continue this process until we achieve the desired parameters, specifically a core size of 2 µm or smaller. As we control the outer diameter, we can deduce the core size from the principle of the homothetic reduction of the core size, which means that the ratio between the initial outer diameter and the target outer diameter is the same for the ratio between the initial core size (6 µm) and the core size in the waist part. In our preliminary tests, we fixed the waist outer diameter at 200 µm in order to get a core size below 2 µm. The figure 63 shows a collapsed fiber obtained with a laser power of 16.73 W applied in the taper transition and 15.06 W in the waist. In addition, the feeding speed applied for this attempt was 0.1 mm/s. We needed then to modify the parameters until reaching the taper with the inner structure perfectly preserved

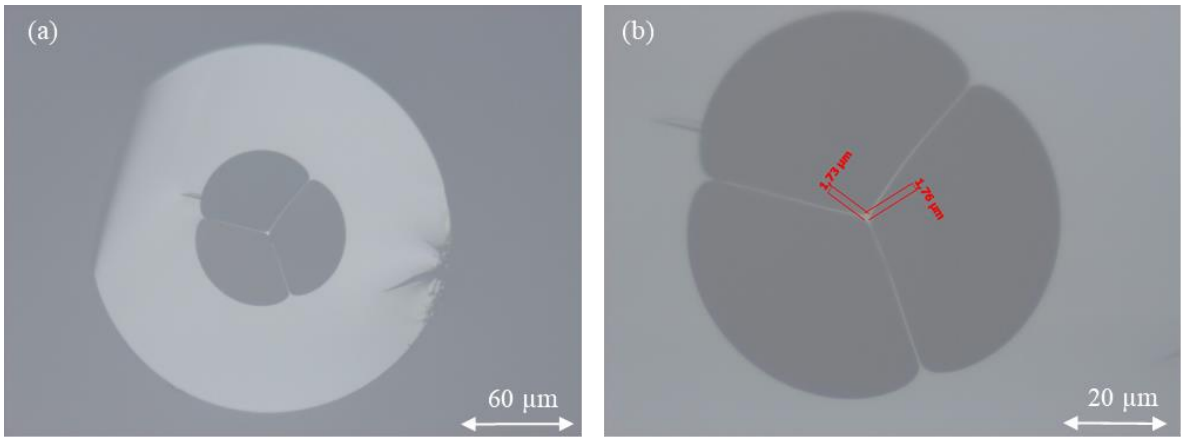

.

Figure 64 (a) Fabricated taper with the preserved inner structure in the waist part. (b) zoom-in on the core region for the fabricated taper.

Figure 64(a) displays an image of the cross-section of the taper at its waist, we achieved this result with a laser power in the taper transition of 16.07 W and 14.4 W in the waist. In addition, we needed to change the feeding speed until reaching 0.06 mm/s as an optimal value. This slower speed is essential as it allows for precise control over the taper shape and preserves the fiber structural integrity during fabrication.

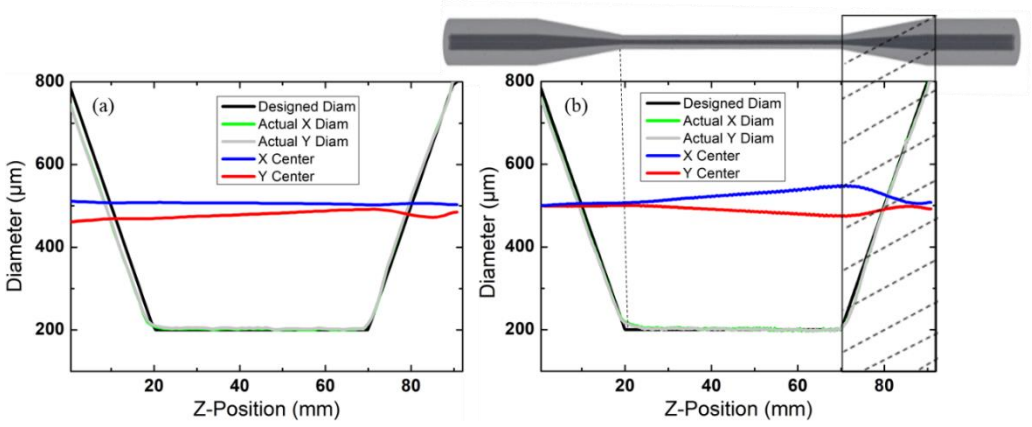

Figure 65 (a) Variation of the outer diameter with Z-position obtained for the first attempt. (b) Variation of the outer diameter with Z-position for the fabricated taper. The red and blue curves represent the variation of the X and Y center of the fiber relative to the screen, respectively.

Another important characteristic to consider during the tapering process is the taper profile, which refers to the variation of the outer diameter along the entire length of the fiber. During fabrication, motor movements can cause misalignment of the central axis along the X and Y directions. To address this, the system is equipped with a camera that not only measures the fiber diameter but also accurately detects any deviations of the central axis in both the X and Y directions. The system software draws the variation of the desired outer diameter (theoretical behavior) based on the initial input geometrical parameters, as shown by the black curve in Figure 65. It is crucial to minimize the discrepancy between the desired diameter and the actual diameter measured by the camera. Additionally, reducing the shift between the X and Y axes enhances the alignment precision of the guided light within the core, ensuring

optimal coupling efficiency, minimizing signal losses, and maximizing transmission efficiency throughout the fiber. Figure 65(a) shows the Z-profile of the taper obtained in the initial attempts, where a small shift between the desired and actual diameters can be observed. Additionally, there is a lack of alignment between the X and Y axes. Figure 65(b) presents the same measurement with a perfect matching between the expected curve and diameter of the fabricated taper. In addition, compared to the figure 65(a), the X- and Y-center are aligned in one side of the slope and there is a minor distortion in the other side, which is the best behavior that we got ever. In order to evaluate the transmission losses and test the taper in SERS measurements, the part where there is a slight shift between X- and Y-center was removed as illustrated with the dashed rectangle.

II.2.3.3. Evaluation of the coupling efficiency of the tapered-PCF

To demonstrate the improvement of the coupling efficiency for the tapered-PCF compared to the standard SuC-PCFs. We calculated the coupling losses of the following fibers: 2 µm-PCF, 3.5 µm-PCF, 6 µm-PCF and tapered-PCF. The figure 66(a) shows the setup used for measuring the coupling efficiency. To accomplish this, we used a power meter to measure the laser power after it passed through the 40x coupling objective lens. The input power (P_{in}) was set at 5.15 mW. Afterward, we adjusted the position of the fiber with an XYZ platform to maximize and measure the output power (P_{out}).

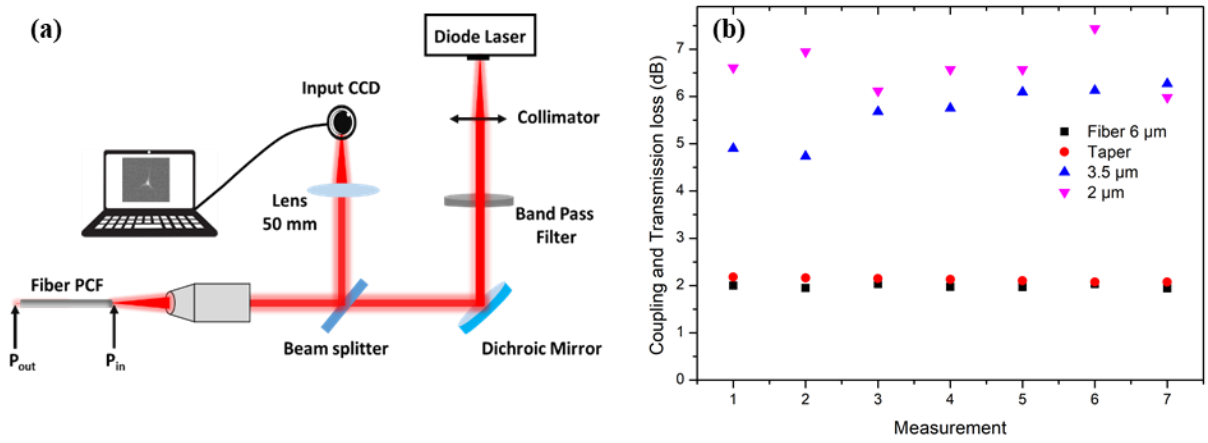

Figure 66 (a) Setup used for light transmission measurements. Pin: laser power measured just after the objective lens. Pout: laser power measured at the fiber output. (b) Coupling loss measurements for (Black) 6 µm-PCF, (Red) Tapered-PCF, (blue) 3.5 µm-PCF and (Magenta) 2 µm-PCF.

The ratio of the two powers enabled us to estimate the coupling and transmission losses. The average coupling efficiency was determined from seven measurements taken for each fiber. The results illustrated in figure 66(b) showed that the tapered-PCF exhibits low coupling losses (2.12 dB). Comparatively to the 2 µm-PCF and 3.5 µm, the fiber 6 µm-PCF improved drastically the coupling loss, from 6.60 dB, 5.63 dB for to 1.98 dB respectively. This behavior matches with the results of the numerical simulation that showed the better coupling efficiency for 6 µm compared to 2 or 3.5 µm. Notably, these measurements encompass both the evaluation of coupling efficiency and the assessment of transmission losses. The slight difference observed between the tapered-PCF and the 6.2 µm-PCF highlights the excellent quality of the taper fabrication process, which introduces only minimal additional losses. Furthermore, the tapered fiber demonstrates superior reproducibility in coupling efficiency compared to the 2 µm-PCF, with a RSD of 1% versus 12%, respectively. These results confirm the effectiveness of using a tapered-PCF with an large core size (6 µm) in excitation end to enhance coupling efficiency and reliability.

II.2.3.4. Evaluation of SERS perfermances of the tapered-PCF

In order to evaluate the performance of the fabricated taper in term of sensitivity and reliability of SERS measurements, a comparative study was conducted between the signal obtained using the taper, 2 µm-PCF, 6 µm-PCF and a conventional cuvette for a 1 mM ATP solution.

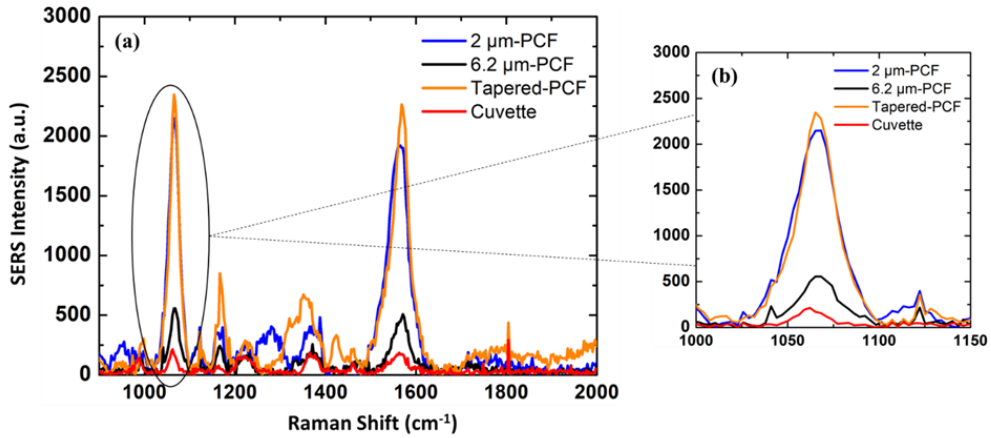

Figure 67 (a) SERS spectra of ATP molecules using 1 mm cuvette, 2 µm-PCF, 6 µm-PCF, and Tapered-PCF. (b) Close-up image of the spectral intensity at the 1080 cm^{-1} peak.

The reason why the comparison is done with the 2 µm-PCF is because as shown in section **II.1.3**, this fiber exhibits the maximal SERS signal among the other fibers, even that the average signal is not the highest, but it still approximately near to the highest one. It is important to compare the efficiency of the taper to the fiber that possesses the highest evanescent field portion to see if the improvement of the coupling efficiency and the short length of the waist part could be better than the 2 µm-PCF. For the cuvette setup, we prepared an ATP solution combined with a colloidal suspension of 60 nm spherical Au NPs, achieving a final ATP concentration of 1 mM. This mixture was then poured into a cuvette with a 1 mm path length. The intensity of the 1080 cm^{-1} peak was employed to evaluate the sensitivity of both SuC-PCFs and the tapered-PCF in comparison to the cuvette configuration. The Raman spectra of the ATP molecule are shown in Figure 67. As expected, the Raman signal obtained with the 6 µm-PCF is roughly four times weaker than that with the 2 µm-PCF, and approximately ten times weaker with the cuvette than with the 2 µm-PCF. The tapered-PCF and the 2 µm-PCF demonstrate comparable sensitivity, with the tapered-PCF showing a slight increase in peak intensity (9%) compared to the 2 µm-PCF. Additionally, the signal from the tapered-PCF was twelve times stronger than that obtained from the cuvette. These findings highlight the tapered-PCF's superior coupling efficiency, which offsets the shorter taper waist length (4 cm) compared to the 10 cm length of the 2 µm-PCF. Additionally, we compared the reliability of the two fibers (2 µm-PCF and tapered-PCF) to demonstrate the advantages of the tapered fiber over the 2 µm-PCF. Reliability was assessed by evaluating reproducibility, which measures a single sensor's consistency across different measurements, and repeatability, which assesses how uniformly multiple sensors prepared under identical conditions produce signals.

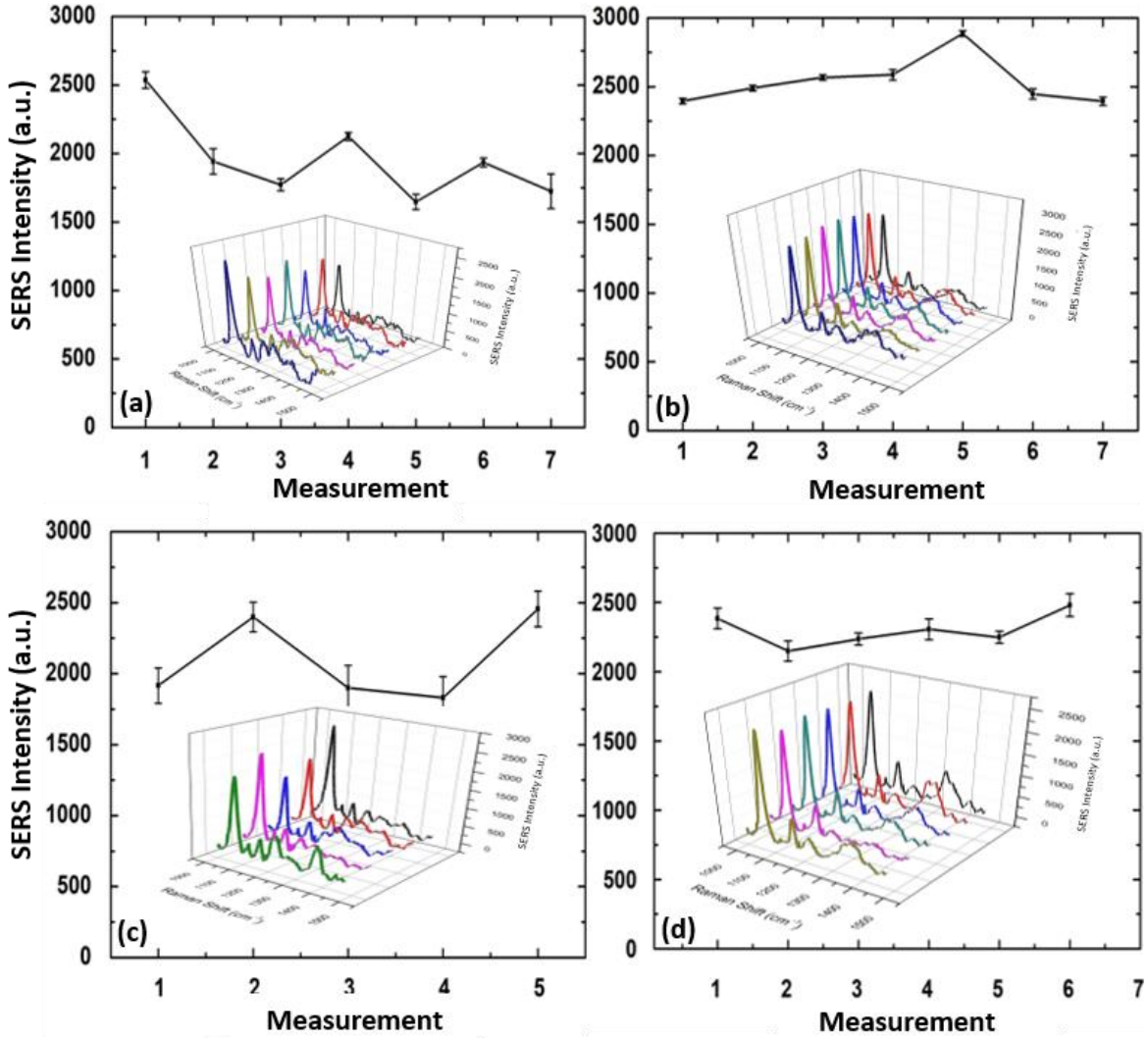

Figure 68 SERS intensity variations of the 1080 cm^{-1} Peak for ATP (Seven Measurements) from (a) a single 2 µm-PCF fiber and (b) a single tapered fiber. Error bars indicate the standard deviation across the seven measurements. Variation in peak SERS intensity at 1080 cm^{-1} using (c) five distinct 2 µm-PCF fibers and (d) Six distinct tapered fibers.

To determine the reproducibility of the SERS measurements, a number of fibers were prepared, seven measurements were conducted for each fiber, and RSD was then computed for each fiber to assess overall reproducibility. To evaluate the RSD in the repeatability of the SERS measurements, we prepared several fibers under identical conditions. For each fiber, we averaged the intensity across all measurements. Subsequently, the RSD was calculated from these averaged intensities to determine repeatability. Notably, between each measurement, the fiber (or tapered fiber) was removed and repositioned in the optical system. For each dataset, three Raman spectra were recorded and averaged to ensure robust and reliable SERS assessments. The results presented in figure 68(a-b) indicate that the tapered-PCF exhibited superior reproducibility compared to the 2 µm-PCF, with the RSD decreasing from 11.08% (for the 2 µm-PCF) to 3.2% (for the tapered-PCF). Improved repeatability was achieved with the tapered-PCF, exhibiting an RSD of just 3.84%, compared to 15.23% for the 2 µm-PCF (figure 68(c-d)). This indicates a notable enhancement in performance with the tapered-PCF. These results highlight the advantages of the tapered-PCF as a practical and highly sensitive SERS sensor, offering reduced signal variations that typically occur from minor misalignments during measurements. Small

misalignments, which are often unavoidable in practical scenarios, can cause substantial signal fluctuations with fibers of smaller core size. However, the tapered-PCF effectively minimizes these issues, making it a dependable and robust option for accurate and consistent SERS applications.

II.2.3.5. Development of a plug-and-play system for SERS sensing.

In order to test the efficiency of the taper to do a plug and play type experiment, a "bare fiber" connector (BFA Thorlabs, figure (69(a)) with an inner diameter of 850 nm is used.

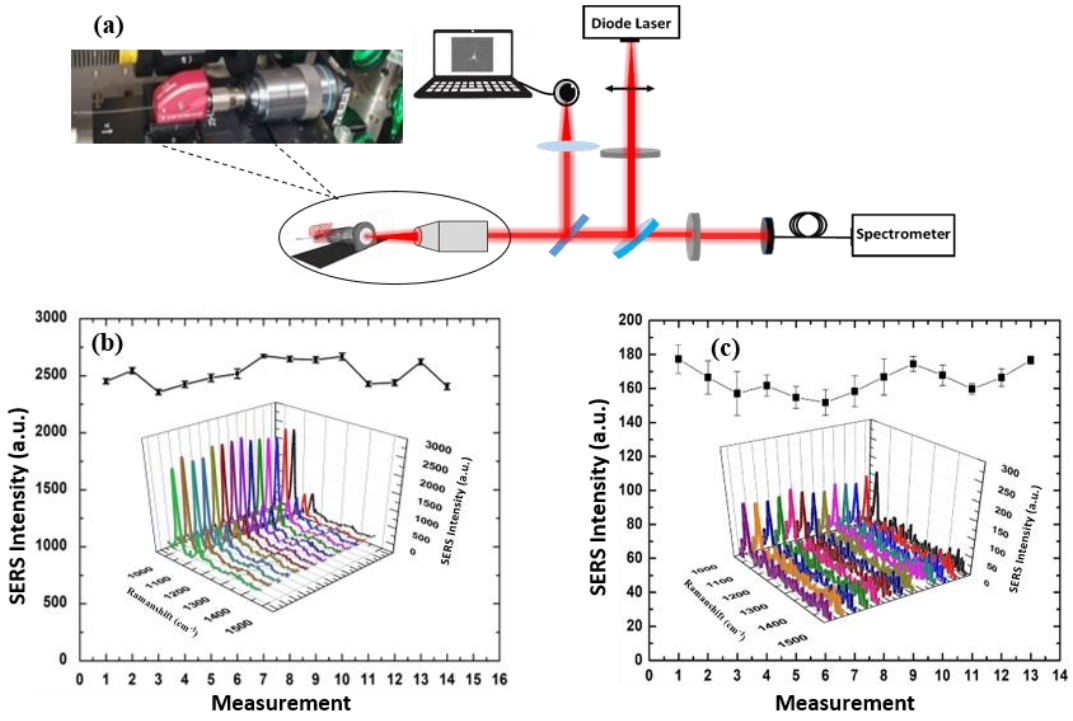

Figure 69 (a) Experimental setup for SERS measurements using the Plug and Play system. The inset image shows a photograph of the Plug and Play system with the Tapered-PCF inserted into a Bare Fiber Connector. (b) SERS intensity variations of the 1080 cm^{-1} Peak for 1 mM ATP (Fourteen Measurements) and (c) 100 nM ATP (Thirteen Measurements) with the PCF-Tapered inserted in the system. Error bars represent the SD of all measurements.

This system allows easy and quick connection without the need for complex alignment procedures. This setup enables us to test the reproducibility of SERS measurements by simply plugging in this connector, thereby enhancing the practicality and user-friendliness of the system. First, we performed an initial measurement by connecting the taper to the fiber connector system (FC/PC fiber adapter plate) and aligning it with the laser beam. Following this, we conducted subsequent measurements without requiring realignment. To evaluate the reproducibility of the SERS measurements with this system, we easily removed and reinserted the BFA connector. The results from this experiment, targeting ATP at a concentration of 1 mM, are shown in Figure 69(b). These results demonstrate highly reproducible SERS signals with minimal variation, achieving an RSD of 4.5%. Additionally, measurements at a lower ATP concentration of 100 nM were conducted, as illustrated in Figure 69(c), showing an RSD of 5.01%. These findings highlight the excellent performance of the plug-and-play system for SERS sensing, offering reliable measurements without the need for frequent fiber realignment. This system proves to be user-friendly, even when dealing with low analyte concentrations. The reproducibility of the

measurements with lower concentration is often encountered in practical applications. Looking ahead, we plan to focus on developing a BFA system that enables repeatable measurements. Currently, the BFA used has a diameter of 850 µm, which is larger than the 800 µm diameter of the fiber, leading to variations in the core position across different fiber connections. This technical mismatch in dimensions causes inconsistencies in the insertion depth and alignment of the fiber core. By resolving this issue, we can ensure consistent taper positioning for each sample, thereby improving the reliability and robustness of future measurements. This solution highlights that the problem is technical in nature and relatively easy to address, underscoring the potential value of our approach. Beyond its benefits of ease of use and cost efficiency, this plug-and-play system can be adapted as an optofluidic biosensor for testing biomarkers in body fluids. In such settings, accurate and repeatable measurements across numerous patient samples are often required. The plug-and-play system could enhance the efficiency and speed of these measurements while minimizing alignment-related errors. Nevertheless, further optimization and refinement are needed to develop this system into a practically viable biosensor for medical applications.

II.3. Conclusion

In this chapter, a development of SERS setup at XLIM was presented. Different experiment works are realized in order to evaluate the performance of the setup in signal improvement using fibers compared to conventional systems as cuvete, in addition to the achievement of low LOD of several analyte within SuC-PCFs. Moreover, through the simulation we presented the impact of core size parameter of the fibers on the evanescent field portion and the coupling of light to the PCFs core in order to get the best overview possible. We also presented the method used for the fabrication of these SERS-based PCF sensors via the stack and draw technique, it allowed us to fabricate fibers with different core sizes. To enhance measurement reliability, a tapered-PCF was developed and characterized, showing significant improvements in performance. Its superior capabilities were compared with those of a standard SuC-PCF, focusing on aspects such as coupling efficiency, sensitivity, and measurement reliability. The tapered-PCF exhibited 3.2 % variation in RSD in reproducibility over a unique sample, and 3.84 % over seven samples prepared with the same protocol (repeatability). These results hold great promise because a key limitation of SERS in biosensing is the reliability of the measurements. Additionally, these results enabled us to showcase the use of SERS fiber platforms in a 'Plug and Play' setup with standard Raman spectrometers, achieving excellent reproducibility with only approximately 5% variation in signal (at 1 mM and 100 nM of ATP). These findings could pave the way for the development of high-performance SERS probes for analyzing body fluids and provide a user-friendly probe for practical biosensing applications.

Chapter III. Investigating Nanoparticle Properties in SERS-active PCFs

As mentioned above, the SERS enhancement depends on the LSPR effect coming from the NP used with the PCFs. An essential parameter is the excitation wavelength and its relationship with the LSPR response that give efficient SERS enhancement. In addition to the excitation wavelength, the LSPR effect relies also on the shape of the NPs. Until now, all the SERS measurements done at XLIM were realized with Au NPs with a diameter of 60 nm (from BBI Solution).

In SERS, an important parameter is also the impact of the nanostructure arrangements, specifically when NPs are close enough to forms dimer. As Illustrated in figure 70(a), a dimer corresponds of two identical gold spheres separated by a gap "g" leading to enhanced field localization within the gap. For an individual Au NP, the peak of LSPR is approximately 540 nm. However, when the NPs are sufficiently close to form a dimer, their interaction shifts the LSPR peak to longer wavelengths, as illustrated in figure 70(b). This interaction also causes the maximum EF to shift towards longer wavelengths, as depicted in figure 70(c). Therefore, an investigation of the effect of the shape of NPs and their arrangements are essentials in order to benefit from the best enhancement possible.

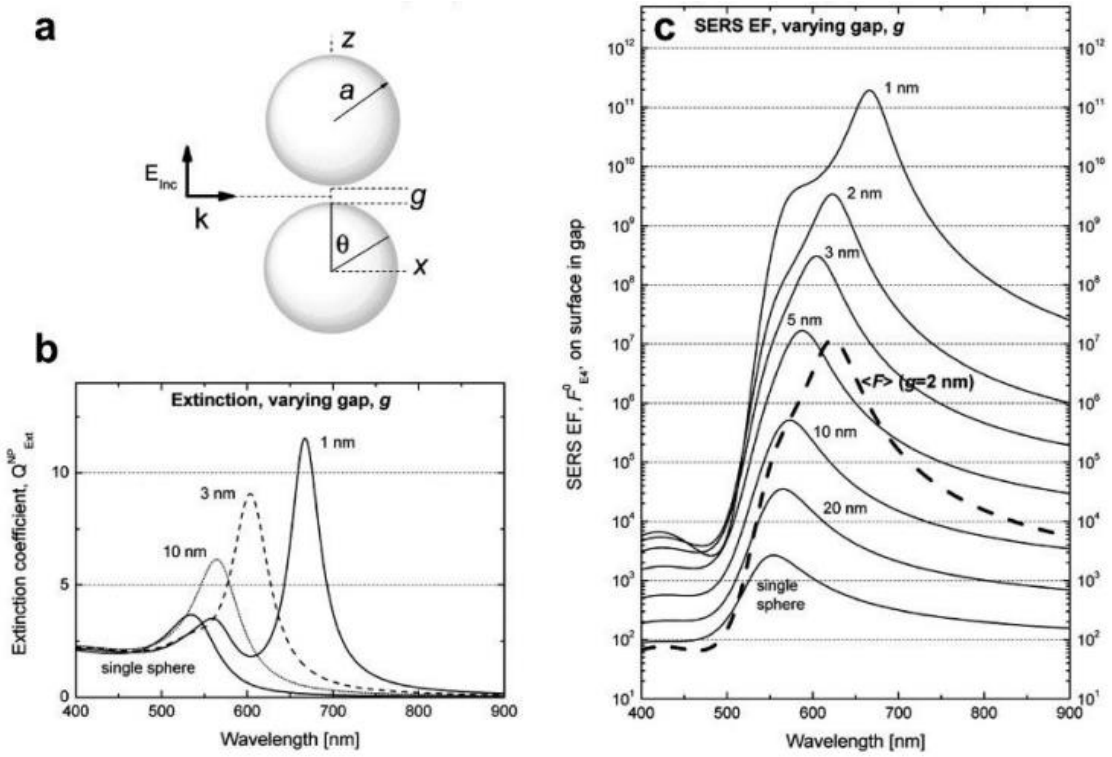

Figure 70 (a) Diagram of the dimer displaying the gap (g) between two NPs, with the excitation light polarized along the primary axis. (b) Coefficient of extinction versus wavelength for a single Au NP and for the dimer with various gaps. (c) SERS EF for several gaps between the two Au NPs compared to a single Au NP, with the dashed line indicating the average SERS enhancement across the full metallic surface for a dimer with a gap of 2 nm. Reproduced from [35].

In this chapter, in order to investigate the role of the NP shape in SERS enhancement inside the fibers, different NPs were employed and characterized by measuring the transmission spectra through the fibers with anchored NPs to determine the LSPR peak position. SERS spectra was measured using different NPs and finally a numerical simulation study using FDTD method (The Finite-Difference Time-

Domain) was realized to understand the performance of SERS of each NP and visualize the electric field enhancement near of the NP.

III.1. Relationship between the excitation wavelength and the LSPR peak position

In SERS applications, many considerations must be taken into account regarding the choice of the excitation wavelength; as it affects the Raman intensity, the fluorescence background, and the time of acquisition, the molecules damage threshold and the cost of the Raman system. Several lasers with different excitation wavelengths are used in Raman from UV to the NIR and beyond. The choice depends also to the analyzed samples that can generate a high fluorescence background and influences the quality of the Raman spectrum. Thus, the intensity of the spectrum acquired from UV and visible region is much higher than in NIR, which make them a better choice for the application that require shorter acquisition time and lower laser power and less risk of sample damages. Nevertheless, NIR laser sources are good options to avoid fluorescence compared to the visible region. A laser source with 785 nm wavelength is frequently employed in Raman spectroscopy due to its ability to minimize the fluorescence background while maintaining a relatively high Raman intensity.

Regarding the relationship between the excitation wavelength and the LSPR response, it was well known that the best location of LSPR peak is close to the excitation wavelength for maximum SERS enhancement [169]. However, the study of this relationship had not been completed. Christy L. Haynes and Richard P. Van Duyne studied the variation of the SERS EF with the variation of the LSPR wavelength (λ_{LSPR}) using a constant excitation wavelength [170]. Figure 71(a) presents the main results of this study. It shows that the maximum EF is obtained when the LSPR maximum is between the excitation wavelength (λ_{exc}) and the Raman-shifted wavelength (λ_R) (1081 cm^{-1}). Other experiments revealed that when the LSPR spectrum covers a 120 nm range and includes both the λ_R and λ_{exc}, the SERS EF is high. Furthermore, A.D. McFarland *et al.* conducted alternative experiments by varying the λ_{exc} from 475 nm to 800 nm. They measured the EF of the 1081 cm^{-1} and 1575 cm^{-1} peaks of benzenethiol molecules adsorbed on a single NSL-fabricated NP array sample characterized by a constant LSPR wavelength [28]. The results illustrated in figure 71(b) indicate that the highest SERS EF occurs when the λ_{exc} is smaller than λ_{LSPR}. In Addition, as illustrated in figure 71(a), the shift between the LSPR maximum and λ_{exc} is in the middle of the shift between λ_{exc} and λ_R. The same relationship is also illustrated in figure 71(c). Other SERS experiments were done in the same study and they showed the same results. Different experiments were realized to evaluate the behavior of the LSPR peak as a function of the λ_R of benzenethiol. It was demonstrated that when λ_R is situated in the higher energies, the shift between λ_{exc} and λ_{LSPR} also shift to the higher energy, this is explained by the fact that LSPR maximum has to be in the middle of λ_R and $\lambda_{exc}$to achieve the maximum of SERS enhancement.

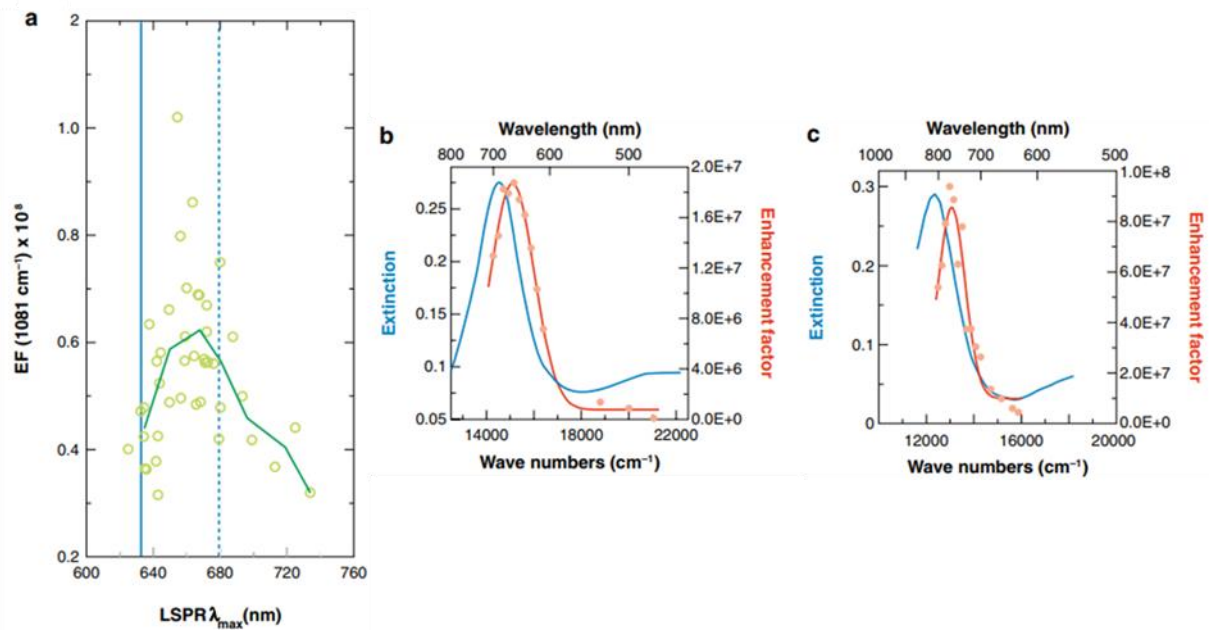

Figure 71 (a) Variation of the SERS EF of the 1081 cm^{-1} peak of benzenethiol (dashed line) (679.27 nm) with an excitation wavelength of 632.8 nm (solid line). Reproduced from [170]. (b) Surface-enhanced Raman excitation spectra of the 1081 cm^{-1} of benzenethiol, LSPR = 690 nm, maximum of the profile fit at 662 nm. (c) The excitation spectra of benzenethiol at 1575 cm^{-1}, enhanced by surface plasmon resonance with a wavelength of 810 nm, exhibit a profile fit maximum at 765 nm. Reproduced from [28].

These studies show the importance of taking into account the Raman-shifted wavelength of the analyte and the excitation wavelength used in order to get the most enhanced SERS signal.

III.2. Investigation of 60 nm BBI Au Nanospheres (Au NP)

III.2.1. Absorption characteristics of Au NP

As mentioned above, the NPs used until now are Au Nanospheres from BBI solutions with a diameter of 60 nm (EM.GC60) and with a density of 2.6×10^{10} particles/mL. The study of the absorption characteristic of these NPs is very important. The absorption and scattering spectra of NPs are crucial for understanding the behavior of NPs with the excitation source. These spectra are characterized by specific wavelengths at which light absorption and scattering are maximized, primarily due to the LSPR as explained above. The absorption spectrum describes how much light is absorbed at different wavelengths. The scattering spectrum illustrates how light is scattered at various wavelengths. When considering both absorption and scattering, the extinction spectrum (which is the sum of absorption and scattering) provides a comprehensive view of how NP interact with light. Usually, for spherical shape of NPs, Mie theory is used to describe the interaction with light and it can be used to predict the UV-visible absorbance spectrum of spherical metallic NPs [171]. This theory was developed by Gustav Mie in 1908 and provides a rigorous mathematical framework for calculating the scattering and absorption properties of spherical NPs interacting with light. It is worth to note that this theory will be used in order to compare its results with the ones obtained with the numerical simulation realized in this study.

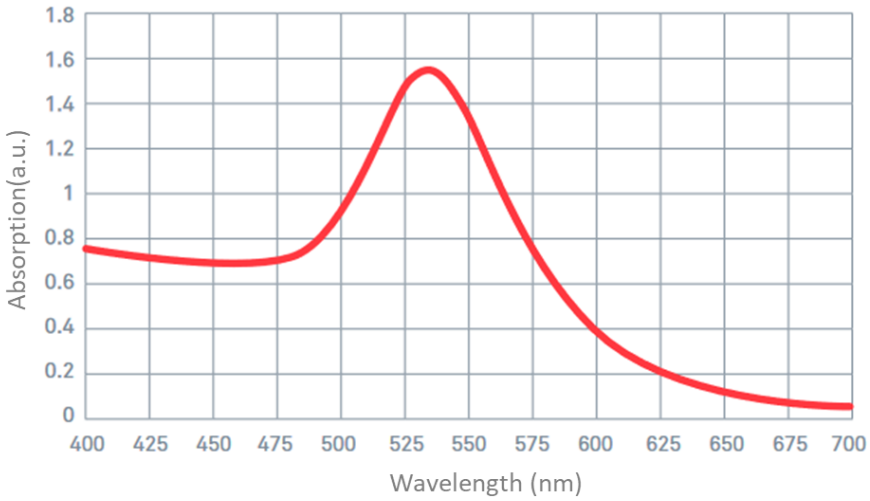

Figure 72 Absorption spectrum of single 60 nm Gold Nanosphere. Reproduced from [172].

The absorption spectrum of a single Au NP obtained using Mie Theory calculator offered by NanoComposix [173] is presented in figure 72. The LSPR maximum occurs around 540 nm for an Au NP with a diameter of 60 nm, which is quiet far from the excitation wavelength we used for SERS measurements (785 nm). Since the NPs are anchored inside the fibers, it is necessary to realize the transmission measurements through the functionalized fibers in order to verify the LSPR maximum position that could be shifted to longer wavelength if the NPs are clustered in the fiber during the protocol of the functionalization. In addition, in the following, the impact of the concentration of NPs on the LSPR maximum position, the attenuation peak, and the SERS performances will be presented.

III.2.2. Transmission measurements through fibers functionalized with NPs

To measure the transmission spectrum of the 3.5 µm-PCF functionalized with NPs, a supercontinuum source based on a non-linear PCF developed at XLIM was used. It has an emission spectrum from 350 nm to 1700 nm with a central wavelength of 1064 nm. The figure 73 shows the setup. An objective lens 40x was used to control the light coupling into the core fiber of a 3.5 µm-PCF, a camera at the output side of the fiber was used in order to optimize the light coupling by visualizing profile of the light guided by the fiber core. Then, an optical spectrum analyzer (OSA) was used to measure the transmission spectrum of the supercontinuum source propagated through the fiber. An iris was used to measure only the light propagated in the core.

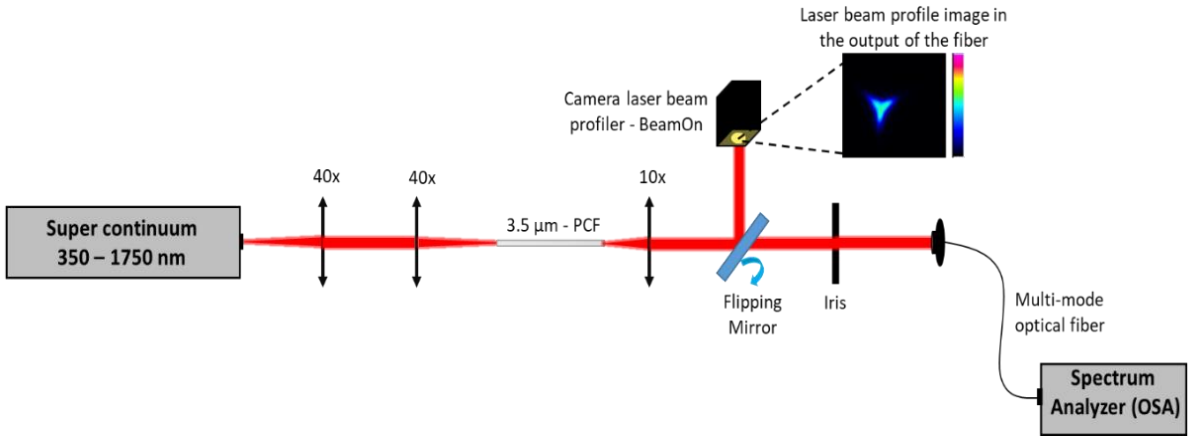

Figure 73 Schematic of the optical setup used for measuring the transmission spectrum of 3.5 µm-PCF with anchored NPs.

Firstly, an empty fiber of 3.5 µm-PCF is used, it is essential to obtain the transmission spectrum with an empty fiber sample that can serve as a baseline reference for allowing the identification of the absorption peaks attributed to the different NPs anchored within the fiber.

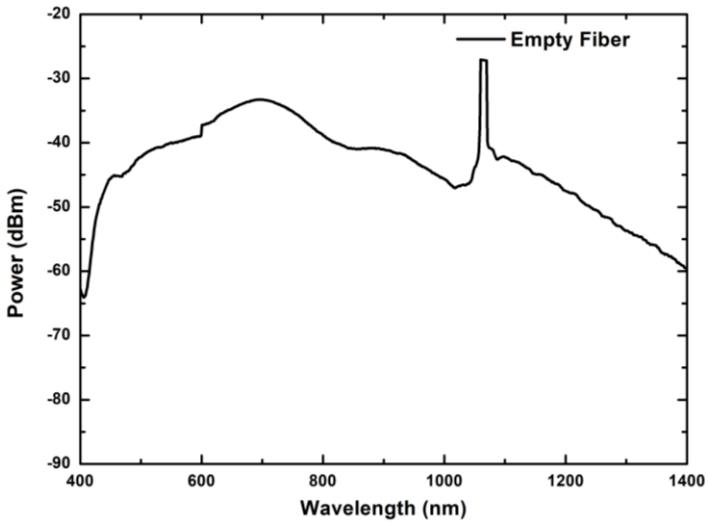

Figure 74 Transmission spectrum of the supercontinuum source through 10 cm long length of an empty fiber of 3.5 µm-PCF

The measured transmission spectrum of the supercontinuum source through this fiber is presented in figure 74. The spectrum extends beyond the pump wavelength of the laser 1064 nm wavelength, producing a broad and continuous spectral range that spans from 400 to 1400 nm. Then, the same experiment is realized with the functionalized 3.5 µm-PCF wit Au NPs with the original concentration (1.0x) and with a length of 10 cm. The measured spectrum shown in figure 75 exhibits a prominent absorption peak centered around 540 nm.

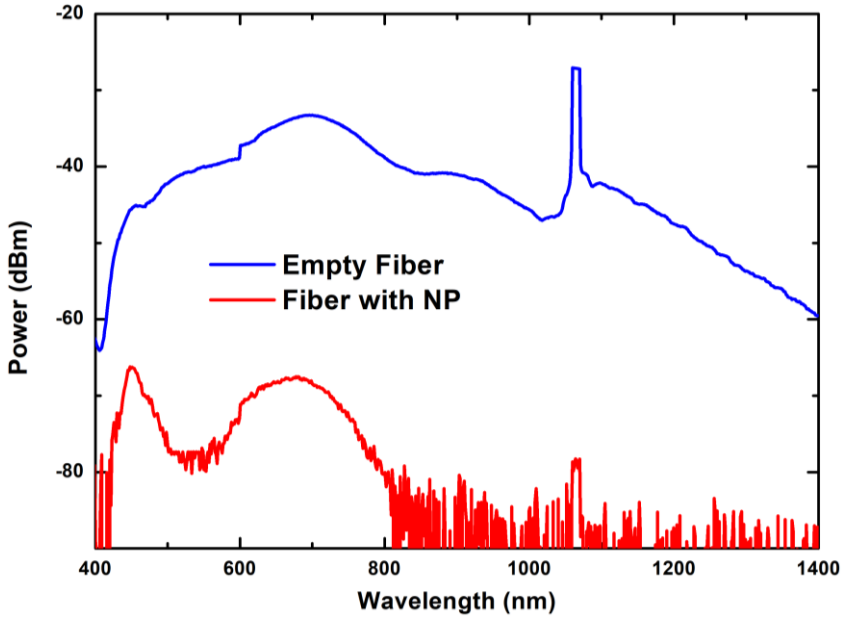

Figure 75 Transmission spectrum of the supercontinuum source through 10 cm long length of an empty 3.5 µm-PCF (bleu curve) and functionalized 3.5 µm-PCF with Au NPs (red curve).

In the subsequent analysis, the absorption peak characteristics of Au NPs were studied for different concentrations of these NPs anchored inside the 3.5 µm-PCF (1.0x, 0.75x, 0.50x and 0.25x) and for different fiber lengths (12 cm, 10 cm, 8 cm, 6 cm and 4 cm). This comprehensive investigation aims to verify any potential effects of the concentration and the length variations on both the attenuation and position of the absorption peak. Specially, the objective is to determine whether changes in concentration and length induce aggregation effects, which could subsequently influence the SERS performance in each experimental configuration.

The absorption spectrum for a concentration of 25% (0.25x) across varying fiber lengths is shown in figure 76(a). A slight appearance of the absorption peak is observed for fiber lengths of 6 cm and 8 cm, indicating a weak but discernible plasmonic response from the Au NP within the fiber. It is interesting to note that we can see an absorption peak, even though it is not clear for fiber lengths of 10 and 12 cm. Conversely no distinct absorption peak is observed for the shortest fiber length of 4 cm, suggesting a lack of sufficient NP density to induce measureable plasmonique effects within the spectral range. Similar measurements realized for different concentrations (50%, 75%, 100%) are plotted in figure 76(b), 76(c) and 76(d), respectively. For each concentration, the longest fiber length (L = 12 cm) consistently exhibits the highest of the absorption peak, corresponding to a more pronounced plasmonic response. The power level achieved across the various NP concentrations reveals a clear trend, at higher concentrations (1.0x and 0.75x), the measured power levels exhibit a gradual decrease, indicating greater attenuation of the transmitted light. Conversely, at lower concentrations (0.50x and 0.25x), the measured power levels are comparatively higher, suggesting reduced attenuation of the transmitted light. This trend underscores the relationship between NP concentration and the attenuation of transmitted light within the fiber, as the concentration decreases, the attenuation diminishes, resulting in higher measured power levels. Most of all, a significant observation across all configurations is the absence of any discernible shift in the position of the LSPR, indicating the absence of aggregation effects inside the fibers, which ensure that the incorporation of the NPs using the anchored configuration does not results in forming aggregations in the inner silica walls of the fibers.

Since a fiber length of 10 cm is generally used in our SERS experiments, for this length, notably, the absorption peaks are in the expected position (540 nm), indicating consistent peak localization across concentrations. This means that the NP remains dispread within the fiber at this length, providing more reliable and consistent result for studying their interactions with the fiber.

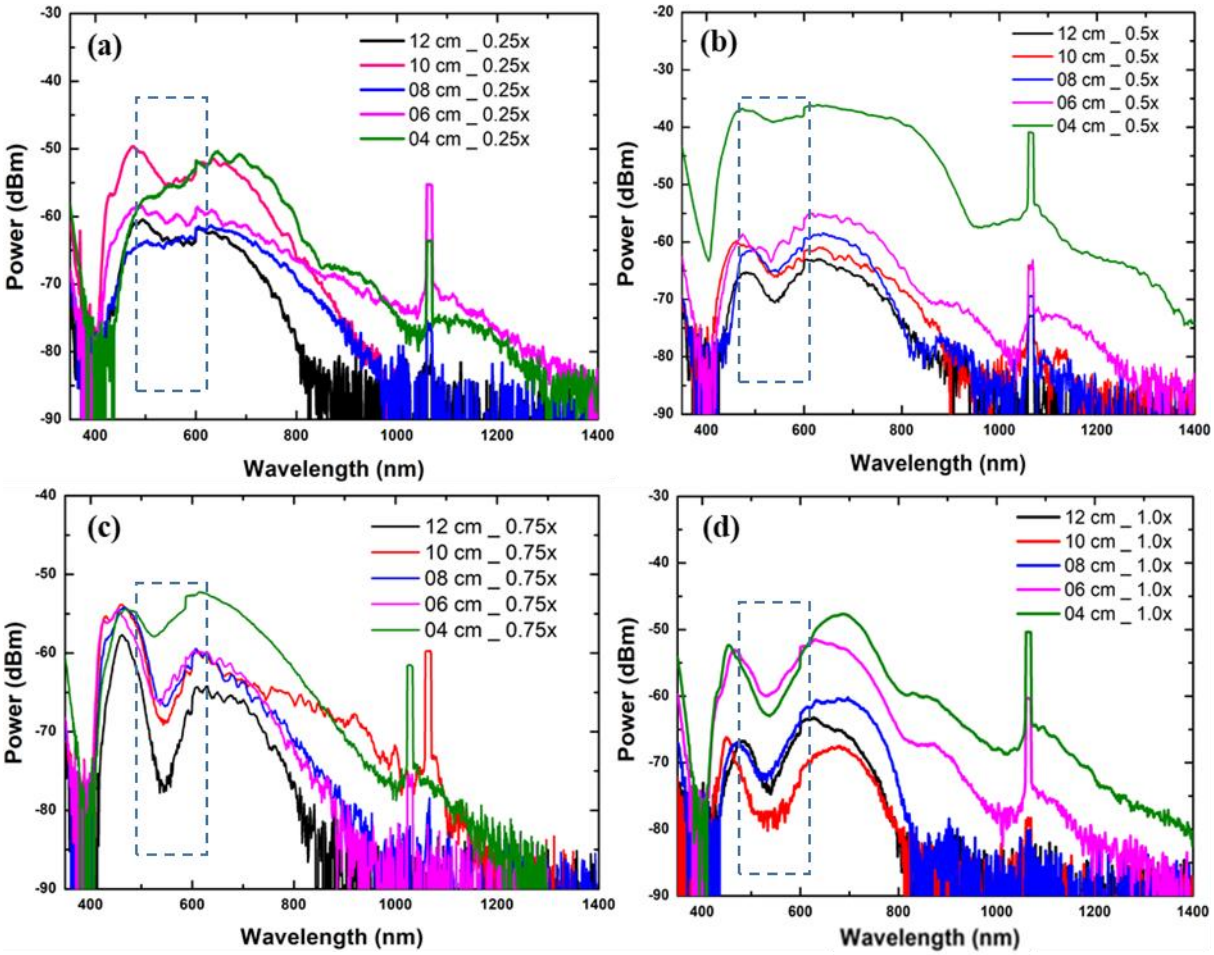

Figure 76 Transmission spectrum of the supercontinuum source through 10 cm long length of functionalized 3.5 µm-PCF with different fiber lengths (from 4 to 12 cm) for (a) 0.25x, (b) 0.50x; (c) 0.75x and (d) 1.0x of Au NP concentrations.

III.2.3. Comparison of SERS signal measured with different concentration of Au NPs & fiber length

In the previous section, it was shown that anchoring the Au NPs inside the fiber does not lead to a shift of the LSPR maximum. To continue in the investigation about the SERS performance of these NPs, a comparison study was done to compare the SERS intensity, in anchored configuration, for different concentrations of Au NP and the fiber length. During the experiment, a 3.5 µm-PCF sample of 12 cm was cut after every set of measurements (ten measurements) until reaching 4 cm. The figure 77 illustrates the results of this experiments and the table 2 represents the summary of SERS intensities of ATP at 1080 cm^{-1}.

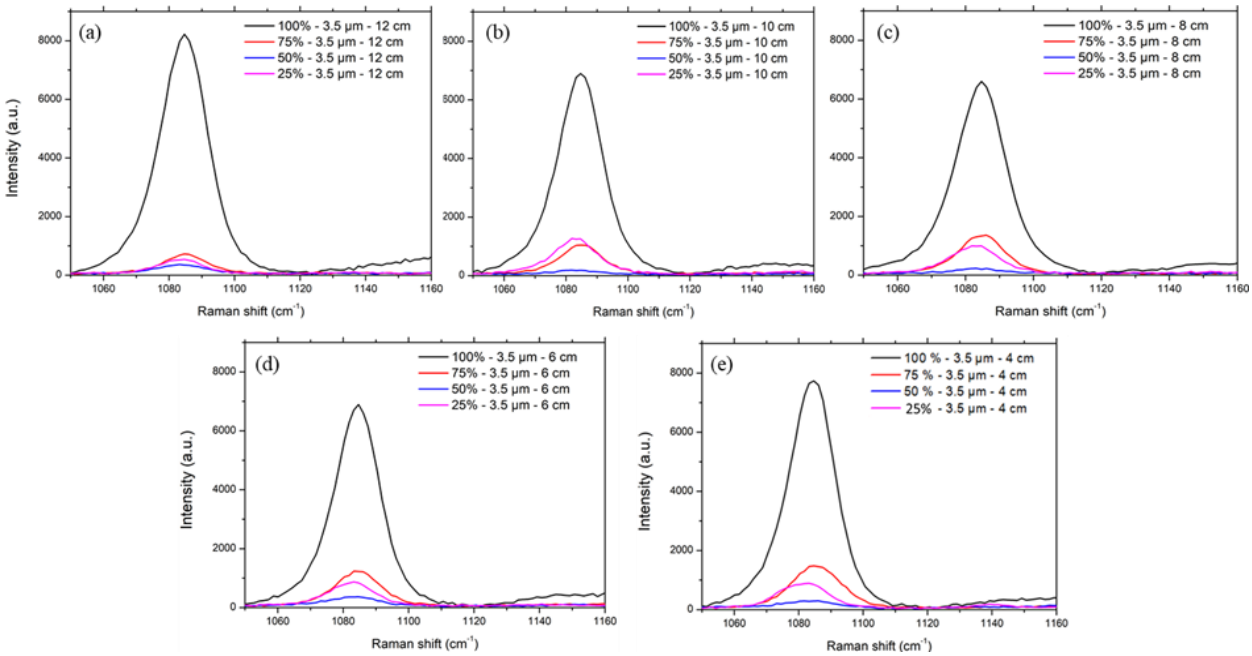

Figure 77 SERS spectra of 1 mM of ATP with functionalized 3.5 µm-PCF with Au NPs and zoomed around the main Raman peak at 1080 cm^{-1}.

Higher concentration of Au NP leads to stronger SERS signal (across all fiber lengths). There is a significant drop in SERS intensity as the concentration decreases from 1.0x to 0.75x. This trend is consistent across all fiber lengths. The 0.75x concentration still shows notable SERS intensity, but the 0.5x and 0.25x concentrations result in much lower values. For the fiber length effect, fiber length of 12 cm exhibits the highest SERS intensity for 1.0x concentration. However, for lower NP concentrations, the effect of the length is less significant. As the intensity of the SERS signal is much lower, additional signal fluctuation could come from slight variation of the light injection on the setup.

The 1.0x concentration of Au NP yields the highest SERS intensities, indicating that higher concentrations are more effective for enhancing SERS signals, particularly when using a longer fiber length. However, this does not imply that longer fibers and higher concentrations are universally optimal. Higher concentrations of Au NPs can lead to increased absorption and scattering losses. In longer fibers, these losses accumulate over the extended interaction length, which can diminish the SERS signal. On the other hand, shorter fibers can mitigate these losses, resulting in relatively higher SERS intensities even at lower concentrations. The shorter interaction length reduces the cumulative effect of absorption and scattering, allowing more effective light propagation and interaction with the NPs. This study demonstrates that the functionalization of the fibers with Au NPs does not lead to aggregation of the NPs yielding a shift of the LSPR maximum to longer wavelengths, close to the one of the excitation laser (at 785 nm). Therefore, the Au NPs used in our experiments do not seem to be adequate. In the following, NPs with different shapes are investigated and then compared to the Au NPs in term of SERS performance.

Table 2 Measured average SERS intensity of ATP at 1080 cm^{-1} in the anchored configuration with 3.5 µm-PCF using different NP's concentrations and different fiber lengths

Fiber Length	SERS intensity – 1.0x (counts.)	SERS intensity – 0.75x (counts)	SERS intensity – 0.5x (counts)	SERS intensity – 0.25x (counts)
12 cm	8225	723	344	535
10 cm	6895	104	180	1257
08 cm	6600	1336	195	993
06 cm	6890	1222	364	840
04 cm	7734	1479	289	847

III.2.4. Investigations of different NPs inside the SuC-PCFs using anchored configuration

The aim of this study is to investigate different NPs with a LSPR maximum closer to the wavelength of our excitation laser (785 nm). 3.5 µm-PCFs functionalized with different NPs are optically characterized to verify the position of the absorption peak of the NPs, and then, their SERS performances are evaluated and compared.

III.2.4.1. Silica-Core Gold Nanoshell

Silica-Core Gold Nanoshells (SC-AuNSH) consist of a silica core in a spherical shape enveloped by a thin layer of gold. Due to their chemical and optical characteristics, they are well-suited and appealing for various medical purposes, particularly in cancer treatment and diagnosis. They have undergone examination for their utility in biosensing, imaging, and photothermal ablation [174]. The SC-AuNSH are interesting because it is possible to shift the wavelength of the LSPR maximum by controlling the thickness of the gold layer. SC-AuNSHs with an outer diameter of 150 nm, and a concentration is 2.4×10^{10} particles/mL have been ordered from NanoComposix (GSCRR150) [175]. The reported LSPR maximum peak is around 770 nm and the Optical Density (OD) of ~ 20. The figure 78(a) shows the Transmission electron microscopy (TEM) image of these NPs while the figure 78(b) represents the absorption peak of a single NP taken from NanoComposix. Even if λ_{LSPR} is not situated between λ_{exc} (785 nm) and λ_R of ATP at 1080 cm^{-1} which is 858 nm, its position seems more favorable than the one of the Au NP already used.

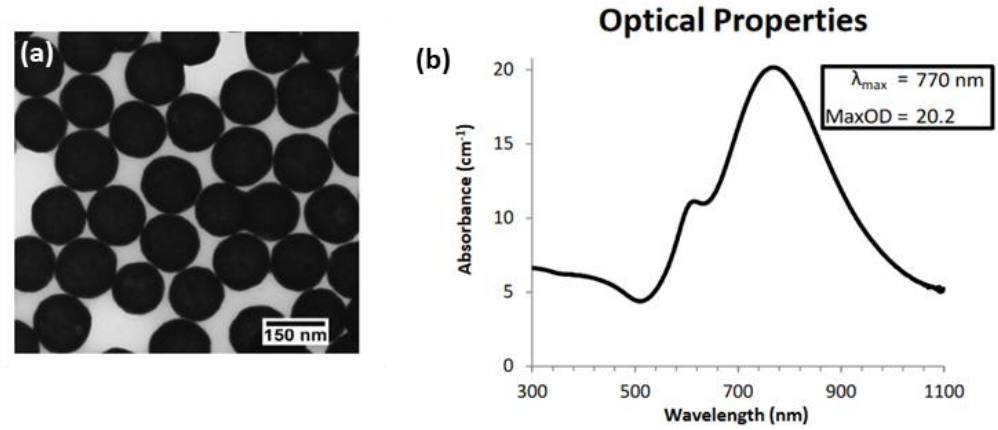

Figure 78 (a) TEM image of 150 nm of SC-AuNSH and (b) absorption spectrum of 150 nm of SC-AuNSH. Reproduced From NanoComposix.

The advantage of these NPs is that the silica core provides structural stability to the gold Nanoshell and maintaining the integrity of the NP structure. Rasch *et al.* [176] conducted an interesting research on producing gold nanoshells (GNS) utilizing silica NPs ranging from 30 to 120 nm. Their findings revealed that as the size of the silica NP decreased, the gold shell surface became more roughen, leading to a higher tendency for particle aggregation. Consequently, this resulted in the absence of a plasmon resonance peak within the water window. This study shows that the using of 150 nm size of these NPs minimize the aggregation effect and ensure effective plasmon resonance.

To ensure accurate comparison between different NPs, it is essential to standardize the OD of the solution. For instance, a NP solution with an OD of 20 (of these NPs) needs to be diluted to match the OD = 1 of the Au NPs. This dilution is crucial because it allows for a fait assessment of each NP performance under similar experimental conditions, eliminating discrepancies due to varying concentrations. Firstly, a transmission spectrum of the super continuum source was measured through 3.5 µm-PCF filled with 1.0x of SC-AuNSH concentration. There is no signal obtained from this fiber. Then, different dilutions of SC-AuNSH solution to get concentrations of 0.1x, 0.05x and 0.01x, then, transmission spectrum was measured as illustrated in figure 79(a).

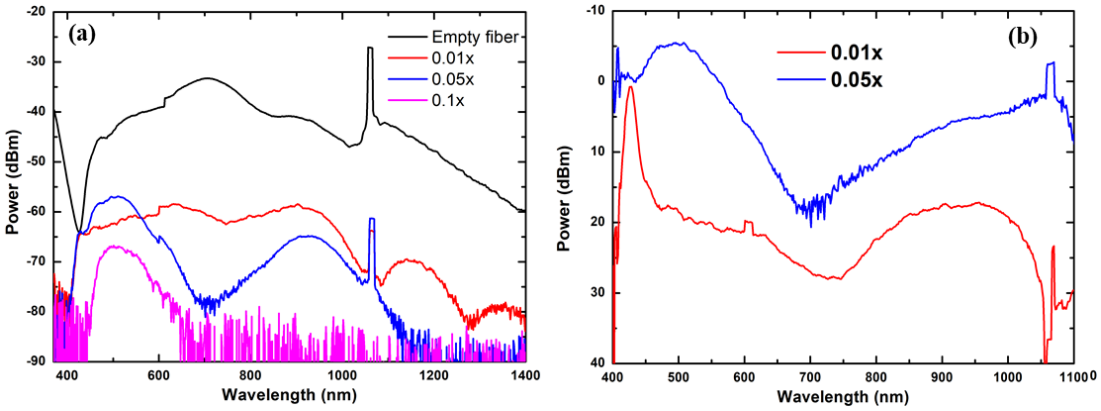

Figure 79 Transmission spectrum of the supercontinuum source through 10 cm long length of empty fiber and different functionalized 3.5 µm-PCFs with (a) 0.25x, (b) 0.50x; (c) 0.75x and (d) 1.0x of SC-AuNSH concentrations.

For the concentration of 0.1x, the spectrum exhibits a strong attenuation above 650 nm. At lower concentration, an attenuation peak is measured at 711 nm for 0.05x, and at 753 nm for 0.01x concentration. To confirm this slight shifting in peak position, the two spectra corresponding to the 0.05x and 0.01x concentrations were subtracted from the spectrum measured within the empty fiber and presented in figure 79(b). The transmission spectra for various fiber lengths at concentration of 0.01x and of 0.05x are plotted in figure 80(a-b). It is obvious that with 0.01x concentration and a fiber length of 11 cm, there is no clear absorption feature, suggesting a lower NP density compared to the fiber length. Anchoring NPs with such a low concentration over relatively long fiber results in insufficient NP density inside the fiber, which in turn leads to the absence of a distinct absorption peak. This is can also be observed with fiber length of 8 cm and 6 cm, where only small absorption peak with low attenuation is noticed (approximately at 750 nm). The increased fiber lengths further dilute the sparse distribution of NPs, reducing their optical impact and significantly diminishing the absorption characteristics. Conversely, at 0.05x concentration, all the lengths of fiber lead to an absorption peak presence with relatively clear attenuation, the 10 cm fiber length exhibits the strongest absorption effect, characterized by a peak at 711 nm. These result demonstrates that while there is a slight shift in the position of the LSPR peak between lower and higher concentrations, the peak remains within a range that makes these NPs particulary interesting for SERS studies and comparison with Au NPs.

In order to evaluate the SERS performance of SC-AuNSHs in SERS, different 3.5 µm-PCFs were functionalized using the anchored configuration for different concentrations of SC-AuNSHs. A solution of 1 mM of ATP was injected inside these functionalized fibers, then the fibers were dried. The laser power and the integration time of the spectrometer were set at 10 mW and 10s, respectively. An average over ten measurements of SERS signal is done for each case. The SERS spectrum is shown in figure 80(c). It shows that the concentration of 0.1x gives a signal higher by 15 times than the signal obtained with 0.05x, while there is no significant signal detected at the 0.01x concentration. This trend can be explained by the density of the NPs, which lead to an enhancement of electromagnetic field for SERS. At 0.1x concentration, the density of SC-AuNSH is high enough to amplify the Raman signal. In contrast, the 0.05x concentration, with less NPs, results in weaker signal. At the 0.01x concentration, the NP density is likely too low and thus leads to a negligible SERS signal.

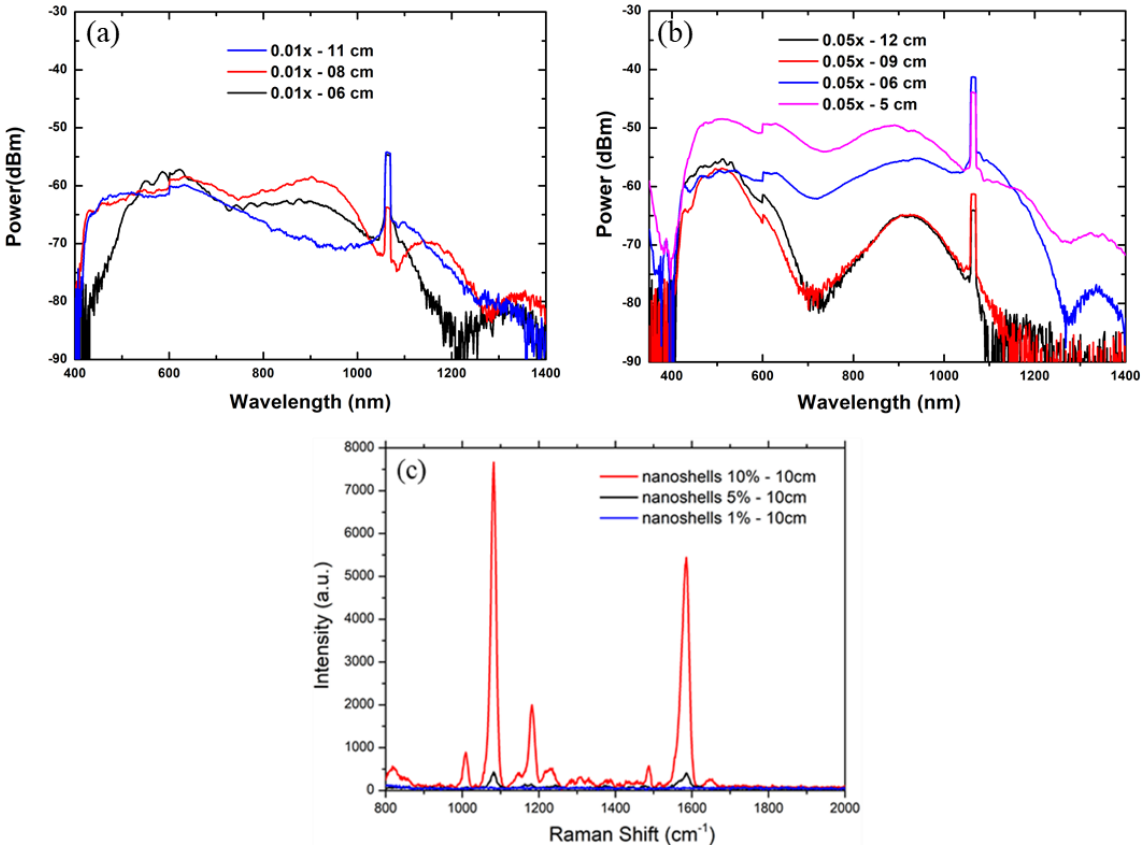

Figure 80 Transmission spectrum of the supercontinuum source through functionalized 3.5 µm-PCFs with a concentration of (a) 0.01x and (b) 0.05x of SC-AuNSH with different fiber lengths. (c) SERS signal of 1 mM of ATP using functionalized 3.5 µm-PCFs with different concentrations of SC-AuNSH.

III.2.4.2. Hollow-Core Gold Nanoshell

Hollow-core gold Nanoshells (HC-AuNSH), unlike their silica-core counterparts, feature a hollow interior surrounded by a thin gold shell. The thickness of the gold enables to shift the LSPR effect to the near infrared range (i.e. wavelengths from 700 to 800 nm) leading to a large enhancement of Raman scattering signal from molecules on their surface. The HC-AuNSH with an external diameter of 60 nm and 7 nm of shell thickness were ordered from Nanopartz (A1H-800) [177].

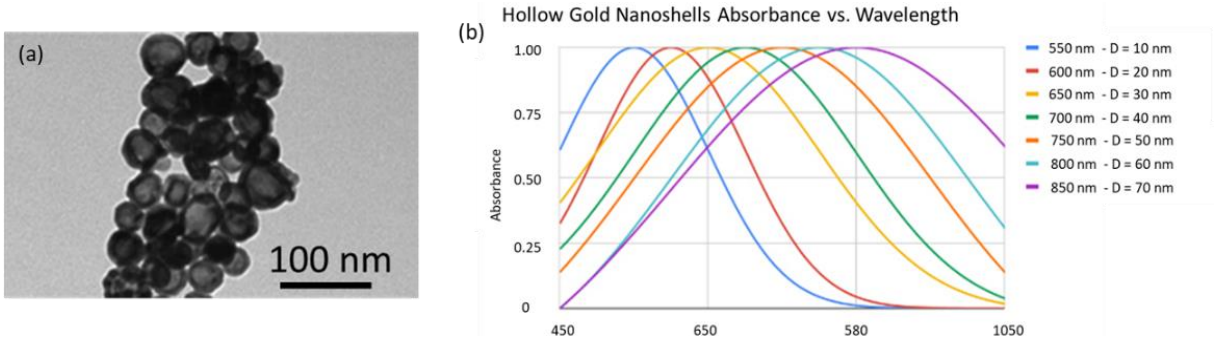

Figure 81 (a) TEM images of HC-AuNSHs with a total diameter of 60 nm and gold shell of 7 nm. (b) Absorbance spectra of HC-AuNSHs with different diameters. Reproduced from [177]

TEM images of these NPs are shown in figure 81(a), while figure 81(b) displays the absorbance peaks for different diameters. In order to obtain an LSPR peak around 800 nm, which is situated between the excitation wavelength and the Raman band of ATP (858 nm), we have ordered the NPs with a diameter of 60 nm.

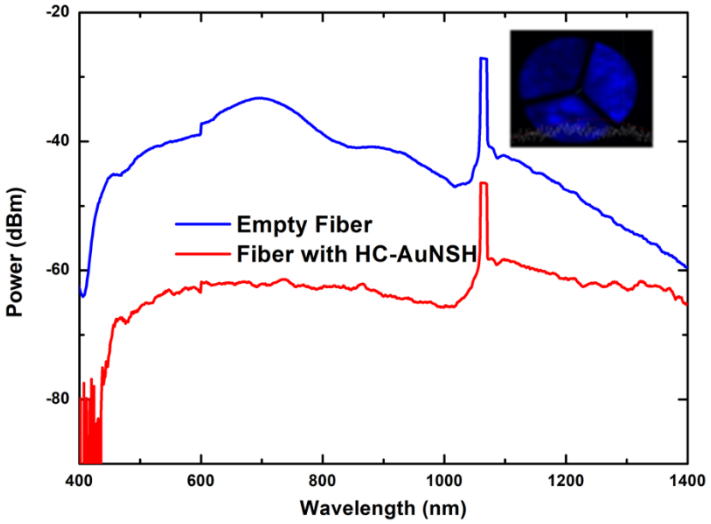

Figure 82 Transmission spectrum of the supercontinuum source through 10 cm long length of functionalized 3.5 µm-PCF with HC-AuNSH (red curve) and through empty fiber (bleu curve). Inset image represents the transverse section of the output side of the fiber.

The transmission spectrum of the supercontinuum source through 10 cm of functionalized 3.5 µm-PCFs with HC-AuNSH is depicted in figure 82. Unlike the previous NPs (Au NPs and SC-AuNSHs), no discernible absorption peak is observable in the measured spectrum. There is nevertheless a large attenuation (~20 dB) of the transmitted spectrum that might be induced by the HC-AuNSH. The inset image shows the transverse section of the fiber, with no light detected in the core at the fiber output, indicating excessive absorption and a lack of interaction between the light and the NPs. These results suggest that the HC-AuNSHs absorb too much light, preventing effective guidance within the fiber core. Consequently, this indicates the need to reconsider the use of HC-AuNSHs for this application due to their high absorption properties

III.2.4.3. Gold Nanostars

Other NP tested in this study is Gold Nanostars from Nanopartz (A1S-850-CIT-DIH-1-5) [178]. They have a shape of stars and exhibit sharp tips and branches that lead to high LSPR effects. The sharp features create intense electromagnetic field at the tips (hot spots), which can amplify the SERS signal of molecules positioned near these regions. These NPs have an external diameter of 130 nm with a core diameter of 80 nm and spikes length of 50 nm. In opposite to the previous presented NPs, in this case, the excitation wavelength is lower than the LSPR wavelength offered by Nanostars.

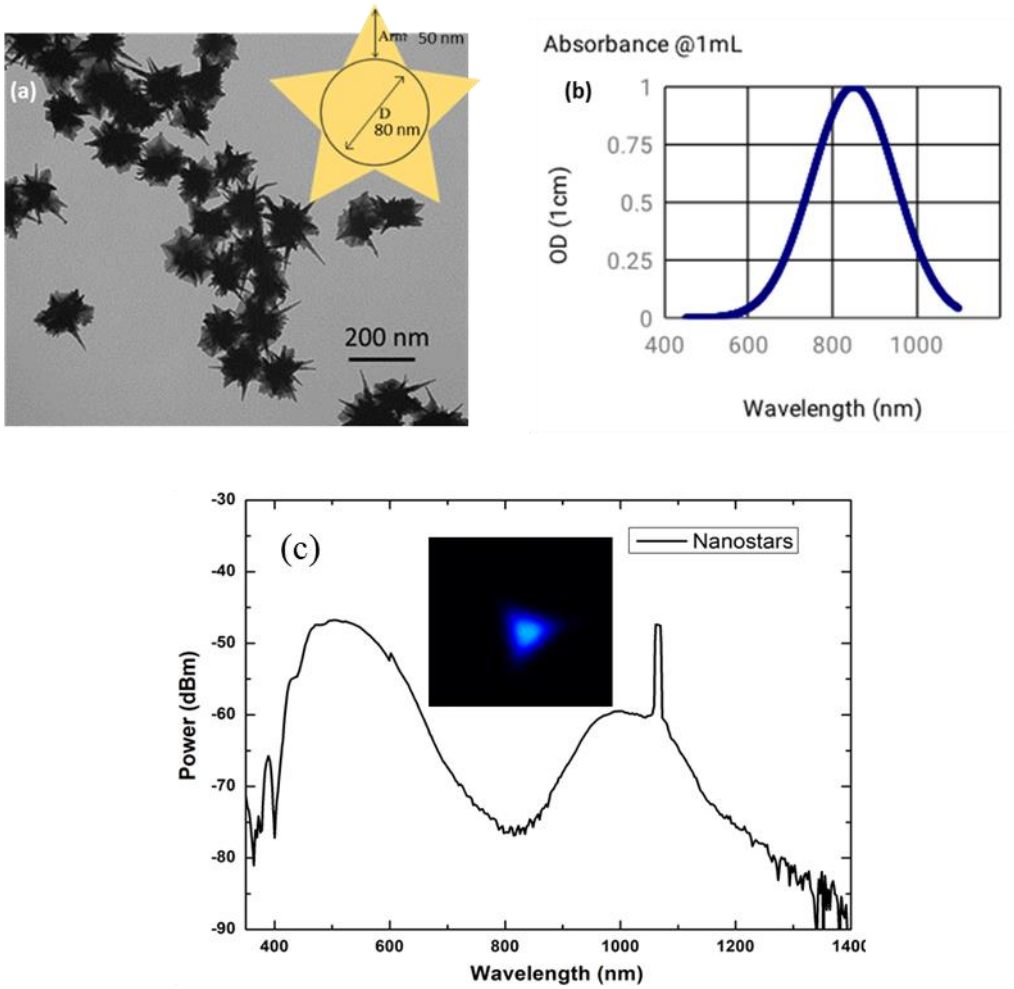

Figure 83 (a) TEM images of Nanostars used in the study. (b) Absorption spectrum of 130 nm Nanostars. Reproduced from [177] (c) Transmission spectrum of the supercontinuum source through 10 cm long length of functionalized 3.5 µm-PCFs with Nanostars. Inset image represents the transverse section of the output side of the fiber.

The figure 83(a) represents the TEM images (from Nanopartz) of the used Nanostars with a LSPR maximum peak at 835 nm as illustrated in figure 83(b). These Nanostars are then anchored using the anchored configuration inside the 3.5 µm-PCF with 10 cm of length. The transmission spectrum shown in figure 83(c) reveals a prominent peak near of 840 nm, which closely aligns with the wavelength of the LSPR maximum peak provided by the supplier (835 nm). This observation confirms the characteristic plasmonic resonance even inside the fibers. Additionally, this results suggests a uniform dispersion of the NPs, without aggregation, within the fiber.

III.2.5. SERS performances of the different NPs

III.2.5.1. Comparison of SERS signal measured from cuvette and fiber (injected configuration)

The aim of this study is to compare the SERS signal of the investigated NPs in a cuvette and inside fibers with the injected configuration. For each NP, 100 µL of a 10 mM ATP solution was mixed with 900 µL of the NP solution, resulting in a final ATP concentration of 1 mM. This mixture was then injected into both the cuvette and the fiber (beforehand cleaned by injecting a solution of acetone). By

monitoring the 1080 cm^{-1} peak of the ATP molecule, the SERS performance of each NP was compared. The conditions during the experiments were the same for all the measurements: a laser power of 10 mW and an integration time of 10s. The presented intensity is averaged over ten measurements.

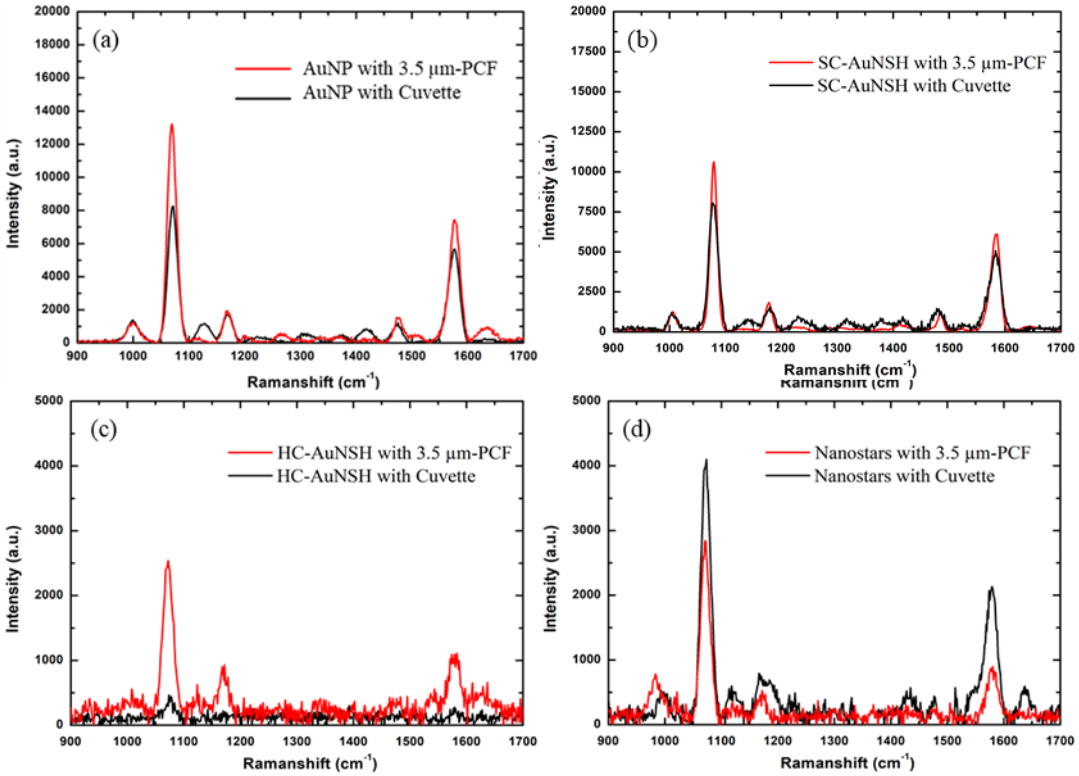

Figure 84 SERS spectrum of 1 mM of ATP measured in a cuvette and into a fiber (injected configuration) with (a) AuNP, (b) 0.1x of SC-AuNSH, (c) HC-AuNSH, (d) Nanostars.

The different spectra presenting the SERS signal obtained with the cuvette and the fiber using the injected configuration are shown in figure 84. The results indicate that, for most NPs, the fiber configuration provides higher SERS signal intensities than the cuvette. However, for Nanostars, the signal obtained with the cuvette is higher than the one obtained with the fiber. A summary of the results are presented in figure 85. The error bars represent the SD across ten measurements.

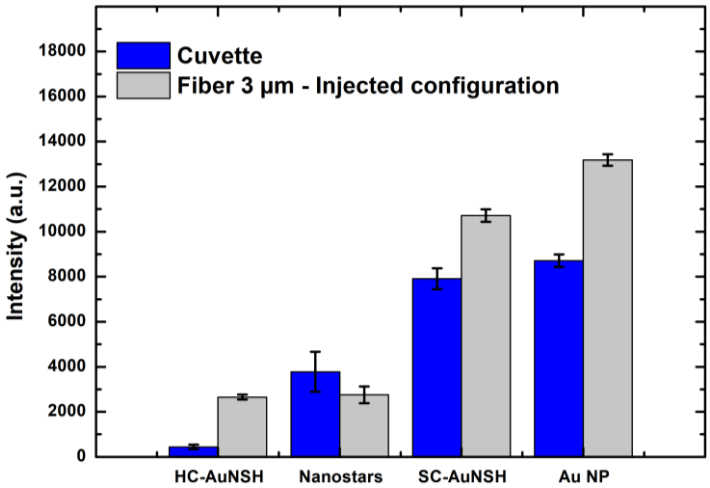

Figure 85 For each NP, average SERS intensity at 1080 cm^{-1} measured in a cuvette and in a 3.5 µm-PCF (core diameter of 3 µm) ; error bars represent the standard deviations across ten measurements.

The Au NPs exhibit the highest SERS intensities in both the cuvette and fiber configurations. It is notable that Au NPs consistently perform well compared to other NPs, both in the fiber and in the cuvette. However, this result warrants further investigation to fully understand the underlying mechanisms and confirm why Au NPs outperform other NPs in various configurations. It is worth to notice that it is important to consider the variability of the measurements (indicated by the error bars). The error bars for the cuvette are generally higher compared to those for the fiber, suggesting larger variability in the SERS signals obtained from the cuvette.

III.2.5.2. Comparison of SERS signal of different NPs functionalized into fibers with the anchored configuration

The objective of this study is to compare the SERS signal of the different NPs anchored inside the 3.5 µm-PCFs using the anchored configuration. For that, 1 mM of ATP solution is prepared and injected inside the fiber. After binding the ATP molecules with NPs, the fiber was dried by pushing the air inside. The experiment conditions were the same as the previous study, and the fiber length was constant (10 cm).

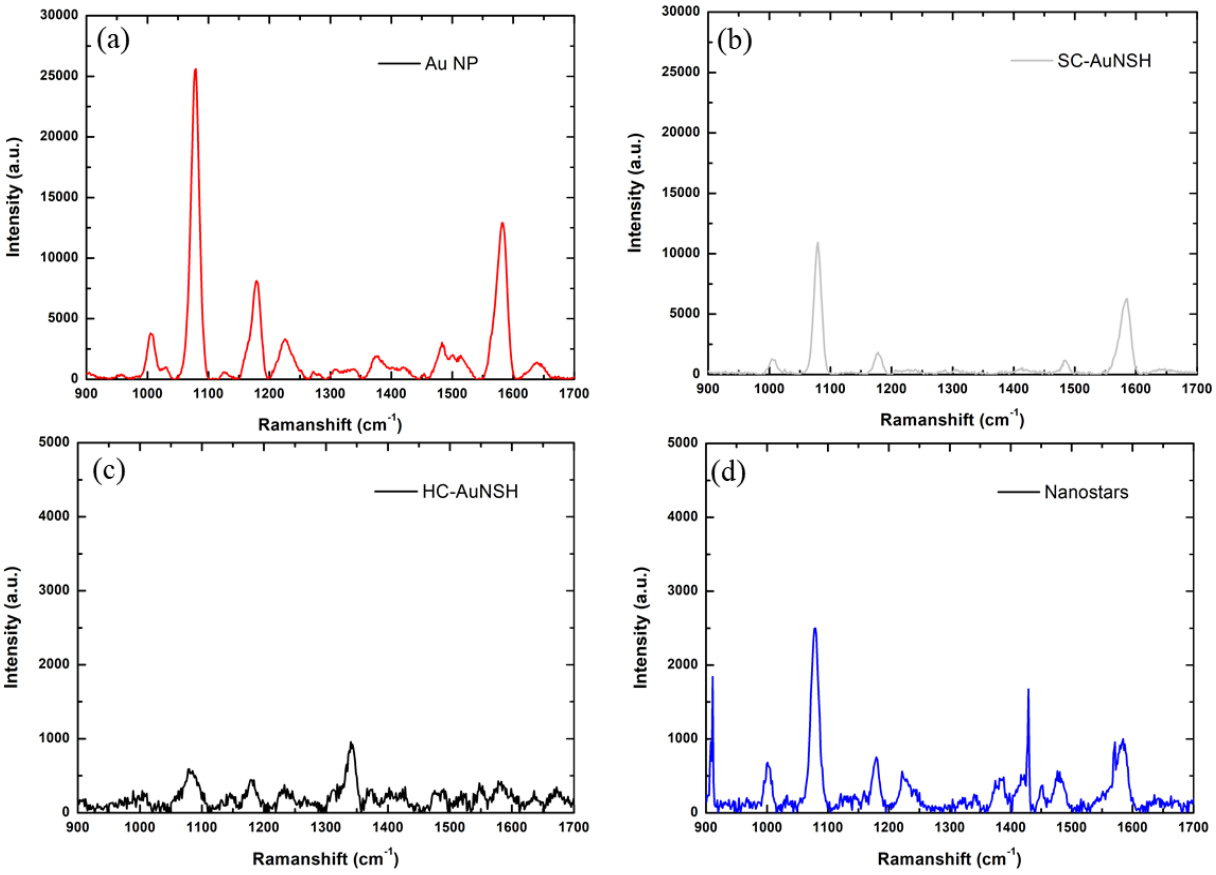

Figure 86 Averaged SERS signal of 1 mM of ATP using 3.5 µm-PCFs functionalized with (a) Au NP , (b) SC-AuNSH, (c) HC-AuNSH and (d) Nanostars.

The results of this experiment are shown in figure 86. The Au NPs continue to give the maximum of the SERS signal compared to the other NPs. In addition, figure 87 summarize the intensity of the Raman peak of 1080 cm^{-1} of ATP molecule. The error bars represent the SD across ten measurements for each NP. The SERS intensity with Au NP is 2.3 times higher than the intensity given by the SC-Nanoshell, and 10.4 times higher than the signal obtained from Nanostars. It is noteworthy that these results align with the previous results obtained with the injected configuration. There is no notable SERS intensity

obtained with HC-AuNSH which confirm that the light is highly absorbed when the NPs are anchored inside the fiber or they are not well anchored inside the fiber.

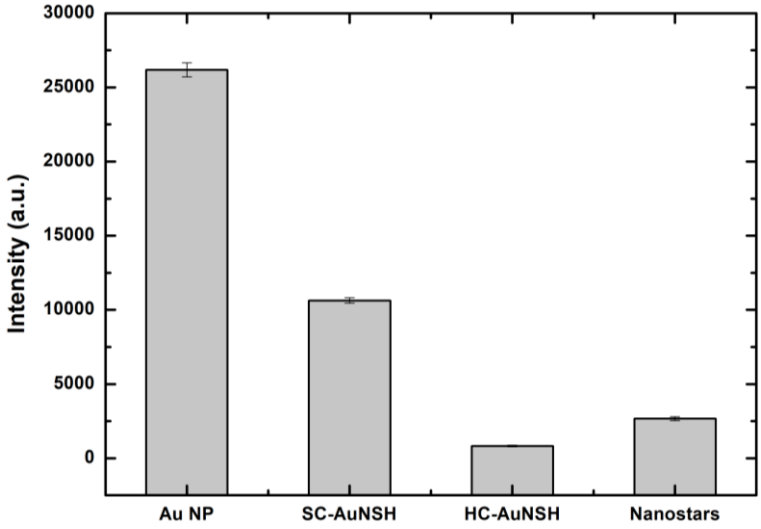

Figure 87 SERS intensity at 1080 cm^{-1} of 1 mM ATP with 3.5 µm-PCF functionalized with different NPs using anchored configuration. The error bars represent the standard deviation across ten measurements

Despite the varying LSPR peaks observed in different types of NPs, such as Nanostars (at 857 nm), HC-AuNSH (at 800 nm), and SC-AuNSH (at 770 nm), our experimental findings consistently demonstrate that Au NPs exhibit superior SERS enhancement. This intriguing result suggests that factors beyond the LSPR peak position play a crucial role in determining the efficacy of SERS enhancement. To investigate deeper into this phenomenon, we will utilize numerical simulations to study the underlying mechanisms governing the SERS performance of Au NPs compared to other NPs. By elucidating the intricate interplay between NP morphology, electromagnetic field enhancement, and absorption efficiency, our simulations aim to explain the performance of the Au NPs in SERS compared to other NPs.

III.2.6. Numerical study of nanoparticles properties

III.2.6.1. Simulation

For the numerical simulation in this study, the FDTD method was employed. It is a powerful computational technique widely used for modeling electromagnetic wave propagation and interactions with nanostructures. Using the Lumerical software, FDTD offers a robust framework for simulating complex optical phenomena with high accuracy and efficiency. This method discretizes Maxwell's equations into finite differences in space and time, allowing for the direct numerical solution of electromagnetic field distributions in three–dimensional space [179]. By incorporating material properties, geometric features, and boundary conditions, FDTD simulations enable the comprehensive analysis of light-matter interactions, including absorption, scattering, and field enhancement effects, at nanoscale resolutions [180].

In this simulation, the RI of gold is modeled according to the Au (Gold) data from Johnson and Christy [181]. The Johnson and Christy model provides experimentally measured values for the complex RI of gold (n - ik) across a broad spectral range. This data is crucial for accurately representing the optical behavior of gold NPs in simulations. The real part of the RI (n) indicates how much the light is slowed down in the material, while the imaginary part (k) accounts for the absorption losses within the material.

By incorporating these values, our simulations can precisely capture the intricate interactions between light and gold NPs, allowing to explore how these interactions influence the SERS performance.

III.2.6.2. FDTD simulation of Au NPs and comparison with the Mie theory

The Mie theory is employed to compare the FDTD simulation results of Au NP in term of absorption spectrum with theoretical predictions from the Mie theory which allow to evaluate the accuracy and reliability of the FDTD simulations in modeling NP interactions with light. The absorption spectrum of different Au NPs with diameter ranging from 20 nm to 120 nm are shown in figure 88. The results are in good agreements.

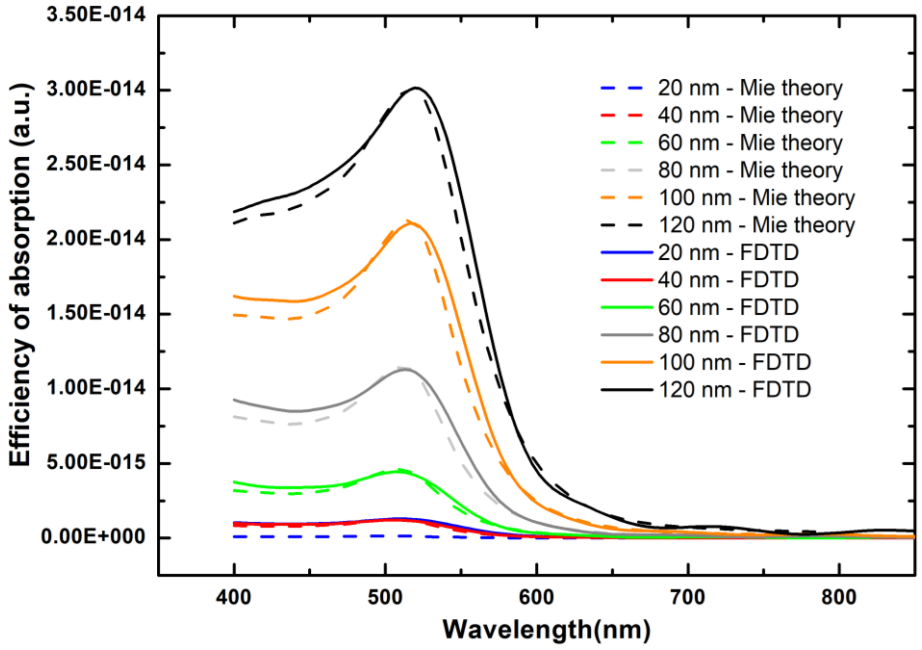

Figure 88 Absorption spectrum for Au NPs with different diameter obtained with FDTD method and Mie theory.

This consistency between the FDTD simulation results and the Mie theory confirms the validity and accuracy of this simulation method for predicting the optical properties of gold NPs across different sizes.

III.2.6.3. Limitation of the FDTD method

In the FDTD method, the mesh plays a crucial role in defining the spatial resolution and accuracy of the results. It refers to a discretized grid or network of computational elements that cover the simulation domain. FDTD simulations commonly used for modeling NP interactions with light, the mesh divides the simulation space into small volumetric cells. Each cell represents a discrete point in space where the properties of the electromagnetic field are calculated. In our case, a finer mesh allows for more precise representation of the NP geometry and electromagnetic field distributions, thereby yielding more accurate predictions. Using a large mesh will create a sphere with a stair-like shape, causing unwanted electromagnetic field localization at the edges. However, increasing the mesh resolution comes with computational costs. For example, a mesh of 1 nm for modeling a sphere larger than 60 nm, can significantly increase the computational load because of the substantial increase in the number of mesh elements necessary to finely discretize in 3D the simulation domain. As a result, the time required for

processing such simulations becomes prohibitively high, posing a practical limitation on the feasibility of employing extremely fine meshes.

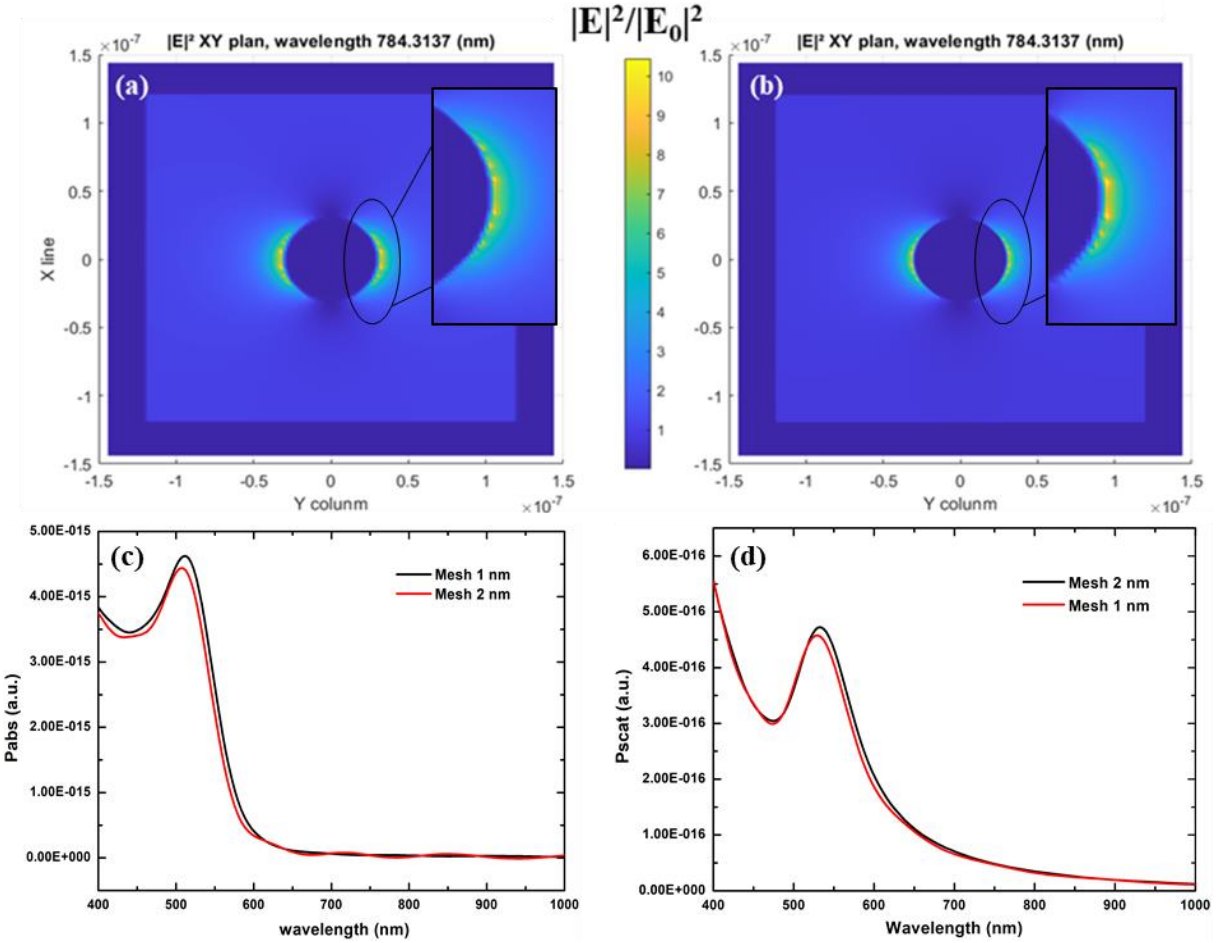

Figure 89 Electric field distribution at XY plan for Au NP at 785 nm using (a) a mesh of 1 nm (Mesh 1) and (b) a mesh of 2 nm (Mesh 2). (c) Absorption spectrum and (d) Scattering spectrum for Au NP using Mesh 1 and 2. The inset pictures shows the pixelating effect obtained with mesh 1 and mesh 2.

The electric field distribution at the XY plane of the Au NP at 785 nm is presented in figure 89(a) and 89(b) using a mesh of 1 nm and 2 nm, respectively. While there is a small difference between the two cases, the 1 nm mesh shows a slightly higher electric field at the surface of the NP compared to the 2 nm mesh. The inset images show the pixelating effect generated by the two meshes. A larger mesh can cause a pixelated effect, where hotspots appear as distinct blocky areas because fine details can't be modeled accurately. Finer mesh provides higher spatial resolution, allowing for a more accurate representation of the NPs geometry and surface features and reduces the pixelation effect, allowing for a more precise depiction of electric field distributions. The absorption and scattering spectra are presented in figure 89(c) and 89(d); they were obtained from simulations using both mesh sizes for Au NP. This result provides insights into the impact of the mesh on these properties. It is shown from the figures that the position of the absorption and the scattering peaks are in the same position for both meshes. Nevertheless, there is a slight variation in amplitude, especially at the maximum of the spectrum. However, notably, at the wavelength of 785 nm, the two spectra coincide, indicating that there is no significant difference between the results obtained using the two mesh sizes in terms of absorption and scattering properties.

The electric field distribution is examined at x=0 for an Au NP along the y-axis over a spectral range is shown in figure 90(a) and the variation of the electric field intensity using mesh 1 and 2 is shown in figure 90(b). Interestingly, it was found that mesh 1 exhibits a higher peak intensity compared to mesh 2, with a difference of 7.5 a.u. . However, at the laser wavelength of 785 nm, less difference between the two meshes was observed (2.56 a.u.). This suggests that while the choice of mesh size can influence the maximum intensity of the electric field enhancement, its impact may vary at different wavelengths. Overall, this comparison emphasizes the importance of the definition of the mesh size to achieve precise and dependable simulation outcomes. Notably, minimal discrepancies were observed despite the utilization of mesh size 2, indicating that even with this mesh, simulation results remain consistent and reliable.

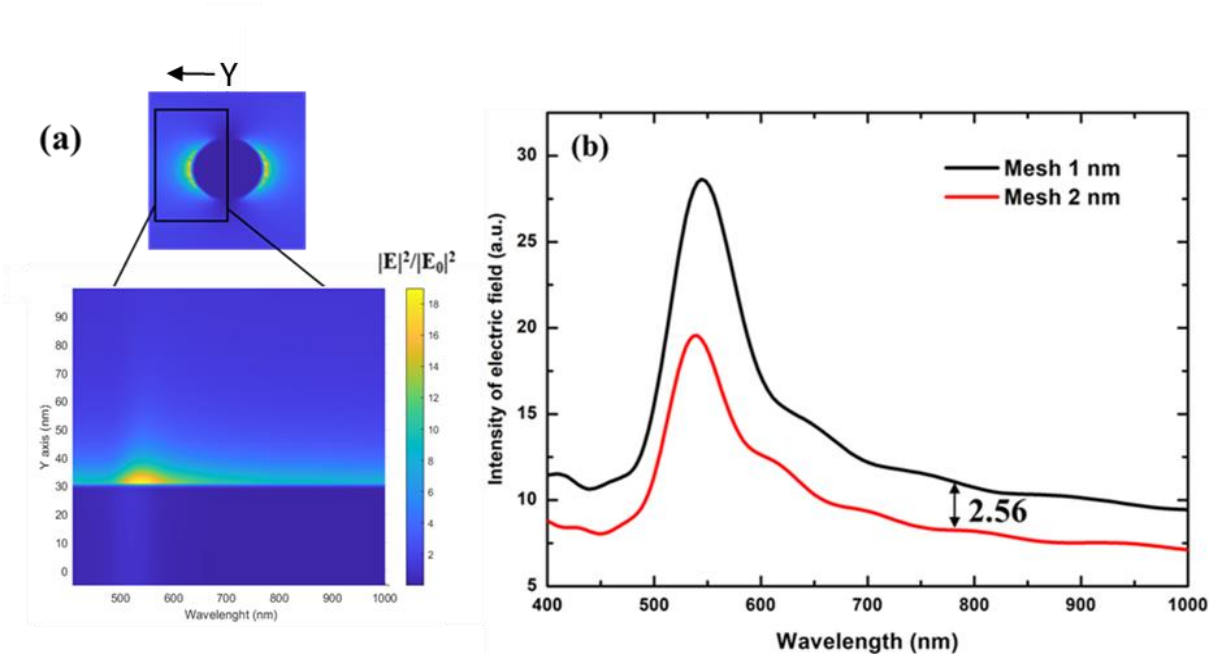

Figure 90 (a) electric field distribution at x=0 for Au NP. (b) Variation of the electric field intensity in the surface of the Au NP using mesh 1 and 2.

III.2.6.4. Electric field localization near the surface of Au NPs with different diameter

In this section, the evaluation of the intensity of the electric field in the surface of the Au NPs with different diameter is realized. The objective is to determine the impact of the NP size on the enhancement of the electric field around the NP, where the molecules to be analyzed are localized. For that, we simulated Au NP from 20 nm to 120 nm. In this study, we decided to work with a mesh size of 2 nm to strike a balance between accuracy and computational efficiency. Figure 91(a) represents the zoom-in the electric field distribution near to the NP. The arrow in the figure indicates the distance from the NP in which the electric field intensity is calculated and plotted in the figure 91(b). This point was selected because the NP surface at this location is flat, eliminating any hot spot effects induced by pixelating effect.

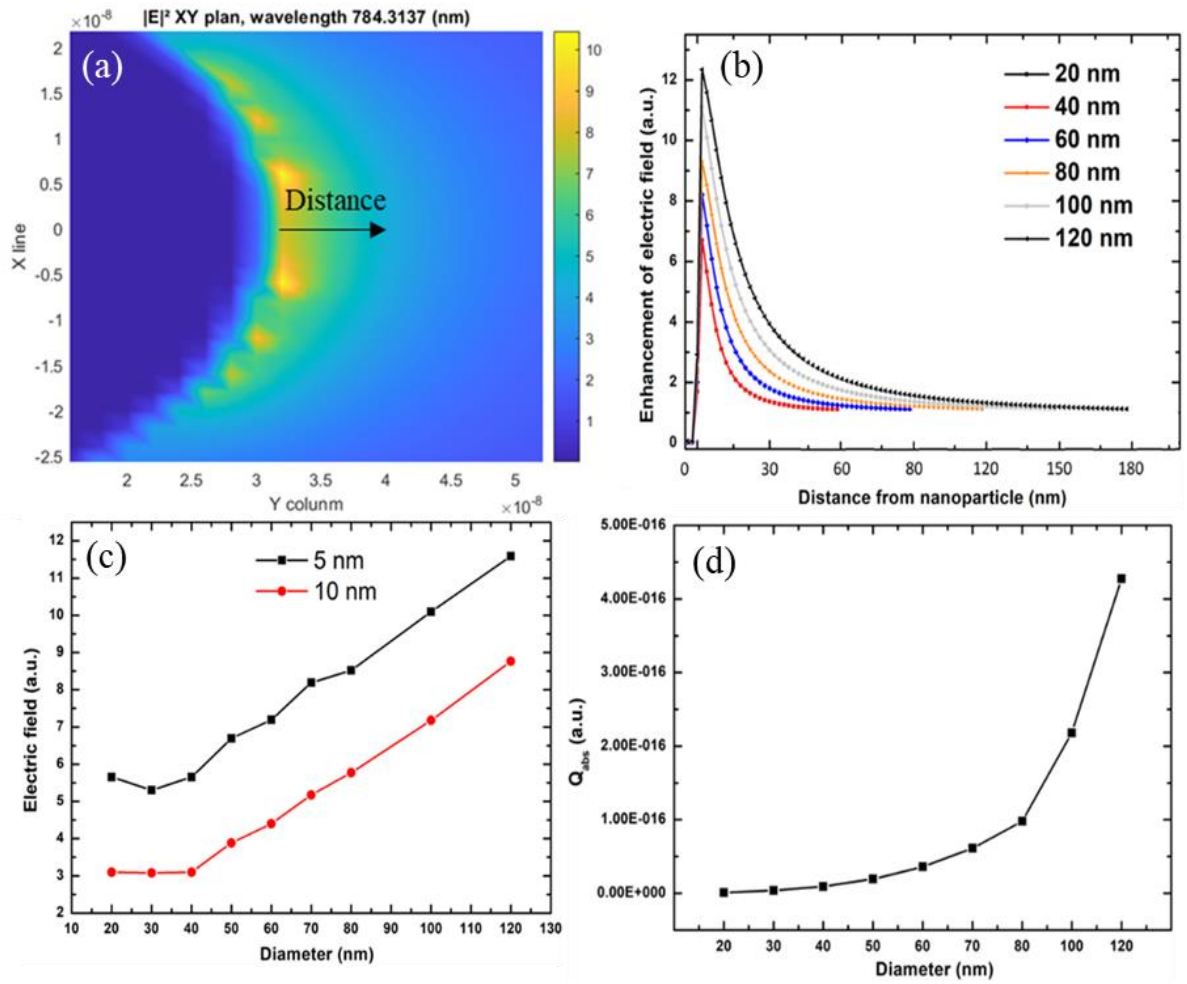

Figure 91 (a) Zoom-in of the electric field distribution near to the NP. The arrow indicates the axis and its origin line in which the intensity of electric field is calculated. (b) Variation of the electric field intensity at 785 nm with distance from the surface of the NP for different diameters. (c) Variation of the electric field intensity at 5 and 10 nm from the surface of the NP for different diameters at 785 nm. (d) The absorption coefficient variation at 785 nm for each Au NP using Mie theory

An interesting trend is noticed in this figure. As the NP diameter increases, the electric field intensity also increases. This observation aligns with our expectations, as larger NPs generally exhibit stronger plasmonic effects due to their larger surface area and higher scattering and absorption cross-sections. In figure 91(c) this relationship is explored by depicting the variation of the electric field intensity versus the NP diameter at distances of 5 and 10 nm from the NP surface. It shows that as the diameter of the nanospheres increases, the electric field enhancement shows an overall increasing trend. For instance, at a diameter of 20 nm, $|E|^2$ is approximately 5.65 a.u, while at 120 nm, it reaches 11.58 a.u. This increases in the electric field enhancement with the size is due to the larger surface area available for plasmon resonance, which facilitates larger field localization. This enhancement does not scale linearly with the particle size. In contrast, as presented in figure 91(d), the absorption efficiency also increases with particle size, but with a steeper slope. For a diameter of 20 nm, Q_{abs} is 1.05 10^{-18} a.u., while for 120 nm, it is 4.27 10^{-16} a.u. The rapid increase in Q_{abs} with size is indicative of greater radiative damping and scattering losses in larger particles. This implies that although larger NPs can support stronger electric fields, they also suffer from higher energy losses due to absorption.

This finding is particularly significant considering our use of 785 nm as an excitation wavelength for SERS. The absorption efficiency at this wavelength directly influences the extent of electromagnetic field enhancement and, consequently, the SERS EF. Therefore, the lower absorption efficiency of 60 nm gold nanospheres at 785 nm compared to larger NPs suggests the potential for enhanced SERS performance due to reduce light absorption. This underscores the importance of considering not only the electric field enhancement but also the absorption properties of NP regarding SERS enhancement for specific excitation wavelengths. By understanding the interplay between NP size, electric field enhancement, and absorption efficiency, one can optimize SERS performance to achieve enhanced sensitivity.

III.2.6.5. Electromagnetic properties of different nanoparticles

In order to understand the SERS performances of SC-AuNSH and HC-AuNSH compared to Au NP, it is important to present the absorption and scattering proprieties of these two NPs also. The objective is to establish a correlation between the intensity of the electric field ($|E|^2$) and the absorption efficiency (Q_{abs}) to elucidate why 60 nm gold nanospheres exhibit higher SERS intensities than other shapes of NPs.

- **Silica-Core gold Nanoshell**

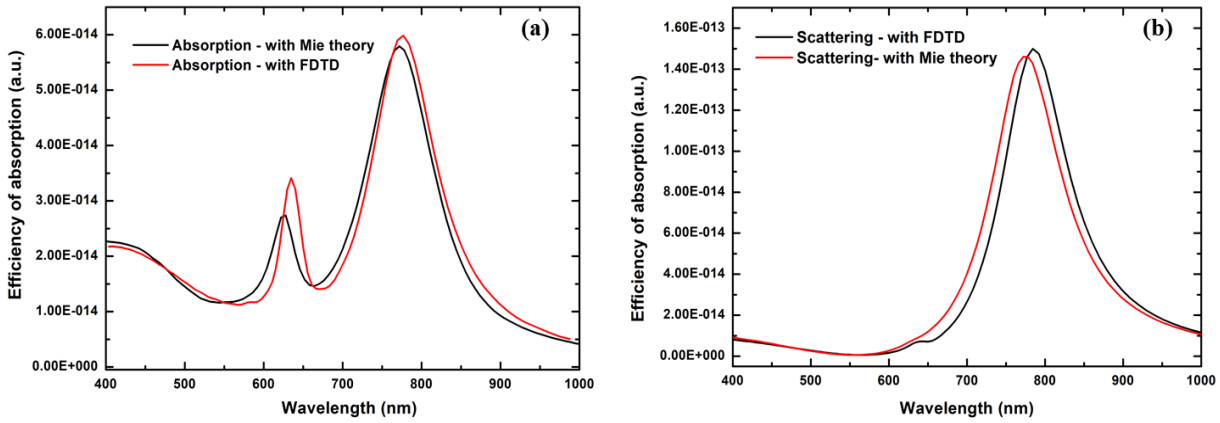

Figure 92 Absorption spectrum of SC-AuNSH given by (a) the FDTD numerical simulation and (b) Mie theory. Scattering spectrum of SC-AuNSH given by (a) the FDTD numerical simulation and (b) Mie theory.

To determine the thickness of the gold shell for various SC-AuNSHs, we used the Mie theory calculator from NanoComposix. Given that the LSPR peak is at 770 nm (figure 78(b)), the corresponding shell thickness was approximately 9 nm, which was then used in the simulation. As a proof of the accuracy of the simulation method, there is no remarkable difference between the absorption and scattering spectra obtained by the FDTD method and the Mie theory for SC-AuNSHs (figure 92). At the LSPR resonance wavelength and at 785 nm, the electric field distribution is presented in figure 93(a) and 93(b) in order to compare the distribution of the electric field around the NP. No difference is noticed from the figure suggesting that at 785 nm, the electric field intensity still important especially near to the NP. In this simulation, a mesh of 4 nm was used in order to have a relatively short time of simulation. In addition, the electric field distribution at x=0 for SC-AuNSH is shown in figure 93(c). It is noticed that there is a confined part of the electric field inside the NP. This is due to the difference of the dielectric constant of the silica core compared to the surrounding medium. This difference causes light to be

partially trapped and concentrated within the core due to internal reflection and refraction at the core-shell interface.

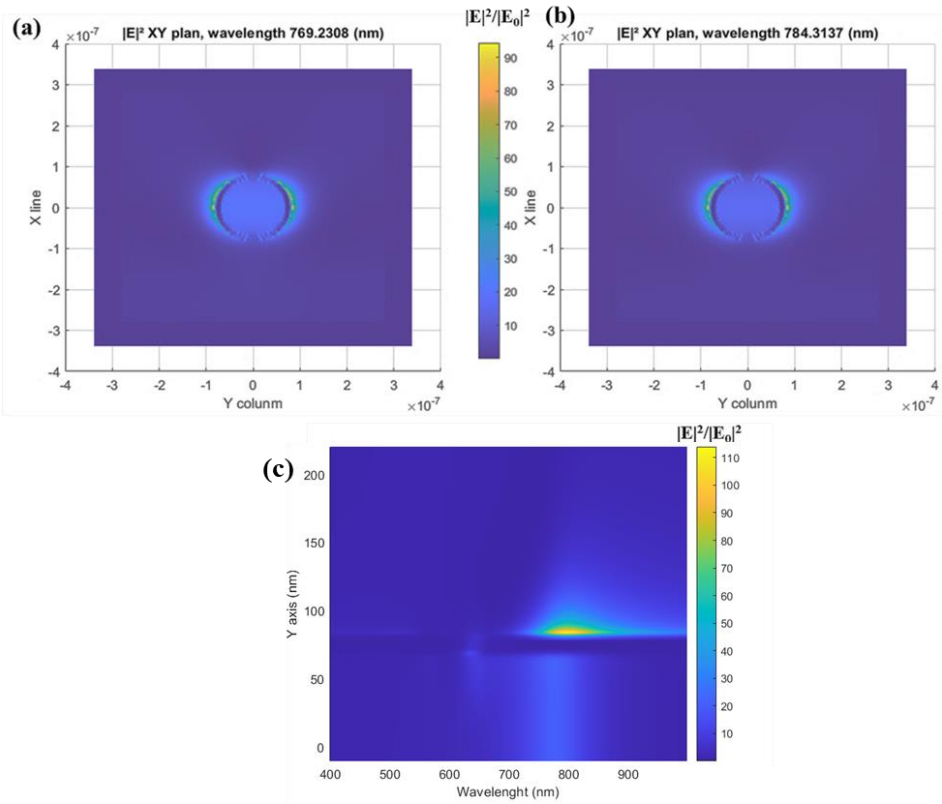

Figure 93 Electric field distribution on the XY plan for SC-AuNSH at (a) the LSPR wavelength and (b) at 785 nm. (c) Electric field distribution at x=0 for SC-AuNSH on the wavelength range (400 nm – 1000 nm).

The variation of the electric field intensity ($|E|^2$) with distance from the SC-AuNSH is presented in figure 94. It is noticed that there is a confinement of electric field inside the NP. Additionally, the electric field intensity gradually increases, peaking near the surface, which indicates a strong localized electric field. Beyond this point, the intensity drops significantly as the distance from the NP increases, showing a reduction in the localized field.

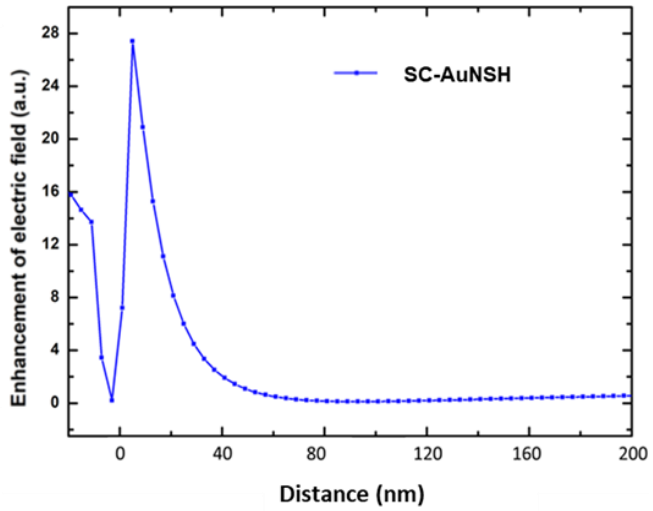

Figure 94 Variation of $|E|^2$ with distance from NP surface for SC-AuNSH at 785 nm.

- **Hollow-Core gold Nanoshell**

The absorption and scattering spectrum of HC-AuNSH are presented in figure 95. It shows the spectra obtained using FDTD simulation and Mie theory. A slight difference is noticed in the absorption spectrum given by the FDTD method and the Mie theory in term of absorption peak position. The FDTD gave a 580 nm of absorption peak. Nevertheless, good agreement between the absorption and scattering curves are obtained.

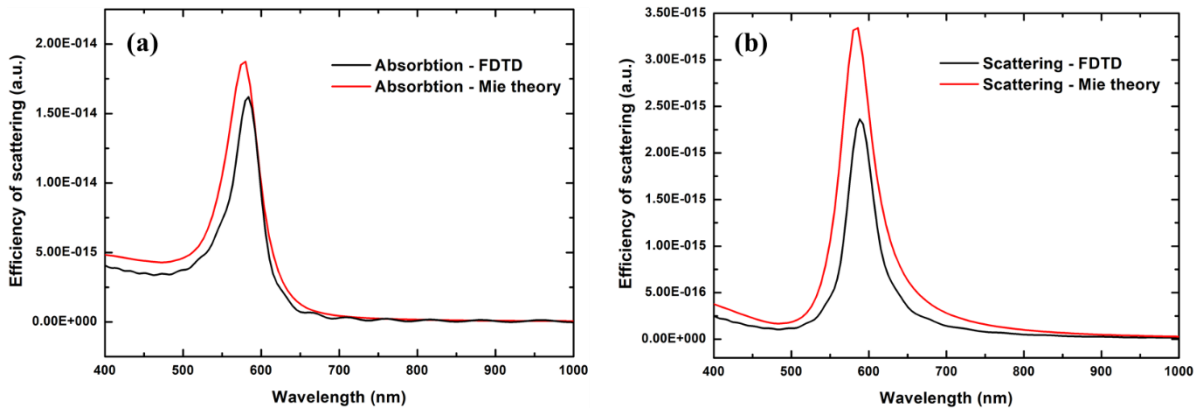

Figure 95 Absorption spectrum of HC-AuNSH given by (a) the FDTD numerical simulation and (b) Mie theory. Scattering spectrum of HC-AuNSH given by (a) the FDTD numerical simulation and (b) Mie theory.

The distribution of the electric field around the HC-AuNSH is presented at the resonance wavelength of 580 nm (figure 96(a)) and at 785 nm (figure 96(b)). A slight difference between the two cases in term of the electric field distribution near to the surface of the NP is observed, the amplitude of the electric field at 789 nm is lower than at the resonance wavelength, which is expected. In the figure 96(c), the electric field distribution at x=0 is shown, in this case also the electric field is larger in the resonance region than at 785 nm, where the intensity is decreased.

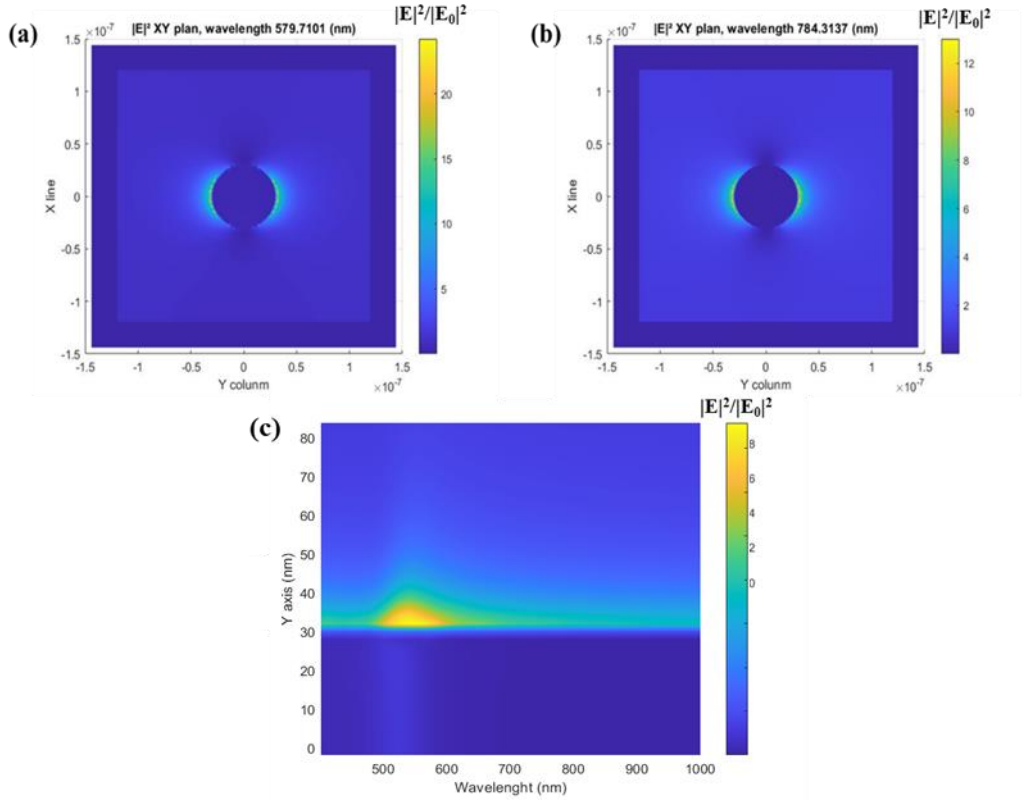

Figure 96 Electric field distribution at XY plan for HC-AuNSH at (a) LSPR wavelength and (b) 785 nm. (c) Electric field distribution at x=0 for HC-AuNSH.

The variation of the electric field intensity with distance from the NP for HC-AuNSH is presented in figure 97. In opposite to the SC-AuNSH, there is no values of the intensity confined inside the NP. It is noticed that the SC-AuNSH exhibits higher intensity levels compared to the HC-AuNSH across various distances from the NP.

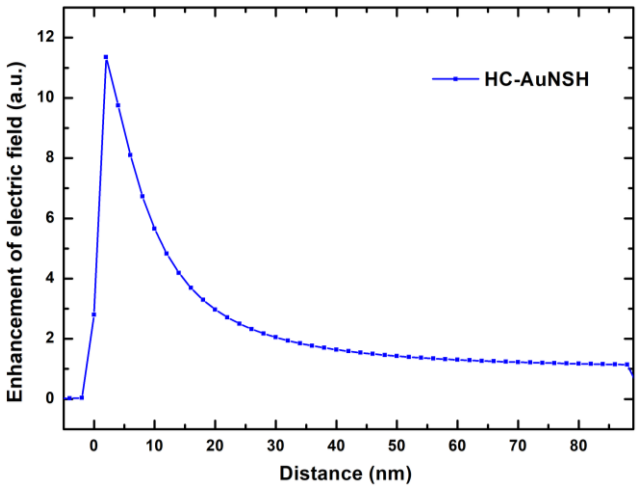

Figure 97 Variation of $|E|^2$ with distance from NP for SC-AuNSH, at 785 nm.

III.2.6.6. Correlation between absorption factor and Electric field intensity

To explain why 60 nm gold nanospheres outperform other NPs in SERS, the ratio $|E|^2/Q_{abs}$ could offer some information about the interplay between the enhancement form the electric field localization and the absorption of the incident light. Interpreting this ratio involves considering how effectively the NP

enhances the electric field relative to its ability to absorb incident light. A higher value for $|E|^2/Q_{abs}$ suggests that the NP produces a stronger electric field relative to the amount of incident light absorbed. Conversely, a lower value indicates that the electric field enhancement is less pronounced compared to its absorption efficiency.

Analyzing the results shown in figure 98 of the ratio $|E|^2/Q_{abs}$ for Au NP with different diameter, at a distance of 5 nm from the NP, reveals interesting insights. The ratio decreases with the increasing of the diameter of the Au NPs. For instance, at 20 nm, this ratio is 5.39 10^{18} a.u. at a distance of 5 nm from the particle, while at 120 nm, it decreases to 2.7 10^{16} a.u. This decreasing is due to the increasing in absorption losses compared to the electric field enhancement. This result suggests that smaller NP diameter might be more efficient than larger ones.

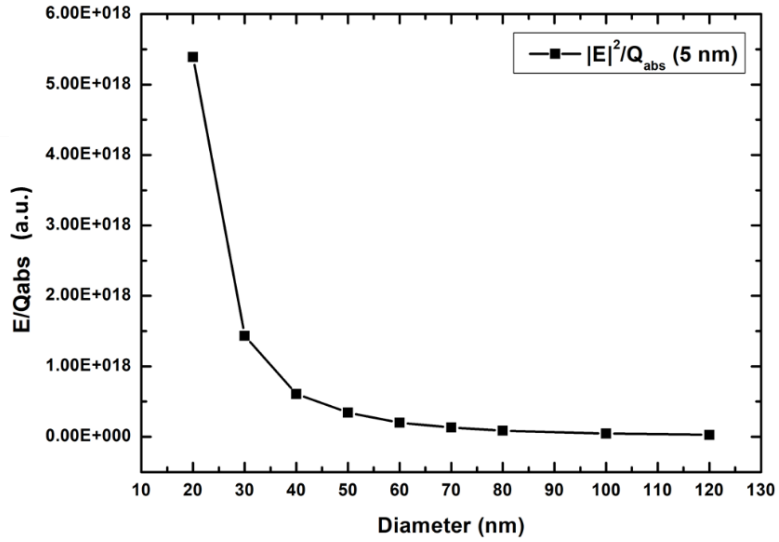

Figure 98 Variation of the ratio $|E|^2/Q_{abs}$ at 5 nm from NP and at 785 nm for different gold nanospheres.

Table 3 Comparison of the ratio $|E|^2/Q_{abs}$ at 785 nm between the 60 nm Au NP, SC-AuNSH and HC-AuNSH.

NP	Qabs (a.u.)	|E|2 / Qabs (a.u.) at 5 nm	|E|2 / Qabs (a.u.) at 10 nm
SC-NSH	3.94 10^{-14}	6.95 10^{14}	5.28 10^{14}
HC-NSH	4.98 10^{-17}	1.96 10^{17}	1.13 10^{17}
60 nm Nanospheres	6.12 10^{-18}	1.17 10^{18}	7.17 10^{17}

In table 3, comparing the ratio $|E|^2/Q_{abs}$ between the 60 nm Au NP, SC-AuNSH and HC-AuNSH further reinforces the superiority of the Au NP. At both 5 nm and 10 nm from the NP, the 60 nm Au NP exhibits significantly higher ratio values compared to the other two NP configurations. This indicates the efficiency in enhancing the electric field relative to the amount of incident light absorbed for Au NP, suggesting its superior potential for SERS measurements. However, it is important to note that for HC-AuNSH, no absorption peak was observed in the previous transmission experiments and when SERS experiments were conducted with the anchored configuration, low signal is detected with injected configuration while almost no signal was detected with anchored configuration. As a result, we cannot make a definitive comparison between HC-AuNSH and the other NP. It is possible that the anchored configuration does not adequately fix the HC-AuNSHs inside the fiber, which could explain the lack of observed signals. We will pursue further studies using Nanospheres from the same company with similar

coating but with different diameters. This will help us evaluate and validate the findings of this study more thoroughly.

III.2.7. Conclusion

In this chapter, the investigation of SERS performance of different NPs was realized illustrating the relationship between NP properties and SERS signal enhancement. Our findings reveal that the most efficient NP do not have λ_{LSPR} close to λ_{exc} . Additionally, our investigation into various factors affecting SERS intensity such as the NP concentration, fiber length and NP shape highlights the superiority of 60 nm Au Nanospheres, which consistently provide the best SERS performance compared to other NP shapes. This study represents the first investigation of the plasmonic properties of NPs anchored within fibers and their impact on SERS intensity. Notably, anchoring the NPs inside the fiber prevents aggregation and eliminates any shift in the LSPR peak, ensuring consistent SERS performance.

Numerical simulations employing the FDTD method provided valuable insights into the electromagnetic properties of NPs. The correlation between electric field intensity and absorption efficiency elucidates why certain NPs, such as 60 nm Au NP, outperform others in SERS enhancement. Additionally, our analysis emphasizes the necessity of complementing these findings with further experiments, particularly those involving Nanospheres of different diameters, to gain a more comprehensive understanding of their behavior. Overall, this comprehensive analysis not only deepens our understanding of SERS mechanisms but also lays the groundwork for optimizing SERS techniques for diverse applications, including biosensing and medical diagnostics. Further research in this area promises to unlock new possibilities for leveraging SERS in sensitive and precise analytical methods.

Chapter IV. Biosensing applications using SuC-PCFs

Chapter IV. Biosensing applications using SuC-PCFs

In this chapter, we aim to illustrate the advantages of using SuC-PCF for detecting biological molecules. In the first part, we will explore the efficiency of detecting disease biomarkers in saliva using Raman-based SuC-PCF sensor compared to the planar substrates that suffer from the limited interaction area and unreliable Raman measurements. This study was realized during a stay at Tyndal institute (Cork, Ireland) where a Raman setup is developed and used to enhance the Raman signal performance using SuC-PCF compared to conventional planar substrates. In the second part, we will introduce a sandwich-based SERS method used for protein detection for the first time within SuC-PCF, which highlight the efficiency and potential of SuC-PCF in biosensing.

IV.1. Disease biomarkers detection in liquid saliva by Raman spectroscopy using an opto-fluidic fiber

IV.1.1. Study context

The biophotonics team in Tyndall institute of research (at Cork, in Ireland) [182] is conducting a project on the detection of oral cancer biomarkers in saliva. Oral cancer often originates from painless white or red patches in the oral cavity. Over 90% of oral malignancies are squamous cell carcinomas, originating from the epithelial cells on the surface of the oral cavity [183]. Survival rates are highly dependent on the stage of the cancer at the time of diagnosis [184]. The rates range from 80 % for early stage cancer (I/II) to 30-50% in advanced stage cancer (III or IV) [183]. At present, the standard method for diagnosing oral cancer involves histopathological analysis of a biopsy sample taken from the tumor location. This biopsy procedure can be invasive and uncomfortable, often necessitating general anesthesia. The major limit is the impracticality of biopsying every potentially premalignant intraoral lesion.

Testing saliva for the diagnosis of oral cancers is highly attractive. It provides a convenient, cost-effective, and non-invasive alternative to blood tests and tissue biopsies. Saliva is composed of approximately 98% water, along with enzymes, electrolytes, minerals, and proteins… Its composition can reflect the overall health of the body, making it a potentially highly effective diagnostic tool for various diseases, especially those affecting the oral cavity. Previous research indicates that saliva is a more effective diagnostic medium for early-stage oral cancer compared to plasma, due to its direct contact with the pathology site [185]. Conversely, serum can be a valuable diagnostic specimen for advanced stages of oral cancer [186]. It is important to highlight that a key distinguishing factor between healthy tissue and various stages of malignancy is the alteration in concentrations of proteins, lipids, and nucleic acids in the epithelium, along with reduced collagen levels and inflammation in the connective tissue [187].

In this context, the biophotonics team at Tyndall is exploring Raman spectroscopy of saliva as a suitable method for distinguishing between non-malignant and early-stage malignant lesions (such as mouth ulcers or sores). This approach aims to enhance early detection of these lesions. As noted, Raman spectroscopy offers several benefits over traditional methods, including lower cost, faster results, greater objectivity, higher sensitivity, painlessness, and ease of use in a clinical setting for real-time diagnosis. For that, it is necessary to detect biochemical changes in bodily fluids and assist in biopsy; among the bodily liquids used for cancer detection is saliva [188]. The biophotonics team has developed a Raman spectroscopy setup for analyzing pellets. Figure 99(a) depicts a setup featuring a spectrometer, a 785 nm wavelength laser for excitation, and a visible light source used for sample visualization, all linked through optical fibers, filters (laser cleaning bandpass filter (BP), long pass filter (LPF)) and dichroic mirrors (DM1, DM2) for isolating the Raman signal. This setup is used in backscattering configuration.

The Raman scattered from the sample passes through the same objective lens used for the excitation and filtered by the dichroic mirror (DM2) and the long pass filter LPF [189]. The specimen can be deposited in a planar substrate and can be illuminated through an objective lens by the white light that is scattered from the sample and collected by the color camera.

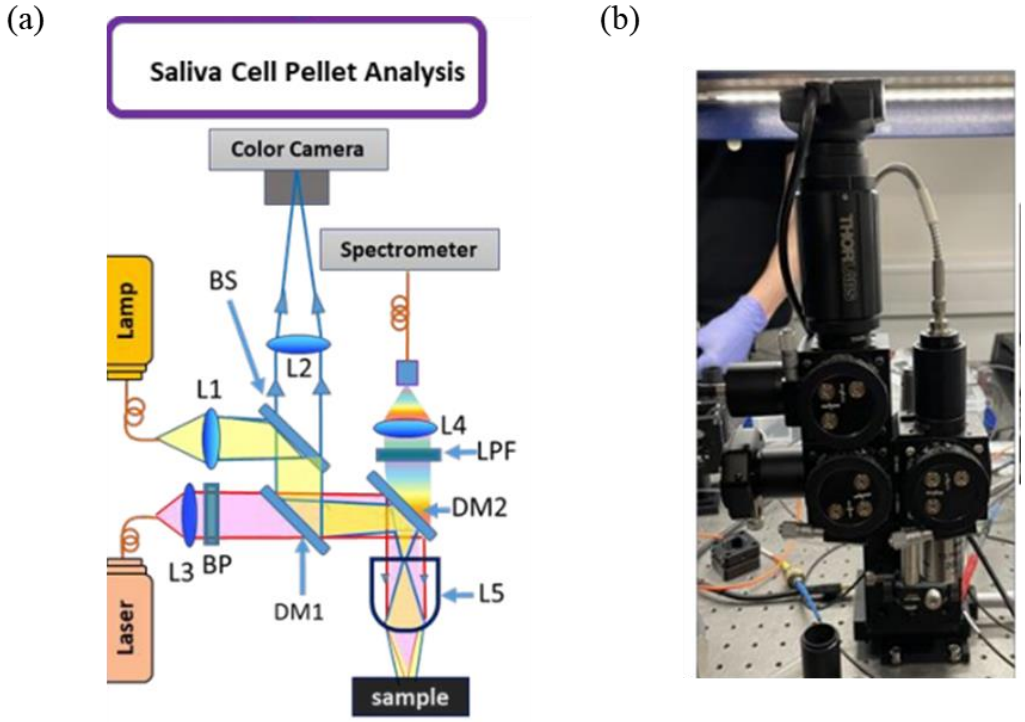

Figure 99 (a) Illustration of the customized upright Raman microscope in combination with optical microscopy. (b) Picture of the built setup. Setup developed by the biophotonics team at Tyndall [189].

The saliva samples obtained from human participants were centrifuged at 10,000 rpm for 10 minutes at room temperature to separate the cell pellets (including cheek and red blood cells) from the supernatant. For saliva sample analysis, 3 drops (~ 10 µL) of saliva supernatant was placed and dried on a piece of aluminum foil for Raman measurements. The team conducted a study for detection of disease biomarkers in saliva, figure 100(a) shows the Raman spectra (measured by the Biophotonics team) from saliva samples in both dried and liquid forms. Additionally, the cheek and red blood cells from the cell pellet were spread onto aluminum foil to obtain Raman spectra from a single cell layer, as depicted in Figures 100(b) and 100(c). When the sample is in liquid form, the spectrum do not show any features, but when the sample is dried it exhibits distinct peaks. The peaks around 1003 cm^{-1}, 1040 cm^{-1} are assignable to the symmetric ring breathing mode of phenylalanine and the C–C stretching vibration of lipids, respectively. In addition, well-known Raman bands characteristic of the Amide-I vibration of salivary proteins are also discernible around 1639 cm^{-1} to 1670 cm^{-1}.

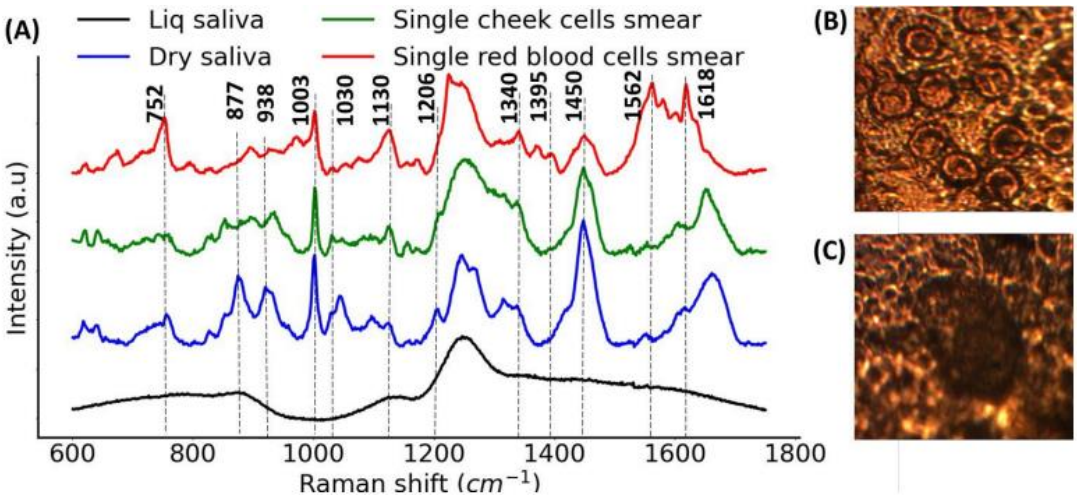

Figure 100 (a) Pre-processed Raman spectra from saliva specimen in liquid and dry form. Right-optical microscope view of (b) Red blood cells (c) Smeared cheek cell on aluminum foil. Study realized by Tyndall [189].

The biomarkers in the saliva liquid (shown as the black curve in figure 100(a)) are not detected due to typically weak signals and significant background interference. Consequently, most studies have focused on dried saliva samples to concentrate the analytes, as saliva is a complex mixture containing proteins, enzymes, and electrolytes... By drying it, water and some volatile substances are removed, concentrating the targeted molecules and reducing the relative intensity of background signals. Nevertheless, the drying process leads to the structural changes of the analytes (proteins), in addition, it is not compatible with fast detection. Additionally, in this system, a focal length of tens of microns limits the interaction of laser light with the sample, which affects the sensitivity of the measurements and requires increasing the integration time to tens of seconds. In order to overcome these limitations, the Raman spectroscopy using SuC-PCF can be used to improve the sensitivity and to detect directly the biomarkers signal in the liquid form of saliva. In the following section, we will describe the setup developed during a one-month research stay at the Tyndall Institute to conduct experimental and comparative between the customized Raman microscopy using planar substrate setups and the free-space Raman setup using SuC-PCFs. Additionally, we will showcase the results obtained from these experiments, highlighting the advantages of SuC-PCFs in improving Raman signal detection.

IV.1.2. Investigation of Raman spectroscopy of liquid saliva with an opto-fluidic fiber

IV.1.2.1. Setup developed at Tyndall institute

During my stay at Tyndall institute, we built a Raman spectroscopy setup similar to the one at XLIM. The objective is to be able to use our opto-fluidic fibers for sensing liquid saliva with the Raman spectrometer of Tyndall. The setup is presented in figure 101. A LED source (Thorlabs, M530L2 - Green (530 nm) Mounted High-Power LED, 1600 mA) was used to illuminate the cross-section of the fiber in order to visualize the fiber core and couple the laser into the core. This light is directed into the fiber via two beam splitters (8:92 (R:T) Pellicle Beam splitters, Uncoated: 400 - 2400 nm) and a dichroic mirror (DM) (785 nm laser BrightLine® single-edge laser dichroic beamsplitter). The LED light scattered from the cross-section of the fiber was redirected by the same objects into the color camera (Thorlabs

CS165MU/M - Zelux® 1.6 MP Monochrome CMOS Camera, M6 Taps) through a lens L2 (Thorlabs, AC254-100-AB-ML - f = 100.0 mm).

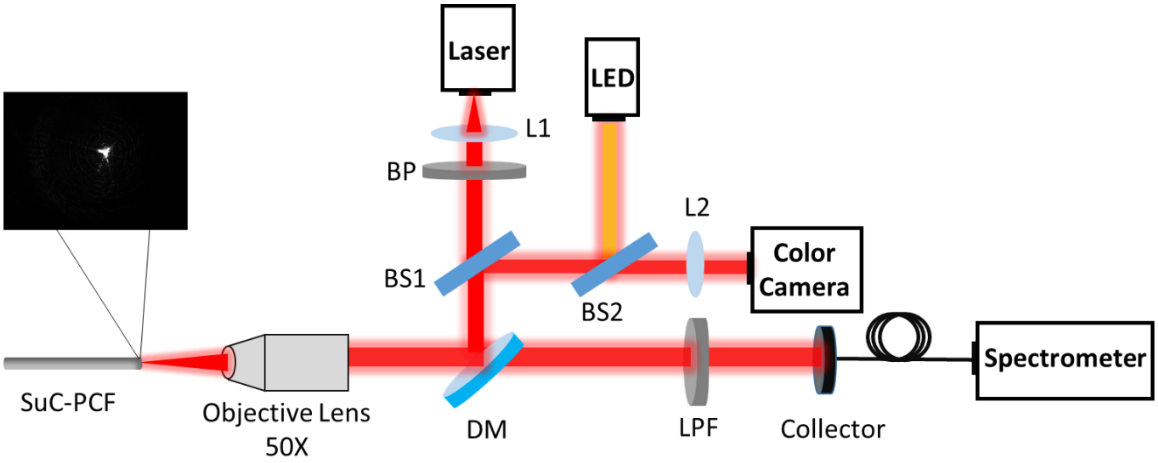

Figure 101 Setup developed during my stay in Tyndall instate for Raman measurements using SuC-PCFs.

The laser used operates at a wavelength of 785 nm with an output power of 90 mW, featuring a wavelength-stabilized laser diode pigtailed with a SMFs and integrated optical isolator for minimizing back reflection (I0783SH0090BX-IS-TH-L-USB), it passes through the lens L1 (f = 45 mm) and a laser cleaning bandpass filter BP (Semrock LD01-785/10-25). Afterwards, the collimated excitation beam is reflected by DM and focused on the fiber core. A part of the laser light scattered from the cross-section of the fiber is going to the camera to visualize the laser on the fiber core and to ensure efficient light coupling. The Raman signal backscattered from the sample is directed into the spectrometer via the long pass filter (Semrock LP02-785RU-25 and analyzed by the Raman spectrometer (Teledyne Princeton Instruments Acton LS785, f/2), and a highly sensitive deep depleted CCD camera (Blaze: 400HR, Teledyne Princeton Instruments, and USA).

IV.1.2.2. Sample preparation

The PCFs were cleaned with the acetone via the syringe pump. For that, the acetone was pumped into the fiber for 3 minutes, then the acetone was removed from the fiber by pushing the air inside manually. After that, the saliva specimen was injected inside the fiber for 3 minutes and was left inside during the Raman measurements.

IV.1.2.3. Results

In this experiment, a laser power of 30 mW and an integration time of 7s were used. Three SuC-PCFs with different core sizes (2, 3 and 3.5 µm) and one tapered-SuC-PCF were employed. For each fiber an average of ten measurement is done to plot the final spectrum. The Raman spectrum of liquid saliva measured with the different SuC-PCFs and on an aluminum foil (in liquid or dried saliva) are shown in figure 102(a). We are particularly interested in the Raman peak at 1003 cm^{-1}, which corresponds to the symmetric ring breathing mode of phenylalanine, a key molecular vibration relevant to our analysis. In contrast with the measurements on the aluminum foil, the use of SuC-PCFs allow the detection of this Raman peak in liquid saliva. A zoom-in of the Raman spectrum around this peak is plotted in figure 102(b), after applying a baseline correction. The amplitude of this peak is larger with the fibers than with the aluminum foil. The measures done with the 3µm -PCF, the Raman peak of 1003 cm^{-1} is 2.5 time more intense than the same Raman peak obtained by the dried saliva deposited in the aluminum foil.

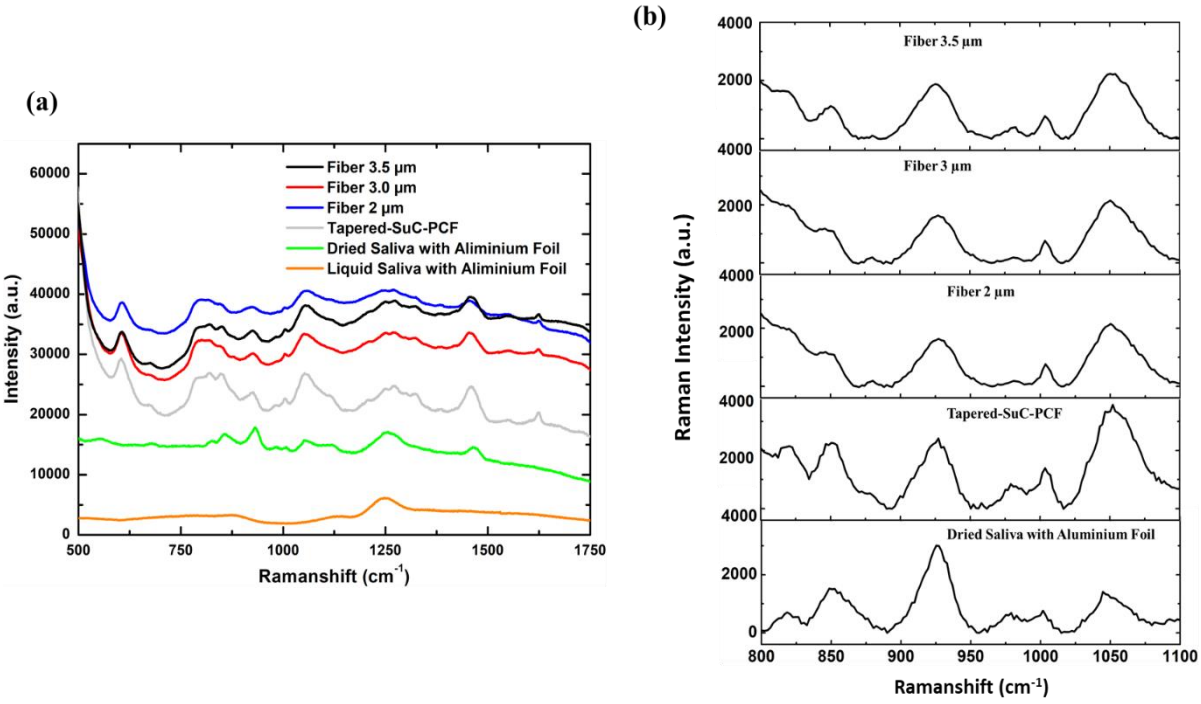

Figure 102 (a) Raman spectra of benign saliva, measured with a SuC-PCF of a core diameter of 3.5 µm (black curve), 3 µm (red curve), 2 µm (blue curve), Tapered-SuC-PCF (grey curve) and on an aluminum foil (dried form (yellow curve) and liquid form (orange curve). (b) Subfigures showing theses Raman spectra around the Raman peak at 1003 cm^{-1} (with a baseline correction).

Table 4 Measured average Raman intensity of saliva at 1003 cm^{-1}, along with the calculated average reproducibility and repeatability, for different fiber core sizes.

Fiber/	Average Raman intensity (a.u.)	Average RSD in reproducibility (a.u.)	RSD in repeatability (a.u.)
2 µm	560	16.34 %	14.92 %
3 µm	1063	10.83 %	12.62 %
3.5 µm	920	12.5 %	11.55 %
Taper	1309	4.4 %	---

Moreover, our investigation extends to the tapered-fiber, which demonstrate similar capabilities in enhancing saliva detection and signal amplification. This underscores the potential of both SuC-PCF and tapered fiber in improving the sensitivity of Raman signal for saliva-based diagnostics and beyond. In the table 4, the average RSD in reproducibility of the tapered-PCF was 4.4% showing excellent reproducibility obtained by the taper because of the larger core diameter in the excitation side. It is worth noting that during the experiment, we removed the fiber and we put it back again between each measurements. This confirmed the useful of our development towards an easy-to-use and efficient probe for Raman or SERS applications.

IV.2. Optofluidic fiber with sandwich-based SERS method

IV.2.1. Context

Biosensors provides vital information about the presence and quantify of a particular substance or diseases biomarker. They can be based on the use of a variety of different molecules including enzymes, DNA and antibodies. The most used bioreceptors in biosensors are antibodies. They are well adapted to this use because of their natural selectivity. Antibodies naturally select certain biomolecules, they are "Y" shaped proteins produced by plasma cells that are an essential part of the immune system. Antibodies identify pathogens by selectively binding to their ends [190]. Each antibody will only bind to one particular antigen.

One on the most known method used using antibodies is sandwich method. It is a highly specific and sensitive method used to detect the presence of proteins [191]. The assay is called "sandwich" because the target analyte (antigen) is in first captured on the sensor by an antibody and then detected by a second antibody (usually conjugated with a fluorophore or a Raman reported for signal emission). One of the most known technique that use sandwich method is ELISA technique. It is useful to detect low concentration of antigen that is sandwiched between two antibodies, and one of them is labelled with an enzyme [191]. This method was widely used in combination with SERS to detect cancer biomarkers (proteins). For SERS applications, the preparation of the immunosensors in the sandwich version consists of several stages. The first step consists in preparing the SERS active immunoprobe by attaching the detection antibody and Raman reporter into Au NPs. Then, the second step is based on the preparation of the SERS active substrates. In this step, the capture antibodies are deposited on the substrate and then the antigen is captured by these antibodies. The final step consists in forming the sandwich-based SERS immunosensor by linking the antigen with the NP functionalized with the detection antibody and the Raman reporter. These steps are presented in figure 103.

Several works have reported the use of sandwich-based SERS method for the determination of the prostate-specific antigen (PSA) which is prostate cancer biomarker [193]. For instance, Hong, W.-J *et al.* have investigated a sandwich-based SERS immunosensor based on using SERS substrate [194], they used the same steps explained in the figure 5 and they were able to detect PSA at very low levels (1 pg/mL) demonstrating good sensitivity and selectivity. In another work, Zhao Feng *et al.* detected PSA through the application of the same protocol but this time with Ag NPs, the sensor exhibited an extremely low LOD of 1.8 fg/mL [195]. In addition to protein detection, the sandwich-based SERS method is used also to detect leukemia virus [196], human epididymis protein 4 (HE4) which is a common biomarker for ovarian cancer diagnosis [197]. We can also cite the work done by Song *et al.* that have developed several immunosensors based on this method and were able to detect CEA a lung cancer biomarker [115]. They have also detected human IgG using glass slides functionalized with silver nanorods arrays (labeled with a Raman reporter, 4-MBA and antibody). Moreover, several works have been reported in the detection of DNA [113] (section I.3.3.2).

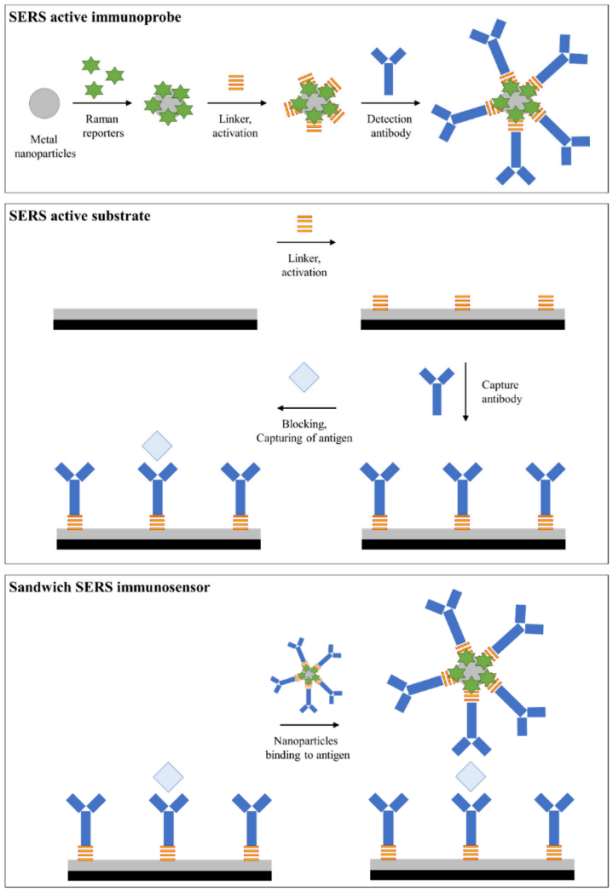

Figure 103 Diagram showing the steps for developing a sandwich-type SERS immunoassay: immunoprobe and substrate preparation and the immunosensor functioning. Reproduced from [192].

Sandwich-based SERS on traditional substrates provides significant signal enhancement. SERS fiber probes might offer more reliability of SERS measurements, flexibility, easier and simple use (ex. our plug-and-play system). Nevertheless, there is no reported work about the realization of the sandwich-based SERS in opto-fluidic fibers. Some works have been reported on the detection of protein using fibers. Dinish *et al.* used a commercial HC-PCF to detect EGFRs [161].

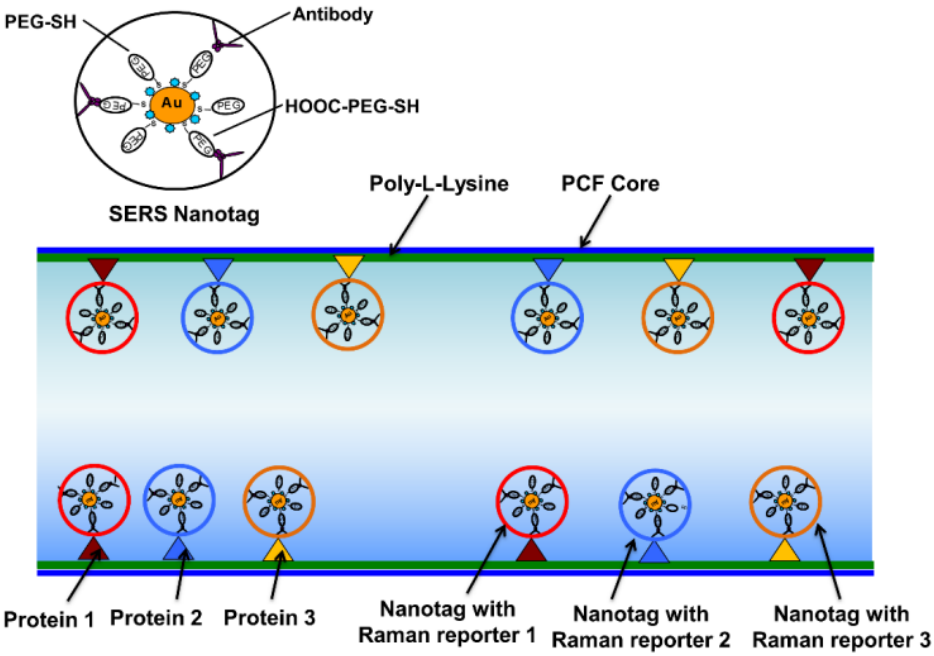

Figure 104 Top: Diagram of a SERS Nanotag, with small blue circles indicating the Raman reporters. bottom: illustration of multiplex detection within an HC-PCF using three Nanotags. Reproduced from [161].

To begin with, the authors treated 8 cm long HC-PCFs with poly-L-lysine, and then introduced a solution of cell lysate into the fiber. This allowed the protein (EGFR) to attach to the poly-L-lysine. Next, they developed a SERS nanotag by using 60 nm gold spheres, anchoring malachite green isothiocyanate (MGITC) and anti-EGFR antibodies to them, with MGITC being a widely recognized Raman reporter. Figure 104 displays a representation of the nanotags at the top. Following this, the fiber was filled with a solution containing the nanotags. The anti-EGFR antibodies on the nanotags successfully bound to the anchored proteins inside the fiber, enabling the detection of the MGITC signal. So that with this configuration, the protein is attached to the silica via a prior chemical preparation. The detection is carried out by injecting Au NPs functionalized with antibody.

Flavien *et al.* detected Haptoglobin (Hp), a biomarker of ovarian cancer, contained within ovarian cyst fluids using a SuC-PCF [151]. The high reliability in SERS measurements of the fiber probe allowed the identification of the cancer stages of the different samples. In this work, the NPs are anchored to the fiber and the Hp solution is then bind to the NPs via a prior chemical preparation. Then, Hp–antibodies conjugated with ATP molecules (Raman reporter) is injected into the fiber for immunodetection.

In the first method realized by Dinish *et al.*, the protein is attached to the silica via a prior chemical preparation, and the detection is performed by injecting Au NPs functionalized with antibodies. In the second method, the Au NPs are anchored within the fiber, and the protein is subsequently attached to the Au NPs via a prior chemical preparation as well. A key limitation in both methods is the necessity to bind the antigen into the NPs or the fiber via a prior chemical preparation of the antigen. In other hand, the advantage of the sandwich method is the capture of the antigen by an antibody without prior chemical preparation of the antigen.

In this study, we aim to develop sandwich-based SERS method within a SuC-PCF. For that, we have selected the Tumor necrosis factor (TNF-alpha) antigen and its antibody, as they are both commercially available. TNF-alpha is a well-studied biomarker that plays a crucial role in mammalian immunity and cellular homeostasis [198]. It is a key indicator for monitoring various human diseases, including inflammatory disorders such as bowel disease [199], osteoarthritis [200] as well as malignant tumors such as oral and breast cancer [201].

In our study, the NPs and the capture antibodies were firstly injected inside the fiber (the NPs bind to the fiber and the capture antibody is then attached to the NPs), then the antigen is injected and bind to the capture antibody before injecting the detection antibody conjugated with the Raman reporter (ATP) as shown in figure 105. The protocol will be detailed in the following. The advantage of this configuration is that the fibers could be functionalized in advance and all we have to do is just to inject the bio-fluid then the conjugated detection antibodies with Raman reporters that could be prepared already in advance.

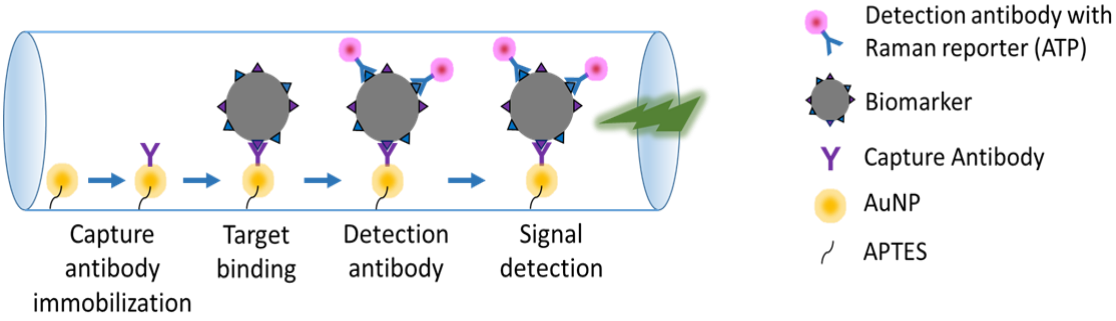

Figure 105 Representation of the sandwich-based SERS immunoassay using fibers based on the use of antibodies and Raman markers.

IV.2.2. Protocol of sandwich-based SERS immuno-detection of TNF-alpha into an SuC-PCF

Tumor necrosis factor-alpha (TNF-alpha) antigen powder and Monoclonal Anti-TNF antibody (0.1 mg/mL) were purchased from Sigma Aldrish, France. A solution of 0.5 mg/mL of TNF-alpha (antigen) was prepared and stored at -20 °C until their use.

The detection of TNF-alpha requires to attach the ATP molecules to TNF-alpha antibodies (TNF-alpha-AB). The carboxylic group in the antibody was activated using N-hydroxysuccinimide (NHS) (Thermo Fisher) and 1-éthyl-3-(3-diméthylaminopropyl) carbodiimide) (EDC) (Thermo Fisher). Then a solution of 1 mM of ATP was added to the activated antibody in order to bind together. The mixture was subjected to centrifugation using a membrane filter to eliminate any excess unreacted ATP and antibodies.

In order to functionalize the SuC-PCF, several steps were done:

- First step consisted of functionalizing the fibers with the exactly same manner done as described in section (II.2.3), where the NPs are immobilized inside the fiber. The only parameter changed is the duration of injection. In this case, the APTES is injected for 30 minutes and the fiber left for 30 minutes. By doing this, APTES molecules have extended time to interact with the silica along the entire length of the fiber. Additionally, the NPs are injected for 30 minutes, followed by a 20-minute incubation period.
- After that, a concentration of 0.01 g/L of capture antibodies were injected inside the fiber for 30 minutes and the fiber was left for 10 minutes. At this step, the antibodies will be anchored into

the surface of the Au NPs. Then the fiber is rinsed using a Phosphate Buffered Saline (PBS) solution to remove the excess of antibodies.

- After that, a solution of 5 µg/L of TNF-alpha (287 nM) was injected for 30 minutes and left for 10 minutes before being rinsed with a PBS solution. At this stage, the antigens (TNF-alpha) are immobilized on the Au NPs inside the fiber via the capture antibodies.
- The final step consist in injecting the solution of AB-ATP (noted AB* in the following), so that the detection antibody binds to the captured TNF-alpha antigen forming the sandwich with the ATP as a Raman reporter. The injection was for 5 minutes and other 5 minutes for incubation. After that, the fiber was rinsed with PBS one last time successively and dried in order to remove the unbound AB* to the antigen. Figure 105 provides schematics illustrating the key steps and the structure of the anchored assembly.

IV.2.3. Results

Using the previously described setup (section II.1), we recorded the SERS spectrum of the SuC-PCF after each step to verify that the final signal originated from the presence of TNF-alpha-AB/ATP following the bonding of the AB* with the TNF-alpha molecules. A laser power of 10 mW and 60 s of integration time were used. The resulted spectrum is averaged over ten measurements (spectra).

The figure 106(a) illustrates the plotted spectra measured from the fiber with NPs combined with capture AB and with NPs combined with capture AB and the antigen TNF-alpha. It shows the absence of any Raman peaks from the AuNPs, the AB and the antigen. This is because TNF-alpha does not possess a clear and strong Raman spectrum. Figure 106(b) represent the spectrum obtained from the mixture NP+AB+TNF-alpha+AB* and shows intense peaks of ATP indicating the presence of the TNF-alpha. As a control sample, figure 106(c) represent the spectrum of the solution and NP+AB+AB*. It serves as a reference to compare and ensure the detection of the TNF-alpha since the ATP could bind to the NPs. We can clearly see the intensity difference between the control sample and the test sample. Very small peaks of ATP are present in the signature of the control sample due to the absence of TNF-alpha molecules and the presence of a low quantity of ATP attached to the AB* in the fiber. The peak at 1080 cm^{-1} is 80 times higher in the test sample compared to the control sample.

To ensure the ATP peak position remains consistent after each step, figure 107 illustrates the different spectra obtained in this study. It demonstrates that the ATP peaks are at the same position for both the detection and control samples, confirming the detection of TNF-alpha bound to the NPs containing the ATP molecule. It is worth to note that the concentration detected of TNF-alpha is 5 µg/L (287 nM) with a volume of mixture inside the fiber of only 1.13 µl. This small sample volume is highly advantageous for biodetection applications, as it allows for more efficient use of reagents and biological samples, significantly reducing waste and cost. Additionally, the ability to detect low concentrations of analytes within such a small volume increases sensitivity and minimizes sample preparation time, making the process more suitable for point-of-care diagnostics.

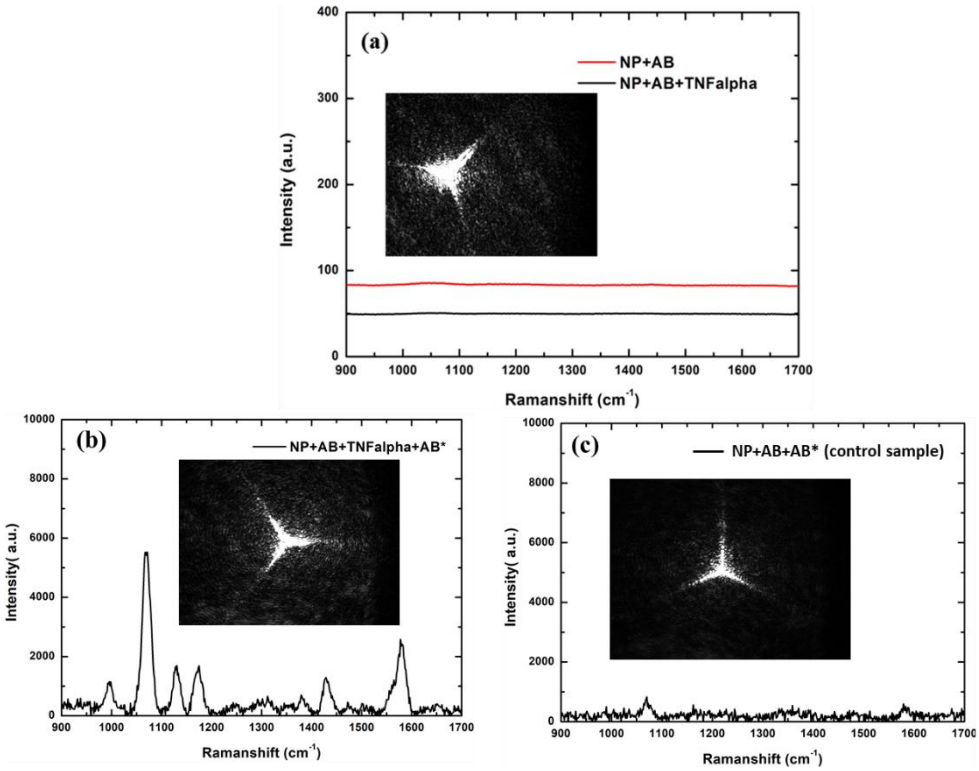

Figure 106 SERS spectra obtained from the fiber after adding (a) NP+AB and NP+AB+TNF-alpha, (b) NP+AB+TNF-alpha+AB* and (c) NP+AB+AB* as a control sample. All prominent peaks of ATP are observed. The inset in each figure represents a photo (acquired with a camera) of the focused laser on the input facet of a 3.5 µm-SuC-PCF. In (a) an offset has been added to each curve to facilitate the comparison.

As a perspective, we aim to use another form of control sample by employing a different antibody that does not bind to the antigen, or by using a different antigen to further validate our result. Additionally, the continuation of this study will involve evaluating the LOD of the antigen using sandwich-based SERS with SuC-PCFs.

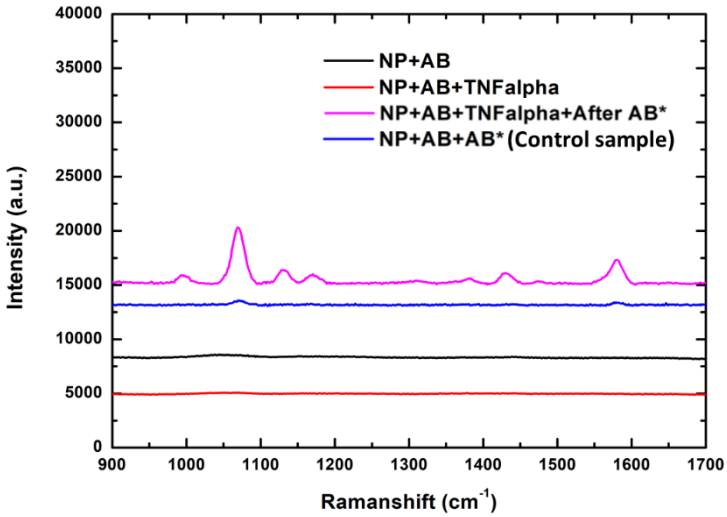

Figure 107 SERS spectra measured from the fiber after each different configurations using 3.5 µm-PCF. An offset has been added to each curve to facilitate the comparison.

In conclusion, we were able to detect TNF-alpha, which is a very known diseases biomarker. This represents the first demonstration of sandwich-based immunoassay in opto-fluidic fibers, also it opens the way to the possibility of realizing different other biosensing applications such as the detection of extracellular vesicles (EVs). The use of ABs for protein detection facilitates the capture of EVs. This capability is crucial for distinguishing between EVs from healthy or cancerous cells. These EVs can contain proteins, lipids, and genomic material that reveal the state of their cells of origin (figure 108). EVs produced by eukaryotic cells carry information specific to their originating cell type, for example EVs from healthy cells differing from those produced by cancerous cells. Additionally, the functionalized ABs within the fiber enable the specific attachment of EVs via surface proteins. Different conjugated ABs can target various proteins on EVs such as epidermal growth factor receptors (EGFR) [203], facilitating the detection and analysis of EVs derived from healthy cells versus those from cancerous cells.

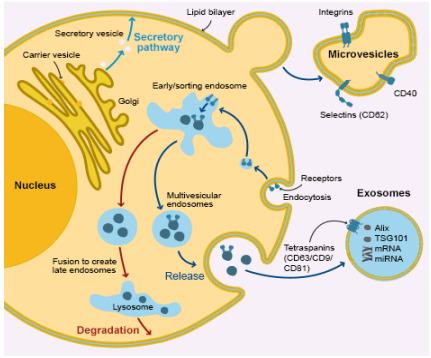

Figure 108 Diagram illustrating the formation of EVs [204].

However, the detection and isolation of EVs remain challenging, especially in body fluids such as blood, urine, and saliva, which contain a complex mixture of biomolecules including proteins, lipids, and other EVs. This complexity can introduce significant background noise in SERS measurements, complicating the differentiation of the specific SERS signal originating from EVs. Thus, the perspective is to detect EVs using SuC-PCFs, which can further underscore the significance of the sandwich-based SERS and the efficiency of SERS-based PCFs. This perspective work will be realized with colleagues from CAPTuR laboratory from Inserm, CHU Limoges, and the University of Limoges.

IV.2.4. Conclusion

In this chapter, two biodetection examples were presented in order to demonstrate the efficiency of the SERS-active SuC-PCFs. They were able to detect diseases biomarkers in saliva using a liquid saliva compared to aluminum foil substrate that was able to detect only with dried saliva. This study demonstrates for the first time the utility of the fibers in detecting body fluid biomarkers directly after collection from patients using Raman spectroscopy. This approach offers a sensitive, reliable, and fast biosensor, showcasing the significant role of fibers and tapering in Raman biodetection. For the second study, TNF-alpha detection using sandwich-based SERS for the first time was realized using SuC-PCF. The biomarker was detected with low concentration and within a very low volume of sample, which opens the way to perform more biodetection applications using opto-fluidic fibers. With this method, the measurement process is simplified into just two steps: first, the injection of the body fluid into the fiber, followed by the injection of the readout probe. This approach reduces complexity and enhances efficiency, making it ideal for rapid biosensing applications.

This study is a proof-of-concept since a more complete study is required in order to evaluate the reliability and also the correlation between the SERS intensity and the antigen concentration. Furthermore, it opens the way to the detection of EVs with SERS-active SuC-PCFs which represent the respective for this work.

Conclusion and Perspectives

General conclusion and Perspectives

This thesis explored the innovative application of SERS using PCFs as a powerful tool for biosensing and medical diagnostics. Unlike traditional tissue and liquid biopsies, which can be invasive, time-consuming, and sometimes unreliable, SERS offers a non-invasive alternative with enhanced sensitivity and specificity. By allowing for real-time analysis and detecting biomarkers at trace levels, SERS-based PCFs overcome many limitations associated with conventional biopsy techniques. Through a comprehensive examination of the design, fabrication, and performance of SERS-based PCFs, several key findings have emerged, highlighting the potential of this technology in sensitive and reliable biomarker detection.

We started in Chapter I by demonstrating the clear advantages of using PCFs over traditional planar SERS substrates that were often used in SERS applications. Unlike planar substrates, PCFs offer a significantly larger interaction surface and enhanced reliability, overcoming issues related to small surface irregularities and optical coupling variations. The cross-sectional design of PCFs facilitates the incorporation of liquids or gases, thereby enhancing the interaction between excitation light and analytes, leading to improved sensitivity. This capability allows for the detection of trace amounts of analytes, which is crucial for early disease diagnostics. Chapter II focused on the development of a SERS setup at XLIM, highlighting the performance gains with SuC-PCFs over traditional systems. Our experiments demonstrated how varying core sizes affected the evanescent field and light coupling efficiency, revealing that the 2 µm-PCF provided the highest SERS intensity and a LOD of 100 nM of ATP. However, it also had a higher RSD of 12%, indicating less reproducibility. In contrast, the 2 µm-PCF, while delivering the highest intensity, demonstrated the best sensitivity for SERS measurements. Conversely, the 3.5 µm-PCF, though providing lower intensity, achieved the highest reproducibility with an RSD of 4.5%, reflecting superior measurement consistency. Then, to optimize SERS performance, it is crucial to find a compromise between these characteristics: smaller core sizes enhance sensitivity but may impact reproducibility, whereas larger core sizes improve coupling efficiency and overall consistency. This balance was confirmed by simulations, which revealed that a core diameter of approximately 6 µm optimizes coupling efficiency between the fiber and the excitation laser and showed that while smaller core sizes improve SERS sensitivity, larger core sizes (6 µm) provide better coupling efficiency and overall measurement reliability. Therefore, future designs should consider this balance to achieve both high sensitivity and robust reproducibility in SERS-based PCFs. Thus, these insights led to the development of tapered-PCFs, which combine a larger core for efficient laser coupling with a smaller core for enhanced SERS sensitivity. Building on this concept, we focused on fabricating and optimizing Tapered-PCF. We detailed the stack-and-draw process used to create a 6 µm core SuC-PCF and its subsequent tapering. The tapered fibers demonstrated superior performance, achieving a remarkable 3.2% RSD variation in reproducibility and only 5% signal variation with a plug-and-play system. These advancements highlight the potential of tapered-PCFs for practical SERS applications, offering both improved performance and ease of use, particularly for biosensing applications such as analyzing body fluids.

In Chapter III, we delved into the relationship between NP properties and SERS signal enhancement. Through experimental investigation, we identified 60 nm Au Nanospheres as the most efficient NP shape, providing consistent and superior SERS performance. Our analysis demonstrated that anchoring NPs within the fibers prevents aggregation. This conclusion is supported by the observation that the LSPR peak for 60 nm Au nanospheres consistently remained at its expected position of approximately 540 nm. The lack of any significant shift in the LSPR peak, despite varying NP concentrations and fiber lengths, indicates that the NPs do not form aggregates within the fibers. This ensures that the NPs

maintain their plasmonic properties, which is crucial for reliable SERS performance. Numerical simulations using the FDTD method validated our experimental observations, revealing a direct link between electric field intensity and absorption efficiency. The FDTD simulations, supported by experimental results, demonstrated that while larger NPs can enhance the electric field more strongly, they also lead to higher absorption losses. Specifically, the ratio $|E|^2/Qabs$ decreases with increasing NP diameter, indicating that smaller NPs, such as the 60 nm gold nanospheres, offer superior electric field enhancement relative to absorption. This makes them particularly effective for SERS applications. In comparing different NPs, the 60 nm Au NPs consistently showed the highest ratio $|E|^2/Qabs$, outperforming SC-AuNSH and HC-AuNSH in terms of field enhancement per unit of absorbed light. This reinforces their effectiveness in SERS applications. In contrast, HC-AuNSH showed inconsistent results, likely due to issues with their configuration within the fiber, leading to poor signal detection. These findings highlight the importance of optimizing NP size for enhanced SERS performance. Further research involving different diameters and types of NPs is crucial for refining SERS technology, particularly for applications in biosensing and medical diagnostics. Such studies will provide deeper insights into the factors influencing SERS efficiency and help develop more effective analytical tools

Chapter IV discusses the application of SuC-PCFs in biosensing, specifically focusing on two experiments that utilize these fibers for detecting disease biomarkers. The first experiment illustrates the significant advantages of SuC-PCFs over traditional substrates like aluminum foil in Raman-based biosensing. Notably, SuC-PCFs were able to detect molecular vibrations, such as the phenylalanine peak, directly in liquid saliva samples, which was not possible with aluminum foil, which could only detect biomarkers in dried saliva. This experiment achieved a remarkable 2.5-fold increase in Raman peak intensity compared to using dried saliva on an aluminum foil substrate, highlighting the superior sensitivity and effectiveness of SuC-PCFs. The second experiment introduces a novel application of SuC-PCFs in the detection of TNF-alpha using a sandwich-based SERS method. This approach leverages the specificity of antibodies to capture and detect TNF-alpha, a key biomarker for diseases like inflammatory disorders and various cancers. The study outlines a detailed protocol for the detection process, where Au NPs and capture antibodies are introduced into the SuC-PCF, followed by the injection of the TNF-alpha antigen and detection antibodies conjugated with ATP as a Raman reporter. This method effectively identifies TNF-alpha at low concentrations (5 µg/L) within a minimal sample volume of 1.13 µL, demonstrating the high sensitivity and efficiency of SuC-PCFs for biomarker detection.

Despite recent progress in the field of SERS-based PCFs, several areas for further research and development are still available. An exciting development within this research is the taper/plug-and-play system designed for SERS sensing. This system utilizes a "bare fiber" connector (BFA Thorlabs) with an inner diameter of 850 nm, allowing for quick and easy connection without the need for complex alignment procedures. This setup enhances the practicality and user-friendliness of the system, potentially increasing the efficiency of SERS measurements in clinical and research settings. However, further refinement is necessary to address the technical mismatch in dimensions between the BFA system and the fiber, which can lead to inconsistencies in fiber core alignment. Resolving these issues will ensure consistent taper positioning for each sample, thereby improving the reliability and robustness of future measurements. The plug-and-play system holds promise as a cost-effective and user-friendly biosensor for practical biosensing applications.

The successful detection of TNF-alpha using SERS-active PCFs marks a significant advancement in opto-fluidic fiber technology and opens the door to broader applications, such as detecting EVs that are pivotal for differentiating between healthy and cancerous cells, offering promising prospects for early

diagnostics and personalized medicine. Future research will focus on expanding the application of SERS-based PCFs beyond TNF-alpha to include complex targets like EVs. To enhance the reliability and specificity of these detections, future work will include using control samples with antibodies that do not bind to the target antigen or alternative antigens, validating the effectiveness of the SERS-based method. Additionally, the research will explore the LOD for TNF-alpha using sandwich-based SERS with SuC-PCFs. Despite the challenges of background noise and complex molecular compositions in these matrices, SuC-PCFs have demonstrated high sensitivity and reliability, simplifying the biodetection process into an efficient two-step procedure. Collaboration with CAPTuR laboratory will further refine these technologies, advancing their practical diagnostic applications.

Bibliogphy

[1] A. B. E. Attia, S. Y. Chuah, D. Razansky, C. J. H. Ho, P. Malempati, U. S. Dinish, R. Bi, C. Y.Fu, S. J. Ford, J. S.-S. Lee, M. W. P. Tan, M. Olivo, and S. T. G. Thng, "Noninvasive real-time characterization of non-melanoma skin cancers with handheld optoacoustic probes," Photoacoustics 7, 20–26 (2017).

[2] C. J. H. Ho, Y. W. Yew, U. S. Dinish, A. H. Y. Kuan, M. K. W. Wong, R. Bi, K. Dev, X. Li, G. Singh, M. Moothanchery, J. Perumal, S. T. G. Thng, and M. Olivo, "Handheld confocal Raman spectroscopy (CRS) for objective assessment of skin barrier function and stratification of severity in atopic dermatitis (AD) patients," Journal of Dermatological Science 98(1), 20–25 (2020).

[3] T. Gong, Y. Cui, D. Goh, K. K. Voon, P. P. Shum, G. Humbert, J.-L. Auguste, X.-Q. Dinh, K.-T. Yong, and M. Olivo, "Highly sensitive SERS detection and quantification of sialic acid on single cell using photonic-crystal fiber with gold nanoparticles," Biosensors and Bioelectronics 64, 227–233 (2015). Rayleigh, J. W. S., "On the light from the sky, its polarization and colour" Philosophical Magazine, Series 5, Volume 41, Issue 269, pages 107-120 (1871).

[4] Rayleigh, J. W. S., "On the light from the sky, its polarization and colour" Philosophical Magazine, Series 5, Volume 41, Issue 269, pages 107-120 (1871).

[5] A. Smekal, "Zur Quantentheorie der Dispersion," Naturwissenschaften 11(43), 873–875 (1923).

[6] C. V. Raman and K. S. Krishnan, "A New Type of Secondary Radiation," Nature 121(3048), 501-502 (1928).

[7] Lily M. Ng and Reiko Simmons, "Infrared Spectroscopy," Anal. Chem. 1999, 71, 12, 343–350.

[8] David I. Ellis, David P. Cowcher, Lorna Ashton, Steve O'Hagan and Royston Goodacre, "Illuminating disease and enlightening biomedicine: Raman spectroscopy as a diagnostic tool", Royal society of chemistry, 2013, 138, 3871-3884.

[9] Catarina F. Araujo, Mariela M. Nolasco, Antonio M.P. Ribeiro, Paulo J.A. Ribeiro-Claro, "Identification of microplastics using Raman spectroscopy: Latest developments and future prospects", Volume 142, 1 October 2018, Pages 426-440.

[10] Misae Otoyama, Yusuke Ito, Akitoshi Hayashi, Masahiro Tatsumisago, "Raman imaging for LiCoO2 composite positive electrodes in all-solid-state lithium batteries using Li2S–P2S5 solid electrolytes", Volume 302, 20 January 2016, Pages 419-425.

[11] Meinhart C.D. et al, "Rapid detection of drugs and explosives for forensic analysis.", (2018). US Army RDECOM.

[12] María José González-Vázquez and Mathieu Hautefeuille, "Controlled Solvent-Free Formation of Embedded PDMS-Derived Carbon Nanodomains with Tunable Fluorescence Using Selective Laser Ablation with A Low-Power CD Laser.", Micromachines, 8. 307. (2017). M. P. Buric, K. P. Chen, J. Falk, and S. D. Woodruff, "Enhanced spontaneous Raman scattering and gas composition analysis using a photonic crystal fiber," Applied Optics 47(23), 4255–4261 (2008).

[13] M. P. Buric, K. P. Chen, J. Falk, and S. D. Woodruff, "Enhanced spontaneous Raman scattering and gas composition analysis using a photonic crystal fiber," Applied Optics 47(23), 4255–4261 (2008).

[14] R. Aroca, Surface-Enhanced Vibrational Spectroscopy, John Wiley & Sons, Ltd (2006).

[15] H. T. Ngo, H.-N. Wang, T. Burke, G. S. Ginsburg, and T. Vo-Dinh, "Multiplex detection of disease biomarkers using SERS molecular sentinel-on-chip," Analytical and Bioanalytical Chemistry 406(14), 3335–3344 (2014).

[16] M. Fleischmann, Hendra P.J, McQuillan A.J, " Raman spectra of pyridine adsorbed at a silver electrode", Volume 26, Issue 2, 15 May 1974, Pages 163-166.

[17] M. G. Albrecht and J. A. Creighton, "Anomalously intense Raman spectra of pyridine at a silver electrode," Journal of the American Chemical Society 99(15), 5215–5217 (1977).[18] avid L. Jeanmaire, Richard P. Van Duyne, " Surface raman spectroelectrochemistry: Part I. Heterocyclic, aromatic, and aliphatic amines adsorbed on the anodized silver electrode, " Journal of Electroanalytical Chemistry and Interfacial Electrochemistry, Volume 84, Issue 1,1977, Pages 1-20.

[18] Jeanmarie DL, Van Duyne RP. 1977. Surface Raman spectroelectrochemistry,part 1: heterocyclic, aromatic, and aliphatic amines adsorbed on the anodized silver electrode. J. Electroanal. Chem. 84:12

[19] Moskovits, Martin. "Surface roughness and the enhanced intensity of Raman scattering by molecules adsorbed on metals." Journal of Chemical Physics 69 (1978): 4159-4161.

[20] Tian, Zhong-Qun, et al. "Surface-Enhanced Raman Scattering: From Noble to Transition Metals and from Rough Surfaces to Ordered Nanostructures." The Journal of Physical Chemistry B, vol. 106, no. 37, 2002, pp. 9463–9483. American Chemical Society, doi:10.1021/jp0257449.[21] D. Pines, "Collective energy losses in solids," Review of Modern Physics 28(3), 184–199 (1956).

[21]Stiles PL, Dieringer JA, Shah NC, Van Duyne RP. Surface-enhanced Raman spectroscopy. Annu Rev Anal Chem (Palo Alto Calif). 2008;1:601-26. doi: 10.1146/annurev.anchem.1.031207.112814. PMID: 20636091.

[22] L. Tonks and I. Langmuir, "Oscillations in Ionized Gases," Physical Review 33, 195–211 (1929).

[23] Schatz, George C., and Richard P. Van Duyne. "Electromagnetic Mechanism of Surface-Enhanced Spectroscopy." Handbook of Vibrational Spectroscopy. Edited by John M. Chalmers and Peter R. Griffiths, vol. 1, Wiley, 2006, pp. 759-774. DOI: 10.1002/0470027320.s0601.

[24] U. Kreibig and M. Vollmer, Optical Properties of Metal Clusters, Springer-Verlag Berlin Heidelberg, Springer Series in Materials Science (1995), 25.

[25] Link S, El-Sayed MA. 1999. Spectral properties and relaxation dynamics of sur-face plasmon electronic oscillations in gold and silver nano-dots and nano-rods.J. Phys. Chem. B 103:8410–26.

[26] R. L. McCreery, Raman Spectroscopy for Chemical Analysis, John Wiley and Sons (2000), 157.

[27] D.-S. Wang and M. Kerker, "Enhanced Raman scattering by molecules adsorbed at the surface of colloidal spheroids," Physical Review B 24(4), 1777–1790 (1981).

[28] McFarland AD, Young MA, Dieringer JA, Van Duyne RP. 2005. Wavelength-scanned surface-enhanced Raman excitation spectroscopy. J. Phys. Chem. B109:11279–85.

[29] A. Otto, "The 'chemical' (electronic) contribution to surface-enhanced Raman scattering,"Journal of Raman Spectroscopy 36(6–7), 497–509 (2005).

[30] Kim, J.; Jang, Y.; Kim, N.–J.; Kim, H.; Yi, G.–C.; Shin, Y.; Kim, M.H.; Yoon, S. Study of chemical enhancement mechanism in nonplasmonic surface enhanced Raman spectroscopy (SERS). Front. Chem. 2019, 7, 582.

[31] R. Pilot, R. Signorini, C. Durante, L. Orian, M. Bhamidipati, L. Fabris, A Review on Surface-Enhanced Raman Scattering, Biosensors. 9 (2019). https://doi.org/10.3390/bios9020057.

[32] L. Jensen, C.M. Aikens, G.C. Schatz, Electronic structure methods for studying surface-enhanced Raman scattering, Chem. Soc. Rev. 37 (2008) 1061–1073. https://doi.org/10.1039/B706023H.

[33] K. Kneipp, Y. Wang, H. Kneipp, L.T. Perelman, I. Itzkan, R.R. Dasari, M.S. Feld, Single Molecule Detection Using Surface-Enhanced Raman Scattering (SERS), Phys. Rev. Lett. 78 (1997) 1667–1670. https://doi.org/10.1103/PhysRevLett.78.1667.

[34] K.L. Wustholz, C.L. Brosseau, F. Casadio, R.P.V. Duyne, Surface-enhanced Raman spectroscopy of dyes: from single molecules to the artists' canvas, Phys. Chem. Chem. Phys. 11 (2009) 7350–7359. https://doi.org/10.1039/B904733F.

[35] E. Le Ru, P. Etchegoin, Principles of Surface-Enhanced Raman Spectroscopy: and related plasmonic effects, Elsevier, 2008.

[36] E.D. Palik, Handbook of Optical Constants of Solids, Academic Press, 1998.

[37] West P.R., Ishii S., Naik G.V., Emani N.K., Shalaev V.M., Boltasseva A. Searching for better plasmonic materials. Laser Photonics Rev. 2010;4:795–808. doi: 10.1002/lpor.200900055.

[38] Cottancin E., Celep G., Lermé J., Pellarin M., Huntzinger J.R., Vialle J.L., Broyer M. Optical properties of noble metal clusters as a function of the size: Comparison between experiments and a semi-quantal theory. Theor. Chem. Acc. 2006;116:514–523. doi: 10.1007/s00214-006-0089-1.

[39] B. Sharma, R.R. Frontiera, A.-I. Henry, E. Ringe, R.P. Van Duyne, SERS: Materials, applications, and the future, Mater. Today.

[40] Jensen TR, Malinsky MD, Haynes CL, Van Duyne RP. 2000. Nanosphere lithography: tunable localized surface plasmon resonance spectra of silver nanoparticles. J. Phys. Chem. B 104:10549–

[41] hang X, Hicks EM, Zhao J, Schatz GC, Van Duyne RP. 2005. Electrochemical tuning of silver nanoparticles fabricated by nanosphere lithography. Nano Lett.5:1503–7.

[42] S. L. Kleinman, R. R. Frontiera, A.-I. Henry, J. A. Dieringer, and R. P. Van Duyne, "Creating,characterizing, and controlling chemistry with SERS hot spots," Phys. Chem. Chem. Phys. 15(1),21–36 (2013).

[43] Kreibig, U.; Vollmer, M.Optical Properties of Metal Clusters;Springer: New York, 1995; and references therein.

[44] E.S. Shibu, M. Hamada, N. Murase, V. Biju, Nanomaterials formulations for photothermal and photodynamic therapy of cancer, J. Photochem. Photobiol. C Photochem. Rev. 15 (2013) 53–72. https://doi.org/10.1016/j.jphotochemrev.2012.09.004.

[45] L. A. Dick, A. J. Haes, and R. P. Van Duyne, "Distance and Orientation Dependence of Heterogeneous Electron Transfer: A Surface-Enhanced Resonance Raman Scattering Study of Cytochrome c Bound to Carboxylic Acid Terminated Alkanethiols Adsorbed on Silver Electrodes," J. Phys. Chem. B 104(49), 11752–11762 (2000).

[46] M. B. Wabuyele and T. Vo-Dinh, "Detection of Human Immunodeficiency Virus Type 1 DNA Sequence Using Plasmonics Nanoprobes," Anal. Chem. 77(23), 7810–7815 (2005).

[47] Stiles P.L., Dieringer J.A., Shah N.C., Van Duyne R.P. Surface-Enhanced Raman Spectroscopy. Annu. Rev. Anal. Chem. 2008;1:601–626. doi: 10.1146/annurev.anchem.1.031207.112814.

[48] C. A. Murray and D. L. Allara, "Measurement of the molecule–silver separation dependence of surface enhanced Raman scattering in multilayered structures," The Journal of Chemical Physics 76(3), 1290–1303 (1982).

[49] J. A. Dieringer, A. D. McFarland, N. C. Shah, D. A. Stuart, A. V. Whitney, C. R. Yonzon, M. A. Young, X. Zhang, and R. P. Van Duyne, "Introductory Lecture Surface enhanced Raman spectroscopy: new materials, concepts, characterization tools, and applications," Faraday Discuss. 132(0), 9–26 (2006).

[50] Masango S.S., Hackler R.A., Large N., Henry A.I., McAnally M.O., Schatz G.C., Stair P.C., Van Duyne R.P. High-Resolution Distance Dependence Study of Surface-Enhanced Raman Scattering Enabled by Atomic Layer Deposition. Nano Lett. 2016;16:4251–4259. doi: 10.1021/acs.nanolett.6b01276.

[51] R. J. C. Brown and M. J. T. Milton, "Nanostructures and nanostructured substrates for surface enhanced Raman scattering (SERS)," J. Raman Spectrosc. 39(10), 1313.

[52] L. Wu, W. Wang, W. Zhang, H. Su, Q. Liu, J. Gu, T. Deng, and D. Zhang, "Highly sensitive, reproducible and uniform SERS substrates with a high density of three-dimensionally distributed hotspots: gyroid-structured Au periodic metallic materials," Npg Asia Materials 10, e462 (2018).

[53] akonen, A.; Rindzevicius, T.; Schmidt, M.S.; Andersson, P.O.; Juhlin, L.; Svedendahl, M.; Boisen, A.; Käll, M. Detection of nerve gases using surface-enhanced Raman scattering substrates with high droplet adhesion. Nanoscale 2016, 8, 1305–1308, doi:10.1039/c5nr06524k.

[54] Zheng, J.; He, L. Surface-Enhanced Raman Spectroscopy for the Chemical Analysis of Food. Compr. Rev. Food Sci. Food Saf. 2014, 13, 317–328, doi:10.1111/1541-4337.12062.

[55] T. C. Dakal, A. Kumar, R. S. Majumdar, and V. Yadav, "Mechanistic Basis of Antimicrobial Actions of Silver Nanoparticles," Front. Microbiol. 7, (2016).

[56] N. D. Israelsen, C. Hanson, and E. Vargis, "Nanoparticle Properties and Synthesis Effects on Surface-Enhanced Raman Scattering Enhancement Factor: An Introduction," The Scientific World Journal 2015, 124582 (2015).

[57] F. Benz, R. Chikkaraddy, A. Salmon, H. Ohadi, B. de Nijs, J. Mertens, C. Carnegie, R. W. Bowman, and J. J. Baumberg, "SERS of Individual Nanoparticles on a Mirror: Size Does Matter, but so Does Shape," J. Phys. Chem. Lett. 7(12), 2264–2269 (2016).

[58] S. Link and M. A. El-Sayed, "Size and Temperature Dependence of the Plasmon Absorption of Colloidal Gold Nanoparticles," J. Phys. Chem. B 103(21), 4212–4217 (1999).

[59] M. Fan, F.-J. Lai, H.-L. Chou, W.-T. Lu, B.-J. Hwang, and A. G. Brolo, "Surface-enhanced Raman scattering (SERS) from Au:Ag bimetallic nanoparticles: the effect of the molecular probe," Chem. Sci. 4(1), 509–515 (2013).

[60] M. J. Natan, "Concluding Remarks Surface enhanced Raman scattering," Faraday Discuss. 132(0), 321–328 (2006).

[61] J. F. Li, Y. F. Huang, Y. Ding, Z. L. Yang, S. B. Li, X. S. Zhou, F. R. Fan, W. Zhang, Z. Y. Zhou, D. Y. Wu, B. Ren, Z. L. Wang, and Z. Q. Tian, "Shell-isolated nanoparticle-enhanced Raman spectroscopy," Nature 464(7287), 392–395 (2010).

[62] Y.-C. Liu, K.-H. Yang, and S.-J. Yang, "Sonoelectrochemical synthesis of spike-like gold–silver alloy nanoparticles from bulk substrates and the application on surface-enhanced Raman scattering," Analytica Chimica Acta 572(2), 290–294 (2006).

[63] O. Péron, E. Rinnert, M. Lehaitre, P. Crassous, and C. Compère, "Detection of polycyclic aromatic hydrocarbon (PAH) compounds in artificial sea-water using surface-enhanced Raman scattering (SERS)," Talanta 79(2), 199–204 (2009).

[64] K. C. Grabar, R. G. Freeman, M. B. Hommer, and M. J. Natan, "Preparation and Characterization of Au Colloid Monolayers," Anal. Chem. 67(4), 735–743 (1995).

[65] Péron O., Rinnert E., Lehaitre M., Crassous P., Compère C. Detection of Polycyclic Aromatic Hydrocarbon (PAH) Compounds in Artificial Sea-Water using Surface-Enhanced Raman Scattering (SERS) Talanta. 2009;79:199–204. doi: 10.1016/j.talanta.2009.03.043.

[66] Fierro-Mercado, P.M.; Hernández-Rivera, S.P. Highly Sensitive Filter Paper Substrate for SERS Trace Explosives Detection. Int. J. Spectrosc. 2012, 2012, 716527. [CrossRef].

[67] Muniz-Miranda, M.; Gellini, C.; Giorgetti, E.; Margheri, G.; Marsili, P.; Lascialfari, L.; Becucci, L.; Trigari, S.; Giammanco, F. Nanostructured Films of Metal Particles Obtained by Laser Ablation. Thin Solid Films 2013,543, 118–121. [CrossRef]

[68] Simo A., Joseph V., Fenger R., Kneipp J., Rademann K. Long-Term Stable Silver Subsurface Ion-Exchanged Glasses for SERS Applications. ChemPhysChem. 2011;12:1683–1688. doi: 10.1002/cphc.201100098.

[69] Wang, H.H.; Liu, C.Y.; Wu, S. Bin; Liu, N.W.; Peng, C.Y.; Chan, T.H.; Hsu, C.F.; Wang, J.K.; Wang, Y.L. Highly raman-enhancing substrates based on silver nanoparticle arrays with tunable sub-10 nm gaps. Adv. Mater. 2006, 18, 491–495, doi:10.1002/adma.200501875.

[70] J. Yang, J. Li, Z. Du, Q. Gong, J. Teng, and M. Hong, "Laser Hybrid Micro/nano-structuring of Si Surfaces in Air and its Applications for SERS Detection," Scientific Reports 4(1), 6657 (2014).

[71] C.-H. Lin, L. Jiang, Y.-H. Chai, H. Xiao, S.-J. Chen, and H.-L. Tsai, "One-step fabrication of nanostructures by femtosecond laser for surface-enhanced Raman scattering," Opt. Express 17(24), 21581–21589 (2009).

[72] Haynes C.L., Van Duyne R.P. Nanosphere Lithography: A Versatile Nanofabrication Tool for Studies of Size-Dependent Nanoparticle Optics. J. Phys. Chem. B. 2001;105:5599–5611.

[73] Domonkos M, Kromka A. Nanosphere Lithography-Based Fabrication of Spherical Nanostructures and Verification of Their Hexagonal Symmetries by Image Analysis. Symmetry. 2022; 14(12):2642. https://doi.org/10.3390/sym14122642.

[74] Haynes C.L., Van Duyne R.P. Nanosphere Lithography: A Versatile Nanofabrication Tool for Studies of Size-Dependent Nanoparticle Optics. J. Phys. Chem. B. 2001;105:5599–5611.

[75] Wu D.-Y., Li J.-F., Ren B., Tian Z.-Q. Electrochemical Surface-Enhanced Raman Spectroscopy of Nanostructures. Chem. Soc. Rev. 2008;37:1025–1041.

[76] C. L. Haynes and R. P. Van Duyne, "Nanosphere Lithography: A Versatile Nanofabrication Tool for Studies of Size-Dependent Nanoparticle Optics," J. Phys. Chem. B 105(24), 5599–5611 (2001).

[77] Jubb A.M., Hatzinger P.B., Gu B. Trace-Level Perchlorate Analysis of Impacted Groundwater by Elevated Gold Ellipse Dimer Nanoantenna Surface-Enhanced Raman Scattering. J. Raman Spectrosc. 2017;48:518–524.

[78] Abu Hatab N.A., Oran J.M., Sepaniak M.J. Surface-Enhanced Raman Spectroscopy Substrates Created via Electron Beam Lithography and Nanotransfer Printing. ACS Nano. 2008;2:377–385.

[79] Yue W., Wang Z., Yang Y., Chen L., Syed A., Wong K., Wang X. Electron-Beam Lithography of Gold Nanostructures for Surface-Enhanced Raman Scattering. J. Micromech. Microeng. 2012;22:125007. doi: 10.1088/0960-1317/22/12/125007.

[80] Hatab N.A., Hsueh C.-H., Gaddis A.L., Retterer S.T., Li J.-H., Eres G., Zhang Z., Gu B. Free-Standing Optical Bowtie Nanoantenna with Variable Gap Size for Enhanced Raman Spectroscopy. Nano Lett. 2010;10:4952–4955. doi: 10.1021/nl102963g.

[81] Yue W., Wang Z., Yang Y., Chen L., Syed A., Wong K., Wang X. Electron-Beam Lithography of Gold Nanostructures for Surface-Enhanced Raman Scattering. J. Micromech. Microeng. 2012;22:125007. doi: 10.1088/0960-1317/22/12/125007.

[82] Zhang, Y.; Wang, G.; Yang, L.; Wang, F.; Liu, A. Recent advances in gold nanostructures based biosensing and bioimaging. Coord. Chem. Rev. 2018, 370, 1–21, doi:10.1016/j.ccr.2018.05.005.

[83] F. S. Ou, M. Hu, I. Naumov, A. Kim, W. Wu, A. M. Bratkovsky, X. Li, R. S. Williams, and Z. Li, "Hot-Spot Engineering in Polygonal Nanofinger Assemblies for Surface Enhanced Raman Spectroscopy," Nano Lett. 11(6), 2538–2542 (2011).

[84] J. Wang, K. M. Koo, E. J. H. Wee, Y. Wang, and M. Trau, "A nanoplasmonic label-free surface enhanced Raman scattering strategy for non-invasive cancer genetic subtyping in patient samples," Nanoscale 9(10), 3496–3503 (2017).

[85] S. Feng, R. Chen, J. Lin, J. Pan, Y. Wu, Y. Li, J. Chen, and H. Zeng, "Gastric cancer detection based on blood plasma surface-enhanced Raman spectroscopy excited by polarized laser light,"Biosensors and Bioelectronics 26(7), 3167–3174 (2011).

[86] Murphy, C.J.; Gole, A.M.; Stone, J.W.; Sisco, P.N.; Alkilany, A.M.; Goldsmith, E.C.; Baxter, S.C. Gold Nanoparticles in Biology: Beyond Toxicity to Cellular Imaging. Acc. Chem. Res. 2008, 41, 1721–1730, doi:10.1021/ar800035u.

[87] J. Kneipp, H. Kneipp, M. McLaughlin, D. Brown, and K. Kneipp, "In Vivo Molecular Probing of Cellular Compartments with Gold Nanoparticles and Nanoaggregates," Nano Lett. 6(10), 2225–2231 (2006).

[88] D'Acunto M. Detection of Intracellular Gold Nanoparticles: An Overview. Materials. 2018; 11(6):882. https://doi.org/10.3390/ma11060882.

[89] Kneipp, K.; Haka, A.S.; Kneipp, H.; Badizadegan, K.; Yoshizawa, N.; Boone, C.; Shafer-Peltier, K.E.; Motz, J.T.; Dasari, R.R.; Feld, M.S. Surface-Enhanced Raman Spectroscopy in Single Living Cells Using Gold Nanoparticles. Appl. Spectrosc. 2002, 56, 150–154, doi:10.1366/0003702021954557.

[90] A. Walter, A. März, W. Schumacher, P. Rösch, and J. Popp, "Towards a fast, high specific and reliable discrimination of bacteria on strain level by means of SERS in a microfluidic device,"Lab Chip 11(6), 1013–1021 (2011).

[91] Han, X.X.; Zhao, B.; Ozaki, Y. Surface-enhanced Raman scattering for protein detection. Anal. Bioanal. Chem. 2009, 394, 1719–1727, doi:10.1007/s00216-009-2702-3.

[92] Xu, H.; Bjerneld, E.J.; Käll, M.; Börjesson, L. Spectroscopy of single hemoglobin molecules by surface enhanced raman scattering. Phys. Rev. Lett. 1999, 83, 4357–4360, doi:10.1103/PhysRevLett.83.4357.

[93] X. X. Han, H. Y. Jia, Y. F. Wang, Z. C. Lu, C. X. Wang, W. Q. Xu, B. Zhao, and Y. Ozaki, "Analytical Technique for Label-Free Multi-Protein Detection Based on Western Blot and Surface-Enhanced Raman Scattering," Anal. Chem. 80(8), 2799–2804 (2008).

[94] Efrima, S., and B. V. Bronk. "Silver Colloids Impregnating or Coating Bacteria." The Journal of Physical Chemistry B, vol. 102, no. 31, American Chemical Society, 1998, pp. 5947–50. doi:10.1021/jp9813903.

[95] Lane, L.A.; Qian, X.; Nie, S. SERS Nanoparticles in Medicine: From Label-Free Detection to Spectroscopic Tagging. Chem. Rev. 2015, 115, 10489–10529, doi:10.1021/acs.chemrev.5b00265.

[96] Wang, Y.; Yan, B.; Chen, L. SERS Tags: Novel optical nanoprobes for bioanalysis. Chem. Rev. 2013, 113, 1391–1428, doi:10.1021/cr300120g.

[97] Abalde-Cela, S.; Aldeanueva-Potel, P.; Mateo-Mateo, C.; Rodríguez-Lorenzo, L.; Alvarez-Puebla, R. A.; Liz-Marzan, L. M.́ J. R. Soc., Interface 2010, 7 (Suppl 4), S435.

[98] Boca, S. C.; Astilean, S. Nanotechnology 2010, 21, 235601.

[99] Jiang, L.; Qian, J.; Cai, F.; He, S. Anal. Bioanal. Chem. 2011, 400,2793.

[100] Wang, Yuan, et al. "Reporter-Embedded SERS Tags from Gold Nanorod Seeds: Selective Immobilization of Reporter Molecules at the Tip of Nanorods." ACS Applied Materials & Interfaces, vol. 8, no. 41, American Chemical Society, 2016, pp. 28105–28115.

[101] Hada, Alexandru-Milentie, et al. “Fabrication of Gold–Silver Core–Shell Nanoparticles for Performing as Ultrabright SERS-Nanotags Inside Human Ovarian Cancer Cells.” Nanotechnology, vol. 30, no. 31, IOP Publishing Ltd, 2019, p. 315701.

[102] Contreras-Caceres, R.; Pastoriza-Santos, I.; Alvarez-Puebla, R.́A.; Perez-Juste, J.; Ferná ndez-Barbero, A.; Liz-Marzá n, L. M.́ Chem.Eur. J. 2010, 16, 9462.

[103] Shen, A. G.; Guo, J. Z.; Xie, W.; Sun, M. X.; Richards, R.; Hu, J.M. J. Raman Spectrosc. 2011, 42, 879.

[104] Fabris, L. Gold-based SERS tags for biomedical imaging. J. Opt. 2015, 17, 114002, doi:10.1088/2040-8978/17/11/114002.

[105] X. Qian, X.-H. Peng, D. O. Ansari, Q. Yin-Goen, G. Z. Chen, D. M. Shin, L. Yang, A. N. Young, M. D. Wang, and S. Nie, "In vivo tumor targeting and spectroscopic detection with surface enhanced Raman nanoparticle tags," Nature Biotechnology 26(1), 83–90 (2008).

[106] Kong, K.V.; Dinish, U.S.; Lau, W.K.O.; Olivo, M. Sensitive SERS-pH sensing in biological media using metal carbonyl functionalized planar substrates. Biosens. Bioelectron. 2014, 54, 135–140, doi:10.1016/j.bios.2013.10.052.

[107] Schafer, F.Q.; Buettner, G.R. Redox environment of the cell as viewed through the redox state of the glutathione disulfide/glutathione couple. Free Radic. Biol. Med. 2001, 30, 1191–1212, doi:10.1016/S0891-5849(01)00480–4.

[108] Kong, K.V.; Dinish, U.S.; Lau, W.K.O.; Olivo, M. Sensitive SERS-pH sensing in biological media using metal carbonyl functionalized planar substrates. Biosens. Bioelectron. 2014, 54, 135–140, doi:10.1016/j.bios.2013.10.052.

[109] Menon, S.G.; Goswami, P.C. A redox cycle within the cell cycle: Ring in the old with the new. Oncogene 2007, 26, 1101–1109, doi.

[110] El-Said, W.A.; Kim, T.H.; Chung, Y.H.; Choi, J.W. Fabrication of new single cell chip to monitor intracellular and extracellular redox state based on spectroelectrochemical method. Biomaterials 2015, 40, 80–87, doi:10.1016/j.biomaterials.2014.11.023.

[111] El-Said, W.A.; Kim, T.H.; Kim, H.; Choi, J.W. Detection of effect of chemotherapeutic agents to cancer cells on gold nanoflower patterned substrate using surface-enhanced Raman scattering and cyclic voltammetry. Biosens. Bioelectron. 2010, 26, 1486–1492, doi:10.1016/j.bios.2010.07.089.

[112] Porter M.D., Lipert R.J., Siperko L.M. SERS as a bioassay platform: Fundamentals, design, and applications. Chem. Rev. 2008;37:1001–1011. doi: 10.1039/b708461g.

[113] Wang, G.; Lipert; R.J.; Jain, M.; Kaur, S.; Chakraboty, S.; Torres, M.P.; Batra, S.K.; Brand, R.E.; Porter, M.D. Detection of the Potential Pancreatic Cancer Marker MUC4 in Serum Using Surface-Enhanced Raman Scattering. Anal. Chem. 2011, 83 (7), 2554–2561, doi: 10.1021/ac102829b.

[114] Krasnoslobodtsev, A.V.; Torres, M.P.; Kaur, S.; Vlassiouk, I.V.; Lipert, R.J.; Jain, M.; Batra, S.K.; Lyubchenko, Y.L. Nano-immunoassay with improved performance for detection of cancer biomarkers. Nanomed. Nanotechnol. Biol. Med. 2015, 11, 167–173, doi:10.1016/j.nano.2014.08.012.

[115] Song, C.; Min, L.; Zhou, N.; Yang, Y.; Yang, B.; Zhang, L.; Su, S.; Wang, L. Ultrasensitive detection of carcino-embryonic antigen by using novel flower-like gold nanoparticle SERS tags and SERS-active magnetic nanoparticles. RSC Adv. 2014, 40, 41666–41669, doi:10.1039/c4ra08402k.

[116] Kavosi, B.; Salimi, A.; Hallaj, R.; Amani, K. A highly sensitive prostate-specific antigen immunosensor based on gold nanoparticles/PAMAM dendrimer loaded on MWCNTS/chitosan/ionic liquid nanocomposite. Biosens. Bioelectron. 2014, 52, 20–28, doi:10.1016/j.bios.2013.08.012.

[117] Diamandis, E.P.; Helle, S.I.; Yu, H.; Melegos, D.N.; Lundgren, S.; Lonning, P.E. Prognostic value of plasma prostate specific antigen after megestrol acetate treatment in patients with metastatic breast carcinoma. Cancer 1999, 85, 891–898, doi:10.1002/(SICI)1097-0142(19990215)85:4<891::AID-CNCR17>3.0.CO;2-K.

[118] G. Bouwmans, F. Luan, J. Knight, P. St. J. Russell, L. Farr, B. Mangan, and H. Sabert, "Properties of a hollow-core photonic bandgap fiber at 850 nm wavelength," Optics Express 11(14), 1613 (2003).

[119] F. Couny, F. Benabid, and P. S. Light, "Large-pitch kagome-structured hollow-core photonic crystal fiber," Opt. Lett. 31(24), 3574–3576 (2006).

[120] T. D. Bradley, G. T. Jasion, J. R. Hayes, Yong Chen, L. Hooper, H. Sakr, M. Alonso, A. Taranta, A. Saljoghei, H. C. Mulvad, M. Fake, I. A. K. Davidson, N. V. Wheeler, E. N. Fokoua, Wei Wang, S. R. Sandoghchi, D. J. Richardson, and F. Poletti, "Antiresonant Hollow Core Fibre with 0.65 dB/km Attenuation across the C and L Telecommunication Bands," in 45th European Conference on Optical Communication (ECOC 2019) (Institution of Engineering and Technology, 2019), 294.

[121] S. Yiou, P. Delaye, A. Rouvie, J. Chinaud, R. Frey, G. Roosen, P. Viale, S. Février, P. Roy, J.-L. Auguste, and J.-M. Blondy, "Stimulated Raman scattering in an ethanol core microstructured optical fiber," Optics Express 13(12), 4786–4791 (2005).

[122] T. A. Birks, D. M. Bird, T. D. Hedley, J. M. Pottage, and P. S. J. Russell, "Scaling laws and vector effects in bandgap-guiding fibres," Optics Express 12(1), 69–74 (2004).

[123] G. Antonopoulos, F. Benabid, T. A. Birks, D. M. Bird, J. C. Knight, and P. S. J. Russell, "Experimental demonstration of the frequency shift of bandgaps in photonic crystal fibers due to refractive index scaling," Optics Express 14(7), 3000–3006 (2006).

[124] E. Nguema, D. Férachou, G. Humbert, J.-L. Auguste, and J.-M. Blondy, "Broadband terahertz transmission within the air channel of thin-wall pipe," Opt. Lett. 36(10), 1782–1784 (2011).

[125] F. Benabid, "Stimulated Raman Scattering in Hydrogen-Filled Hollow-Core Photonic Crystal Fiber," Science 298(5592), 399–402 (2002).

[126] F. Couny, F. Benabid, and P. S. Light, "Large-pitch kagome-structured hollow-core photonic crystal fiber," Opt. Lett. 31(24), 3574–3576 (2006).

[127] J. C. Knight, T. A. Birks, P. S. J. Russell, and D. M. Atkin, "All-silica single-mode optical fiber with photonic crystal cladding," Optics Letters 21(19), 1547–1549 (1996).

[128] G. K. L. Wong, A. Y. H. Chen, S. W. Ha, R. J. Kruhlak, S. G. Murdoch, R. Leonhardt, J. D. Harvey, and N. Y. Joly, "Characterization of chromatic dispersion in photonic crystal fibers using scalar modulation instability," Opt. Express 13(21), 8662–8670 (2005).

[129] F. Beffara, J. Perumal, A. Puteri Mahyuddin, M. Choolani, S. A. Khan, J.-L. Auguste, S. Vedraine, G. Humbert, U. S. Dinish, and M. Olivo, "Development of highly reliable SERS-active photonic crystal fiber probe and its application in the detection of ovarian cancer biomarker in cyst fluid," Journal of Biophotonics 13(3), e201960120 (2020).

[130] N. Zhang, G. Humbert, T. Gong, P. P. Shum, K. Li, J.-L. Auguste, Z. Wu, D. J. J. Hu, F. Luan, Q. X. Dinh, M. Olivo, and L. Wei, "Side-channel photonic crystal fiber for surface enhanced Raman scattering sensing," Sensors and Actuators B: Chemical 223, 195–201 (2016).

[131] Y. Guo, M. K. Khaing Oo, K. Reddy, and X. Fan, "Ultrasensitive Optofluidic Surface-Enhanced Raman Scattering Detection with Flow-through Multihole Capillaries," ACS Nano 6(1), 381–388 (2012).

[132] I. Shavrin, S. Novotny, and H. Ludvigsen, "Mode excitation and supercontinuum generation in a few-mode suspended-core fiber," Optics Express 21(26), 32141–32150 (2013).

[133] N. Zhang, K. Li, Y. Cui, Z. Wu, P. P. Shum, J.-L. Auguste, X. Q. Dinh, G. Humbert, and L. Wei, "Ultra-sensitive chemical and biological analysis via specialty fibers with built-in microstructured optofluidic channels," Lab Chip 18(4), 655–661 (2018).

[134] A. M. Apetrei, M. C. Phan Huy, N. Belabas, J. A. Levenson, J.-M. Moison, J. M. Dudley, G. Mélin, A. Fleureau, L. Galkovsky, and S. Lempereur, "A dense array of small coupled waveguides in fiber technology: trefoil channels of microstructured optical fibers," Optics Express 16(25), 20648–20655 (2008).

[135] B. Lee, S. Roh, J. Park, "Current status of micro- and nano-structured optical fiber sensors", Opt. Fiber Technol., 15 (2009), pp. 209-221.

[136] A.M. Cubillas, S. Unterkofler, T.G. Euser, B.J.M. Etzold, A.C. Jones, P.J. Sadler, P. Wasserscheid, P.St.J. Russell, Photonic crystal fibers for chemical sensing and photochemistry", Chem. Soc. Rev., 42 (2013), pp. 8629-8648.

[137] Z. Tan, X. Li, Y. Chen, P. Fan, "Improving the sensitivity of fiber surface plasmon resonance sensor by filling liquid in a hollow core photonic crystal fiber", Plasmonics, 9 (2013), pp. 167-173.

[138] X. Yang, C. Shi, R. Newhouse, J.Z. Zhang, C. Gu, "Hollow-core photonic crystal fibers for surface-enhanced Raman scattering probes", Int. J. Opt., 2011 (2011),754610.

[139] X. Fan, I.M. White, "Optofluidic microsystems for chemical and biological analysis", Nat. Phot., 5 (2011), pp. 591-597.

[140] F. M. Cox, A. Argyros, M. C. J. Large, and S. Kalluri, "Surface enhanced Raman scattering in a hollow core microstructured optical fiber," Optics Express 15(21), 13675–13681 (2007).

[141] X. Yang, A. S. P. Chang, B. Chen, C. Gu, and T. C. Bond, "High sensitivity gas sensing by Raman spectroscopy in photonic crystal fiber," Sensors and Actuators B: Chemical 176, 64–68 (2013).

[142] S. Unterkofler, R. J. McQuitty, T. G. Euser, N. J. Farrer, P. J. Sadler, and P. S. J. Russell, "Microfluidic integration of photonic crystal fibers for online photochemical reaction analysis," Optics Letters 37(11), 1952–1954 (2012).

[143] L. Xiao, N. V. Wheeler, N. Healy, and A. C. Peacock, "Integrated hollow-core fibers for nonlinear optofluidic applications," Optics Express 21(23), 28751–28757 (2013).

[144] Flavien Beffara, Georges Humbert, Jean-Louis Auguste, Jayakumar Perumal, U. S. Dinish, and Malini Olivo, "Optimization and performance analysis of SERS-active suspended core photonic crystal fibers," Opt. Express 28, 23609-23619 (2020).

[145] Y. Han, S. Tan, M. K. K. Oo, D. Pristinski, S. Sukhishvili, and H. Du, "Towards Full-Length Accumulative Surface-Enhanced Raman Scattering-Active Photonic Crystal Fibers," Advanced Materials 22(24), 2647–2651 (2010).

[146] V. S. Tiwari, A. Khetani, M. Naji, and H. Anis, "Study of surface enhanced Raman scattering (SERS) within hollow core photonic crystal fiber," in 2009 IEEE Sensors (IEEE, 2009),Christchurch, New Zealand, 367–370.

[147] M. K. Khaing Oo, Y. Han, J. Kanka, S. Sukhishvili, and H. Du, "Structure fits the purpose: photonic crystal fibers for evanescent-field surface-enhanced Raman spectroscopy," Optics Letters 35(4), 466–468 (2010).

[148] Y. Zhang, D. Yong, X. Yu, L. Xia, D. Liu, and Y. Zhang, "Amplification of Surface-Enhanced Raman Scattering in Photonic Crystal Fiber Using Offset Launch Method," Plasmonics 8(2), 209–215 (2013).

[149] Eijkelenborg, M. V. Imaging with Microstructured Polymer Fibre. Opt. Express 2004, 12, 342–346.

[150] Beffara F, Humbert G, Auguste JL, Perumal J, Dinish US, Olivo M. Optimization and performance analysis of SERS-active suspended core photonic crystal fibers. Opt Express. 2020 Aug 3;28(16):23609-23619.

[151] Beffara F, Perumal J, Puteri Mahyuddin A, Choolani M, Khan SA, Auguste JL, Vedraine S, Humbert G, Dinish US, Olivo M. Development of highly reliable SERS-active photonic crystal fiber probe and its application in the detection of ovarian cancer biomarker in cyst fluid. J Biophotonics. 2020 Mar;13(3):e201960120.

[152] Y. Liu, Y. Zhang, M. Tardivel, M. Lequeux, X. Chen, W. Liu, J. Huang, H. Tian, Q. Liu, G. Huang, R. Gillibert, M. L. de la Chapelle, and W. Fu, "Evaluation of the Reliability of Six Commercial SERS Substrates," Plasmonics 15(3), 743–752 (2020).

[153] Bantz, Kyle C., et al. "Recent Progress in SERS Biosensing." Physical Chemistry Chemical Physics, vol. 13, no. 24, 2011, pp. 11551–11567. Royal Society of Chemistry,

[154] Pinkie J. Eravuchira, Martina Banchelli, Cristiano D'Andrea, Marella De Angelis, Paolo Matteini, Israel Gannot, "Hollow core photonic crystal fiber-assisted Raman spectroscopy as a tool for the detection of Alzheimer's disease biomarkers," J. Biomed. Opt. 25(7) 077001 (2 July 2020).

[155] X. Yang, A. Y. Zhang, D. A. Wheeler, T. C. Bond, C. Gu, and Y. Li, "Direct molecule-specific glucose detection by Raman spectroscopy based on photonic crystal fiber," Analytical and Bioanalytical Chemistry 402(2), 687–691 (2012).

[156] Yan Di, et al. "Highly Sensitive Broadband Raman Sensing of Antibiotics in Step-Index Hollow-Core Photonic Crystal Fibers." ACS Photonics, vol. 4, no. 1, American Chemical Society, 2017, pp. 138-145.

[157] S. Hanf, R. Keiner, D. Yan, J. Popp, T. Frosch, Fiber-enhanced Raman multigas spectroscopy: a versatile tool for environmental gas sensing and breath analysis, Anal. Chem. 86 (2014) 5278e5285.

[158] A. Khetani, A. Momenpour, E. I. Alarcon, and H. Anis, "Hollow core photonic crystal fiber for monitoring leukemia cells using surface enhanced Raman scattering (SERS)," Biomedical Optics Express 6(11), 4599–4609 (2015).

[159] A. Khetani, V. S. Tiwari, A. Momenpour, and H. Anis, "Monitoring of adenosine within hollow core photonic crystal fiber by surface enhanced Raman scattering (SERS)," in 2011 11th IEEE International Conference on Nanotechnology (2011), 973–977.

[160] U SD, Fu CY, Soh KS, Ramaswamy B, Kumar A, Olivo M. Highly sensitive SERS detection of cancer proteins in low sample volume using hollow core photonic crystal fiber. Biosens Bioelectron. 2012; 33: 293-8.

[161] Dinish US, Balasundaram G, Chang YT, Olivo M. Sensitive multiplex detection of serological liver cancer biomarkers using SERS-active photonic crystal fiber probe. J Biophotonics. 2014; 7: 956-65.

[162] T. Gong, N. Zhang, K. V. Kong, D. Goh, C. Ying, J.-L. Auguste, P. P. Shum, L. Wei, G. Humbert, K.-T. Yong, and M. Olivo, "Rapid SERS monitoring of lipid-peroxidation-derived protein modifications in cells using photonic crystal fiber sensor.

[163] Dai, P.; Li, H.; Huang, X.; Wang, N.; Zhu, L. Highly Sensitive and Stable Copper-Based SERS Chips Prepared by a Chemical Reduction Method. Nanomaterials 2021, 11, 2770.

[164] N. S. Kapany and J. J. Burke, "Waveguide Mode Lauching," in Optical Waveguides, Quantum Electronics–Principles and Applications (Academic Press, 1972), 159–179.

[165] T. Ma, A. Markov, L. Wang, and M. Skorobogatiy, "Graded index porous optical fibers – dispersion management in terahertz range," Opt. Express 23(6), 7856–7869 (2015).

[166] T. A. Birks, W. J. Wadsworth, and P. S. J. Russell, "Supercontinuum generation in tapered fibers," Optics Letters 25(19), 1415–1417 (2000).

[167] G. Humbert, W. Wadsworth, S. Leon-Saval, J. Knight, T. Birks, P. St. J. Russell, M. Lederer, D. Kopf, K. Wiesauer, E. Breuer, and D. Stifter, "Supercontinuum generation system for optical coherence tomography based on tapered photonic crystal fibre," Optics Express 14(4), 1596–1603 (2006).

[168] T. G. Euser, J. S. Y. Chen, M. Scharrer, P. S. J. Russell, N. J. Farrer, and P. J. Sadler, "Quantitative broadband chemical sensing in air-suspended solid-core fibers," Journal of Applied Physics 103(10), 103108 (2008).

[169] Willets KA, Van Duyne RP. Localized surface plasmon resonance spectroscopy and sensing. Annu Rev Phys Chem. 2007;58:267-97. doi: 10.1146/annurev.physchem.58.032806.104607. PMID: 17067281.

[170] Haynes CL, Van Duyne RP. 2003. Plasmon-sampled surface-enhanced Raman excitation spectroscopy. J. Phys. Chem. B 107:7426–33.

[171] Wriedt, T. (2012). Mie Theory: A Review. In: Hergert, W., Wriedt, T. (eds) The Mie Theory. Springer Series in Optical Sciences, vol 169. Springer, Berlin, Heidelberg. https://doi.org/10.1007/978-3-642-28738-1_2.

[172] https://www.bbisolutions.com/en/product/gold-colloid-60nm-100ml.

[173] https://nanocomposix.com/pages/mie-theory-calculator.

[174] García-Soto, M.J., González-Ortega, O. Synthesis of silica-core gold nanoshells and some modifications/variations. Gold Bull 49, 111–131 (2016). https://doi.org/10.1007/s13404-016-0188-2.

[175] https://nanocomposix.com/products/150-nm-bioready-gold-nanoshells-for-passive-conjugation.

[176] Rasch MR, Sokolov KV, Korgel BA (2009) Limitations on the optical tunability of small diameter gold nanoshells. Langmuir 25:11777–11785.

[177] https://www.nanopartz.com/hollow-gold-nanoshells.asp.

[178] https://www.nanopartz.com/bare-gold-nanostars.asp.

[179] Kane Yee, "Numerical solution of initial boundary value problems involving maxwell's equations in isotropic media," in IEEE Transactions on Antennas and Propagation, vol. 14, no. 3, pp. 302-307, May 1966.

[180] Taflove, A., & Hagness, S. C. (2005). Computational Electrodynamics: The Finite-Difference Time-Domain Method (3rd ed.). Artech House.

[181] P.B. Johnson, R.W. Christy, Optical Constants of the Noble Metals, Phys. Rev. B.6 (1972) 4370–4379. https://doi.org/10.1103/PhysRevB.6.4370.

[182] https://www.tyndall.ie/.

[183] Markopoulos, A.K. Current aspects on oral squamous cell carcinoma. Open Dent. J. 2012, 6, 126.

[184] Chen, X.-J.; Zhang, X.-Q.; Liu, Q.; Zhang, J.; Zhou, G. Nanotechnology: A promising method for oral cancer detection and diag nosis. J. Nanobiotechnology 2018, 16, 52.

[185] Kah, J.C.Y.; Kho, K.W.; Lee, C.G.L.; James, C.; Sheppard, R.; Shen, Z.X.; Soo, K.C.; Olivo, M.C. Early diagnosis of oral cancer based on the surface plasmon resonance of gold nanoparticles. Int. J. Nanomed. 2007, 2, 785–798.

[186] Connolly, J.M.; Davies, K.; Kazakeviciute, A.; Wheatley, A.M.; Dockery, P.; Keogh, I.; Olivo, M. Non-invasive and label-free detection of oral squamous cell carcinoma using saliva surface-enhanced Raman spectroscopy and multivariate analysis. Nano med. Nanotechnol. Biol. Med. 2016, 12, 1593–1601.

[187] Wang, Q.; Gao, P.; Wang, X.; Duan, Y. Investigation and identification of potential biomarkers in human saliva for the early diagnosis of oral squamous cell carcinoma. Clin. Chim. Acta 2014, 427, 79–85.

[188] Ibrahim, O.; Toner, M.; Flint, S.; Byrne, H.J.; Lyng, F.M. The Potential of Raman Spectroscopy in the Diagnosis of Dysplastic and Malignant Oral Lesions. Cancers 2021, 13, 619.

[189] Siddra Maryam, Sanathana Konugolu Venkata Sekar, M. Daniyal Ghauri, Edward Fahy, Marcelo Saito Nogueira, et al.. Mobile multi-configuration clinical translational Raman system for oral cancer application. Analyst, 2023, 148 (7), pp.1514-1523. ⟨10.1039/d2an01921c⟩. ⟨hal-04306138⟩.

[190] Pantaleo, G., Correia, B., Fenwick, C. et al. Antibodies to combat viral infections: development strategies and progress. Nat Rev Drug Discov 21, 676–696 (2022). https://doi.org/10.1038/s41573-022-00495-3.

[191] Pollap, A.; Świt, P. Recent Advances in Sandwich SERS Immunosensors for Cancer Detection. Int. J. Mol. Sci. 2022, 23, 4740. https://doi.org/10.3390/ijms23094740.

[192] Wiercigroch, E.; Swit, P.; Brzozka, A.; Pięta, Ł.; Malek, K. Dual-enhancement and dual-tag design for SERS-based sandwich immunoassays: Evaluation of a metal–metal effect in 3D architecture. Microchim. Acta 2022, 189, 32.

[193] Turan, E.; Zengin, A.; Suludere, Z.; Kalkan, N.O.; Tamer, U. Construction of a sensitive and selective plasmonic biosensor for prostate specific antigen by combining magnetic molecularly-imprinted polymer and surface-enhanced Raman spectroscopy. Talanta 2022, 237, 122926.

[194] Hong, W.-J.; Seo, H.K.; Jung, Y.M. SERS Immunoassay Using Microcontact Printing for Application of Sensitive Biosensors. Bull. Korean Chem. Soc. 2011, 32, 4281–4285.

[195] Feng, Z.; Zhou, J.; Chen, D.; Wang, S.-M.; Wang, X.-J.; Xie, S.-S. Hypersensitization Immunoassay of Prostate-specific Antigen Based on SERS of Sandwich-type Au/Ag Nanostructure. Chin. J. Lumin. 2015, 36, 1064–1070.

[196] Baniukevic, J.; Boyaci, J.H.; Bozkurt, A.G.; Tamer, U.; Ramanavicius, A.; Ramanaviciene, A. Magnetic gold nanoparticles in SERS-based sandwich immunoassay for antigen detection by well oriented antibodies. Biosens. Bioelectron. 2013, 43, 281–288.

[197] Ge, M.; Wei, C.; Xu, M.M.; Fang, C.W.; Yuan, Y.X.; Gua, R.; Yao, J.L. Ultra-sensitive magnetic immunoassay of HE4 based on surface enhanced Raman spectroscopy. Anal. Methods 2015, 7, 6489–6495.

[198] M. Yamashita, E. Passegue, TNF-alpha coordinates hematopoietic stem cell survival and myeloid regeneration. Cell Stem Cell 25, 357–372 (2019). https://doi.org/10.1016/j.stem.2019.05.019.

[199] B. Ungar, I. Levy, Y. Yavne, M. Yavzori, O. Picard et al., Optimizing anti-TNF-α therapy: Serum levels of infliximab and adalimumab are associated with mucosal healing in patients with inflammatory bowel diseases. Clin. Gastroenterol. Hepatol. 14, 550-557.e552 (2016).

[200] Y. Wang, J. Xu, X. Zhang, C. Wang, Y. Huang et al., TNF-α-induced LRG1 promotes angiogenesis and mesenchymal stem cell migration in the subchondral bone during osteoarthritis. Cell Death Dis. 8, e2715 (2017).

[201] H.A. Sahibzada, Z. Khurshid, R.S. Khan, M. Naseem, K.M. Siddique et al., Salivary IL-8, IL-6 and TNF-alpha as potential diagnostic biomarkers for oral cancer. Diagnostics 7(2), 21 (2017).

[202] Y. Ma, Y. Ren, Z.J. Dai, C.J. Wu, Y.H. Ji et al., IL-6, IL-8 and TNF-alpha levels correlate with disease stage in breast cancer patients. Adv. Clin. Exp. Med. 26, 421–426 (2017).

[203] Elena Castellanos-Rizaldos, Dominik G. Grimm, Vasisht Tadigotla, James Hurley, John Healy, Patricia L. Neal, Mia Sher, Raajdeep Venkatesan, Chris Karlovich, Mitch Raponi, Anne Krug, Mikkel Noerholm, Jihane Tannous, Bakhos A. Tannous, Luis E. Raez, Johan K. Skog; Exosome-Based Detection of EGFR T790M in Plasma from Non–Small Cell Lung Cancer Patients. Clin Cancer Res 15 June 2018; 24 (12): 2944–2950.

[204] www.abcam.com

Published work and conferences

Papers

Benazza A, Beffara F, Auguste JL, Olivo M, Dinish US, Humbert G. “Reliable and easy-to-use SERS spectroscopy probe using a tapered opto-fluidic photonic crystal fiber”. Opt Express. 2024 Jan 29;32(3):3440-3450. doi: 10.1364/OE.501911. PMID: 38297564.

Conferences

Benazza A, Beffara F, Auguste JL, Olivo M, Dinish US, Humbert G, “ Reliable and easy-to-use SERS spectroscopy platform based on a tapered opto-fluidic photonic crystal fiber”, Proc. SPIE PC12372, Optical Fibers and Sensors for Medical Diagnostics, Treatment and Environmental Applications XXIII, PC1237203 (6 March 2023) (**oral**).

M. Daniyal Ghauri, Siddra Maryam, **Benazza A**, Georges Humbert, Giovanni Santacroce, Marietta Iacucci, Katarzyna Komolibus, Sanathana Konugolu Venkata Sekar, Stefan Andersson-Engels, Rekha Gautam, “Waveguide-Enhanced Raman Spectroscopy Analysis of Biofluids”, "13th International Conference on Clinical Spectroscopy" FP20(PP84), SPEC 2024, 02-06 June 2024, Loannina, Greece (poster)

Benazza A, Beffara F, Auguste JL, Olivo M, Dinish US, Humbert G, “Plateforme de spectroscopie SERS fiable et facile d’emploi fondée sur une fibre opto-fluidique effilée”, Diagnostic optique et photonique, Journées Nationales d'Optique Guidée (OPTIQUE), NICE, 07/2022 (**oral**).

Benazza A, Beffara F, Auguste JL, Olivo M, Dinish US, Humbert G, “plateforme de spectroscopie sers fiable et facile d’emploi fondée sur une fibre opto-fluidique effilée”, Journée de la photonique, Limoges, FRANCE 18 Novembre, 2022 (**Poster**)

Benazza A, Beffara F, Auguste JL, Olivo M, Dinish US, Humbert G, “ Photonic crystal fiber based biosensing platform: Towards next generation liquid biopsy needle-probe”, 11th Doctoral Student Workshop, March 28, 2023 (**oral**).

INNOV-FIBRE 2024 - Thematic school dedicated to optical fibers, Oléron, France, on June 10-14, 2024

Development of optofluidic fiber-based SERS platform for efficient biosensing applications

Current methods for disease detection, such as traditional tissue and liquid biopsies, often face challenges related to invasiveness, limited sensitivity, and lengthy procedures, which can impede early diagnosis and effective treatment. Surface-Enhanced Raman Spectroscopy (SERS) offers a promising alternative due to its non-invasive nature, high sensitivity, and ability to detect trace levels of biomarkers with specificity. However, conventional SERS platforms struggle with issues of reproducibility and practicality. This thesis investigates the use of photonic crystal fibers (PCFs) as innovative sensors for SERS, addressing these challenges and enhancing its application in biosensing and medical diagnostics. PCFs offer increased interaction surfaces and reliability compared to traditional planar substrates, enabling effective analyte detection crucial for early diagnostics. Through the optimization of tapered PCFs, we achieve improved light coupling efficiency and measurement consistency, balancing core size to enhance both sensitivity and reproducibility. The development of a plug-and-play SERS sensing system further enhances usability and consistency, proving its practicality for real-world clinical applications. In addition to fiber design, the research delves into the relationship between nanoparticle (NP) properties and SERS signal enhancement. Experimental investigations identified 60 nm gold nanospheres as the most efficient shape for providing consistent and superior SERS performance. Our analysis shows that anchoring NPs within the fibers prevents aggregation, maintaining their plasmonic properties essential for reliable SERS performance. Numerical simulations validate that these NPs offer optimal electric field enhancement relative to absorption, making them particularly effective for SERS applications. Practical applications of SERS-based PCFs are demonstrated in detecting disease biomarkers, such as TNF-alpha, using a novel sandwich-based approach. Future research will continue to expand these applications to more complex targets, such as extracellular vesicles, increasing the impact of SERS-based PCFs in medical diagnostics.

Keywords: Surface enhanced Raman spectroscopy, optical fiber, Nanoparticle, biosensing.

Développement d'une plateforme SERS basée sur des fibres optofluidiques pour des applications de biosensibilité efficaces.

Les méthodes actuelles de détection des maladies, telles que les biopsies traditionnelles de tissus et de liquides, rencontrent souvent des défis liés à l'invasivité, à la sensibilité limitée et à la durée des procédures, ce qui peut entraver le diagnostic précoce et le traitement efficace. La Spectroscopie Raman exaltée de Surface (SERS) offre une alternative prometteuse grâce à sa nature non invasive, sa haute sensibilité et sa capacité à détecter des niveaux traces de biomarqueurs avec spécificité. Cependant, les plateformes SERS conventionnelles rencontrent des problèmes de fiabilité des mesures. Cette thèse explore l'utilisation de fibres à cristaux photoniques (PCFs) comme capteurs innovants pour SERS, abordant ces défis et améliorant son application dans la biodétection et le diagnostic médical. Les PCFs offrent des surfaces d'interaction accrues et une fiabilité supérieure par rapport aux substrats planaires traditionnels, permettant une détection efficace des analytes cruciale pour les diagnostics précoces. Grâce à l'optimisation des PCFs effilées, nous obtenons une meilleure efficacité de couplage de la lumière, en équilibrant la taille du cœur pour améliorer à la fois la sensibilité et la reproductibilité. La mise au point d'un système de détection SERS plug-and-play simplifie l'utilisation, démontrant ainsi son efficacité pour les applications cliniques pratiques. En plus de la conception des fibres, la recherche explore la relation entre les propriétés des nanoparticules (NP) et l'amélioration du signal SERS. Des investigations expérimentales ont identifié les nanosphères d'or de 60 nm comme la forme la plus efficace pour offrir des performances SERS constantes et supérieures. Notre analyse montre que l'ancrage des NP à l'intérieur des fibres empêche leur agrégation, préservant ainsi leurs propriétés plasmoniques essentielles pour une performance SERS fiable. Des simulations numériques valident que ces NPs offrent un renforcement optimal du champ électrique par rapport à l'absorption, les rendant particulièrement efficaces pour les applications SERS. Les applications pratiques des PCFs basés sur SERS sont démontrées dans la détection de biomarqueurs de maladies, tels que le TNF-alpha, en utilisant une approche innovante basée sur le sandwich. Les recherches futures continueront à élargir ces applications à des cibles plus complexes, telles que les vésicules extracellulaires, augmentant ainsi l'impact des PCFs basés sur SERS dans le diagnostic médical.

Mots clés: Spectroscopie Raman exaltée en surface, fibre optique, nanoparticules, biodétection.